

**Non-linear Finite Element Thermo-Hydrodynamic Analysis of Oil  
Ring Seals Used in High Pressure Centrifugal Compressors**

by  
**Sanjay K. Baheti**

Dissertation submitted to the Faculty of the  
Virginia Polytechnic Institute and State University  
in partial fulfillment of the requirements for the degree of  
Doctor of Philosophy  
in  
Mechanical Engineering

**APPROVED:**



---

Dr. R. G. Kirk (Chair)



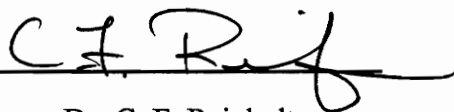
---

Dr. C. E. Knight



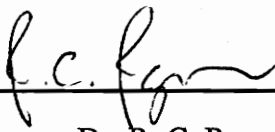
---

Dr. R. G. Mitchiner



---

Dr. C. F. Reinholtz



---

Dr. R. C. Rogers

August, 1995  
Blacksburg, Virginia

c.2

LD  
5655  
V856  
1995  
B344  
c.2

DEDICATED TO

MY PARENTS

# **Non-linear Finite Element Thermo-Hydrodynamic Analysis of Oil Ring Seals Used in High Pressure Centrifugal Compressors**

by

Sanjay K. Baheti

Dr. R. G. Kirk, Chairman

Mechanical Engineering

(ABSTRACT)

The analysis of oil seals is of great concern for the proper design of high pressure centrifugal compressors, because they can have significant influence on the dynamic stability of the compressor rotor. The lack of adequate analytical tools highlight the need for this type of study. An analytical tool to evaluate the oil seal characteristics, perform linear stability analysis of the compressor rotor and nonlinear transient analysis of the compressor rotor and the seal ring has been developed. An iterative finite element method is used to solve the non-linear and coupled hydrodynamic and thermal equations for the pressure and temperature distributions in oil seals. The perturbation technique is employed to determine the static and dynamic characteristics of oil seals. The hydrodynamic forces are calculated by integrating the pressure distribution along and around the oil seal. Eigenvalue analysis is performed to do the linear stability analysis of the compressor rotor. A numerical integration technique is used to solve the non-linear equations of motion of the seal ring and compressor rotor. This analysis has the ability to handle tapered seals, circumferentially grooved seals and seals with shaft misalignment.

Results obtained from linear stability analysis and non-linear transient analysis for different seal geometries, including shaft misalignment, are presented. For centered seals, results obtained are in good agreement with a previous finite difference analysis. At an

operating eccentricity of 0.098, the maximum percentage differences in the cross-coupled stiffness and direct damping coefficients obtained from this analysis and the finite difference analysis are 5.1 % and 1.5 % respectively. For eccentric seals, use of the true temperature distribution gives significantly different results. At an operating eccentricity of 0.497, the maximum percentage differences in the cross-coupled stiffness and direct damping coefficients obtained from this analysis and the finite difference analysis are 17.7 % and 22.9 % respectively. This analysis shows that the sharp edge grooves decrease the axial flow rate. In addition, groove depth typically applied to industrial seals is shown to be effective in breaking up the hydrodynamic pressures. Tapered and circumferentially grooved seals are shown to enhance both the locking mechanism in the seal ring and the dynamic stability of the compressor rotor. The resulting computer program gives the designer of compressors with liquid seals a much needed capability that is not available from any other known source.

## **Acknowledgments**

A special thanks extended to the members of my advisory committee: Dr. R. G Kirk, Dr. C E. Knight, Dr. R. G. Mitchiner, Dr. C. F. Reinholtz and Dr. R. C. Rogers. I am deeply indebted to my advisor, Dr. R. G. Kirk, for the support, guidance and encouragement he provided throughout this research effort.

I would like to thank all my family members for their love, understanding and unconditional support in all my endeavors. I would also like to thank my special friends Jyutika, Ramesh, Erik and Raju for their help.

## Table of Contents

<b>1.0</b>	<b>INTRODUCTION</b>	<b>1</b>
<b>2.0</b>	<b>GOVERNING EQUATIONS FOR OIL SEAL ANALYSIS</b>	<b>10</b>
2.1	Reynolds Equation	12
2.2	Ocvirk's Short Bearing Solution	14
2.3	Energy Equation	14
2.4	Perturbation Technique	16
2.4.1	Stiffness Coefficients	17
2.4.2	Damping Coefficients	18
2.5	Mathematical Model for Linear Stability Analysis	19
2.6	Mathematical Model for Non-linear Transient Analysis	21
2.6.1	Equations of Motion of Journal	23
2.6.2	Equations of Motion of the Seal Ring	25
2.7	Flow Equation	30
<b>3.0</b>	<b>IMPLEMENTATION OF FINITE ELEMENT METHOD</b>	<b>32</b>
3.1	Discretization of the Domain	33
3.2	Finite Element Formulation of the Reynolds Equation	33
3.2.1	Variational Formulation of the Reynolds Equation	33
3.2.2	Finite Element Model of the Reynolds Equation	38
3.3	Finite Element Formulation of the Energy Equation	40
3.3.1	Variational formulation of the Energy Equation	40
3.3.2	Finite Element Model of the Energy Equation	41

3.4	Boundary Conditions	43
3.4.1	Pressure Boundary Condition	43
3.4.2	Adaptive Temperature Boundary Condition	43
3.5	Interpolation Functions	44
3.6	Nonlinearity	46
3.7	Cavitation	48
3.8	Solution Procedure for Temperature and Pressure Distributions	48
3.9	Solution Procedure for Linear Stability Analysis	49
3.10	Solution Procedure for Non-linear Transient Analysis	50
<b>4.0</b>	<b>OPTIMIZATION, CONVERGENCE AND STABILITY OF THE NUMERICAL SOLUTION</b>	<b>54</b>
4.1	Constraint Equations	54
4.2	Bandwidth Optimization of the Finite Element Stiffness Matrices	56
4.3	Convergence of Finite Element Results	58
4.4	Convergence and Stability of the Numerical Solution for Non-linear Transient Analysis	61
<b>5.0</b>	<b>RESULTS AND DISCUSSION OF STRAIGHT SEALS</b>	<b>63</b>
5.1	Comparison of the Results of a Typical Seal	63
5.2	Linear Stability Analysis Results	69
5.3	Non-linear Transient Analysis Results	85
<b>6.0</b>	<b>INFLUENCE OF TAPERED GEOMETRY ON THE SEAL CHARACTERISTICS</b>	<b>102</b>
6.1	Tapered Seals	102
6.2	Linear Stability Analysis Results	104

6.3	Non-linear Transient Analysis Results	119
<b>7.0</b>	<b>INFLUENCE OF CIRCUMFERENTIAL GROOVES ON THE SEAL CHARACTERISTICS</b>	<b>128</b>
7.1	Circumferentially Grooved Seals	128
7.1.1	Seal with Circumferential Groove	130
7.1.2	Seal with Circumferential Groove and Step	130
7.2	Linear Stability Analysis Results	132
7.3	Non-linear Transient Analysis Results	155
<b>8.0</b>	<b>INFLUENCE OF SHAFT MISALIGNMENT ON THE SEAL CHARACTERISTICS</b>	<b>167</b>
8.1	Shaft Misalignment	167
8.2	Linear Stability Analysis Results	169
<b>9.0</b>	<b>CONCLUSIONS AND FUTURE WORK</b>	<b>187</b>
9.1	Conclusions from Linear Stability Analysis Results	187
9.2	Conclusions from Non-linear Transient Analysis Results	189
9.3	Recommendations for Future Work	190
	<b>REFERENCES</b>	<b>191</b>
	<b>VITA</b>	<b>193</b>

## List of Figures

<u>Number</u>	<u>Title</u>	<u>Page</u>
1	Picture of One-Land Oil Ring Seal	2
2	Picture of Three-Land Oil Ring Seal	3
3	Cross-section of a Typical Seal Assembly	5
4	Seal Cross-section Showing General Coordinate System	11
5	Schematic Model for Linear Stability Analysis	20
6	Coordinate System Used for Non-linear Transient Analysis	22
7	Schematic Model for Non-linear Transient Analysis	24
8	Free Body Diagram of the Seal Ring	26
9	Figure Showing Axial Pressure Load and Spring Load on the Seal Ring	27
10	Figure Showing the Velocity Vectors of the Seal Ring at Two Consecutive Points in Transient analysis	28
11	Typical Finite Element Mesh	34
12	Typical Infinitesimal Element	36
13	Four-noded Bilinear Element	45
14	Block Diagram of the Program for Linear Stability Analysis	51
15	Block Diagram of the Program for Non-linear Transient Analysis	53
16	Different Node Numbering Schemes (For Discussion)	57
17	Temperature and Pressure Distribution in the Straight Seal Operating Speed = 33.333 Hz (2000 RPM); Operating Eccentricity ( $e_{rY}$ ) = 0.098	66

## List of Figures (Continued)

<u>Number</u>	<u>Title</u>	<u>Page</u>
18	Temperature and Pressure Distribution in the Straight Seal Operating Speed = 133.333 Hz (8000 RPM); Operating Eccentricity ( $e_{rY}$ ) = 0.497	67
19	Temperature and Pressure Distribution in the Straight Seal Operating Speed = 133.333 Hz (8000 RPM); Operating Eccentricity ( $e_{rY}$ ) = 0.7	70
20	Temperature and Pressure Distribution in the Straight Seal Operating Speed = 133.333 Hz (8000 RPM); Operating Eccentricity ( $e_{rY}$ ) = 0.8	71
21	Plot of Direct Stiffness vs. Eccentricity Ratio for Different Speeds. Supply Pressure = 4.136 MPa	72
22	Plot of Direct Stiffness vs. Eccentricity Ratio for Different Speeds. Supply Pressure = 4.136 MPa	73
23	Plot of Cross-coupled Stiffness vs. Eccentricity Ratio for Different Speeds. Supply Pressure = 4.136 MPa	75
24	Plot of Cross-coupled Stiffness vs. Eccentricity Ratio for Different Speeds. Supply Pressure = 4.136 MPa	76
25	Plot of Direct Damping vs. Eccentricity Ratio for Different Speeds Supply Pressure = 4.136 MPa	77
26	Plot of Direct Damping vs. Eccentricity Ratio for Different Speeds Supply Pressure = 4.136 MPa	78
27	Plot of Cross-coupled Damping vs. Eccentricity Ratio for Different Speeds. Supply Pressure = 4.136 MPa	79
28	Plot of Cross-coupled Damping vs. Eccentricity Ratio for Different Speeds. Supply Pressure = 4.136 MPa	80

## List of Figures (Continued)

<u>Number</u>	<u>Title</u>	<u>Page</u>
29	Plot of Damped Natural Frequency vs. Eccentricity Ratio for Different Speeds. Supply Pressure = 4.136 MPa	81
30	Plot of Growth Factor vs. Eccentricity Ratio for Different Speeds Supply Pressure = 4.136 MPa	82
31	Plot of Axial Flow Rate vs. Eccentricity Ratio for Different Speeds Supply Pressure = 4.136 MPa	83
32	Plot of Maximum Temperature vs. Eccentricity Ratio for Different Speeds. Supply Pressure = 4.136 MPa	84
33	Plot of Direct Stiffness vs. Eccentricity Ratio for Different Speeds Supply Pressure = 0.827 MPa	86
34	Plot of Growth Factor vs. Eccentricity Ratio for Different Speeds Supply Pressure = 0.827 MPa	87
35	Plot of Axial Flow Rate vs. Eccentricity Ratio for Different Speeds. Supply Pressure = 0.827 MPa	88
36	Plot of Maximum Temperature vs. Eccentricity Ratio for Different Speeds. Supply Pressure = 0.827 MPa	89
37	Plots of Eccentricities and Absolute Seal Positions vs. Time for a Straight Seal. Operating Speed = 100 Hz (6000 RPM); Frictional Force = 444.8 N	91
38.	Plots of Eccentricities and Absolute Seal Positions vs. Time for a Straight Seal. Operating Speed = 133.33 Hz (8000 RPM); Frictional Force = 444.8 N	92
39	Plots of Hydrodynamic Forces and Maximum Temperature vs. Time for a Straight Seal. Operating Speed = 133.33 Hz (8000 RPM); Frictional Force = 444.8 N	93

## List of Figures (Continued)

<u>Number</u>	<u>Title</u>	<u>Page</u>
40	Transient Response of the Straight Seal and the Rotor Operating Speed = 133.33 Hz (8000 RPM); Frictional Force = 444.8 N	94
41	Plots of Eccentricities and Absolute Seal Positions vs. Time for a Straight Seal. Operating Speed = 133.33 Hz (8000 RPM); Frictional Force = 889.6 N	96
42	Plots of Hydrodynamic Forces and Maximum Temperature vs. Time for a Straight Seal. Operating Speed = 133.33 Hz (8000 RPM); Frictional Force = 889.6 N	97
43	Transient Response of the Straight Seal and the Rotor Operating Speed = 133.33 Hz (8000 RPM); Frictional Force = 889.6 N	98
44	Plots of Eccentricities and Absolute Seal Positions vs. Time for a Straight Seal. Operating Speed = 200 Hz (12000 RPM); Frictional Force = 889.6 N	99
45	Plots of Eccentricities and Absolute Seal Positions vs. Time for a Straight Seal. Operating Speed = 200 Hz (12000 RPM); Frictional Force = 1334.4 N	100
46	Geometry of a Typical Tapered Seal	103
47	Temperature and Pressure Distributions in the Tapered Seal $C_i = 0.1016$ mm (0.004 in); $C_e = 0.0889$ mm (0.0035 in) Operating Speed = 133.333 Hz (8000 RPM); Operating Eccentricity ( $e_{rY}$ ) = 0.7	105
48	Plot of Direct Stiffness vs. Eccentricity Ratio for Seals with and without Taper. Operating Speed = 166.67 Hz (10000 RPM)	107
49	Plot of Direct Stiffness vs. Eccentricity Ratio for Seals with and without Taper. Operating Speed = 166.67 Hz (10000 RPM)	108

## List of Figures (Continued)

<u>Number</u>	<u>Title</u>	<u>Page</u>
50	Plot of Cross-coupled Stiffness vs. Eccentricity Ratio for Seals with and without Taper Operating Speed = 166.67 Hz (10000 RPM)	109
51	Plot of Cross-coupled Stiffness vs. Eccentricity Ratio for Seals with and without Taper Operating Speed = 166.67 Hz (10000 RPM)	110
52	Plot of Direct Damping vs. Eccentricity Ratio for Seals with and without Taper. Operating Speed = 166.67 Hz (10000 RPM)	111
53	Plot of Direct Damping vs. Eccentricity Ratio for Seals with and without Taper. Operating Speed = 166.67 Hz (10000 RPM)	112
54	Plot of Cross-coupled Damping vs. Eccentricity Ratio for Seals with and without Taper Operating Speed = 166.67 Hz (10000 RPM)	113
55	Plot of Cross-coupled Damping vs. Eccentricity Ratio for Seals with and without Taper Operating Speed = 166.67 Hz (10000 RPM)	114
56	Plot of Damped Natural Frequency vs. Eccentricity Ratio for Seals with and without Taper. Operating Speed = 166.67 Hz (10000 RPM)	115
57	Plot of Growth Factor vs. Eccentricity Ratio for Seals with and without Taper. Operating Speed = 166.67 Hz (10000 RPM)	116
58	Plot of Axial Flow Rate vs. Eccentricity Ratio for Seals with and without Taper. Operating Speed = 166.67 Hz (10000 RPM)	117
59	Plot of Maximum Temperature vs. Eccentricity Ratio for Seals with and without Taper Operating Speed = 166.67 Hz (10000 RPM)	118

## List of Figures (Continued)

<u>Number</u>	<u>Title</u>	<u>Page</u>
60	Plots of Eccentricities and Absolute Seal Positions vs. Time for a Tapered Seal. Operating Speed = 133.33 Hz (8000 RPM); Frictional Force = 444.8 N; Exit Clearance = 0.0889 mm	120
61	Plots of Hydrodynamic Forces and Maximum Temperature vs. Time for a Tapered Seal. Operating Speed = 133.33 Hz (8000 RPM); Frictional Force = 444.8 N; Exit Clearance = 0.0889 mm	121
62	Transient Response of the Tapered Seal and the Rotor Operating Speed = 133.33 Hz (8000 RPM); Frictional Force = 444.8 N; Exit Clearance = 0.0889 mm	122
63.	Plots of Eccentricities and Absolute Seal Positions vs. Time for a Tapered Seal. Operating Speed = 200 Hz (12000 RPM); Frictional Force = 889.6 N; Exit Clearance = 0.0889 mm	123
64	Plots of Hydrodynamic Forces and Maximum Temperature vs. Time for a Tapered Seal. Operating Speed = 200 Hz (12000 RPM); Frictional Force = 889.6 N; Exit Clearance = 0.0889 mm	124
65	Plots of Eccentricities and Absolute Seal Positions vs. Time for a Tapered Seal. Operating Speed = 200 Hz (12000 RPM); Frictional Force = 1334.4 N; Exit Clearance = 0.0889 mm	126
66	Plots of Eccentricities and Absolute Seal Positions vs. Time for a Tapered Seal. Operating Speed = 200 Hz (12000 RPM); Frictional Force = 889.6 N; Exit Clearance = 0.0635 mm	127
67	Circumferentially Grooved Seal	129
68	Seal having Circumferential Groove with Sinusoidal Cross-section	131
69	Seal having Circumferential Groove and Step with Sinusoidal Cross-sections	133

## List of Figures (Continued)

<u>Number</u>	<u>Title</u>	<u>Page</u>
70	Temperature and Pressure Distributions in a Seal with Circumferential Groove. Groove Depth = 0.381 mm (0.015 in); Operating Speed = 183.33 Hz (11000 RPM); Operating Eccentricity ( $e_{rY}$ ) = 0.5	135
71	Temperature and Pressure Distributions in a Seal with Circumferential Groove. Groove Depth = 0.762 mm (0.030 in); Operating Speed = 183.33 Hz (11000 RPM); Operating Eccentricity ( $e_{rY}$ ) = 0.5	136
72.	Temperature and Pressure Distributions in a Seal with Circumferential Groove. Groove Depth = 1.270 mm (0.05 in); Operating Speed = 183.33 Hz (11000 RPM); Operating Eccentricity ( $e_{rY}$ ) = 0.5	137
73	Temperature and Pressure Distributions in a Seal with Circumferential Groove and Step. Groove Depth = 0.762 mm (0.030 in); Operating Speed = 183.33 Hz (11000 RPM); Operating Eccentricity ( $e_{rY}$ ) = 0.5	138
74	Plot of Direct Stiffness vs. Eccentricity ratio for Seals with and without Circumferential Grooves Operating Speed = 183.33 Hz (11000 RPM)	139
75	Plot of Cross-coupled Stiffness vs. Eccentricity ratio for Seals with and without Circumferential Grooves Operating Speed = 183.33 Hz (11000 RPM)	140
76	Plot of Cross-coupled Stiffness vs. Eccentricity ratio for Seals with and without Circumferential Grooves Operating Speed = 183.33 Hz (11000 RPM)	141
77	Plot of Direct Damping vs. Eccentricity ratio for Seals with and without Circumferential Grooves Operating Speed = 183.33 Hz (11000 RPM)	142

## List of Figures (Continued)

<u>Number</u>	<u>Title</u>	<u>Page</u>
78	Plot of Direct Damping vs. Eccentricity ratio for Seals with and without Circumferential Grooves Operating Speed = 183.33 Hz (11000 RPM)	143
79	Plot of Cross-coupled Damping vs. Eccentricity ratio for Seals with and without Circumferential Grooves Operating Speed = 183.33 Hz (11000 RPM)	144
80	Plot of Cross-coupled Damping vs. Eccentricity ratio for Seals with and without Circumferential Grooves Operating Speed = 183.333 Hz (11000 RPM)	145
81	Plot of Growth Factor vs. Eccentricity ratio for Seals with and without Circumferential Grooves Operating Speed = 183.33 Hz (11000 RPM)	147
82	Plot of Axial Flow Rate vs. Eccentricity ratio for Seals with and without Circumferential Grooves Operating Speed = 183.33 Hz (11000 RPM)	148
83	Plot of Maximum Temperature vs. Eccentricity ratio for Seals with and without Circumferential Grooves Operating Speed = 183.33 Hz (11000 RPM)	149
84	Plot of Direct Stiffness vs. Eccentricity ratio for Seals with and without Circumferential Grooves and Steps. Groove Depth = 0.762 mm; Operating Speed = 183.33 Hz (11000 RPM)	150
85	Plot of Cross-coupled Stiffness vs. Eccentricity ratio for Seals with and without Circumferential Grooves and Steps. Groove Depth = 0.762 mm; Operating Speed = 183.33 Hz (11000 RPM)	151
86	Plot of Direct Damping vs. Eccentricity ratio for Seals with and without Circumferential Grooves and Steps. Groove Depth = 0.762 mm; Operating Speed = 183.33 Hz (11000 RPM)	152

## List of Figures (Continued)

<u>Number</u>	<u>Title</u>	<u>Page</u>
87	Plot of Growth Factor vs. Eccentricity ratio for Seals with and without Circumferential Grooves and Steps. Groove Depth = 0.762 mm; Operating Speed = 183.33 Hz (11000 RPM)	153
88	Plot of Axial Flow Rate vs. Eccentricity ratio for Seals with and without Circumferential Grooves and Steps. Groove Depth = 0.762 mm; Operating Speed = 183.33 Hz (11000 RPM)	154
89	Plots of Eccentricities and Absolute Seal Positions vs. Time for a Seal with Circumferential Groove. Operating Speed = 200 Hz (12000 RPM); Frictional Force = 889.6 N; Groove Depth = 0.381 mm	156
90	Plots of Eccentricities and Absolute Seal Positions vs. Time for a Seal with Circumferential Groove. Operating Speed = 200 Hz (12000 RPM); Frictional Force = 889.6 N; Groove Depth = 0.762 mm	157
91	Plots of Hydrodynamic Forces and Axial Flow Rates vs. Time for a Seal with Circumferential Groove. Operating Speed = 200 Hz (12000 RPM); Frictional Force = 889.6 N; Groove Depth = 0.381 mm	158
92	Plots of Hydrodynamic Forces and Axial Flow Rates vs. Time for a Seal with Circumferential Groove. Operating Speed = 200 Hz (12000 RPM); Frictional Force = 889.6 N; Groove Depth = 0.762 mm	159
93	Plots of Eccentricities and Absolute Seal Positions vs. Time for a Seal with Circumferential Groove and Taper. Operating Speed = 200 Hz (12000 RPM); Frictional Force = 889.6 N; Groove Depth = 0.381 mm; Exit Clearance = 0.0889 mm	161
94	Plots of Eccentricities and Absolute Seal Positions vs. Time for a Seal with Circumferential Groove and Taper. Operating Speed = 200 Hz (12000 RPM); Frictional Force = 1334.4 N; Groove Depth = 0.381 mm; Exit Clearance = 0.0889 mm	162

## List of Figures (Continued)

<u>Number</u>	<u>Title</u>	<u>Page</u>
95	Plots of Hydrodynamic Forces and Maximum Temperature vs. Time for a Seal with Circumferential Groove and Taper. Operating Speed = 200 Hz (12000 RPM); Frictional Force = 889.6 N; Groove Depth = 0.381 mm; Exit Clearance = 0.0889 mm	163
96	Plots of Hydrodynamic Forces and Maximum Temperature vs. Time for a Seal with Circumferential Groove and Taper. Operating Speed = 200 Hz (12000 RPM); Frictional Force = 1334.4 N; Groove Depth = 0.381 mm; Exit Clearance = 0.0889 mm	164
97	Plots of Eccentricities and Absolute Seal Positions vs. Time for a Seal with Circumferential Groove and Taper. Operating Speed = 200 Hz (12000 RPM); Frictional Force = 889.6 N; Groove Depth = 0.381 mm; Exit Clearance = 0.0635 mm	165
98	Transient Response of the Tapered and Circumferentially Grooved Seal and the Rotor. Operating Speed = 200 Hz (12000 RPM); Frictional Force = 889.6 N; Groove Depth = 0.381 mm; Exit Clearance = 0.0635 mm	166
99	Misalignment of Shaft in X-Y and X-Z Planes	168
100	Temperature and Pressure Distributions in Seal with Shaft Misalignment. $\gamma_Z = 0.102^\circ$ ; Operating Speed = 166.67 Hz (10000 RPM); Operating Eccentricity ( $e_{rYC}$ ) = 0.4	170
101	Temperature and Pressure Distributions in Seal with Shaft Misalignment. $\gamma_Y = -0.102^\circ$ ; Operating Speed = 166.67 Hz (10000 RPM); Operating Eccentricity ( $e_{rYC}$ ) = 0.4	171
102	Plot of Direct Stiffness vs. Shaft Misalignment Angle for Seals Operating at Different Eccentricity Ratios Operating Speed = 166.67 Hz (10000 RPM)	173

## List of Figures (Continued)

<u>Number</u>	<u>Title</u>	<u>Page</u>
103	Plot of Direct Stiffness vs. Shaft Misalignment Angle for Seals Operating at Different Eccentricity Ratios Operating Speed = 166.67 Hz (10000 RPM)	174
104	Plot of Cross-coupled Stiffness vs. Shaft Misalignment Angle for Seals Operating at Different Eccentricity Ratios Operating Speed = 166.67 Hz (10000 RPM)	175
105	Plot of Direct Damping vs. Shaft Misalignment Angle for Seals Operating at Different Eccentricity Ratio Operating Speed = 166.67 Hz (10000 RPM)	176
106	Plot of Growth Factor vs. Shaft Misalignment Angle for Seals Operating at Different Eccentricity Ratios Operating Speed = 166.67 Hz (10000 RPM)	177
107	Plot of Damped Natural Frequency vs. Shaft Misalignment Angle for Seals Operating at Different Eccentricity Ratios Operating Speed = 166.67 Hz (10000 RPM)	178
108	Plot of Axial Flow Rate vs. Shaft Misalignment Angle for Seals Operating at Different Eccentricity Ratios Operating Speed = 166.67 Hz (10000 RPM)	179
109	Plot of Maximum Temperature vs. Shaft Misalignment Angle for Seals Operating at Different Eccentricity Ratios Operating Speed = 166.67 Hz (10000 RPM)	180
110	Plot of Direct Stiffness vs. Shaft Misalignment Angle for Seals Operating at Different Eccentricity Ratios Operating Speed = 166.67 Hz (10000 RPM)	182
111	Plot of Direct Stiffness vs. Shaft Misalignment Angle for Seals Operating at Different Eccentricity Ratios Operating Speed = 166.67 Hz (10000 RPM)	183

## List of Figures (Continued)

<u>Number</u>	<u>Title</u>	<u>Page</u>
112	Plot of Cross-coupled Stiffness vs. Shaft Misalignment Angle for Seals Operating at Different Eccentricity Ratios Operating Speed = 166.67 Hz (10000 RPM)	184
113	Plot of Direct Damping vs. Shaft Misalignment Angle for Seals Operating at Different Eccentricity Ratios Operating Speed = 166.67 Hz (10000 RPM)	185
114	Plot of Growth Factor vs. Shaft Misalignment Angle for Seals Operating at Different Eccentricity Ratios Operating Speed = 166.67 Hz (10000 RPM)	186

## List of Tables

<u>Number</u>	<u>Title</u>	<u>Page</u>
1	Results of a typical seal obtained from different mesh sizes	60
2	Common Specifications Used for the Results in this Dissertation	64
3.	Comparison of Results Obtained from Current Analysis and Finite Difference Analysis	68

## Nomenclature

$C$	clearance ( L )
$C_b$	bearing damping ( F-t/L )
$C_c$	coefficient of contraction
$C_e$	clearance at the exit ( L )
$C_i$	clearance at the inlet ( L )
$C_p$	specific heat of fluid ( FL/TM )
$C_{ZZ}, C_{ZY}, C_{YZ}, C_{YY}$	damping coefficients of seal ( F-t/L )
$D_g$	depth of the groove ( L )
$e_d$	resultant eccentricity ( L )
$e_{dY}$	eccentricity in Y-direction ( L )
$e_{dZ}$	eccentricity in Z-direction ( L )
$e_{dYC}$	eccentricity in Y-direction at the seal center ( L )
$e_{dZC}$	eccentricity in Z-direction at the seal center ( L )
$e_r$	resultant eccentricity ratio
$e_{rY}$	eccentricity ratio in Y-direction
$e_{rZ}$	eccentricity ratio in Z-direction
$e_{rYC}$	eccentricity ratio in Y-direction at the seal center
$e_{rZC}$	eccentricity ratio in Z-direction at the seal center
$F_u$	force due to unbalanced mass ( F )
$F_Y$	hydrodynamic force in Y-direction ( F )
$F_Z$	hydrodynamic force in Z-direction ( F )
$F^f$	frictional force between the seal ring and the lapped face ( F )
$F_Y^f, F_Z^f$	components of $F^f$ in Y and Z directions ( F )

$h$	fluid film thickness ( L )
$H_s$	height of the step ( L )
$K_b$	bearing damping ( F/L )
$K_{ZZ}, K_{ZY}, K_{YZ}, K_{YY}$	stiffness coefficients of seal ( F/L )
$L$	length of the seal ( L )
$L_g$	length of the groove ( L )
$L_s$	length of the step ( L )
$L_l$	length of the land ( L )
$m_s$	mass of seal ( M )
$m_u$	unbalanced mass of the shaft ( M )
$M_j$	half mass of journal ( M )
$N$	number of nodes in the mesh
$O_j$	journal center
$O_s$	seal center
$P$	pressure ( F/L <sup>2</sup> )
$P_d$	discharge pressure ( F/L <sup>2</sup> )
$P_s$	supply pressure ( F/L <sup>2</sup> )
$Q_v$	volume flow rate or leakage ( L <sup>3</sup> /t )
$Q_i$	internal force at node i
$R$	radius of journal ( L )
$t$	time ( t )
$T$	temperature ( T )
$T_M$	maximum temperature ( T )
$T_s$	supply temperature ( T )
$T_w$	weighted average exit temp. with respect to mass flowrate ( T )

$U$	journal speed ( L/t )
$U_i$	temperature or pressure at node i
$V_{Y'}, V_{Z'}$	velocities of the journal with respect to seal ( L/t )
$x - y$	plane used to draw the mesh
$Y - Z$	fixed coordinate system
$Y' - Z'$	coordinate system fixed to seal
$Y_j, Z_j$	journal positions ( L )
$\dot{Y}_j, \dot{Z}_j$	journal velocities ( L/t )
$\ddot{Y}_j, \ddot{Z}_j$	journal accelerations ( L/t <sup>2</sup> )
$Y_s, Z_s$	seal positions ( L )
$\dot{Y}_s, \dot{Z}_s$	seal velocities ( L/t )
$\ddot{Y}_s, \ddot{Z}_s$	seal accelerations ( L/t <sup>2</sup> )
$\alpha$	attitude angle
$\gamma$	fluid density ( M/L <sup>3</sup> )
$\gamma_Y$	misalignment of the shaft about Y-axis
$\gamma_Z$	misalignment of the shaft about Z-axis
$\delta$	convergence tolerance
$\zeta$	growth factor
$\theta$	angle from the negative Y' -axis
$\lambda$	damped natural frequency (1/t)
$\mu$	oil viscosity ( Ft/L <sup>2</sup> )
$\Psi_i$	interpolation function
$\hat{\Psi}_i$	interpolation function in terms of normalized coordinates
$\omega$	rotational speed of shaft ( 1/t )

# Chapter 1

## INTRODUCTION

During the last fifteen years, very serious problems have been encountered due to unstable subsynchronous vibration of centrifugal compressors. Usually, this subsynchronous vibration takes place when the running speeds are greater than twice the lowest rotor critical speed and magnifies so sharply with increase in running speed that either further increase in running speed is impossible or the equipment is damaged severely. These instabilities not only demand expensive redesigns or modifications, but also cause major delays in the engineering projects. One potential source for these subsynchronous instabilities is oil seals. Oil seals are used in centrifugal compressors to prevent the leakage of the compressor gas as a result of the positive sealing of the liquid gas interface on each end of the compressor. No less than eight rotors during the past two years have been identified as having rotor vibration above specification as a direct result of the oil seal ring design. Hence, it is important to include oil seals in the stability analysis of the compressor rotor.

Oil seals are also called floating ring seals because they have zero rotational velocity and are not rigidly fixed to the compressor casing. Figures 1 and 2 show pictures

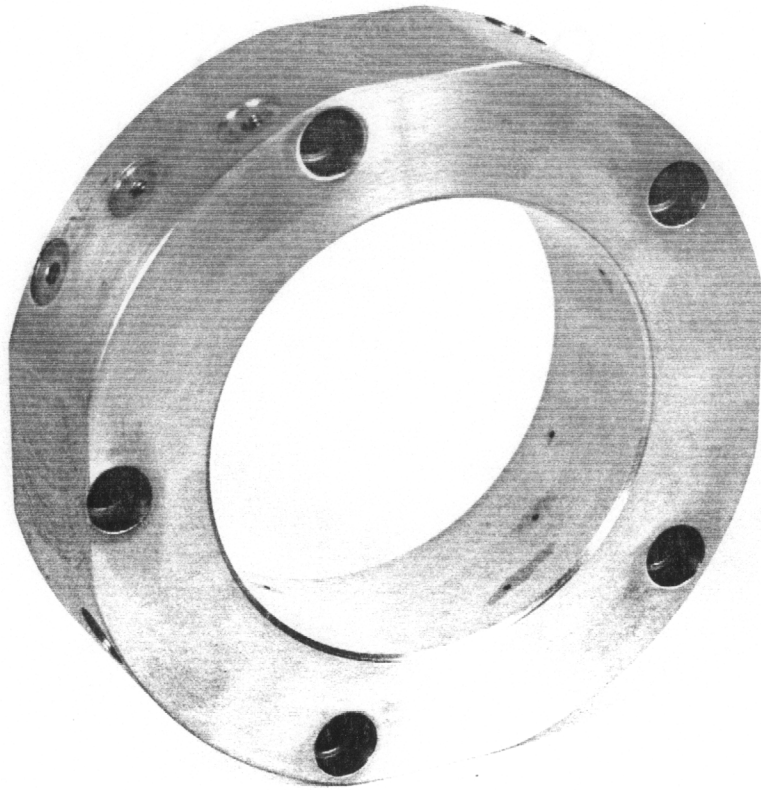


**Figure 1. Picture of One-Land Oil Ring Seal**

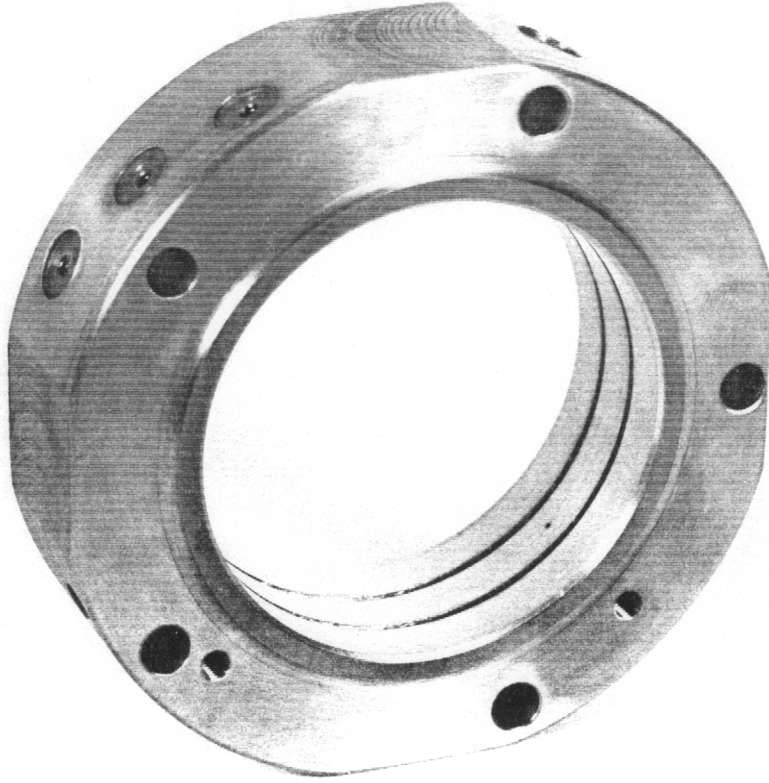


**Figure 2. Picture of Three-Land Oil Ring Seal**

of one-land and three-land oil ring seals respectively. It can be seen that they are similar to  $360^\circ$  fluid film bearings in geometry but they behave differently because they are not fixed like journal bearings and have different pressure and temperature boundary conditions. The seals can be locked or floating depending upon the operating conditions. When the seals are locked they behave like journal bearings but are usually under much higher pressures and proper consideration must be given for cavitation of the fluid film.

Figure 3 shows the longitudinal section of a typical floating ring seal assembly. The inner seal and the outer seal are both preloaded by springs which help the initial seating of the seals on their lapped faces. An anti rotation pin is provided for the outer seal ring. Oil enters the seal assembly at the supply pressure of  $P + \Delta P$ . The pressure of the oil that flows through the outer seal falls to  $P_d$  and the pressure of the oil that flows through the inner seal falls to  $P$ , the suction pressure of the compressor. So, as the oil flows through the seal, its pressure decreases and temperature increases because of fluid friction. Pressurized fluid in-between the shaft and the seal generates hydrodynamic forces on the shaft and the seal. In general, the hydrodynamic forces are non-linear functions of the relative position and velocities of the shaft with respect to the seal. If the seal is locked and the shaft whirls with a small radius then the hydrodynamic forces can be linearized and expressed in terms of linear stiffness and damping coefficients. Subsequently, eigenvalue analysis can be performed to study the stability of the compressor shaft. But if the seal is floating, it typically whirls with a large enough radius to make the hydrodynamic forces non-linear functions of the velocities and displacements of the seal and journal. So, non-linear transient analysis needs to be done to study the locking conditions of the seal ring or the dynamic stability of the compressor rotor and the seal ring while it is floating.

It is also important to study the leakage flow rate of the sealant fluid, because the discharged fluid is degassed and cooled before recycling. For economical operation, the

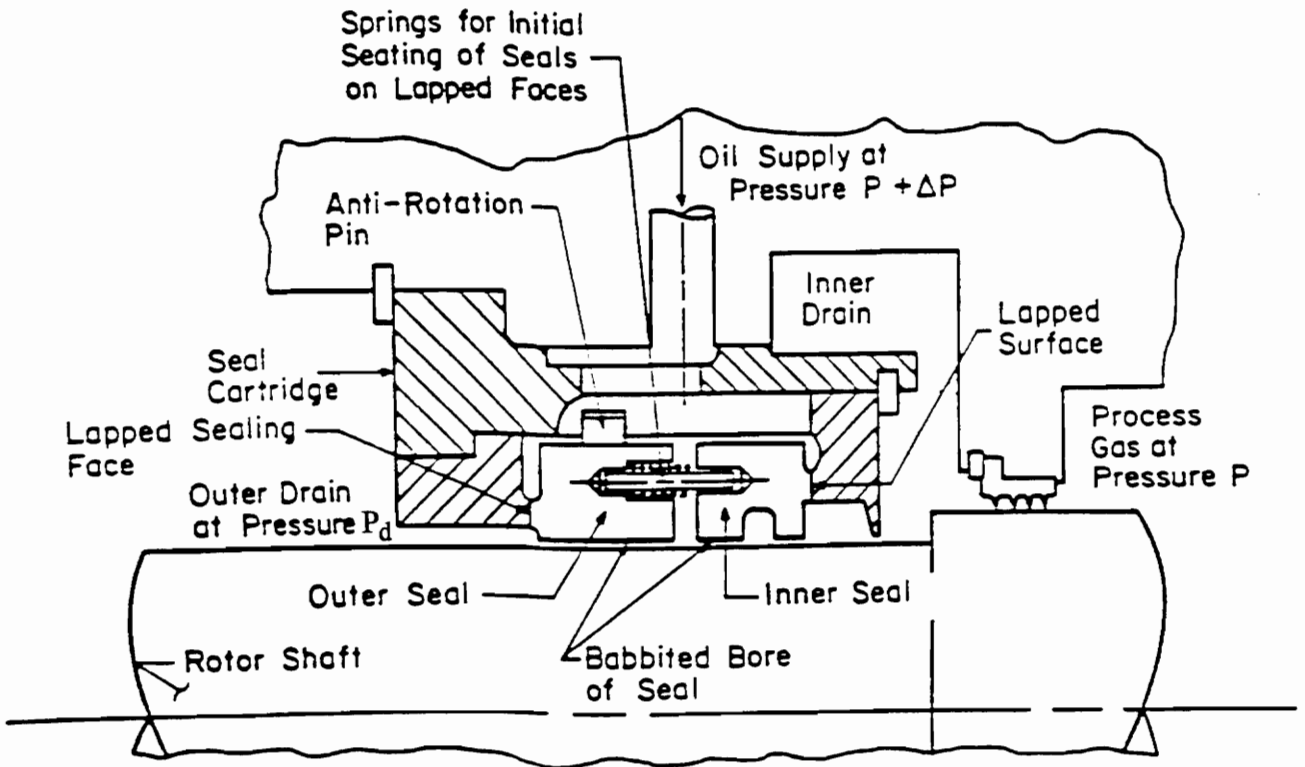


**Figure 3. Cross-section of a Typical Seal Assembly**  
 (The above figure is taken from reference 18)

leakage should be minimized. The study of maximum temperature in the oil seals is important for the thermal design of the oil seal. The babbitt on the inner surface of oil seal is known to melt at about 165 °C and maximum fluid-film temperatures are predicted to exceed this value for some operating conditions studied in this research.

The latest designs of oil seals include axial taper in addition to circumferential grooves on their inner surface. The primary motive behind using the axial taper and the circumferential grooves is to suppress the oil seal induced subsynchronous vibration mentioned above. These modifications change the oil seal characteristics significantly. Hence, it is important to study the effect of axial taper and circumferential grooves on the stability, leakage flow, and maximum temperature.

Most of the previous oil seal analyses (to be discussed below) assumed that the seal becomes locked because of the frictional force between the lapped face and the compressor casing. The shaft then moves with a small whirl radius about a fixed operating eccentricity. With this as a basis, linearized hydrodynamic forces expressed in terms of stiffness and damping coefficients were obtained and used to analyze the stability of the shaft. Black (1,2) has documented the analysis of high-axial flow seals (Reynolds number > 2000) which is applicable for small clearance, high pressure water seals, but not the lower Reynolds number axial flow typical of turbo-compressor oil seals. In most of the earlier analyses calculation of viscosity and temperature distribution was not addressed accurately. Kirk and Miller (3) applied the classical short bearing theory as developed by Ockvirk (4) to model the inner and outer seal rings. They used constant fluid viscosity in their model. Later, Kirk and Nicholas (5) discussed an approximate temperature flow balance to determine the operating fluid film temperature. Solution of the energy equation was not included in that analysis. Kirk (6) presented a method of calculating the operating eccentricity of a single breakdown seal cartridge. However, the actual swirling flow in the

axial flow seal was ignored in all of these early investigations. More recent publications (7,8) have used an improved linear axial temperature distribution for single and multiple ring designs with an iterative solution to find the individual operating eccentricities for a given flow balance. Thermal effects due to fluid friction and extrusion were considered. This assumption will be shown to be valid for the seals that are almost centered and operating at low speeds and invalid for seals operating at high eccentricities and high speeds. In the case of eccentric seals the true temperature distribution should be determined by solving the energy equation. The true temperature is also important for the thermal design of oil seals. All these previous analyses did not have the capability to analyze the tapered and grooved seals.

Emerick (9) documented an operating experience of a compressor which presented an interesting history of sporadic increase in subsynchronous shaft vibration. He concluded that locked seals exert significant destabilizing forces on the rotor and hence seal lock-up should be avoided. He also concluded that in the case of locked seals, stable operation of the compressor is possible if the effective length of the seal is reduced with circumferential grooves.

In some experimental studies, Kirk, Browne and Dorton, (10,11) noticed that axial shaft misalignment plays an important role in oil seal ring locking calculation. A minor shaft misalignment was found to have a significant influence on the seal ring centering forces. The concern that misalignment affects the dynamic characteristics of the seal has been verified by this analysis.

The goal of this research is to develop an analytical tool to:

- 1) Determine the pressure and temperature distributions in the oil seal by solving the non-linear and coupled hydrodynamic and thermal equations.
- 2) Determine the stiffness and damping coefficients of oil seals.

- 3) Perform linear stability analysis of the compressor rotor using the above stiffness and damping coefficients when the seal is locked.
- 4) Perform non-linear transient analysis of the seal ring and the compressor shaft in the case of floating seals to study its locking conditions.
- 5) Model seals with taper, circumferential grooves, and shaft misalignment.
- 6) Determine the leakage flow through the oil seal.

A discussion of the contents of the remaining chapters follows to serve as an outline for the work presented in this dissertation. Chapter 2 discusses the basic governing equations used to determine the pressure, temperature distributions and leakage in oil seals. Perturbation techniques used to evaluate the linear static and dynamic coefficients of oil seals and the mathematical model to do the linear stability analysis of the compressor in the case of locked seals are presented. Equations of motion required for the non-linear transient analysis of the compressor rotor and the seal ring are given.

The variational form and the finite element models of the coupled and non-linear Reynolds and the energy equations, for the pressure and temperature distributions respectively, are developed in Chapter 3. Boundary conditions and an iterative technique to handle the non-linearity in these equations are also presented. In addition, cavitation phenomenon in oil seals is discussed. Solution procedures of the mathematical models for linear stability analysis and non-linear transient analysis are also discussed at the closure of Chapter 3.

Next, Chapter 4 presents an appropriate node numbering scheme used to optimize the bandwidth of the stiffness matrix of the finite element models. Different methods of solving the matrix equations of finite element model are discussed. Details of the convergence of the finite element solution is given. Perturbation constants used in the evaluation of linear stiffness and damping coefficients and convergence tolerances used for

the non-linear transient analysis and linear stability analysis are also given. Finally, details of numerical integration scheme to do non-linear transient analysis are presented.

In Chapter 5 a comparison of the results for a straight seal obtained from this analysis and from another finite difference analysis are presented. More results in terms of temperature and pressure distributions, stiffness and damping characteristics, growth factor, damped natural frequency, axial flow rate for straight seals operating in field and test stand conditions are presented. Different parameters from the transient analysis of the rotor and the seal ring in the case of straight seals for different speeds and frictional forces are presented.

The modification required in the governing equations to handle tapered seals is presented in Chapter 6. The results comparing the various parameters from linear stability analysis of tapered seals with straight seals are presented. Finally, the results obtained from transient analysis of tapered seals are presented.

Chapter 7 presents the modification required in the governing equations to handle seals with rounded and sharp edged circumferential grooves. The results comparing the various parameters from linear stability analysis of circumferentially grooved seals with straight (ungrooved) seals are given. Finally, the results obtained from non-linear transients analysis of various circumferentially grooved seals are discussed using various forms of data presentation.

The modification required in the governing equations to handle seals having shaft misalignment is presented in Chapter 8. The results showing the influence of shaft misalignment on various parameters obtained from linear stability analysis are given.

Finally, Chapter 9 presents the conclusions drawn from the results presented in this dissertation and gives recommendations for future work in this area.

## **Chapter 2**

### **GOVERNING EQUATIONS FOR OIL SEAL ANALYSIS**

This chapter reviews how the Reynolds equation and the energy equation originally derived for fluid film bearings may be extended to oil ring seals. The limitations of the past approaches which assumed a temperature distribution and neglected the circumferential pressure gradient are given. The perturbation technique used to evaluate the stiffness and damping coefficients is discussed. The mathematical models used for linear stability analysis and non-linear transient analysis are derived. Finally, this chapter will present the equation used to calculate the axial flow rate through the seal.

Reynolds and the energy equations, used in this study, were originally derived for pressure and temperature distributions in the fluid film bearings. Since oil seals have the same geometry as the fluid film bearings, the same equations can be used to solve the pressure and temperature distributions in the seals. Figure 4 shows the basic configuration and terminology used in this analysis. The Reynolds and the energy equations depend upon the relative position and the relative velocity of the shaft with respect to the seal. So, in this configuration only the relative position and velocity of the shaft with respect to the

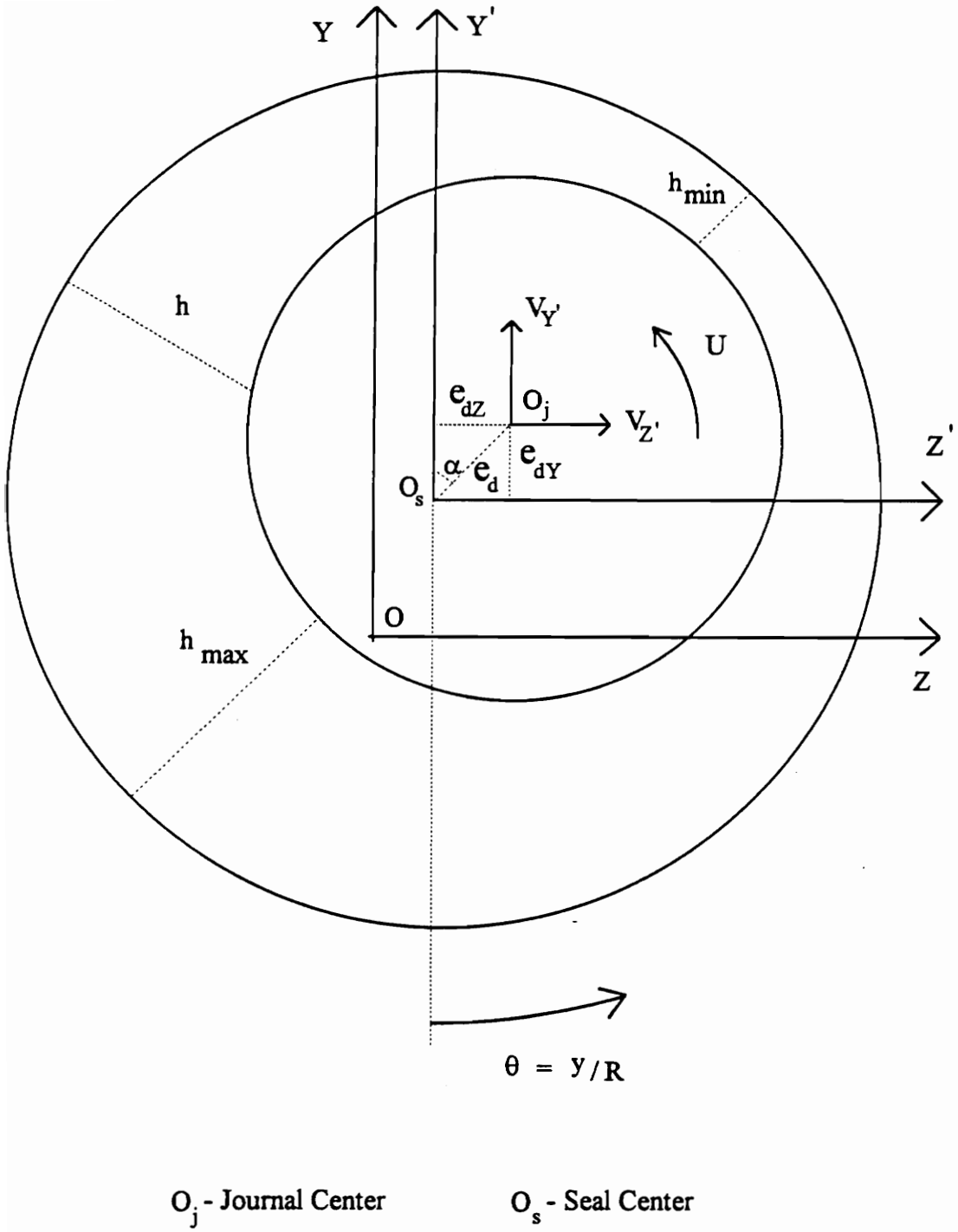


**Figure 4. Seal Cross-section Showing General Coordinate System**

seal are shown.  $Z - Y$  is a fixed (Newtonian) coordinate system.  $Z' - Y'$  coordinate system is fixed to the center of the seal,  $O_s$ .  $O_j$  is the center of the journal.  $e_d$  is the resultant relative eccentricity of rotor with respect to the seal,  $\alpha$  is the attitude angle,  $e_{dZ}$  and  $e_{dY}$  are the components of  $e_d$  in the  $Z$  and  $Y$  directions respectively.  $V_{Z'}$  and  $V_{Y'}$  are the relative velocities of the journal with respect to the seal.

## 2.1 Reynolds Equation

This equation is essentially developed from the equations of conservation of mass or continuity equation and conservation of momentum or Navier-Stokes equations. The basic assumptions in the derivation of the original Reynolds equations are:

1. Fluid is Newtonian and incompressible.
2. Laminar flow conditions prevail in the fluid.
3. No slip condition on the seal and shaft surface.
4. Inertial forces resulting from acceleration of the liquid are small.
5. Pressure, viscosity and density gradient in the radial direction are negligible because of the thin fluid.

Reynolds equation can be written in rectangular coordinates as follows (12):

$$\frac{\partial}{\partial x} \left( \frac{h^3}{\mu} \frac{\partial P}{\partial x} \right) + \frac{\partial}{\partial y} \left( \frac{h^3}{\mu} \frac{\partial P}{\partial y} \right) = 6U \frac{\partial h}{\partial y} + 12 \frac{\partial h}{\partial t} \quad [1]$$

where,  $P$  = pressure

$\mu$  = viscosity of the fluid

$U$  = rotational speed of the shaft

$h$  = local fluid film thickness

$R$  = journal radius

From Fig. 4, the fluid film thickness,  $h$ , is given by

$$h = C + e_d \cos\left(\frac{y}{R} + \alpha\right) \quad [2]$$

$$e_d = \sqrt{e_{dZ}^2 + e_{dY}^2} \quad \text{and} \quad \alpha = \tan^{-1}\left(\frac{e_{dZ}}{e_{dY}}\right) \quad [3]$$

where  $C$  is the radial clearance. Differentiating  $h$  with respect to  $y$ ,

$$\frac{\partial h}{\partial y} = -\frac{e_d}{R} \sin\left(\frac{y}{R} + \alpha\right) \quad [4]$$

Differentiating  $h$  with respect to time,  $t$ ,

$$\frac{\partial h}{\partial t} = \frac{\partial e_d}{\partial t} \cos\left(\frac{y}{R} + \alpha\right) - e_d \frac{\partial \alpha}{\partial t} \sin\left(\frac{y}{R} + \alpha\right) \quad [5]$$

where,

$$\frac{\partial e_d}{\partial t} = V_{Z'} \sin(\alpha) + V_{Y'} \cos(\alpha) \quad \text{and} \quad e_d \frac{\partial \alpha}{\partial t} = V_{Z'} \cos(\alpha) - V_{Y'} \sin(\alpha) \quad [6]$$

Using Eqs. [5] and [6]  $\frac{\partial h}{\partial t}$  can be written as

$$\frac{\partial h}{\partial t} = V_{Y'} \cos\left(\frac{y}{R}\right) - V_{Z'} \sin\left(\frac{y}{R}\right) \quad [7]$$

Substituting Eqs. [7] and [4] into Eq. [1], the Reynolds equation can be written as

$$\frac{\partial}{\partial x} \left( \frac{h^3}{\mu} \frac{\partial P}{\partial x} \right) + \frac{\partial}{\partial y} \left( \frac{h^3}{\mu} \frac{\partial P}{\partial y} \right) = -\frac{6Ue_d}{R} \sin\left(\frac{y}{R} + \alpha\right) + 12 \left[ V_{Y'} \cos\left(\frac{y}{R}\right) - V_{Z'} \sin\left(\frac{y}{R}\right) \right]$$

[8]

## 2.2 Ocvirk's Short Bearing Solution

The Ocvirk's short bearing solution is a very popular method to evaluate the pressure distribution in short bearings. In the past, a few oil seal analyses have also adopted this method. However, it is strictly applicable only when the length to diameter ratio of the seal is less than 0.25. The principal assumptions in Ocvirk's method is that the circumferential flow or the  $h^3 / \mu (\partial P / \partial y)$  term in the Reynolds equation is considered to be negligible compared to magnitude of the other terms and, in addition, the fluid viscosity is assumed to be constant. This assumption simplifies the analysis tremendously but is liable to give inaccurate results in long or highly eccentric seals. In the current analysis the complete Reynolds equation is solved to obtain the pressure distribution, including the variation in film temperature as discussed in the next section.

## 2.3 Energy Equation

In the literature the energy equation, for the temperature distribution, is derived for the specific conditions of hydrodynamic lubrication. The one that is used in this analysis is derived under the following assumptions (13):

1. Heat transfer to the mating surfaces (seal and journal surfaces) is ignored.
2. Pressure or temperature does not vary across the fluid film which is the basic hydrodynamic lubrication postulate.
3. Dilation work is negligible, because of the incompressible fluid.
4. Heat transfer due to fluid conduction is negligible.

The energy equation can be written in rectangular coordinates as follows (13):

$$6UC_p h \gamma \left[ \left( 1 - \frac{h^2}{6\mu U} \frac{\partial P}{\partial y} \right) \left( \frac{\partial T}{\partial y} \right) - \frac{h^2}{6\mu U} \left( \frac{\partial P}{\partial x} \right) \frac{\partial T}{\partial x} \right] = \frac{12\mu U^2}{h} \left\{ 1 + \frac{h^4}{12\mu^2 U^2} \left[ \left( \frac{\partial P}{\partial x} \right)^2 + \left( \frac{\partial P}{\partial y} \right)^2 \right] \right\} \quad [9]$$

where, T = temperature

$C_p$  = specific heat of the fluid

$\gamma$  = fluid density

The two terms on the left hand side of the equation represent the convective heat flow and the term on the right hand side of the equation represents the viscous dissipation in the fluid. This is a first-order differential equation for temperature and contains pressure derivatives,  $\partial P / \partial \theta$  and  $\partial P / \partial x$ , both unknown functions of x and  $\theta$ . These have to be obtained from the Reynolds equation. Also, both the energy and the Reynolds equation are nonlinear since viscosity,  $\mu$ , depends on the pressure and temperature both and density,  $\gamma$ , and specific heat,  $C_p$ , depend on temperature. To determine the pressure and temperature in the oil seal, the coupled and non-linear Reynolds and the energy equations must be solved simultaneously. In the current research work the finite element technique is used to solve these equations individually. The direct or picard iterative technique is utilized to handle the nonlinearity and the coupling in these equations. The details of these techniques are discussed in the next chapter.

Once the pressure field is obtained, the hydrodynamic forces on the seal in Y and Z directions are determined by summing the appropriate components of forces due to fluid pressure on each element of the finite element mesh.

$$F_Y = -\sum_{i=1}^N P_i A_i \cos \theta_i \quad \text{and} \quad F_Z = \sum_{i=1}^N P_i A_i \sin \theta_i \quad [10]$$

where,  $F_Z$  = hydrodynamic force on the seal in the Z direction

$F_Y$  = hydrodynamic force on the seal in the Y direction

$P_i$  = pressure at the center of i-th the element in the finite element mesh

$A_i$  = area of the i-th element in the finite element mesh

$\theta_i$  = circumferential coordinate of the center of the i-th element

$N$  = number of elements in the finite element mesh

## 2.4 Perturbation Technique

Linear stiffness and damping coefficients of the seal are determined using a perturbation technique. The stiffness and damping coefficients are used to perform the stability analysis of the compressor when the seal is locked and the rotor is whirling with a small radius. Since the seal is assumed to be locked, the coordinate system  $Z' - Y'$  shown in Fig. 4 does not move relative to the coordinate system  $Z - Y$  and the velocities  $V_{Z'}$  and  $V_{Y'}$  become the absolute velocities of the journal.

### 2.4.1 Stiffness coefficients

Small displacement perturbations  $\Delta e_{dY}$  and  $\Delta e_{dZ}$  are given to the shaft in Y and Z directions for the evaluation of the stiffness coefficients. After each perturbation new resultant eccentricity,  $e_d$ , and the attitude angle,  $\alpha$ , are determined. Before perturbation  $e_d$  and  $\alpha$  are given by Eq. [3]. After perturbation in Y direction,

$$e_d = \sqrt{e_{dZ}^2 + (e_{dY} + \Delta e_{dY})^2} \quad \text{and} \quad \alpha = \tan^{-1}\left(\frac{e_{dZ}}{e_{dY} + \Delta e_{dY}}\right) \quad [11]$$

After perturbation in Z direction,

$$e_d = \sqrt{(e_{dZ} + \Delta e_{dZ})^2 + e_{dY}^2} \quad \text{and} \quad \alpha = \tan^{-1}\left(\frac{e_{dZ} + \Delta e_{dZ}}{e_{dY}}\right) \quad [12]$$

The expression for the new fluid film thickness,  $h$ , is determined using the above expressions for  $e_d$  and  $\alpha$ . Subsequently, new temperature and pressure fields and hydrodynamic forces are determined. Stiffness coefficients are determined as follows:

Perturbation in the Y direction gives the following stiffness values:

$$K_{YY} = -\frac{\Delta F_Y}{\Delta e_{dY}} \quad K_{ZY} = -\frac{\Delta F_Z}{\Delta e_{dY}} \quad [13]$$

Perturbation in the Z direction gives the following stiffness values:

$$K_{ZZ} = -\frac{\Delta F_Z}{\Delta e_{dZ}} \quad K_{YZ} = -\frac{\Delta F_Y}{\Delta e_{dZ}} \quad [14]$$

where  $\Delta F_Y$  and  $\Delta F_Z$  are the differences between the hydrodynamic forces in Y and Z directions before and after perturbation.

#### 2.4.2 Damping Coefficients

Small velocity perturbations are given to the shaft for evaluating damping coefficients. Velocity perturbations,  $V_{Z'}$  and  $V_{Y'}$ , in the Reynolds equation (see Eq. [8] ), do not change the expression for fluid film thickness like displacement perturbations, but alter the right hand side of the Reynolds equation.  $V_{Z'}$  and  $V_{Y'}$  are zero at equilibrium position of the seal.  $V_{Y'}$  is given a small value to evaluate  $C_{ZY}$  and  $C_{YY}$ . They can be written as

$$C_{YY} = -\frac{\Delta F_Y}{V_{Y'}} \quad C_{ZY} = -\frac{\Delta F_Z}{V_{Y'}} \quad [15]$$

Similarly,  $V_{Z'}$  is given a small value to evaluate  $C_{ZZ}$  and  $C_{YZ}$ . They can be written as

$$C_{ZZ} = -\frac{\Delta F_Z}{V_{Z'}} \quad C_{YZ} = -\frac{\Delta F_Y}{V_{Z'}} \quad [16]$$

## 2.5 Mathematical Model for Linear Stability Analysis

A linear stability analysis considers the seal to be locked while the rotor whirls with a small radius about a certain point. Figure 5 shows the schematic model of the compressor rotor used in this research for the linear stability analysis. The shaft is assumed to be rigid and symmetric about the midspan. Usually, tilting pad bearings are used in compressors to support the rotor because of their negligible cross-coupled stiffness and damping coefficients, which reduces the mechanism for subsynchronous instability. Since the shaft is assumed to be rigid the deflection of the shaft will be same along its axis. Subsequently, the stiffness and damping coefficients of the bearings and the seal can be added directly to obtain the total external stiffness and damping. As the shaft is assumed to be symmetric about the midspan only half of the shaft is modeled. The equations of motion for the linear stability analysis can be written as

$$[M][\ddot{q}] + [C][\dot{q}] + [K][q] = 0 \quad [17]$$

where each dot represents time derivative.  $[M]$ ,  $[C]$ ,  $[K]$ , and  $[q]$  are the mass matrix, damping matrix, stiffness matrix and displacement vector respectively and are given by

$$[M] = \begin{bmatrix} M_j & 0 \\ 0 & M_j \end{bmatrix} \quad [C] = \begin{bmatrix} C_{ZZ} + C_b & C_{ZY} \\ C_{YZ} & C_{YY} + C_b \end{bmatrix}$$

$$[K] = \begin{bmatrix} K_{ZZ} + K_b & K_{ZY} \\ K_{YZ} & K_{YY} + K_b \end{bmatrix} \quad [q] = \begin{bmatrix} Z_j \\ Y_j \end{bmatrix}$$

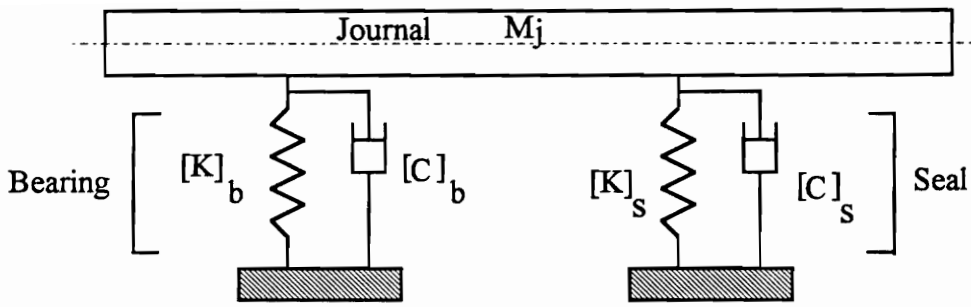


**Figure 5. Schematic Model for Linear Stability Analysis**

In the above matrices,  $M_j$  is the half mass of the journal,  $Z_j$  and  $Y_j$  are the displacements of the journal in the  $Z - Y$  coordinate system.  $K_b$  and  $C_b$  are the direct stiffness and damping of the tilting pad bearing. The cross-coupled stiffness and damping coefficients of the tilting pad bearings are negligible. Hence, they are not included in the above matrices. The solution procedure for linear stability analysis will be discussed in section 3.9.

## 2.6 Mathematical Model for Non-linear Transient Analysis

Non-linear transient analysis should be conducted when the seal is floating or the journal is whirling with a large radius which causes the hydrodynamic forces to be non-linear functions of both the relative position and the velocity of the shaft with respect to the seal. The main purpose of the transient analysis is to study the locking conditions of the floating seal and the dynamic stability of the compressor rotor. In this study, transient analysis of the system is performed at a given operating speed, starting from assumed initial conditions given in Section 5.3. Figure 6 shows a suitable configuration for the non linear transient analysis of the seal and the journal. In this configuration the positions of the seal and the journal are shown with reference to a fixed  $Y-Z$  coordinate system.  $Y_j, Z_j, Y_s, Z_s$  are the displacements of the journal and the seal.  $\dot{Y}_j, \dot{Z}_j, \dot{Y}_s, \dot{Z}_s$  are the corresponding velocities. The  $Y' - Z'$  coordinate system is fixed to the center of the seal and moves with it while it is floating. The following relations can be arrived at by comparing the two configurations given in Figs. 4 and 6.

$$e_{dZ} = Z_j - Z_s \quad e_{dY} = Y_j - Y_s \quad V_{Z'} = \dot{Z}_j - \dot{Z}_s \quad V_{Y'} = \dot{Y}_j - \dot{Y}_s \quad [18]$$

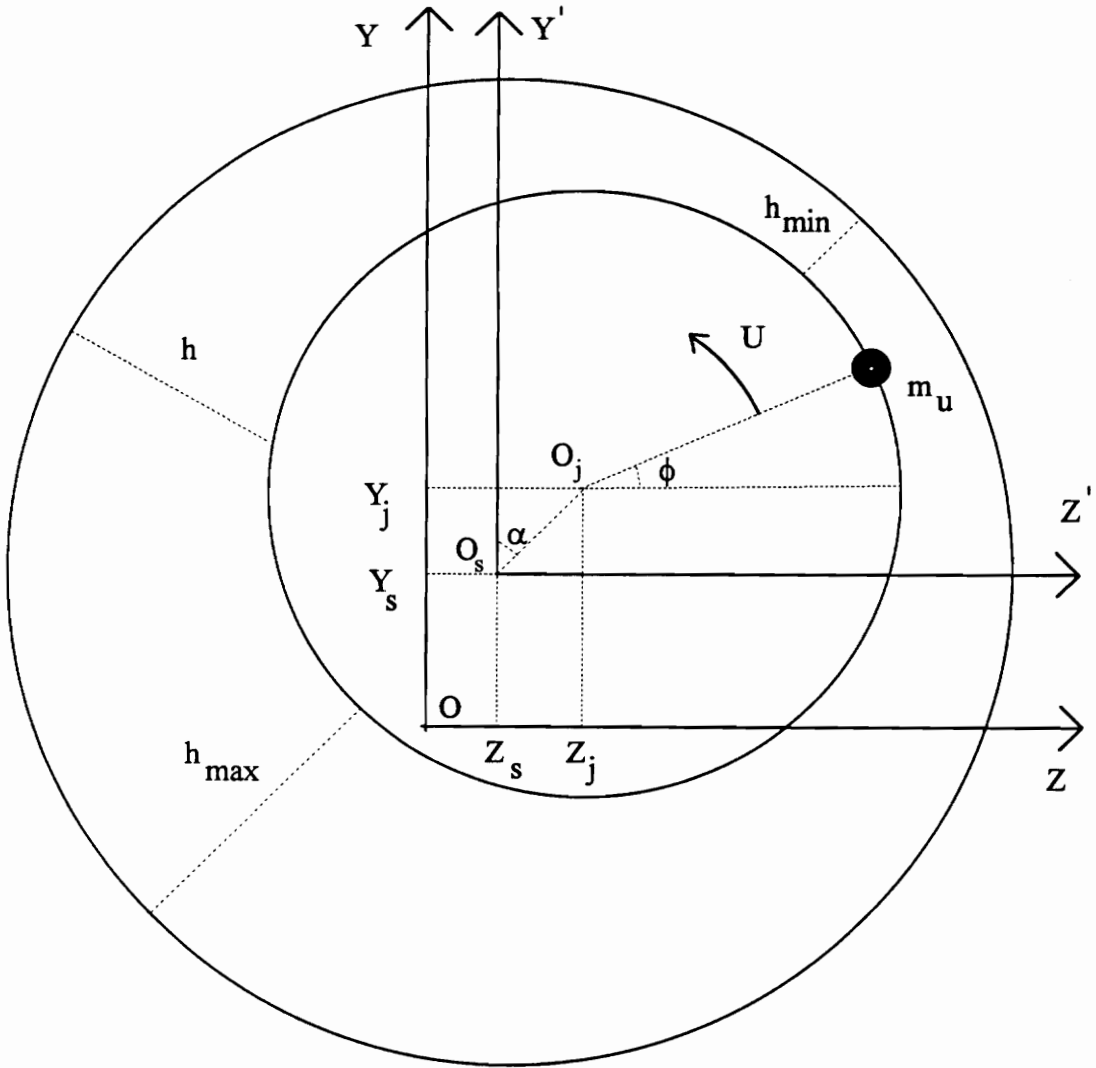


**Figure 6. Coordinate System Used for Non-linear Transient Analysis**

To perform the transient analysis of both the journal and the seal, four non-linear second order differential equations resulting from the application of Newton's second law to both the journal and the seal must be solved.

### 2.6.1 Equations of motion of journal

Figure 7 shows the schematic model used for non-linear transient analysis. The shaft is assumed to be rigid. At any given time, knowing the positions and the velocities of the seal and the journal, relative velocities and the eccentricities of the journal with respect to the seal are calculated using Eq. [18]. Subsequently, the hydrodynamic forces  $F_Z$  and  $F_Y$  can be determined by solving the Reynolds and the energy equations. Applying Newton's second law to the journal (see Figs. 6 & 7) , gives the following equation of motion for the journal:

$$\begin{bmatrix} F_u \cos(\phi) \\ F_u \sin(\phi) \end{bmatrix} - \begin{bmatrix} F_Z(Y_j, Z_j, Y_s, Z_s, \dot{Y}_j, \dot{Z}_j, \dot{Y}_s, \dot{Z}_s) \\ F_Y(Y_j, Z_j, Y_s, Z_s, \dot{Y}_j, \dot{Z}_j, \dot{Y}_s, \dot{Z}_s) \end{bmatrix} - \begin{bmatrix} K_b & 0.0 \\ 0.0 & K_b \end{bmatrix} \begin{bmatrix} Z_j \\ Y_j \end{bmatrix} - \begin{bmatrix} C_b & 0.0 \\ 0.0 & C_b \end{bmatrix} \begin{bmatrix} \dot{Z}_j \\ \dot{Y}_j \end{bmatrix} = M_j \begin{bmatrix} \ddot{Z}_j \\ \ddot{Y}_j \end{bmatrix} \quad [19]$$

In the above equations,  $M_j$  is the half mass of the journal,  $K_b$ ,  $C_b$  are the direct stiffness and damping coefficients of the bearings on which the shaft is supported.  $\ddot{Z}_j$  and  $\ddot{Y}_j$  are the accelerations of the journal in Z and Y directions.  $F_u$  is the centrifugal force due to the shaft unbalance and is given by  $F_u = m_u \omega^2 R$ , where  $m_u$  is the unbalance mass on the shaft and  $\omega$  is the rotational speed of the shaft in radians per second.  $\phi$  is the angle made by the unbalanced mass with the Z axis and is given by  $\phi = \omega t$ , where t is the time.

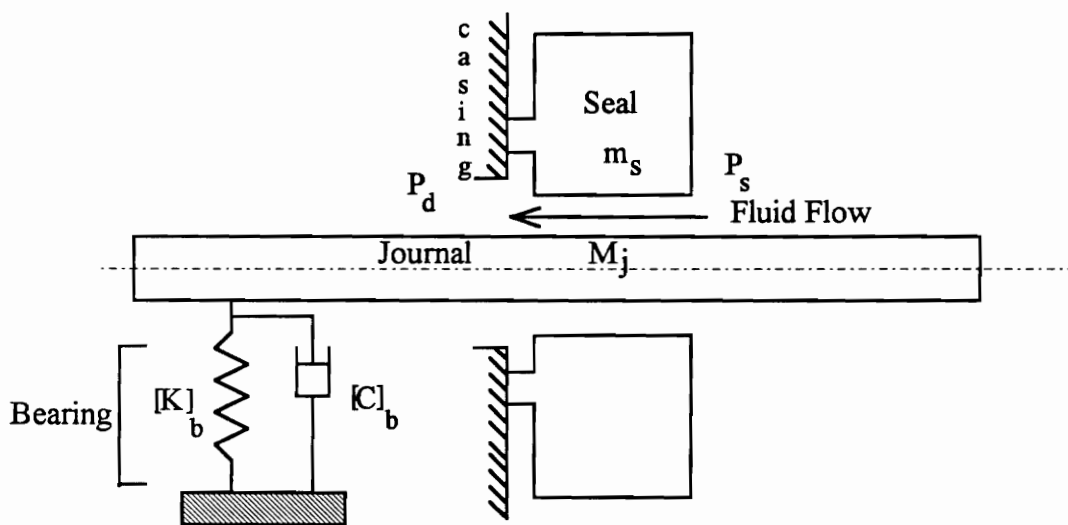


**Figure 7. Schematic Model for Non-Linear Transient Analysis**

### 2.6.2 Equations of motion of the seal ring

Figure 8 shows the free body diagram of the seal ring. The forces shown with the dashed lines do not act in the vertical direction in general. Figure 9 shows the axial forces acting on the seal needed to evaluate the total frictional force. The total frictional force is the product of the total axial load and the coefficient of friction between the lapped face and the compressor casing. Total axial load is the sum of the axial pressure load and the spring load on the seal. A linear variation in the pressure is assumed along the width of the lapped face to calculate the total axial pressure load. The static coefficient of friction or the dynamic coefficient of friction is used to calculate the frictional force depending upon whether the seal is locked or floating. Applying Newton's second law to the seal ring, gives the following equation of motion of the seal ring:

$$\begin{bmatrix} F_Z \\ F_Y \end{bmatrix} - \begin{bmatrix} 0.0 \\ m_s g \end{bmatrix} - \begin{bmatrix} F_Z^f \\ F_Y^f \end{bmatrix} = m_s \begin{bmatrix} \ddot{Z}_s \\ \ddot{Y}_s \end{bmatrix} \quad [20]$$

In the above equation,  $m_s g$  is the weight of the seal ring which can be significant in some cases. Because of the contact between the lapped face of the seal and the compressor casing  $F_Z^f$  and  $F_Y^f$  are the frictional forces acting on the seal ring. The frictional forces always act in the direction opposite to the velocity vector of the seal ring. Figure 10 shows the motion of the center of the seal ring during a particular time step,  $\Delta t$ . Let the velocities of the seal ring in the Z and Y directions at points 1 and 2 be  $\dot{Z}_s$ ,  $\dot{Y}_s$  and  $\dot{Z}_{sn}$ ,  $\dot{Y}_{sn}$  respectively.  $\vec{V}_s$  and  $\vec{V}_{sn}$  are the resultant velocities of the seal at points 1 and 2. When the seal ring is traveling from point 1 to 2, the resultant frictional force is assumed to act in the direction opposite to the velocity vector  $\vec{V}_{sn}$ , because the

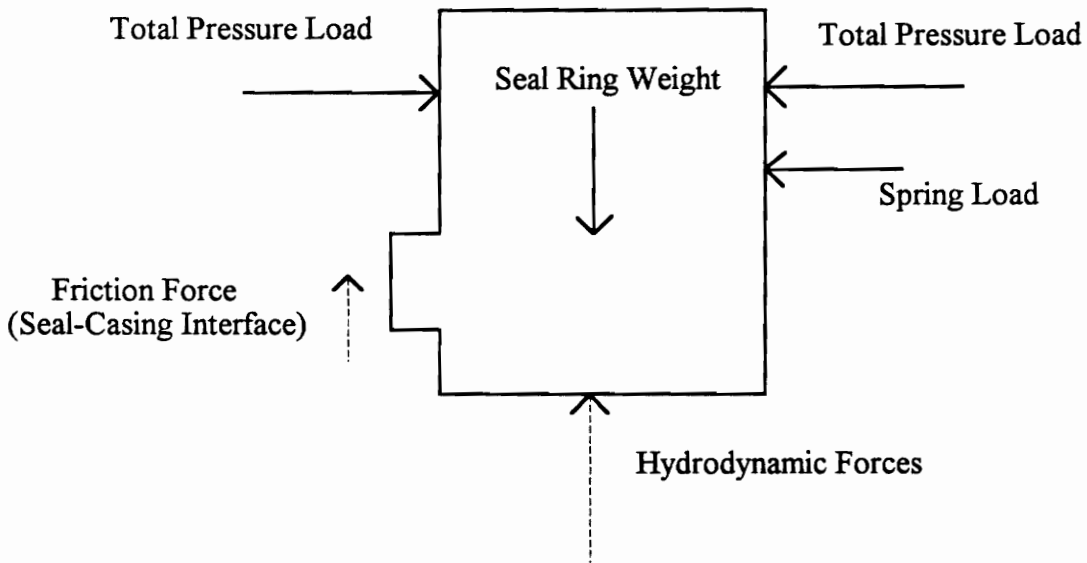


**Figure 8. Free Body Diagram of the Seal Ring**

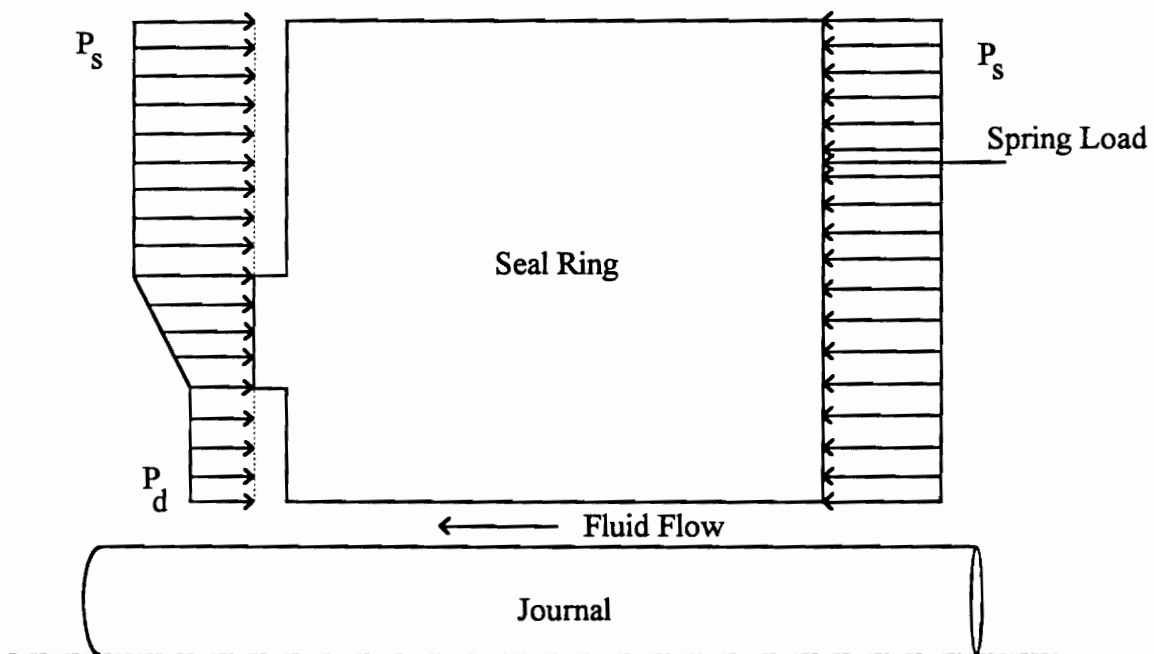


**Figure 9. Figure Showing Axial Pressure Load and Spring Load on the Seal Ring**

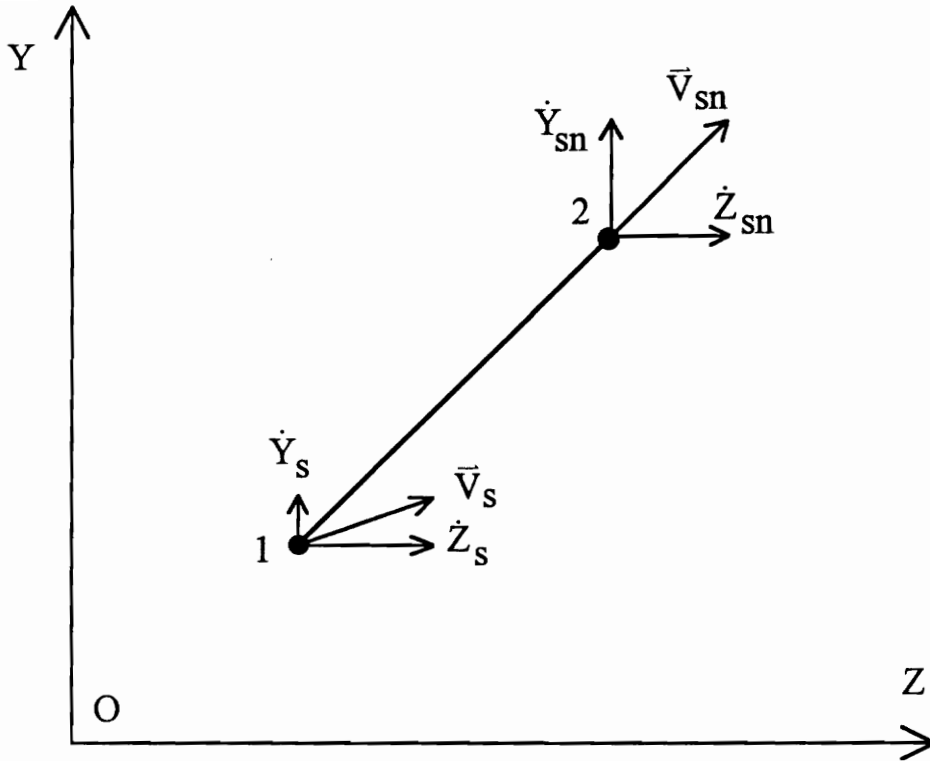


**Figure 10. Figure Showing the Velocity Vectors of the Seal Ring at Two Consecutive Points in Transient Analysis**

backward difference method, in which the displacement of the seal from point 1 to 2 is calculated based on the velocity at point 2,  $\bar{V}_{sn}$ , is used for the results in this dissertation. The expressions for  $F_Z^f$  and  $F_Y^f$  can be written as follows:

$$F_Z^f = F^f \frac{\dot{Z}_{sn}}{\sqrt{\dot{Z}_{sn}^2 + \dot{Y}_{sn}^2}} \quad \text{and} \quad F_Y^f = F^f \frac{\dot{Y}_{sn}}{\sqrt{\dot{Z}_{sn}^2 + \dot{Y}_{sn}^2}} \quad [21]$$

where  $F^f$  is the magnitude of the total frictional force.

Also,

$$\dot{Z}_{sn} = \dot{Z}_s + \Delta t \ddot{Z}_s \quad \text{and} \quad \dot{Y}_{sn} = \dot{Y}_s + \Delta t \ddot{Y}_s \quad [22]$$

Substituting Eqs. [20 & 21] into Eq. [22] gives

$$\dot{Z}_{sn} = \dot{Z}_s + \frac{\Delta t}{m_s} \left[ F_Z - F^f \frac{\dot{Z}_{sn}}{\sqrt{\dot{Z}_{sn}^2 + \dot{Y}_{sn}^2}} \right] \quad [23]$$

$$\dot{Y}_{sn} = \dot{Y}_s + \frac{\Delta t}{m_s} \left[ F_Y - m_s g - F^f \frac{\dot{Y}_{sn}}{\sqrt{\dot{Z}_{sn}^2 + \dot{Y}_{sn}^2}} \right] \quad [24]$$

From Eqs. [23 & 24] it can be shown that,

$$\frac{\dot{Z}_{sn}}{\sqrt{\dot{Z}_{sn}^2 + \dot{Y}_{sn}^2}} = \frac{a}{\sqrt{a^2 + b^2}} \quad \text{and} \quad \frac{\dot{Y}_{sn}}{\sqrt{\dot{Z}_{sn}^2 + \dot{Y}_{sn}^2}} = \frac{b}{\sqrt{a^2 + b^2}} \quad [25]$$

where,

$$a = \dot{Z}_s + F_Z \frac{\Delta t}{m_s} \quad \text{and} \quad b = \dot{Y}_s + (F_Y - m_s g) \frac{\Delta t}{m_s} \quad [26]$$

Substituting Eq.[25] in Eq.[21] gives the following expressions.

$$F_Z^f = F^f \frac{a}{\sqrt{a^2 + b^2}} \quad \text{and} \quad F_Y^f = F^f \frac{b}{\sqrt{a^2 + b^2}} \quad [27]$$

Substituting the expressions for  $F_Z^f$  and  $F_Y^f$  given by the above equation in the equations of motion for the seal ring given by Eq. [20], the following equation can be obtained.

$$\begin{bmatrix} F_Z \\ F_Y \end{bmatrix} - \begin{bmatrix} 0.0 \\ m_s g \end{bmatrix} - \begin{bmatrix} F^f \frac{a}{\sqrt{a^2 + b^2}} \\ F^f \frac{b}{\sqrt{a^2 + b^2}} \end{bmatrix} = m_s \begin{bmatrix} \ddot{Z}_s \\ \ddot{Y}_s \end{bmatrix} \quad [28]$$

where a and b are given by Eq. [26].

The solution procedure for the equations of motion of the seal ring and the journal and the locking conditions of the seal ring are given in section 3.10.

## 2.7 Flow Equation

Axial flow rate or leakage per unit length through the seal is given by (12)

$$q_v = -\frac{h^3}{12\mu} \frac{\partial P}{\partial x} \quad [29]$$

Total leakage through the seal is calculated by summing up the leakage through each element along the circumference at the exit or discharge end of the seal.

## **Chapter 3**

### **IMPLEMENTATION OF FINITE ELEMENT METHOD**

In this chapter, implementation of the finite element method to solve the nonlinear and coupled Reynolds and energy equation for pressure and temperature fields will be explained. Discretization of the domain, variational formulation of the equations over an element, the finite element model of the equations, imposition of boundary conditions and direct or picard iteration to handle nonlinearity will also be explained in this chapter. Finally, modeling of cavitation zone and the solution procedures for linear stability analysis and non-linear transient analysis are presented.

The finite element method is one of the most powerful numerical techniques available today. This technique was initially developed for structural analyses. Later, it was applied to problems in other areas including fluid film lubrication. Prior to the use of the finite element method in this area, the finite difference method was the most commonly used technique. The finite difference method is slowly losing its importance in the thin fluid film lubrication problem because it becomes inherently difficult to use when there is an abrupt change in the fluid properties such as fluid film thickness (14). In oil seal

analysis, the fluid film thickness changes abruptly in the case of grooved seals. This condition can be handled without any additional considerations by using the finite element method.

### **3.1 Discretization of the Domain**

The domain is made up of a thin fluid film between the rotor and the seal. Figure 4 shows the side view of the domain. This problem is not axisymmetric because the fluid film around the rotor is not of constant thickness. Consequently, the governing equations are solved over the whole domain. For convenience the domain shown in Fig. 4 is unrolled into the x-y plane as shown in Fig. 11 and the governing equations are solved over the resulting rectangular domain. The domain is discretized into rectangular elements. The number of elements in both the axial direction and the circumferential direction can be specified by the user. The splitting of the closed domain into the x-y plane gives rise to unbalanced internal forces which are shown in Fig. 11 by arrows. The internal forces are dealt with in the next chapter.

### **3.2 Finite Element Formulation of the Reynolds Equation**

#### *3.2.1 Variational Formulation of the Reynolds Equation*

The Reynolds equation given by Eq. [8] is of the form

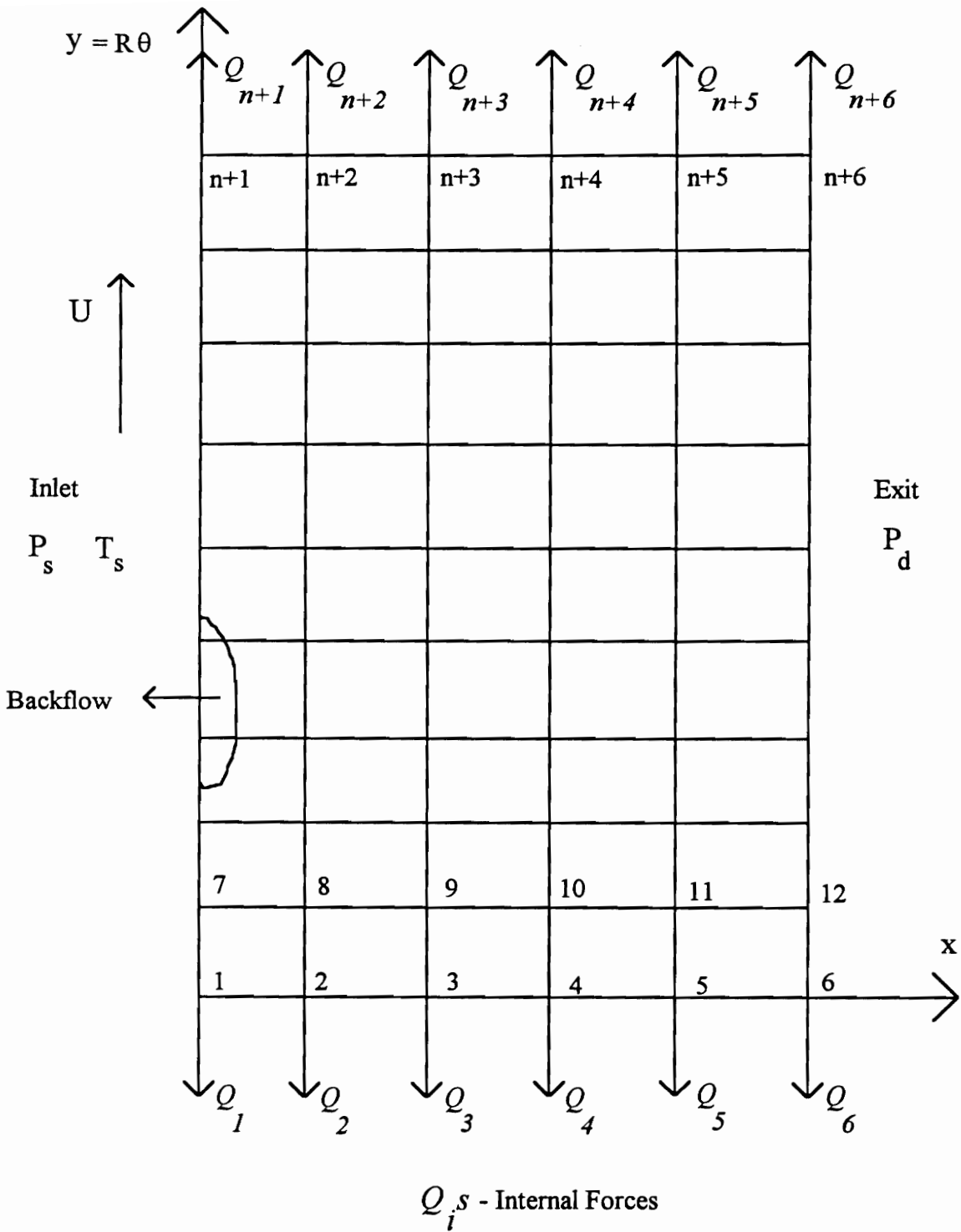


**Figure 11. Typical Finite Element Mesh**

$$-\frac{\partial}{\partial x}\left(a_{11}\frac{\partial P}{\partial x}\right)-\frac{\partial}{\partial y}\left(a_{22}\frac{\partial P}{\partial y}\right)-f(y)=0 \quad [30]$$

where,  $a_{11} = a_{22} = \frac{h^3}{\mu}$  and

$$f(y) = \frac{6Ue_d}{R}\sin\left(\frac{y}{R} + \alpha\right) - 12\left[V_Y\cos\left(\frac{y}{R}\right) - V_Z\sin\left(\frac{y}{R}\right)\right] \quad [31]$$

Multiplying the above equation by a test function  $V$  (arbitrary continuous function) and integrating over a typical element shown in Fig. 12, the following equation is obtained.

$$\int_{\Omega^e} V\left[-\frac{\partial}{\partial x}\left(a_{11}\frac{\partial P}{\partial x}\right)-\frac{\partial}{\partial y}\left(a_{22}\frac{\partial P}{\partial y}\right)-f(y)\right]dxdy = 0 \quad [32]$$

In order to distribute the differentiation among  $P$  and  $V$  equally, the first two terms in the above equation are written as follows. From the chain rule of differentiation

$$\begin{aligned} -V\frac{\partial}{\partial x}\left(a_{11}\frac{\partial P}{\partial x}\right) &= -\frac{\partial}{\partial x}\left(Va_{11}\frac{\partial P}{\partial x}\right) + a_{11}\frac{\partial V}{\partial x}\frac{\partial P}{\partial x} \\ -V\frac{\partial}{\partial y}\left(a_{22}\frac{\partial P}{\partial y}\right) &= -\frac{\partial}{\partial y}\left(Va_{22}\frac{\partial P}{\partial y}\right) + a_{22}\frac{\partial V}{\partial y}\frac{\partial P}{\partial y} \end{aligned} \quad [33]$$

Recalling the component form of the gradient (or divergence) theorem (15)

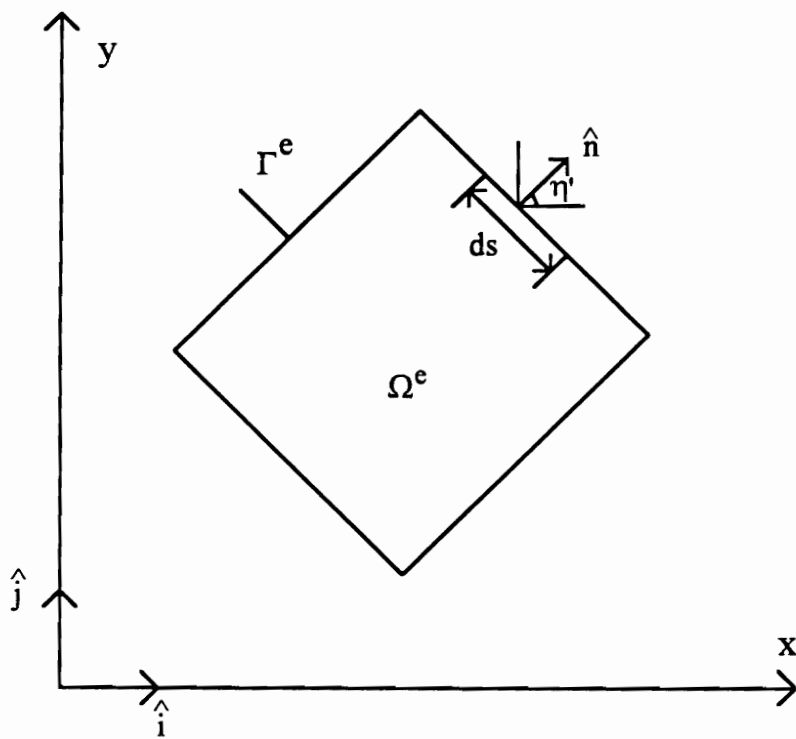


**Figure 12. Typical Infinitesimal Element**

$$\int_{\Omega^e} \frac{\partial}{\partial x} \left( V a_{11} \frac{\partial P}{\partial x} \right) dx dy = \oint_{\Gamma^e} V a_{11} \frac{\partial P}{\partial x} n_x ds$$

[34]

$$\int_{\Omega^e} \frac{\partial}{\partial y} \left( V a_{22} \frac{\partial P}{\partial y} \right) dx dy = \oint_{\Gamma^e} V a_{22} \frac{\partial P}{\partial y} n_y ds$$

where  $n_x$  and  $n_y$  are the components (direction cosines) of the unit normal  $\hat{n}$  on the boundary  $\Gamma_e$ , and  $ds$  is the arc length of the element along the boundary ( see Fig. 12 ).

The unit vector  $\hat{n}$  is given by

$$\hat{n} = n_x \hat{i} + n_y \hat{j} = \cos \eta \hat{i} + \sin \eta \hat{j}$$

[35]

Substituting Eq. [33] and Eq. [34] in Eq. [32] gives

$$\int_{\Omega^e} \left[ \frac{\partial V}{\partial x} \left( a_{11} \frac{\partial P}{\partial x} \right) + \frac{\partial V}{\partial y} \left( a_{22} \frac{\partial P}{\partial y} \right) - V f \right] dx dy - \oint_{\Gamma^e} V \left[ a_{11} \frac{\partial P}{\partial x} n_x + a_{22} \frac{\partial P}{\partial y} n_y \right] ds = 0$$

[36]

Let

$$q_n = a_{11} \frac{\partial P}{\partial x} n_x + a_{22} \frac{\partial P}{\partial y} n_y$$

[37]

In Eq. [37],  $q_n$  is the secondary variable and  $P$  is the primary variable. Physically,  $q_n$  is proportional to volume flow rate across the boundary of the element.

The variational form of Eq. [30] is given by

$$\int_{\Omega^e} \left[ \frac{\partial V}{\partial x} \left( a_{11} \frac{\partial P}{\partial x} \right) + \frac{\partial V}{\partial y} \left( a_{22} \frac{\partial P}{\partial y} \right) - Vf \right] dx dy - \int_{\Gamma^e} V q_n ds = 0 \quad [38]$$

### 3.2.2 Finite Element Model of the Reynolds Equation

The Galerkin method (15) is used to derive the finite element formulation of the Reynolds equation as it results in a symmetric stiffness matrix in this case. The variational form in Eq. [38] indicates that the approximation chosen for P should be at least bilinear in x and y so that the first two terms in the Eq. [38] are non zero. Therefore, pressure is approximated as

$$P = \sum_{j=1}^n P_j \psi_j \quad [39]$$

where  $\psi_j$  are the interpolation functions for bilinear four-noded elements,  $P_j$  are nodal pressures of the element, and n is the number of nodes in each element. In the Galerkin method the test function V is substituted for by the interpolation function. This is stated as

$$V = \psi_i \quad [40]$$

After substituting Eq. [39] and Eq. [40] in the variational form Eq. [38], the following equation is obtained.

$$\sum_{j=1}^n \left\{ \int_{\Omega^e} \left[ \frac{\partial \psi_i}{\partial x} \left( a_{11} \frac{\partial \psi_j}{\partial x} \right) + \frac{\partial \psi_i}{\partial y} \left( a_{22} \frac{\partial \psi_j}{\partial y} \right) \right] dx dy \right\} P_j - \int_{\Omega^e} f \psi_i dx dy - \int_{\Gamma^e} q_n \psi_i ds = 0 \quad [41]$$

where,

$$i = 1, 2, \dots, n$$

and,

$n$  is the number of nodes per element

Equation [41] can be written as

$$\sum_{j=1}^n K_{ij}^{(e)} P_j^{(e)} = F_i^{(e)} \quad [42]$$

where,

$$K_{ij}^{(e)} = \int_{\Omega^e} \left[ \frac{\partial \psi_i}{\partial x} \left( a_{11} \frac{\partial \psi_j}{\partial x} \right) + \frac{\partial \psi_i}{\partial y} \left( a_{22} \frac{\partial \psi_j}{\partial y} \right) \right] dx dy \quad [43]$$

$$F_i^{(e)} = \int_{\Omega^e} f \psi_i dx dy + \int_{\Gamma^e} q_n \psi_i ds \quad [44]$$

Equation [42] represents the finite element model of the Reynolds equation.

### 3.3 Finite Element Formulation of the Energy Equation

#### 3.3.1 Variational Formulation of the Energy Equation

The energy equation given by Eq. [9] is of form

$$a'_{11} \frac{\partial T}{\partial x} + a'_{22} \frac{\partial T}{\partial y} - f' = 0 \quad [45]$$

where,

$$a'_{11} = -6UC_p h \left( \frac{h^2}{6\mu U} \right) \frac{\partial P}{\partial x} \gamma \quad a'_{22} = 6UC_p h \left( 1 - \frac{h^2}{6\mu U} \frac{\partial P}{\partial y} \right) \gamma \quad [46]$$

$$f' = \frac{12\mu U^2}{h} \left\{ 1 + \frac{h^4}{12\mu^2 U^2} \left[ \left( \frac{\partial P}{\partial x} \right)^2 + \left( \frac{\partial P}{\partial y} \right)^2 \right] \right\} \quad [47]$$

Multiplying Eq. [45] by a test function  $V'$  and integrating over a typical element shown in Fig. 12, the following equation is obtained.

$$\int_{\Omega^e} V' \left[ a'_{11} \frac{\partial T}{\partial x} + a'_{22} \frac{\partial T}{\partial y} - f' \right] dx dy = 0 \quad [48]$$

Since the energy equation is first order, there is no advantage of transferring the derivative to the test function. Therefore, there is no secondary variable for the energy equation.

### 3.3.2 Finite Element Model of the Energy Equation

Equation [48] indicates that the approximation chosen for  $T$  should be at least bilinear in  $x$  and  $y$  so that the first two terms in Eq. [48] are non zero. Therefore, temperature is approximated as

$$T = \sum_{j=1}^n T_j \psi_j \quad [49]$$

where  $\psi_j$  are the interpolation functions for bilinear four-noded elements,  $T_j$  are nodal temperatures of the element, and  $n$  is the number of nodes in each element.

The least-squares method is used to derive the finite element model of the energy equation for the following reasons:

1. For the energy equation the least-squares method gives a symmetric stiffness matrix and hence requires less computer space and solution time, whereas the Galerkin method gives a non-symmetric stiffness matrix which requires more computer space and solution time.

2. The Galerkin model causes some mathematical problems in the convergence of temperature distribution due to the highly unstable nature of the energy equation.

In the least-squares method the test function  $V'$  is substituted as

$$V' = a'_{11} \frac{\partial \psi_i}{\partial x} + a'_{22} \frac{\partial \psi_i}{\partial y} \quad [50]$$

After substituting Eqs. [49] and [50] in Eq. [48], the following equation can be obtained.

$$\sum_{j=1}^n \left\{ \int_{\Omega^e} \left( a'_{11} \frac{\partial \psi_i}{\partial x} + a'_{22} \frac{\partial \psi_i}{\partial y} \right) \left( a'_{11} \frac{\partial \psi_j}{\partial x} + a'_{22} \frac{\partial \psi_j}{\partial y} \right) dx dy \right\} T_j - \int_{\Omega^e} \left( a'_{11} \frac{\partial \psi_i}{\partial x} + a'_{22} \frac{\partial \psi_i}{\partial y} \right) f' dx dy = 0 \quad [51]$$

where,

$$i = 1, 2, \dots, n$$

and,

$n$  is the number of nodes per element

Equation [51] can be written as

$$\sum_{j=1}^n K'_{ij} T_j^{(e)} = F_i^{(e)} \quad [52]$$

where,

$$K'_{ij} = \int_{\Omega^e} \left( a'_{11} \frac{\partial \psi_i}{\partial x} + a'_{22} \frac{\partial \psi_i}{\partial y} \right) \left( a'_{11} \frac{\partial \psi_j}{\partial x} + a'_{22} \frac{\partial \psi_j}{\partial y} \right) dx dy \quad [53]$$

and,

$$F_i^{(e)} = \int_{\Omega^e} \left( a'_{11} \frac{\partial \psi_i}{\partial x} + a'_{22} \frac{\partial \psi_i}{\partial y} \right) f' dx dy \quad [54]$$

Equation [52] represents the finite element model of the energy equation.

### 3.4 Boundary Conditions

Two types of boundary conditions are imposed. They are pressure and temperature boundary conditions.

#### 3.4.1 Pressure Boundary Condition

Reynolds equation is a second-order differential equation. So, either the essential boundary condition, i.e. pressure, or the natural boundary condition, i.e.  $q_n$ , has to be specified at the boundaries of the mesh shown in Fig. 11. In a seal, inlet and outlet pressures are specified. These are used as essential boundary conditions on the vertical edges. Horizontal edges are physically the same because the domain is split at these edges. Internal forces resulting from the splitting of the domain act as natural boundary condition. The internal forces are not known but are related by the constraint equations discussed in the next chapter.

#### 3.4.2 Adaptive Temperature Boundary Condition

Only supply oil temperature is known for the seal ring. Outlet oil temperature is not known for a seal ring in general and is determined in the analysis. As the energy equation is a first-order differential equation, only one boundary condition is required to solve it using the finite element method.

Usually in an oil seal, at the inlet, fluid flows into the seal because of high pressure of the supply fluid in which case the supply temperature is specified on all the nodes at the

inlet. However, when the operating eccentricity is high there can be a backflow of the fluid (see Fig. 11) at the inlet because of very high pressure generated in the fluid due to the hydrodynamic action. When there is a back flow, the hot fluid inside the seal flows out from the inlet. So, the temperature in the region of backflow is different from the supply temperature and hence not specified. Since an iterative technique, explained in the later section, is used to solve the Reynolds and the energy equation, adaptive temperature boundary condition needs to be specified to handle backflow. Constraint equations, similar to those mentioned with reference to boundary condition for Reynolds equation, occur in the case of the energy equation too and are discussed in the next chapter.

### 3.5 Interpolation Functions

As mentioned earlier, rectangular elements are used to discretize the domain, subsequently bilinear four-noded elements are used to approximate the temperature and pressure distributions. The interpolation functions  $\psi_i$  are the standard bilinear Lagrangian functions (15). Figure 13 shows a four-noded bilinear element in non-dimensional coordinates,  $-1 \leq \xi \leq +1$ ,  $-1 \leq \eta \leq +1$ .

The interpolation functions (in terms of non-dimensional coordinates) for the node-numbering shown in Fig. 13, are given by

$$\begin{aligned} \hat{\psi}_1 &= \frac{1}{4}(1-\xi)(1-\eta) & \hat{\psi}_2 &= \frac{1}{4}(1+\xi)(1-\eta) \\ \hat{\psi}_3 &= \frac{1}{4}(1+\xi)(1+\eta) & \hat{\psi}_4 &= \frac{1}{4}(1-\xi)(1+\eta) \end{aligned} \quad [55]$$

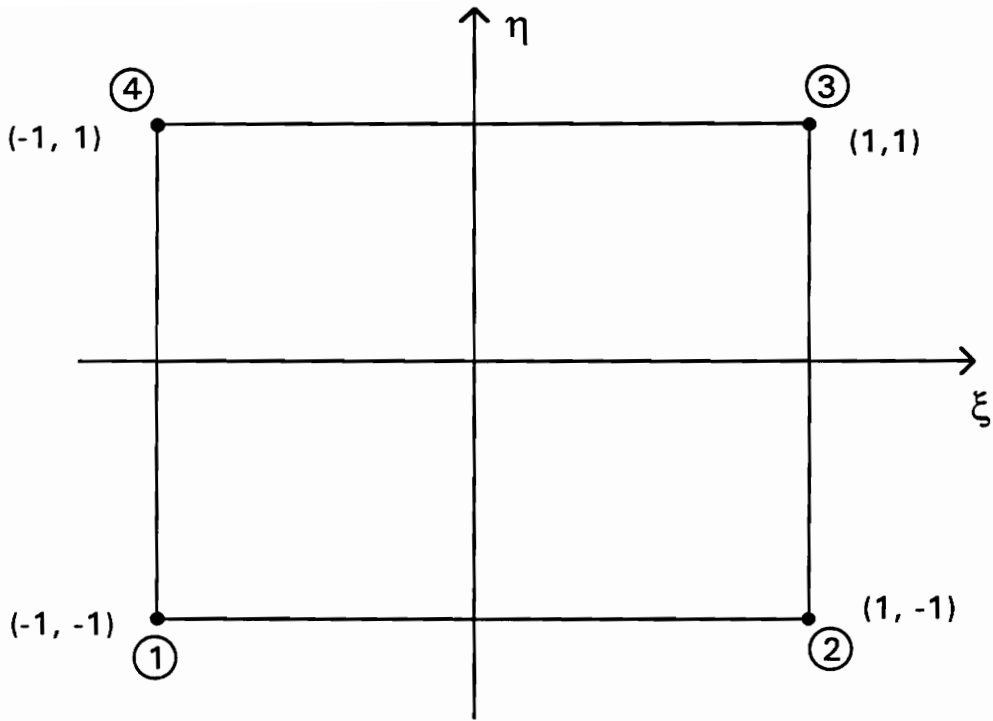


**Figure 13. Four-noded Bilinear Element**

The elements used in this analysis are isoparametric elements. Thus, the same interpolation functions are used for the coordinate transformation and the approximation of pressure and temperature fields. Therefore,  $x$  and  $y$  are approximated as

$$x = \sum_{j=1}^n x_j \hat{\psi}_j \quad y = \sum_{j=1}^n y_j \hat{\psi}_j \quad [56]$$

where  $x_j$  and  $y_j$  are the nodal coordinates of the element and  $n$  is the number of nodes per element.

### 3.6 Nonlinearity

The Reynolds equation and the energy equation are nonlinear as the terms specific heat,  $C_p$ , viscosity,  $\mu$ , and density,  $\gamma$ , depend upon temperature and pressure also has some influence on the viscosity. Earlier analyses could not account for the effect of nonlinearities because the energy equation was not included and an assumed viscosity was used to simplify the problem. For most fluids,  $C_p$ ,  $\mu$ ,  $\gamma$  are related to temperature and pressure as follows:

$$\mu = \mu' e^{PB_P} \quad [57]$$

where,

$$B_P = \frac{B_1 - B_2}{B_3 - B_4} [T - B_3] + B_1 \quad \text{and} \quad \mu' = \frac{\mu_1}{T^{\mu_2}} \quad [58]$$

$B_1$  and  $B_2$  are pressure coefficients at temperatures  $B_3$  and  $B_4$  respectively.

$$C_p = C_1 + C_2 T \quad [59]$$

$$\gamma = \gamma_1 - \gamma_2 T \quad [60]$$

$C_1$ ,  $C_2$ ,  $\gamma_1$ ,  $\gamma_2$ ,  $\mu_1$  and  $\mu_2$  are constants of the fluid.

Direct or Picard iteration (15) is used in this analysis to handle the nonlinearity. Iteration is started by evaluating  $C_p$ ,  $\gamma$ ,  $\mu$  for each element at initially guessed temperature and pressure distributions. After every iteration  $C_p$ ,  $\gamma$ ,  $\mu$  are evaluated at the center of each element using the updated temperature and pressure distribution. Iteration is continued until the difference between two consecutive temperature and pressure distributions is less than a preselected value  $\delta$ . The convergence criterion for the direct or Picard iteration scheme is as follows:

$$\sqrt{\frac{\sum_{i=1}^N \left( U_i^{(r)} - U_i^{(r-1)} \right)^2}{\sum_{i=1}^N \left( U_i^{(r)} \right)^2}} < \delta \quad [61]$$

where,

$\delta$  = convergence tolerance

$N$  = number of nodes in the mesh

$U_i$  = temperature or pressure at the  $i$ -th node

$r$  = iteration number

### 3.7 Cavitation

Cavitation is not as commonly encountered in oil seals as in fluid film bearings because of the high pressure level in the oil seals. However, occasionally, low discharge pressure and high operating eccentricities can cause cavitation. At a sufficiently low pressure level, i.e., a pressure level near the liquid vapor pressure, gases and vapor form cavities within the liquid. In oil seals low pressure fluid near the exit initiates cavitation. Air at the discharge end can also enter into the seal. As a result, the cavitation region is filled with a mixture of liquid, gas-vapor, and air streamlets. Naturally, fluid cavitation affects both temperature and pressure in the seal. It is very complicated to model the cavitation zone exactly because of the uncertainty as to what form the cavitating film assumes. In the past there have been discrepancies between conventional predictions and experimental evidence as far as the thermal picture is concerned (13). In this analysis, all the pressures below the cavitation pressure,  $P_{cav}$ , are eliminated. Mathematically,

$$\text{if } P_i < P_{cav}, \text{ then } P_i = P_{cav} \quad [62]$$

Since the fluid in the cavitation region fills the seal clearance partially the fluid viscous dissipation can be assumed to be negligible. Subsequently, the viscous dissipation term on the right hand side of the energy equation given by Eq. [9] is ignored in the cavitation zone.

### 3.8 Solution Procedure for Temperature and Pressure Distributions

The steps involved in the determination of the temperature and pressure distributions using the finite element method are as follows:

1. Assume temperature and pressure fields.
2. Evaluate fluid properties,  $C_p$ ,  $\gamma$ ,  $\mu$ , at assumed temperature and pressure.
3. Solve the Reynolds equation for pressure distribution.
4. Account for cavitation if necessary.
5. Check for the backflow at the inlet side of the seal.
6. Solve the energy equation for temperature distribution using the new pressure profile and the modified boundary condition in the case of backflow.
7. Continue iteration from step 3 until both temperature and pressure distributions are converged in the same iteration.

### 3.9 Solution Procedure for Linear Stability Analysis

The mathematical model for the linear stability analysis of the compressor rotor was given in section 2.5 by Eq. [17]. The standard solution of this equation is

$$[q] = \text{Real}[Q]e^{at} \quad [63]$$

where  $[Q]$  represents the complex vector displacements and  $a$  represents the complex eigenvalues of the system.

$$a = \zeta + i\lambda \quad [64]$$

The real part of the eigenvalue,  $\zeta$ , is called the temporal growth factor and  $\lambda$  is called the oscillatory frequency of the perturbed motion. The above system has 4 eigenvalues that are obtained using standard techniques. The stability of the system depends upon the sign of the temporal growth factor,  $\zeta$ . The system is said to be stable only if  $\zeta$ 's corresponding to all the eigenvalues are negative. If the  $\zeta$  corresponding to a single eigenvalue is positive, then the system is unstable. Figure 14 shows a block diagram of the program used to perform linear stability analysis of the compressor rotor.

### **3.10 Solution Procedure for Non-linear Transient Analysis**

To perform the non-linear transient analysis of the seal and the journal four second order coupled non-linear differential equations given by Eqs. [19 & 28] in section 2.6 need to be solved. At any given time, knowing the positions and velocities of the seal and journal, the left hand sides of these equations are evaluated from which the accelerations of the seal and journal are determined. The accelerations are integrated using forward difference method to obtain the new velocities. The forward difference method, Crank-Nicholson method and backward difference method were tried for the integration of velocities to obtain the new displacements. A detailed explanation of these techniques is given in reference 15. Almost the same results were obtained using the three methods. All of the results presented in this dissertation are obtained using backward difference method for integrating velocities. Also, an adaptive time step scheme, in which the size of each time step depends on the number of iterations required to solve the temperature and pressure distributions in the same time step, is used to avoid numerical instabilities in the solution procedure. The details of this scheme are given in section 4.4.

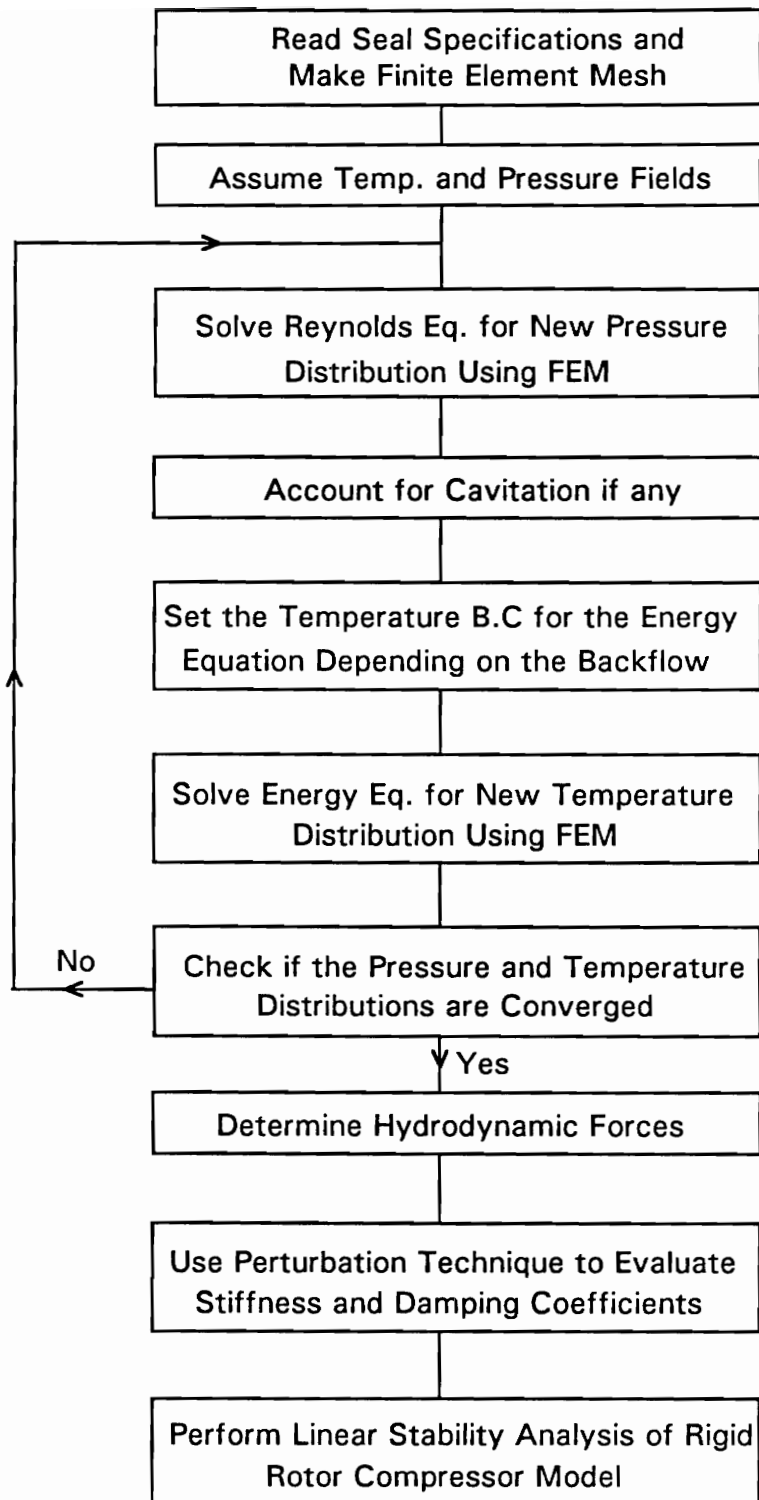
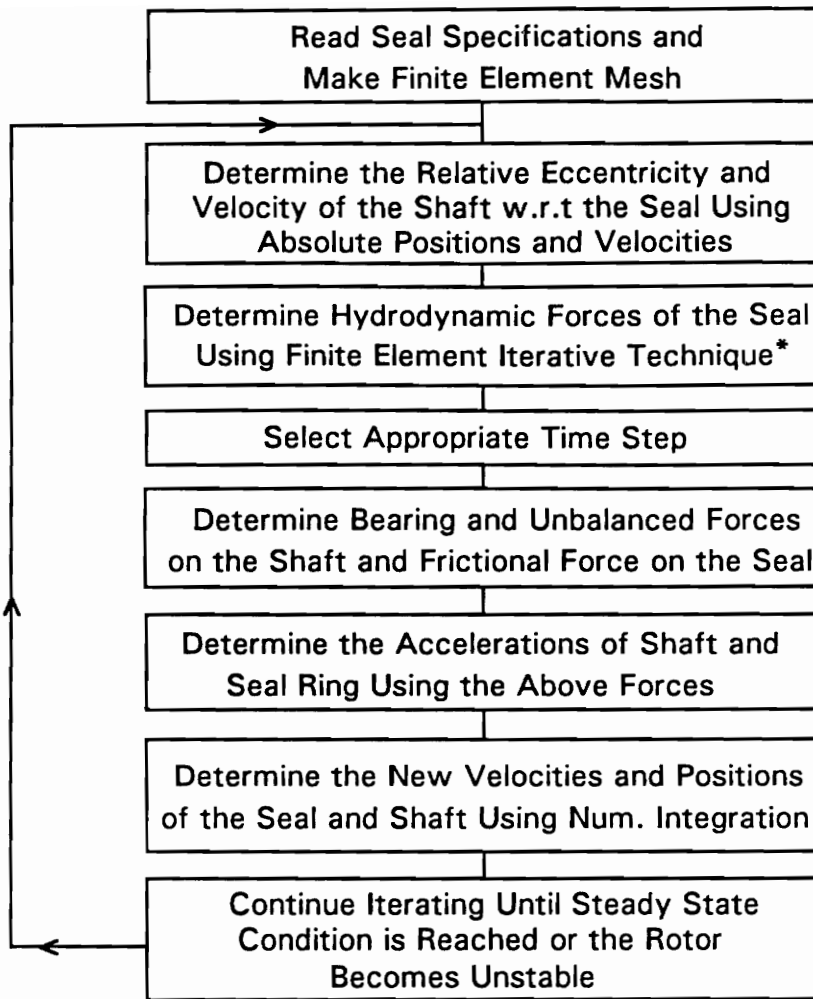


**Figure 14. Block Diagram of the Program for Linear Stability Analysis**

The main purpose of the non-linear transient analysis is to study the locking conditions of the seal ring. To check if the ring becomes locked or not in any time step of transient analysis, the signs of the two components  $\dot{Z}_s$  and  $\dot{Y}_s$  of the ring velocity before and after this particular time step are checked. If the signs of these velocities change in any time step, then it is assumed that the ring becomes locked in this time step as the velocity goes through zero. The velocities  $\dot{Z}_s$  and  $\dot{Y}_s$  are made zero once the ring is locked. It can become unlocked again if the total external force (resultant of hydrodynamic forces and the ring weight) on the seal ring becomes greater than the static friction force on the seal at any time in the transient analysis. Figure 15 shows a block diagram of the program used to perform non-linear transient analysis of the compressor rotor.



\* The logic of this technique is given in the block diagram in Figure 14

**Figure 15. Block Diagram of the Program for Non-Linear Transient Analysis**

## **Chapter 4**

# **OPTIMIZATION, CONVERGENCE AND STABILITY OF THE NUMERICAL SOLUTION**

In this chapter, incorporation of constraint equations into the finite element models of both the Reynolds and the energy equations and appropriate node numbering scheme to optimize the bandwidth of the stiffness matrix which is influenced by the constraint equations are presented. Different methods used to solve the matrix equations of finite element models are discussed. Details of the convergence of the finite element solution are also presented. Perturbation constants used in the evaluation of linear stiffness and damping coefficients and convergence tolerances used for the non-linear transient analysis and linear stability analysis are given. Finally, details of numerical integration scheme for the non-linear transient analysis is presented.

### **4.1 Constraint Equations**

As mentioned earlier, the arrows shown in Fig. 11 are the internal forces that are necessary as a result of the splitting of the cylindrical domain into a rectangular one. These

internal forces, whose values are not known, act as secondary variables in the new domain. The primary variables at the nodes having unbalanced internal forces are also not known. However, in any given domain the sum of the internal forces coming from various elements at a given node is equal to the value of the secondary variable at that node. Which means (see Fig. 11)

$$Q_i + Q_{n+i} = \text{Secondary Variable} = 0.0 \text{ ( for } i = 2,3,4,5 \text{ in this problem )}$$

The secondary variable of the Reynolds equation is proportional to the supply flow rate of the fluid at each node and is zero at all the nodes except at the nodes on entrance and exit of the seal because there is no external supply of fluid to the internal nodes.

The secondary variable for the energy equation does not exist because it is a first-order differential equation.

Also, nodes 1, 2, 3, 4, 5, 6 are physically the same as nodes n+1, n+2, n+3, n+4, n+5, n+6 respectively.

Therefore,

$$U_i = U_{n+i}$$

where  $U_i$  is either pressure or temperature at the i-th node.  $i = 1,2,3,4,5,6$

The above constraint equations are incorporated by adding appropriate equations of both the finite element models and the resulting finite element models are solved.

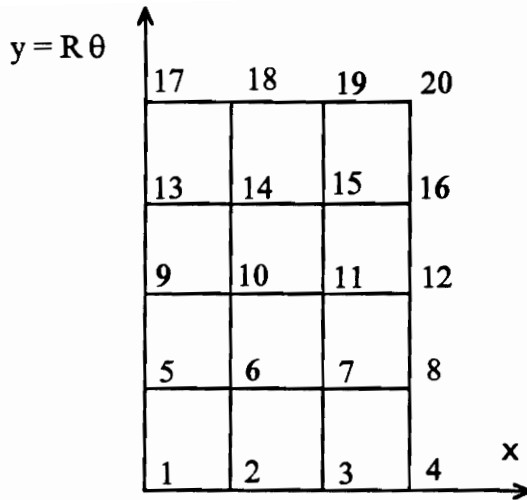
## 4.2 Bandwidth Optimization of the Finite Element Stiffness Matrices

The term optimization here is referred to the computational efficiency of the numerical procedure used in this analysis. One important factor that affects the computational efficiency in finite element methodology is the bandwidth of the stiffness matrix. Usually, it depends upon the node numbering scheme used in the finite element mesh. In the current problem, it also depends upon the constraint equations discussed above. Bandwidth should be minimized to reduce the computational time and the memory storage used.

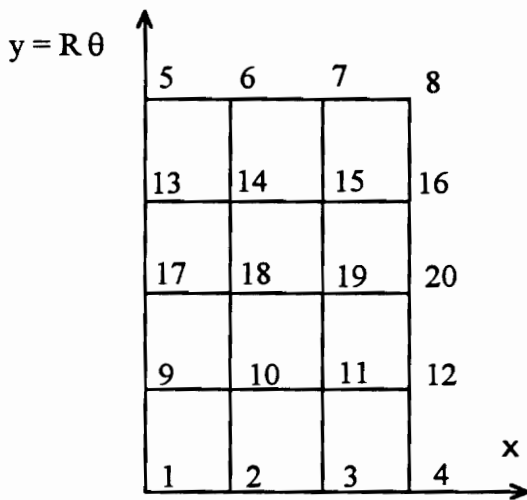
Incorporation of the constraint equations, which is necessary because of the unrolling of the cylindrical domain into the x-y plane, alters the stiffness matrix. Consequently, the bandwidth of the stiffness matrix changes depending upon how the nodes are numbered. For example, consider two meshes shown in Fig. 16 with different node numbering. These meshes are very crude compared to the actual mesh used in the analysis. They are used here to explain how bandwidth in the actual mesh is minimized.

Before incorporating the constraint equations the half-bandwidth of mesh A is 6 and that of mesh B is 10. After incorporating the constraint equations the half-bandwidth of mesh A becomes 14 and half-bandwidth of mesh B remains 10. This is because in mesh A, to incorporate the constraint equations, the seventeenth row of the stiffness matrix is added to the first row and so on, whereas, in mesh B first row of the stiffness matrix is added to the fifth row and so on.

A typical mesh in this analysis has 80 elements in the circumferential direction and 9 elements in axial the direction. Half-bandwidth of the stiffness matrix corresponding to mesh similar to mesh B will be 22, whereas it will be 792 for the mesh similar to mesh A.



Mesh (A) - Standard Numbering Scheme



Mesh (B) - Alternate Numbering Scheme  
to Minimize Bandwidth

**Figure 16. Different Node Numbering Schemes (For Discussion)**

So if the techniques such as Gaussian-elimination technique or Cholesky's (16) method are used to solve the linear system of equations of the finite element models, then the computer time can be minimized by using mesh B. Both the techniques were used and the time consumed by them were about the same. The half-bandwidth of the stiffness matrix corresponding to mesh A is very high only because of few non-zero elements in the first few rows and the last few columns as a result of the constraint equations. In general, the effective band-width and computer time involved in solving such matrix equations can be reduced by using column-solver (17). But, in the current work, it was found that the column-solver used to solve the stiffness matrix obtained from mesh A was not any less time consuming than the Gaussian-elimination technique used to solve the stiffness matrix obtained from mesh B. Hence mesh B, with Gaussian-elimination technique to solve the linear system of equations of the finite element models is used in the current work.

### **4.3 Convergence of Finite Element Results**

In this research, the finite element technique is used to solve the non-linear and coupled Reynolds and the energy equations for the pressure and temperature distributions. As in any numerical solution technique, proper convergence of the results obtained from this finite element iterative method has to be assured.

In finite element iterative procedure, accuracy of the results depend upon the number of elements or mesh size, and the value of the convergence tolerance,  $\delta$ , used in the direct or Picard iteration technique (given in section 3.6). The following discussion gives the details of the convergence study performed in this analysis.

Meshes of different sizes were employed to study the convergence of different parameters in various oil seal cases including different running speeds, operating eccentricities, seal geometries, pressure conditions. Some of the mesh sizes used in this study are 4x40 (4 elements in the axial direction and 40 elements in the circumferential direction), 9x80, and 18x160. Results of a typical ungrooved seal obtained from different mesh sizes are shown in Table 1. The operating eccentricity used is 0.4. The time in the Table 1 is the solution time required to obtain the hydrodynamic forces on the IBM RISC 6000 workstation (model 560). The values in the parentheses are the percentage changes with respect to the results corresponding to the mesh size 18x160. The mesh of size 9x80 is optimum in terms of computational efficiency and accuracy of results because doubling the mesh size further in both the directions changes the axial flow rate,  $Q_v$ , temperature (near the minimum fluid film thickness),  $T$ , and the total hydrodynamic force,  $F_T$ , by 0.002 %, 0.16 % and 1.27 % only but increases the solution time by a factor of 4.6. As the operating eccentricity is increased, the percentage changes of the axial flow rate and the temperature (near the minimum fluid film thickness) when the mesh size is doubled in both the directions, increase. The percentage change of the total hydrodynamic force when the mesh size is doubled in both the directions, does not change significantly with the increase in operating eccentricity. At the operating eccentricity of 0.8 (the highest eccentricity used for the results in this dissertation) the axial flow rate and the temperature (near the minimum fluid film thickness) change by 0.07 % and 3.1 % respectively when the mesh size is changed from 9x80 to 18x160. All the results of ungrooved seals presented in this dissertation are obtained using the mesh of size 9x80. In the case of grooved seals, a separate convergence study was performed and the results will be discussed in chapter 7.

**Table 1. Results of a typical seal obtained from different mesh sizes**

Operating speed = 8000 RPM; Operating eccentricity = 0.4

Mesh Size	$Q_v \times 10^{-3}$ ( $m^3/s$ )	T ( $^{\circ}C$ )	$F_T$ (N)	Time (sec)
4x40	0.486593 (-0.008)	60.93 (-1.24)	919.08 (-7.68)	42
9x80	0.486618 (-0.002)	61.60 (-0.16)	982.85 (-1.27)	95
18x160	0.486631	61.70	995.53	435

The influence of the size of convergence tolerance,  $\delta$ , on various results was studied. As the value of convergence tolerance,  $\delta$ , is made smaller the accuracy of the results improves but the number of iterations required also increases. An optimum value needs to be used depending upon the objective of the analysis. The following discussion gives the details of the study performed to obtain the optimum values of convergence tolerance for the non-linear transient analysis and the linear stability analysis.

To do non-linear transient analysis, only the hydrodynamic forces are needed. After performing transient analysis with different values of convergence tolerance, a value of 0.001 was found to be suitable for this purpose. Because, further reduction in the value of  $\delta$  results in the increase in the number of iterations without improving the values of hydrodynamic forces or the results of transient analysis significantly. For example, in a typical case the change in hydrodynamic forces was about 0.20 % when the convergence tolerance was changed from 0.001 to 0.000001, but the number of iterations increased from 5 to 10. In a particular case the eccentricity ratio was found to change by about 0.08 % towards the end of the transient analysis when the convergence tolerance was changed from 0.001 to 0.000001.

For the linear stability analysis the stiffness and damping coefficients are needed. The perturbation technique described in section 2.4 is used to obtain the stiffness and

damping coefficients. The appropriate convergence tolerance required to obtain the stiffness and damping coefficients depend upon the size of the perturbation. Perturbations,  $\Delta e_{dZ}$  and  $\Delta e_{dY}$ , should be as small as possible for the linear perturbation theory to be applicable. But smaller the perturbation, the tighter the convergence tolerance should be for the analysis to be sensitive to the perturbation. The number of iterations for the convergence of pressure and temperature distributions increases with the decrease in the size of convergence tolerance. After studying numerous cases, the optimum values arrived at for perturbation size and convergence tolerance are  $0.0001C$  and  $1E-6$  respectively. Where  $C$  is the radial clearance of the seal. The velocity perturbations used are  $V_{Z'} = \omega x \Delta e_{dZ}$  and  $V_{Y'} = \omega x \Delta e_{dY}$ .

#### **4.4 Convergence and Stability of the Numerical Solution for Non-linear Transient Analysis**

A numerical integration technique as mentioned in section 3.10 is used for the non-linear transient analysis. In this numerical integration technique an adaptive time step is used to overcome the numerical instabilities (discussed below) encountered when a constant time step was used. In some cases of transient analysis, when the relative operating eccentricity and the seal velocity became high, the number of iterations required for the convergence of the pressure and temperature increased significantly if a constant time step is used through out the transient analysis. This happens because, when the seal velocity and the relative eccentricity are high, a constant time step could cause relatively large displacements of the seal and the journal, which can then fluctuate the hydrodynamic forces and eventually make the numerical solution unstable. To overcome this problem an

adaptive time step scheme (unique for this research) is used. In this scheme the size of the time step is adjusted depending on the number of iterations required for the convergence of the pressure and temperature distributions. The higher the number of iterations required for the convergence of temperature and pressure distributions in the current time step, the larger the change in the seal and the journal displacements in the previous time step. This is because the temperature and pressure distributions of the previous time step are used as the initial guess in the iterative solution of the pressure and temperature distributions for the current time step. So, as the number of iterations for the convergence of temperature and pressure distributions increase a smaller and smaller time step is required for the stability of the numerical solution. The smaller time steps reduce the change in the seal and the journal displacements in the current time step which reduces the number of iterations required for the convergence of the pressure and temperature distributions in the next time step and stabilizes the numerical solution.

All the transient analysis results presented in this analysis were obtained using the above adaptive time scheme, which adjusts the time step, so that the number of iterations required for the convergence of the pressure and temperature distributions were about two. Larger number of iterations would result in larger time steps, but will not save the computational time which mainly depends on the number of iterations required for the convergence of pressure and temperature distributions. To ensure convergence, transient analysis results for different cases obtained from the adaptive time step scheme mentioned above were compared with those obtained by reducing each time step of the adaptive time step scheme by a factor of two, four and ten. The orbits traced by the rotor and the seal for the different sizes of the time step were found to be essentially the same. In a typical case the eccentricity ratio towards the end of the transient analysis changed by about 0.3 % when the time step was reduced by a factor of four.

## **Chapter 5**

### **RESULTS AND DISCUSSION OF STRAIGHT SEALS**

In this chapter comparison of the results for a straight seal obtained from the new finite element analysis and a previously developed finite difference analysis (18) will be presented. Additional results in terms of temperature and pressure distributions, stiffness and damping characteristics, growth factor, damped natural frequency, axial flow rate will be presented for straight seals operating in both field and test stand conditions. Finally, results from transient analysis of the straight seals will be presented.

#### **5.1 Comparison of the results of a typical seal**

From the results obtained in this analysis, the importance of using the true temperature profile can be realized, as it influences the static and dynamic characteristics and hydrodynamic forces significantly. In this section results from this analysis and from an existing finite difference code (18), which assumes a linear axial temperature variation, are compared. Table 2 gives the common specifications used for all the results in this

**Table 2. Common Specifications Used for the Results in this Dissertation**

Journal Diameter	127.0 mm (5.0 in)
Total Length of the Seal	22.860 mm (0.9 in)
Radial Clearance of the Seal	0.1016 mm (0.004 in)
Discharge Pressure	0.101 Mpa (14.7 psi)
Cavitation Pressure	0.101 Mpa (14.7 psi)
Supply Temperature	48.89° C (120° F)
Sealing Fluid	Light Turbine Oil
Fluid Constants of the Sealant *	$B_1 = 0.000137$ , $B_2 = 0.000104$ , $B_3 = 100$ , $B_4 = 180$ , $C_1 = 3737.47$ , $C_2 = 5.59$ , $\gamma_1 = 0.0327$ , $\gamma_2 = 1.28 \times 10^{-5}$ , $\mu_1 = 0.558$ , $\mu_2 = 2.573$
Bearing Stiffness	3.16E+7 N/m (180000 lbf/in)
Bearing Damping	3.511E+4 N-s/m (200 lbf-s/in)
Half Journal Mass	181.44 Kg (400 lbm)
Mass of the Seal Ring	2.72 Kg (6 lbm)
Unbalanced Mass of the Journal	8.88 gm (0.0196 lbm)
Static Coefficient of Friction	0.16
Dynamic Coefficient of Friction	0.15

\* This analysis is performed in English system and the results are converted into SI units. The fluid constants specified above and used in Eqs. [57]-[60] are in English system.

dissertation. Length to diameter (L/D) ratio of the seal is 0.18. Radial clearance of the seal is 0.1016 mm. Discharge and cavitation pressures are 0.101 MPa, supply temperature of the oil is 48.89 °C. The sealing fluid used is light turbine oil. The stiffness and the damping coefficients of the shaft support bearings are 3.16E+7 N/m and 3.511E+4 N-s/m. The half mass of the journal is 181.44 Kg. The mass of the seal ring and unbalanced mass of the journal are 2.72 Kg and 8.88 gm respectively. The static and dynamic coefficients of friction between the lapped face of the seal and the compressor casing are 0.16 and 0.15.

Figure 17 shows the temperature and pressure distributions in the above seal with running speed of 2000.0 RPM and an eccentricity ratio,  $e_{rY}$ , of 0.098.  $e_{rY}$  is the non-dimensional eccentricity in the Y-direction and is the ratio of the eccentric distance,  $e_{dY}$ , and the clearance, C. Supply pressure used is 4.136 MPa. As this particular case is almost centered, pressure and temperature variations in the circumferential directions are relatively small. Figure 18 shows the temperature and pressure distributions in the same seal with running speed of 8000.0 RPM and an eccentricity ratio of 0.497. It can be seen that temperature is no longer linear in the axial direction and changes significantly in the circumferential direction which influences the results significantly.

In Table 3, results in terms of stiffness and damping coefficients, stability parameters, hydrodynamic forces, axial flow rates, weighted average and maximum temperatures obtained by this analysis for the above cases are compared with the results of an existing finite-difference code (18), which assumes a linear axial temperature variation. For the case with the eccentricity ratio of 0.098 and operating speed of 33.33 Hz (2000.0 RPM), the results are in good agreement as expected, because for this case the temperature predicted by the current analysis is also almost linear in the axial direction (see Fig. 17). For the case with eccentricity ratio of 0.497 and operating speed of 133.33 Hz (8000.0 RPM) there is significant discrepancy in the results because the temperature

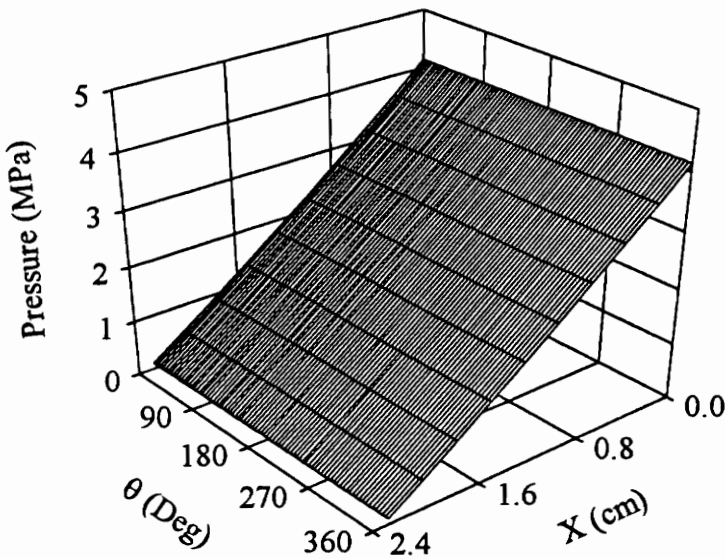
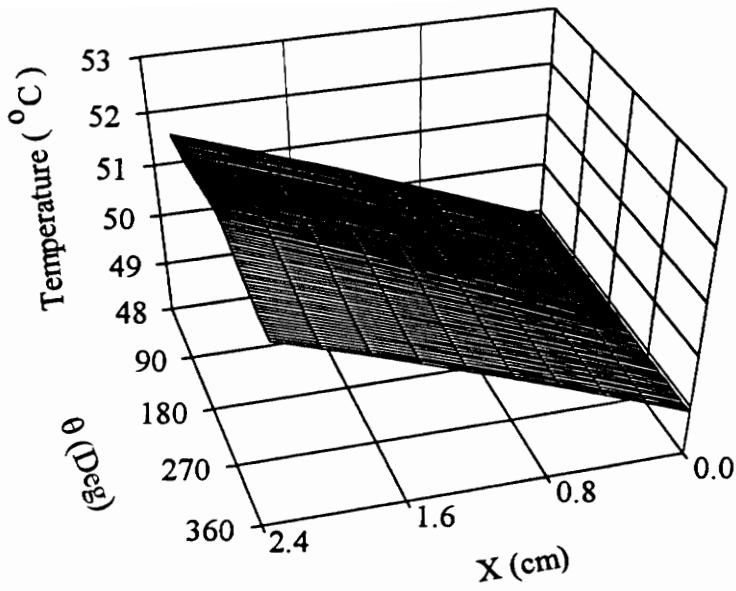


**Figure 17. Temperature and Pressure Distributions in the Straight Seal**

**Operating Speed = 33.33 Hz (2000 RPM)**

**Operating Eccentricity ( $e_{rY}$ ) = 0.098**

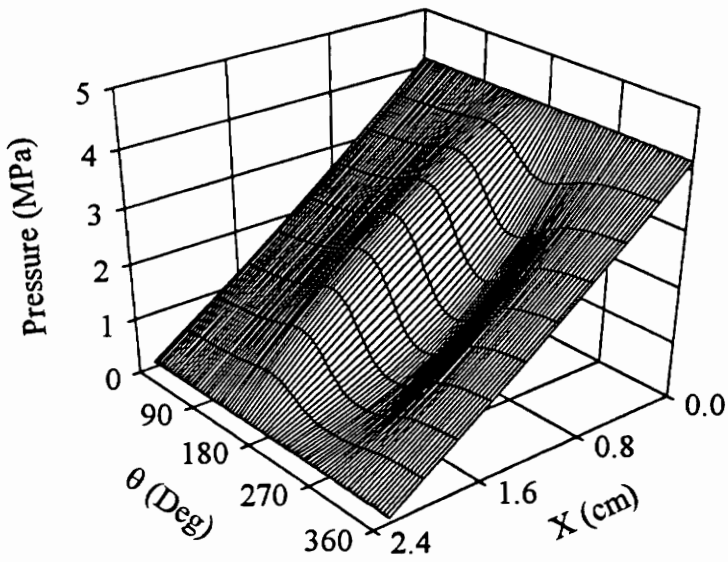
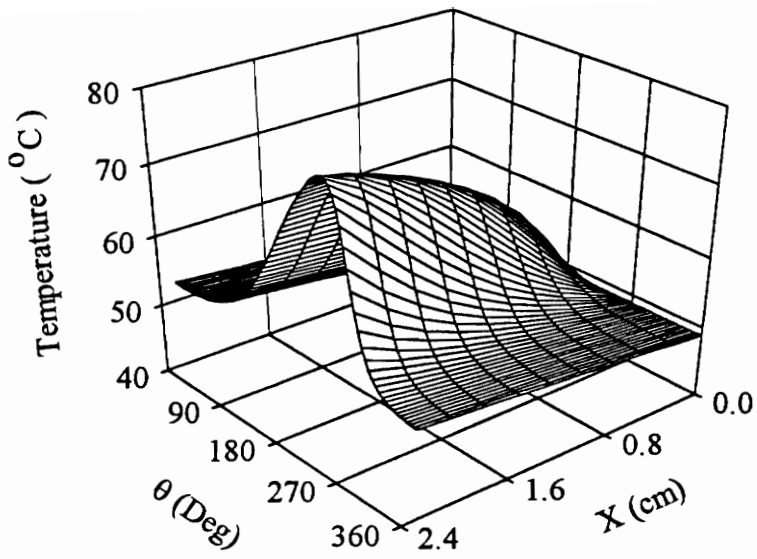


**Figure 18. Temperature and Pressure Distributions in the Straight Seal**  
**Operating Speed = 133.33 Hz (8000 RPM)**  
**Operating Eccentricity ( $e_{r,y}$ ) = 0.497**

**Table 3. Comparison of Results Obtained from Current Analysis and Finite Difference Analysis.**

% difference = (finite diff. analysis-current analysis)x100/current analysis

	operating speed = 2000 RPM $e_{rY} = 0.098$			operating speed = 8000 RPM $e_{rY} = 0.497$		
	current analysis	finite difference analysis	% difference	current analysis	finite difference analysis	% difference
$K_{ZZ}$ (MN/m)	-0.932	0.000	-100.0	-6.932	0.021	-100.3
$K_{ZY}$ (MN/m)	4.256	4.040	-5.1	40.728	42.000	3.1
$K_{YZ}$ (MN/m)	-4.140	-3.930	-5.1	-25.526	-21.000	-17.7
$K_{YY}$ (MN/m)	-1.037	0.000	-100.0	-2.113	0.000	-100.0
$C_{ZZ}$ (KN/m)	38.056	37.500	-1.5	45.264	50.400	11.3
$C_{ZY}$ (KN/m)	0.056	0.000	-100.0	4.259	0.000	-100.0
$C_{YZ}$ (KN/m)	0.186	0.000	-100.0	2.970	0.000	-100.0
$C_{YY}$ (KN/m)	39.076	38.600	-1.2	81.286	99.900	22.9
$F_Z$ (N)	40.938	39.15	-4.4	1284.249	1066.553	-16.9
$F_Y$ (N)	-9.297	0.0	-100.0	-356.808	0.000	-100.0
$\zeta$	-170.659	-171.635	0.6	-23.742	-73.149	208.1
$\lambda$ (rad/s)	358.418	366.662	2.3	366.593	371.597	1.4
$Q_v$ (cm <sup>3</sup> / s)	368.672	383.000	3.9	532.434	567.000	6.5
$T_w$ ( ° C )	51.534	51.700	0.3	55.178	56.500	2.4
$T_M$ ( ° C )	51.893	51.700	-0.4	78.383	56.500	-27.9

for this condition is not linear as shown in Fig. 18. This establishes the importance of having the best possible temperature distribution in an oil seal analysis.

## 5.2 Linear Stability Analysis Results

The phrase “linear stability analysis results” is used in this report for the results in terms of pressure and temperature distributions, stiffness and damping characteristics, stability parameters, and axial-flow rates for the seals that are locked at a particular eccentricity. Figures 19 and 20 show the pressure and temperature distributions in the above seal operating at eccentricities of 0.7 and 0.8 respectively. The effect of cavitation can be seen on the pressure and temperature distributions in these cases. The pressure remains constant in the cavitation zone. The case corresponding to an eccentricity ratio of 0.7 has less cavitation than the case corresponding to 0.8 because as the eccentricity is increased, the hydrodynamic action in the fluid increases which enhances the cavitation. The temperature distribution corresponding to an eccentricity ratio of 0.7 is not affected significantly by cavitation because the cavitation region is very small in this case.

Figures 21-32 show the plots of various parameters versus the eccentricity ratio,  $e_{rY}$ , for the same seal. Figures 21 and 22 show the plots of the direct stiffness coefficients versus the eccentricity ratio,  $e_{rY}$ , for different speeds. The direct stiffness  $K_{ZZ}$  and  $K_{YY}$  are negative at low eccentricities. This is because the perturbation given to the journal to evaluate the stiffness coefficients reduces the fluid film thickness and increases the temperature by increasing viscous dissipation. The increase in temperature decreases the viscosity. The effect of the reduction in the fluid film thickness is to increase the value of hydrodynamic forces and the effect of the reduction in the fluid viscosity is to

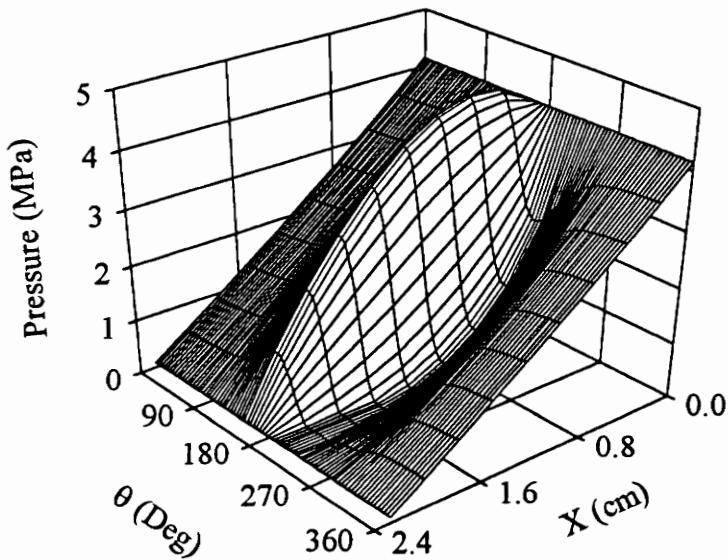
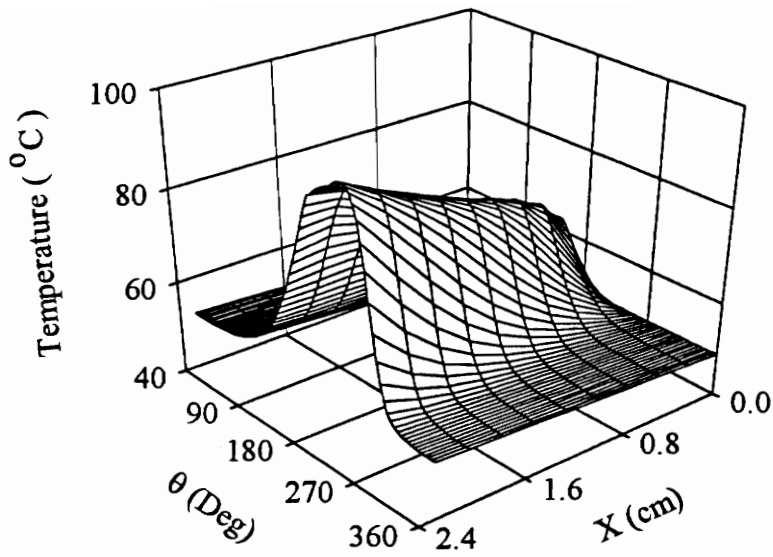


**Figure 19. Temperature and Pressure Distributions in the Straight Seal**  
**Operating Speed = 133.33 Hz (8000 RPM)**  
**Operating Eccentricity ( $e_{rY}$ ) = 0.7**

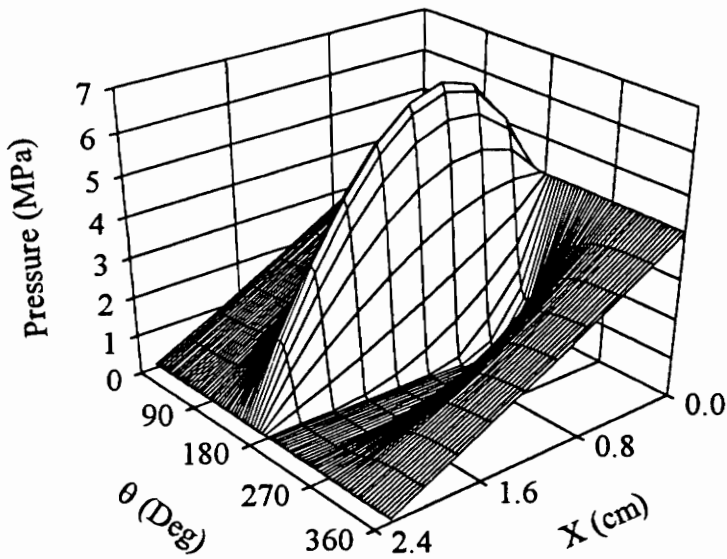
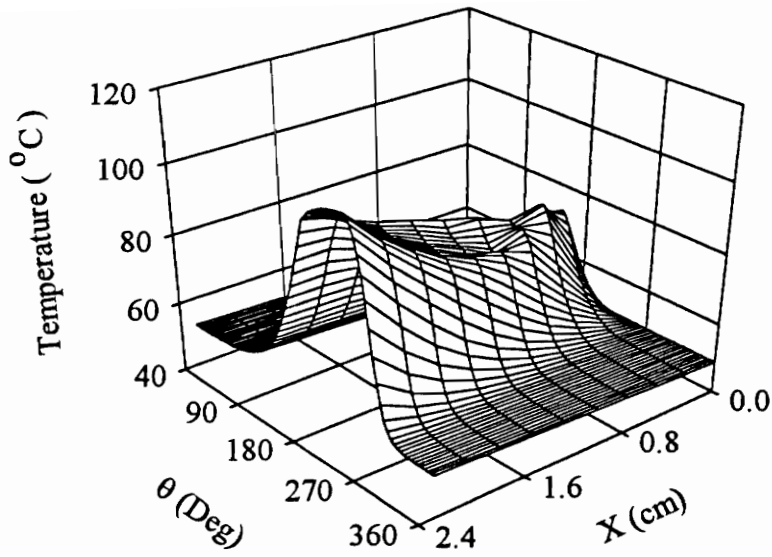


**Figure 20. Temperature and Pressure Distributions in the Straight Seal**  
**Operating Speed = 133.33 Hz (8000 RPM)**  
**Operating Eccentricity ( $e_{rY}$ ) = 0.8**

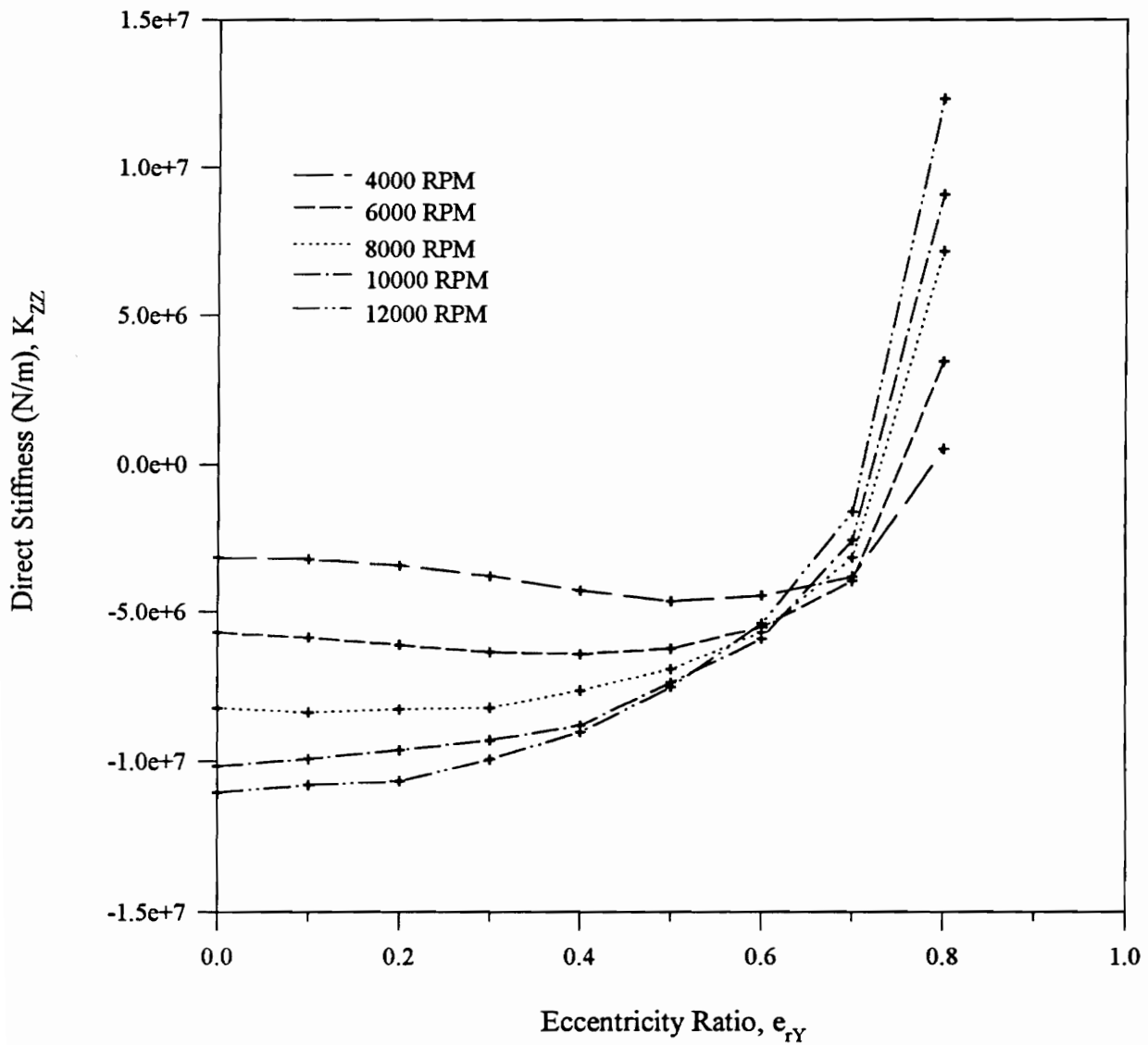


**Figure 21. Plot of Direct Stiffness vs. Eccentricity Ratio for Different Speeds  
Supply Pressure = 4.136 MPa**

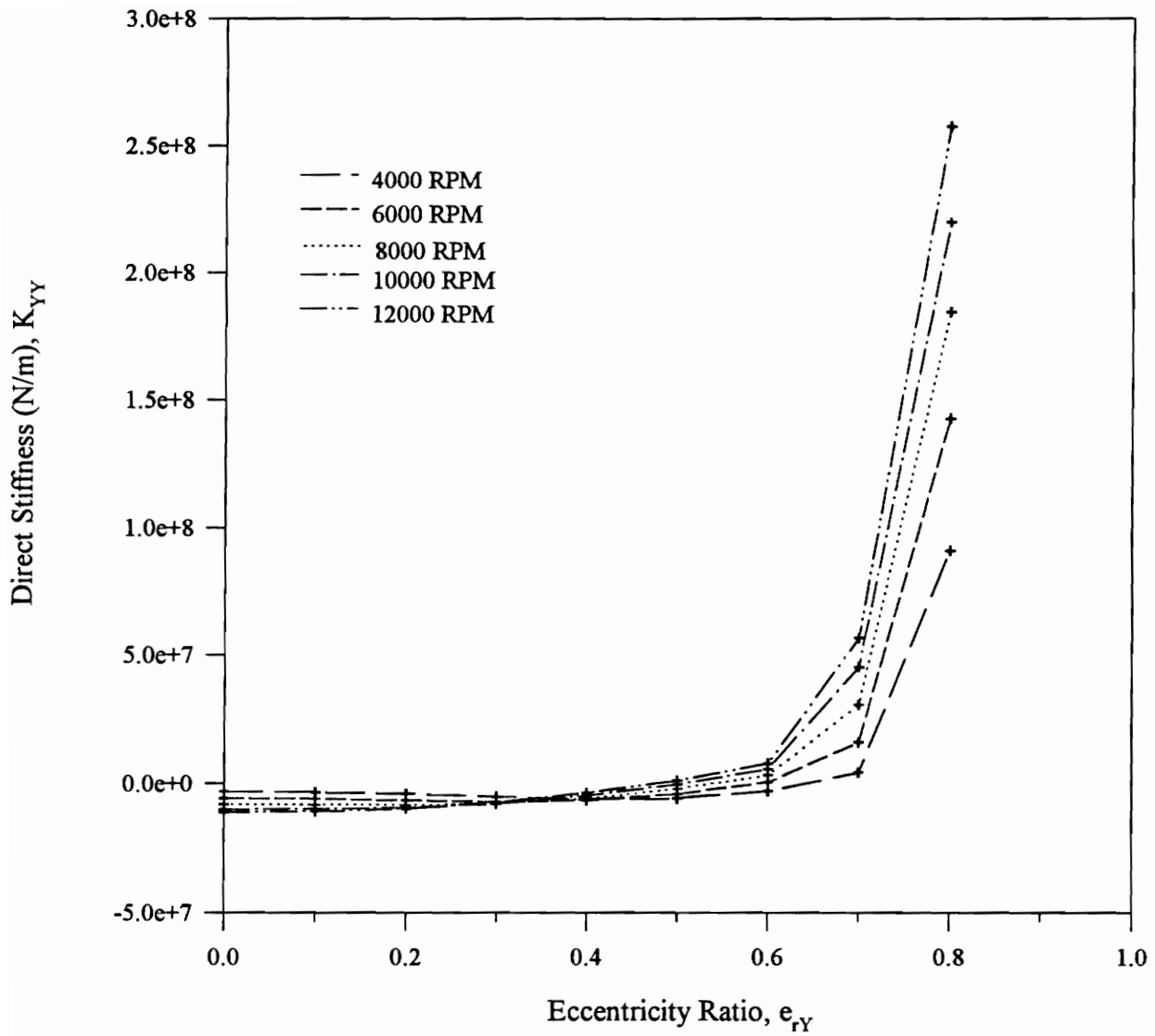
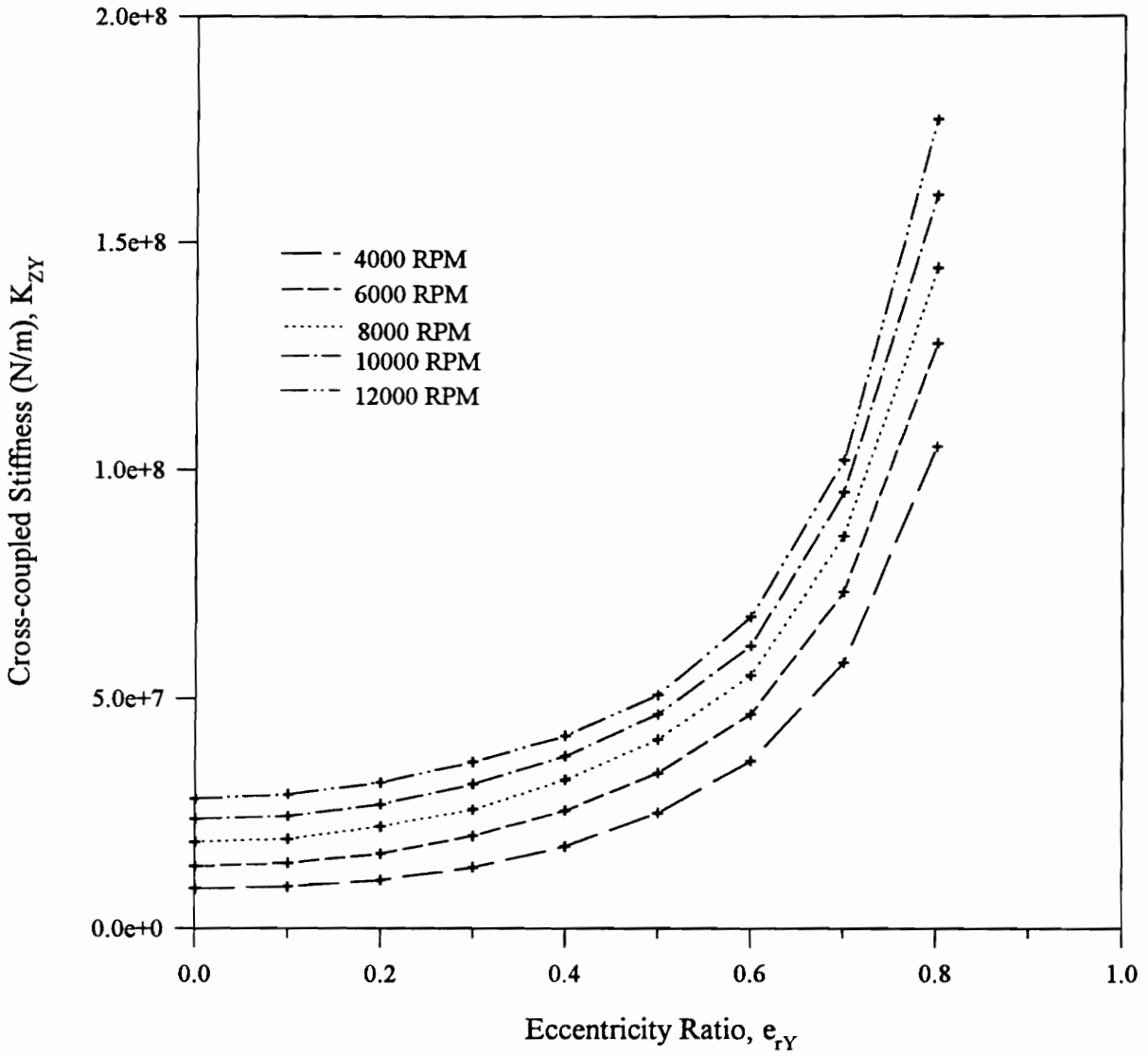


**Figure 22. Plot of Direct Stiffness vs. Eccentricity Ratio for Different Speeds  
Supply Pressure = 4.136 MPa**

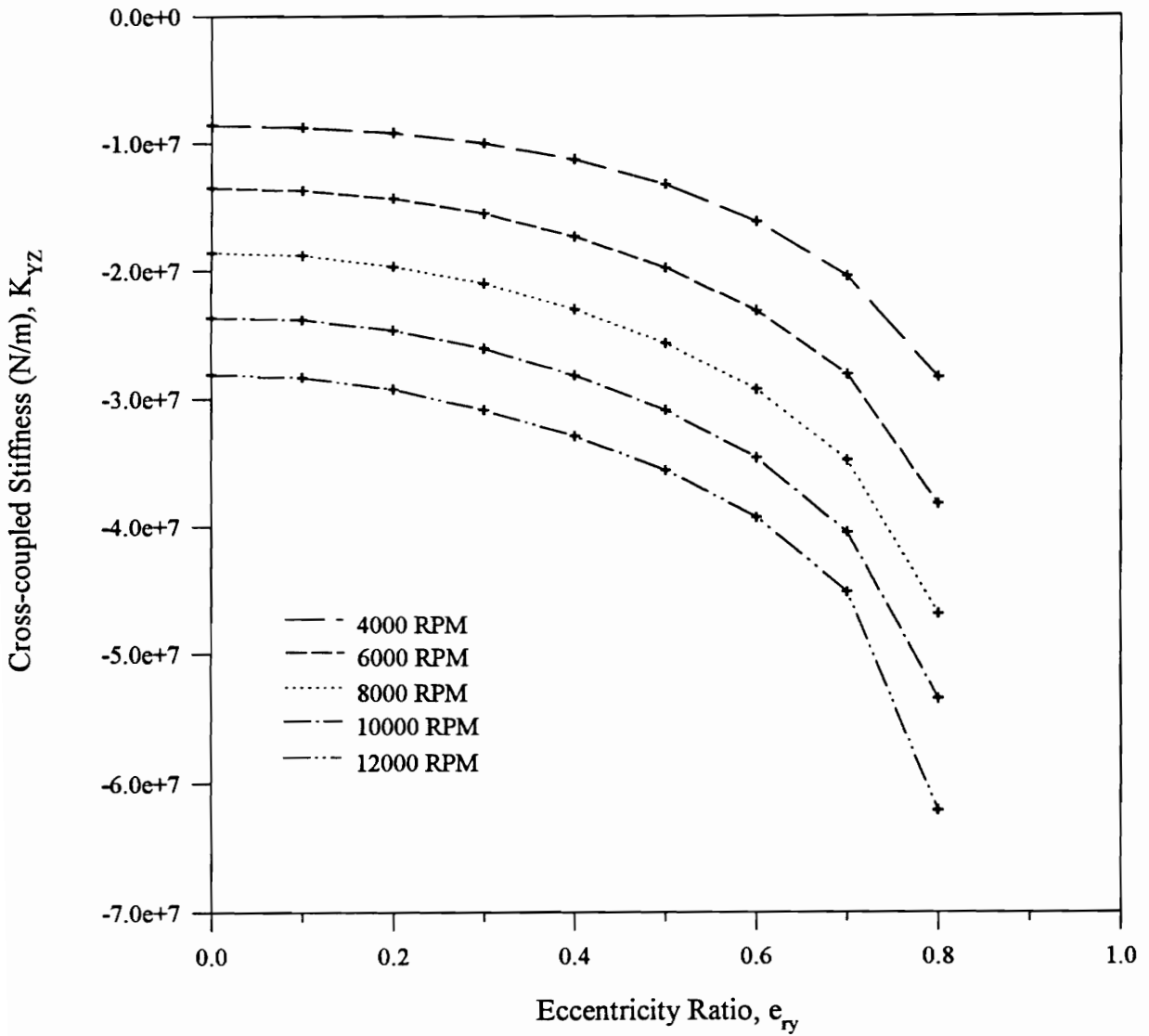
decrease the value of hydrodynamic forces. At low eccentricities the effect of perturbation is more significant on the change of viscosity. Hence, the direct stiffness is negative. This phenomenon magnifies as the speed increases, which makes the direct stiffness more and more negative with the increase in speed. At high eccentricities the direct stiffness increases with the speed because of cavitation, which becomes more and more predominant as the speed increases. Figures 23 and 24 show the plots of cross-coupled stiffness coefficients versus the eccentricity ratio,  $e_{rY}$ , for different speeds. The magnitude of the cross-coupled stiffness increases with the increase in the operating eccentricity and the speed as the hydrodynamic forces increase.

Figure 25 and 26 show the plots of direct damping coefficients. The direct damping increases as the eccentricity ratio is increased. It decreases as the speed is increased because the fluid viscosity decreases with the increase in speed. Figures 27 and 28 show the plots of cross-coupled damping coefficients. The sudden increase in the cross-coupled damping for eccentricity ratio beyond 0.7 is because of cavitation.

Figures 29 and 30 show the plots of damped natural frequency and growth factor corresponding to the forward whirl of the rotor. Again, the change in the trends at eccentricity ratio of 0.7 is because of cavitation. The stability of the compressor rotor diminishes with the increase in speed as the growth factor decreases which happens because the direct damping reduces and cross-coupled stiffness increases with increase in operating speed. From Fig. 30 it can be seen that the onset speed of instability in this case is about 166.67 Hz (10000 RPM). Figures 31 and 32 show the plots of axial flow rate through the seal and maximum temperature. The axial flow rate increases with the eccentricity and speed as expected. It can increase by a factor of two from the centered case to the highly eccentric case as seen in Fig. 31. The maximum temperature also increases with the eccentricity and the speed as the viscous dissipation increases.



**Figure 23. Plot of Cross-coupled Stiffness vs. Eccentricity Ratio for Different Speeds  
Supply Pressure = 4.136 MPa**



**Figure 24. Plot of Cross-coupled Stiffness vs. Eccentricity Ratio for Different Speeds  
Supply Pressure = 4.136 MPa**

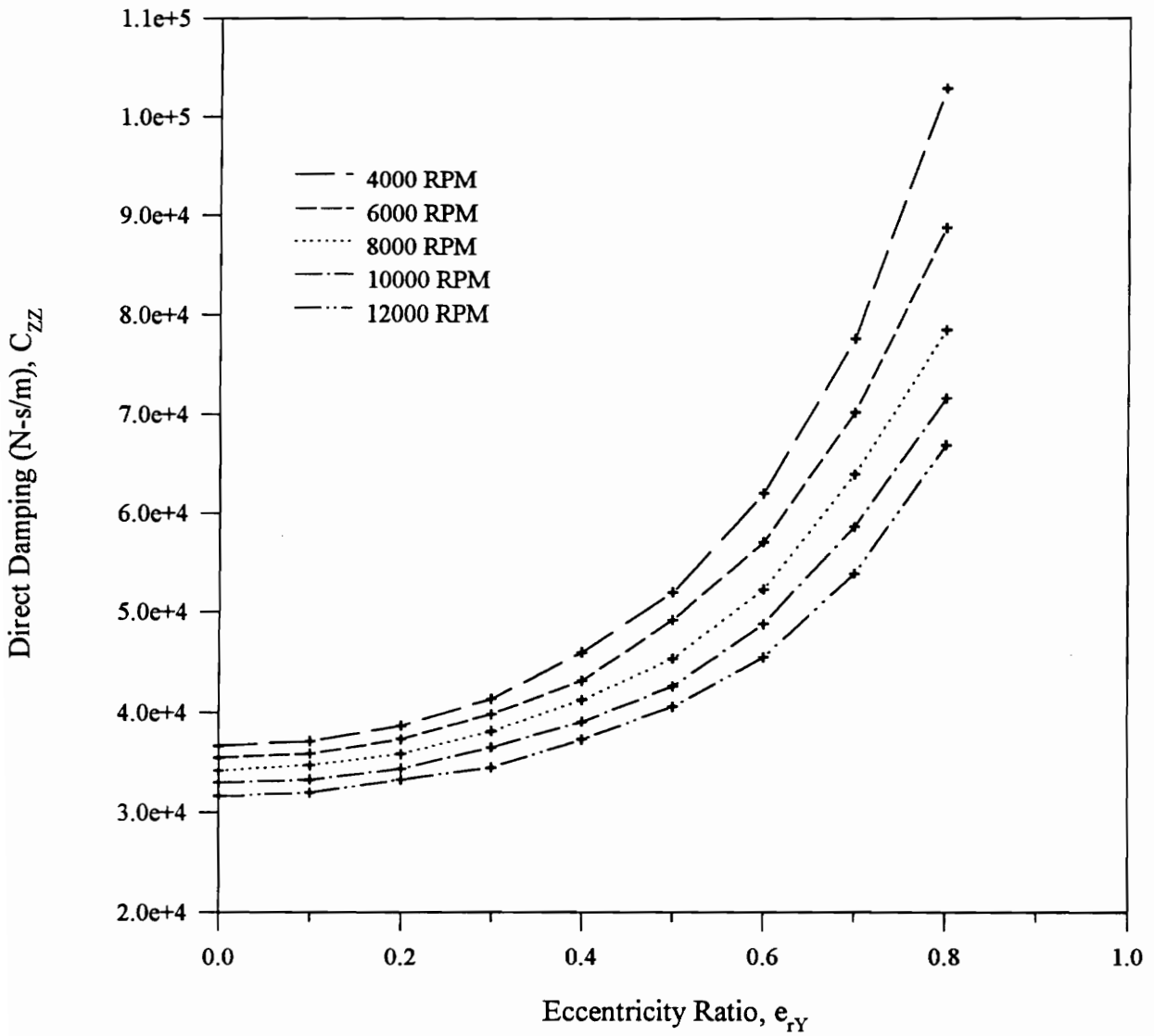


**Figure 25. Plot of Direct Damping vs. Eccentricity Ratio for Different Speeds  
Supply Pressure = 4.136 MPa**

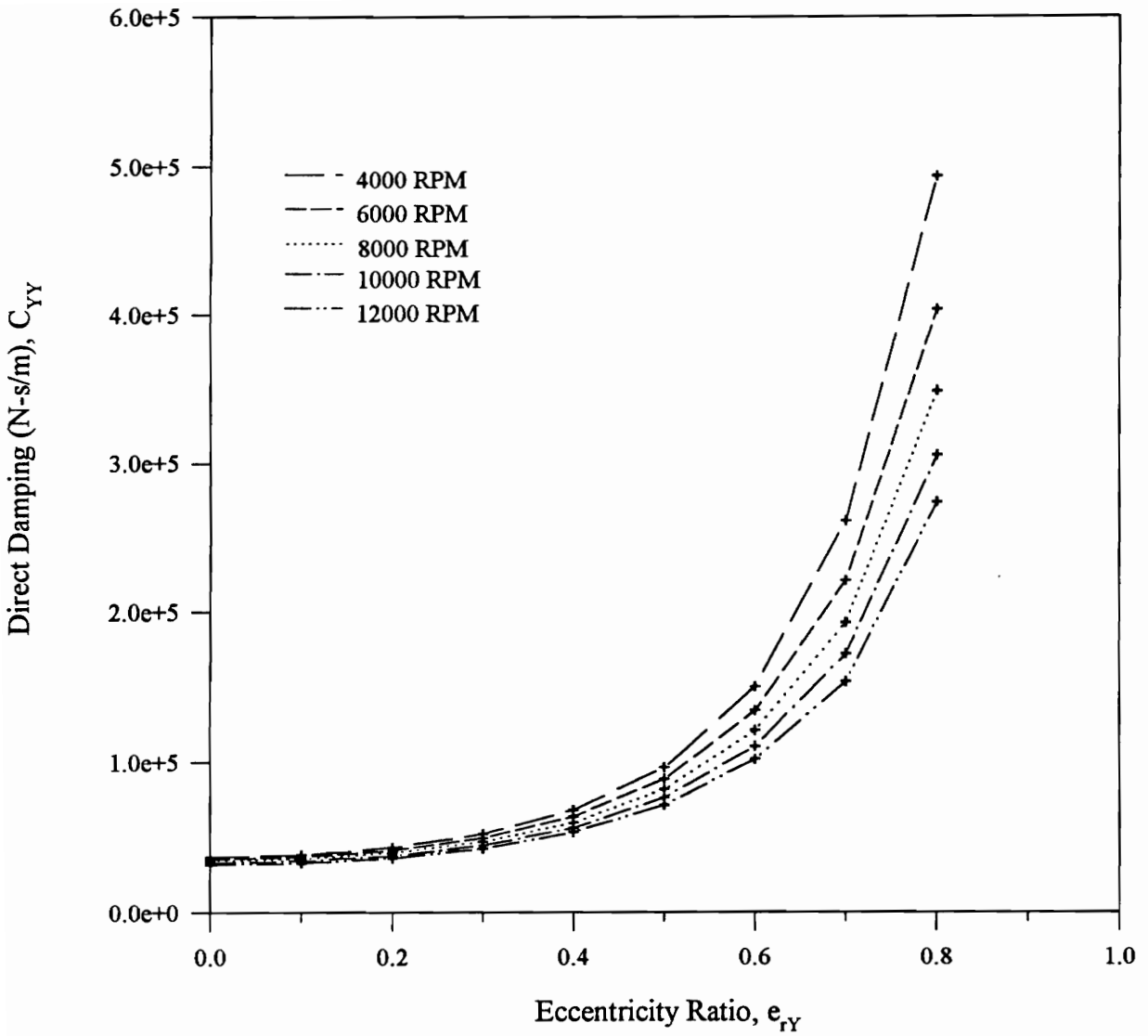


**Figure 26. Plot of Direct Damping vs. Eccentricity Ratio for Different Speeds  
Supply Pressure = 4.136 MPa**

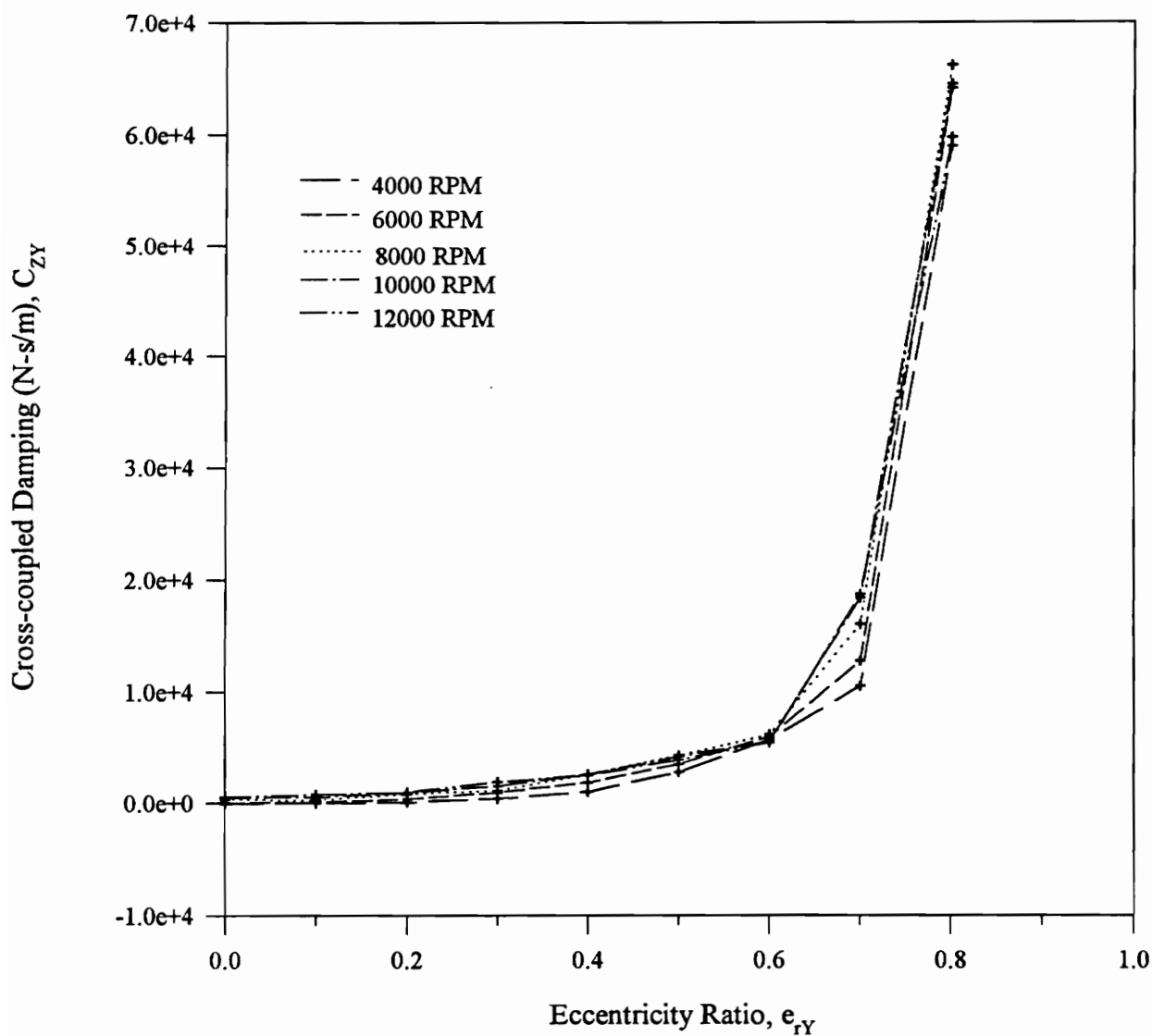


**Figure 27. Plot of Cross-coupled Damping vs. Eccentricity Ratio for Different Speeds  
Supply Pressure = 4.136 MPa**

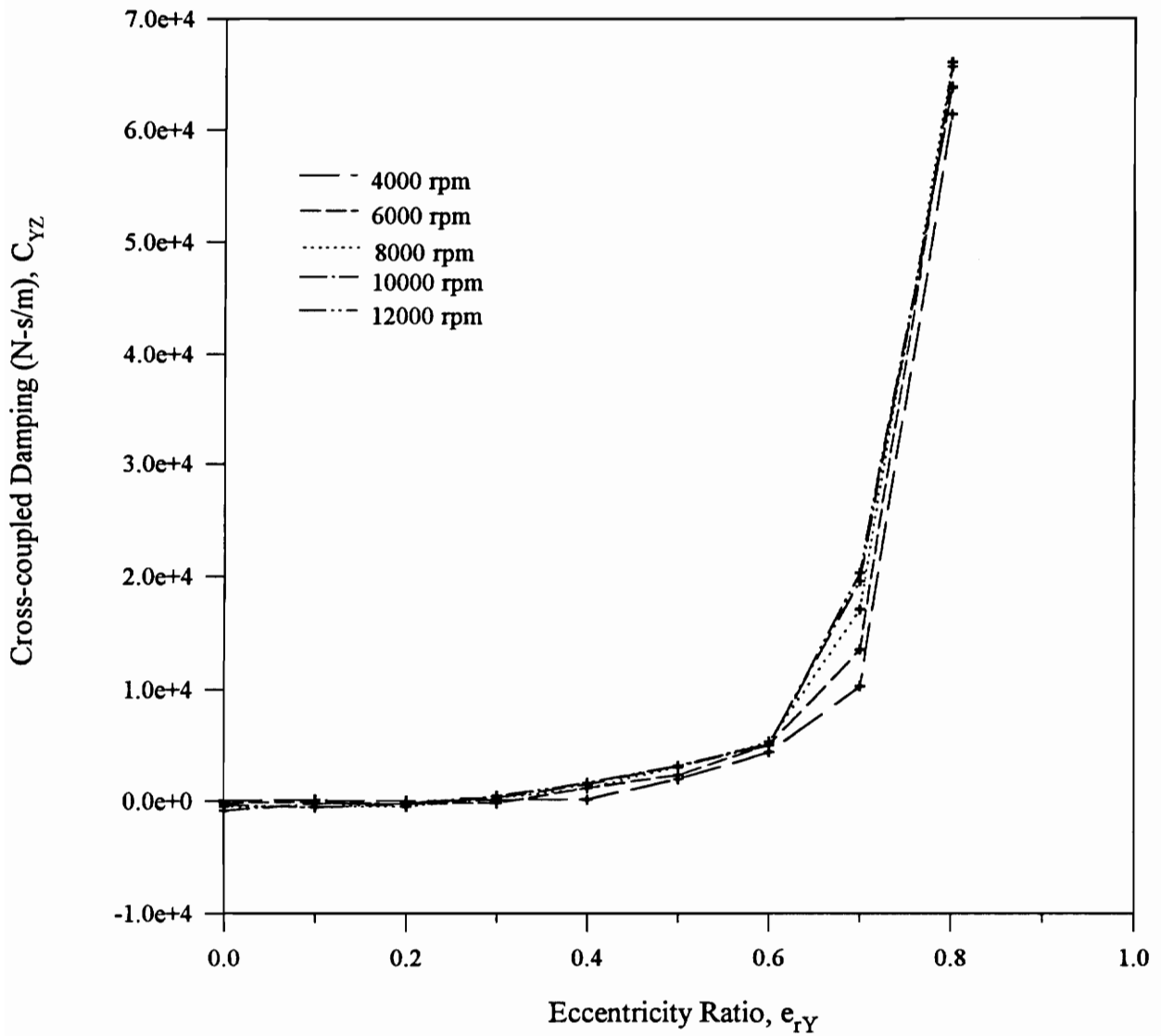


**Figure 28. Plot of Cross-coupled Damping vs. Eccentricity Ratio for Different Speeds  
Supply Pressure = 4.136 MPa**

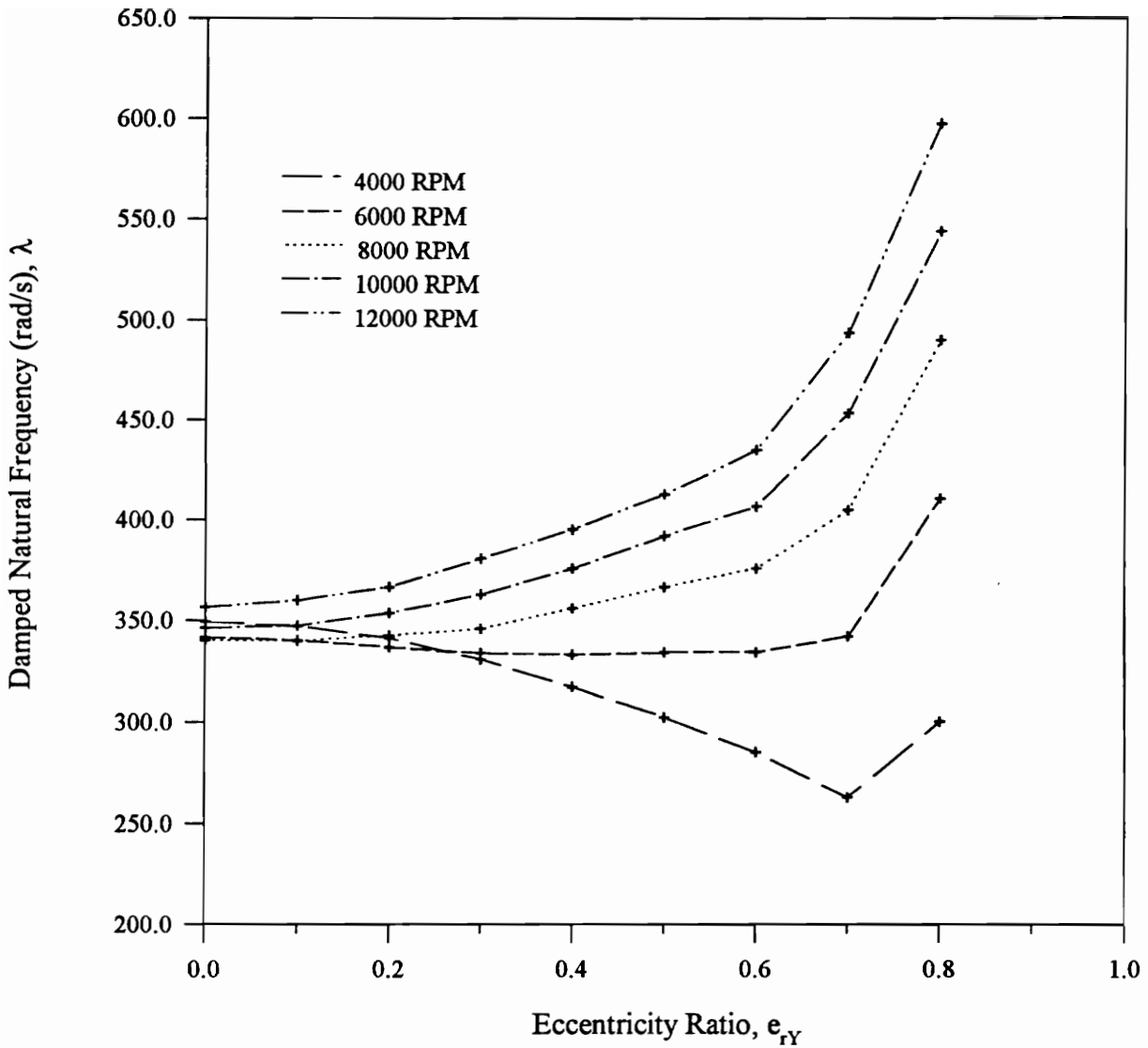


**Figure 29. Plot of Damped Natural Frequency vs. Eccentricity Ratio for Different Speeds  
Supply Pressure = 4.136 MPa**

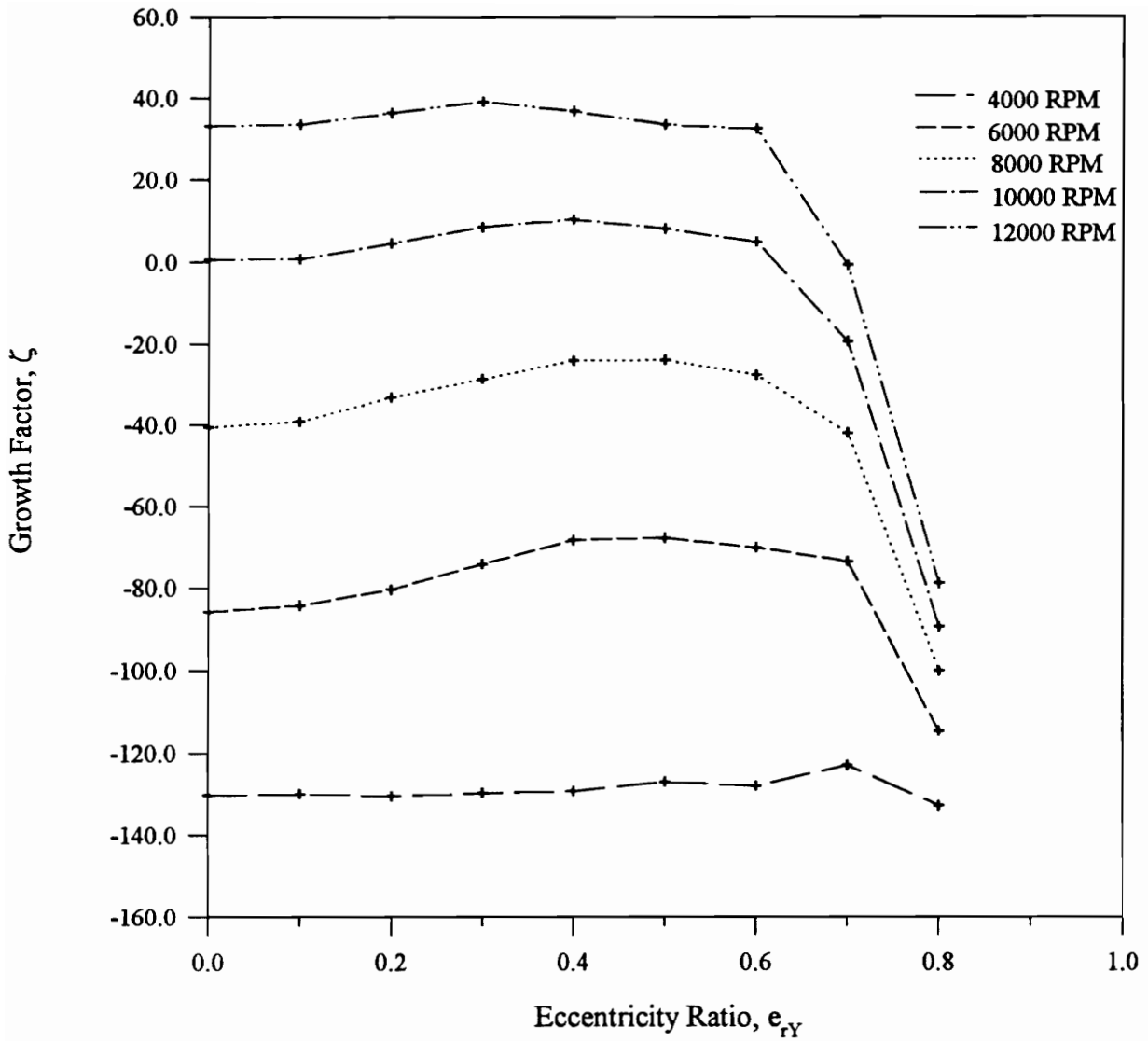


**Figure 30. Plot of Growth Factor vs. Eccentricity Ratio for Different Speeds  
Supply Pressure = 4.136 MPa**

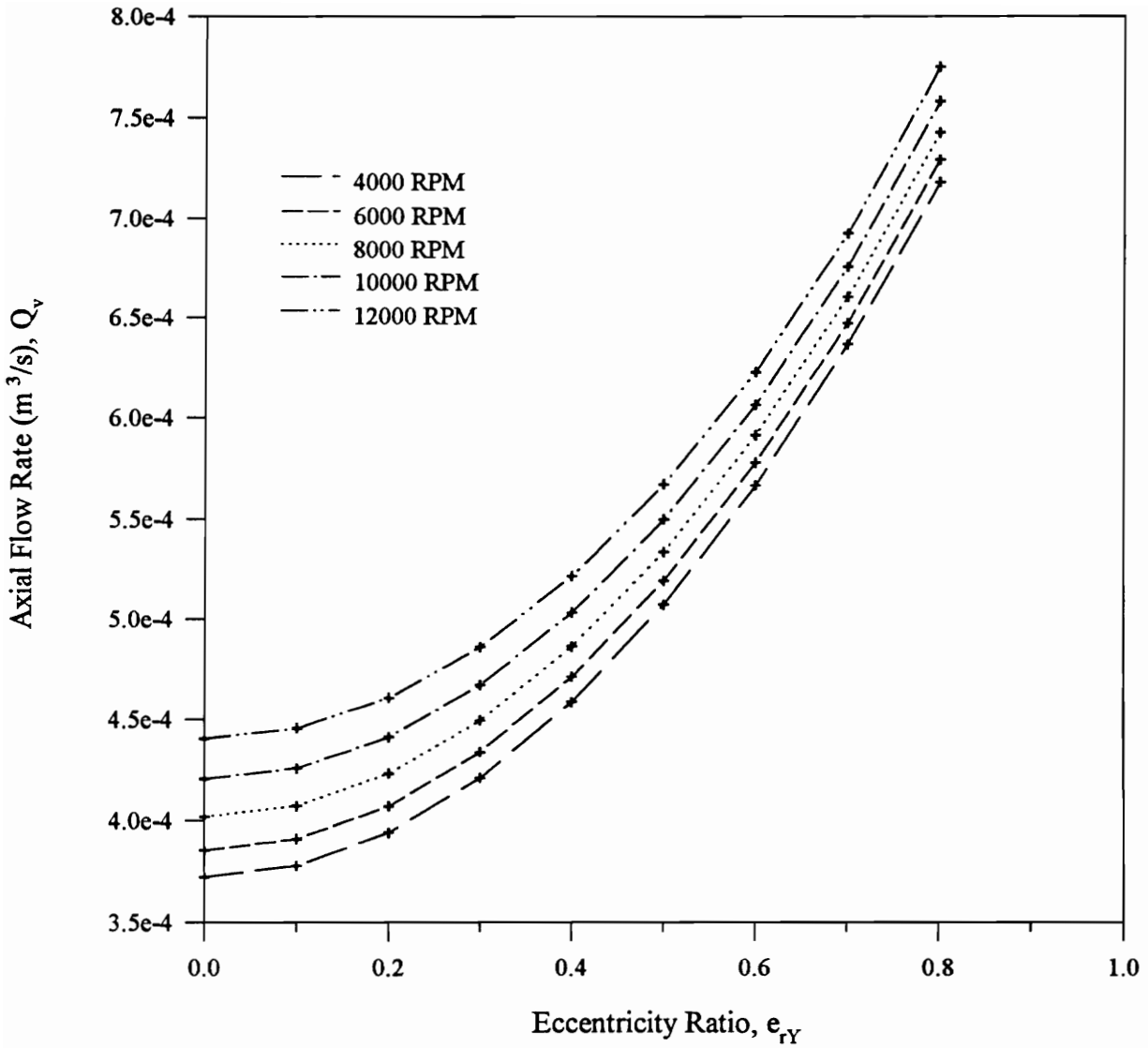


**Figure 31. Plot of Axial Flow Rate vs. Eccentricity Ratio for Different Speeds  
Supply Pressure = 4.136 MPa**

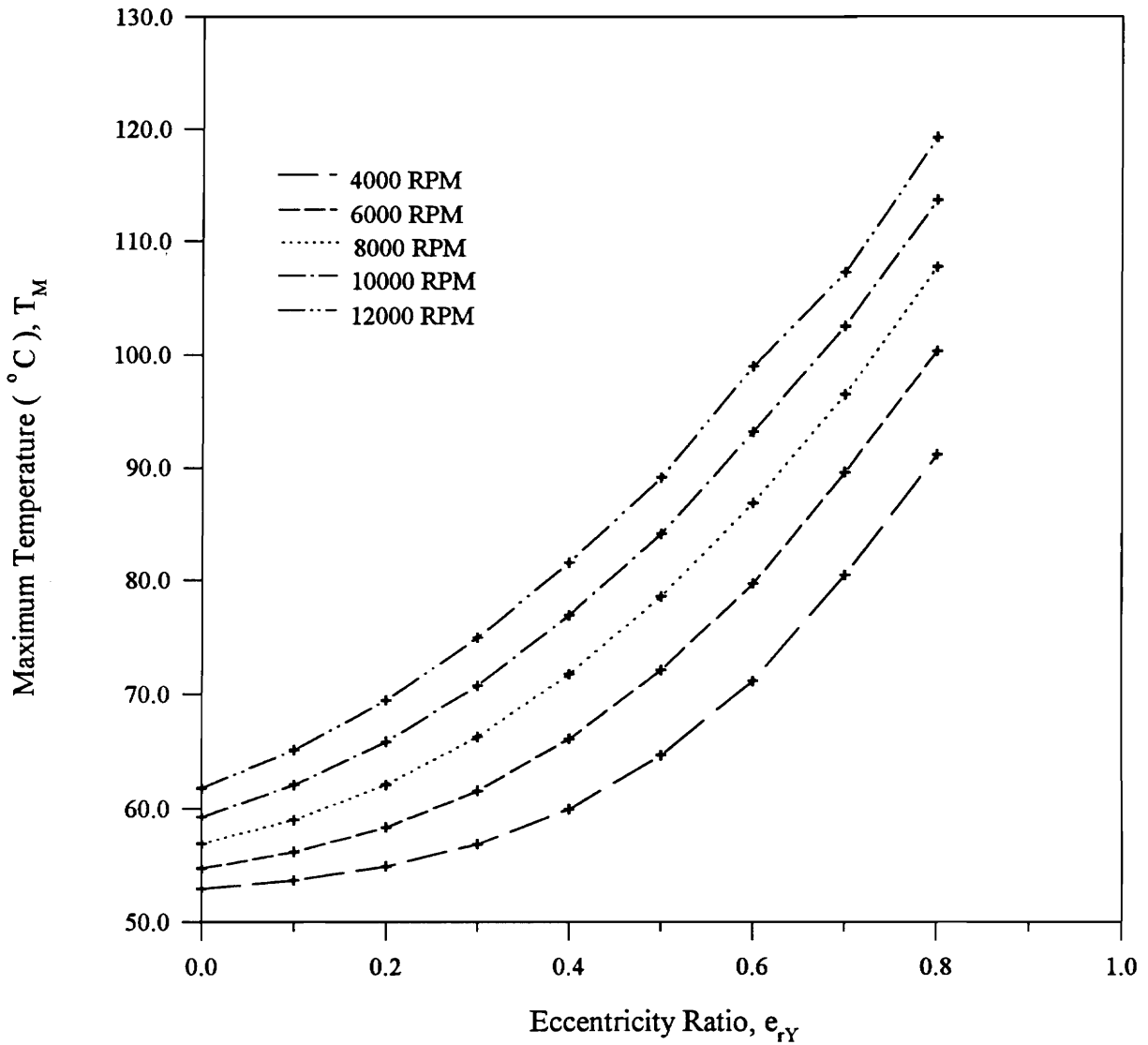


**Figure 32. Plot of Maximum Temperature vs. Eccentricity Ratio for Different Speeds  
Supply Pressure = 4.136 MPa**

Figures 33-36 show the plots of different parameters for the above seal with a supply pressure of 0.827 MPa which is typical of a compressor in test stand conditions. Figure 33 shows the plot of direct stiffness,  $K_{ZZ}$ , as a function of the eccentricity ratio,  $e_{rY}$ , for different speeds. It is interesting to note that even at low eccentricities the direct stiffness increases with the speed as against its decrease in the Fig. 21 when the supply pressure is 4.136 MPa. The other features of the stiffness and damping characteristics remain same but for the change in their magnitude.

Figure 34 shows the plot of growth factor. With the decrease in the supply pressure the growth factors for all speeds become negative indicating an enhancement in the stability of the compressor rotor. Figure 35 shows the plot of axial flow rate. It decreases with the decrease in supply pressure as expected. Figure 36 shows the plot of maximum temperature. At low eccentricities the maximum temperature is more than its value for the case with higher supply pressure (see Fig. 32) because the axial flow rate is reduced with the reduction of the supply pressure. Hence, less heat is taken away by the discharged fluid. At high eccentricities the maximum temperature corresponding to lower supply pressure is less than that corresponding to higher supply pressure as the seal with the lower supply pressure has more cavitation and less viscous dissipation.

### 5.3 Non-linear Transient Analysis Results

In this section plots of different parameters obtained from the transient analysis of the above seal and the rotor are presented. The supply pressure used is 4.136 MPa. The transient analysis is performed for different operating speeds and frictional forces assuming certain initial conditions. The frictional force depends upon the total axial load on the seal,

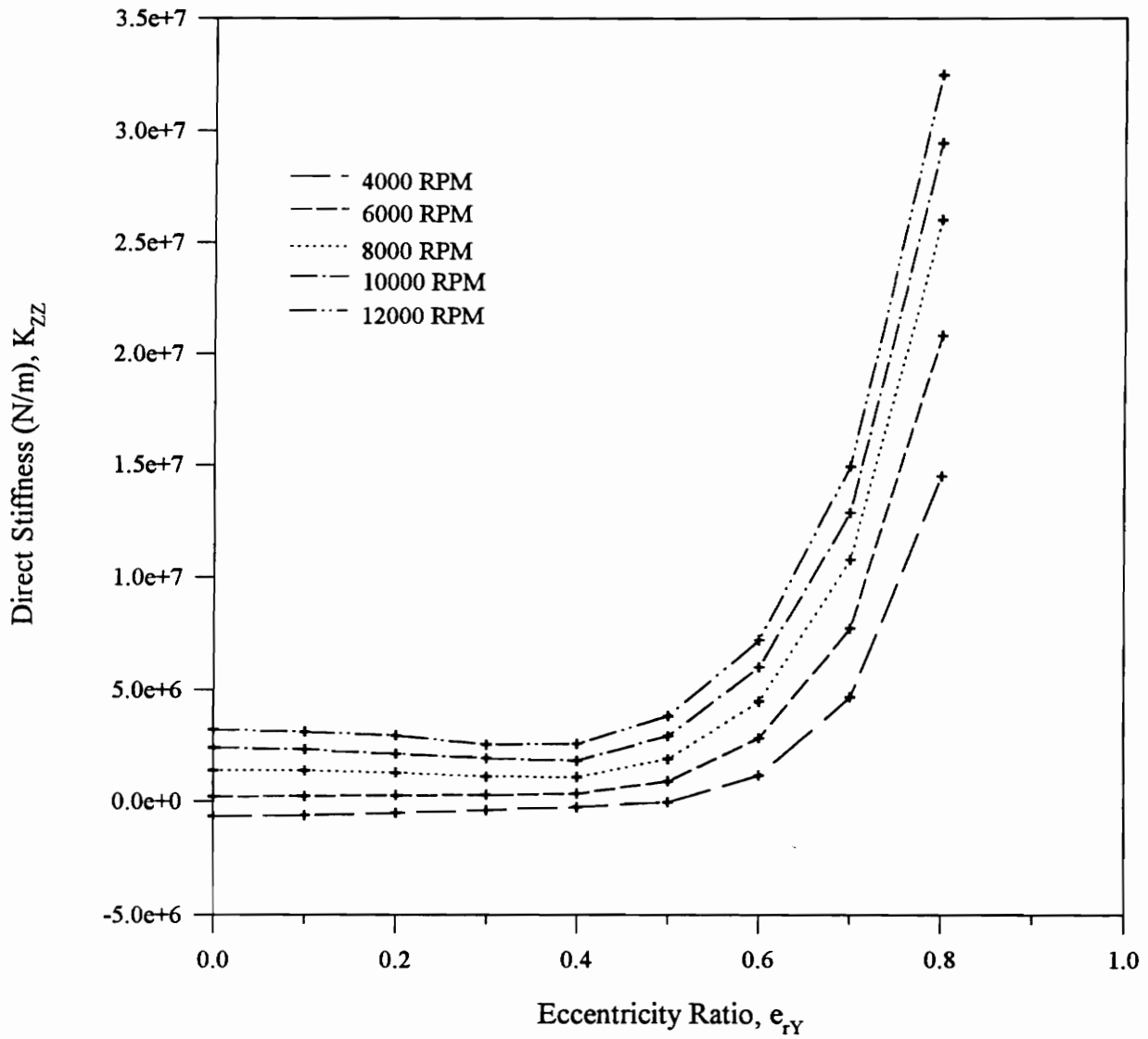


**Figure 33. Plot of Direct Stiffness vs. Eccentricity Ratio for Different Speeds  
Supply Pressure = 0.827 MPa**

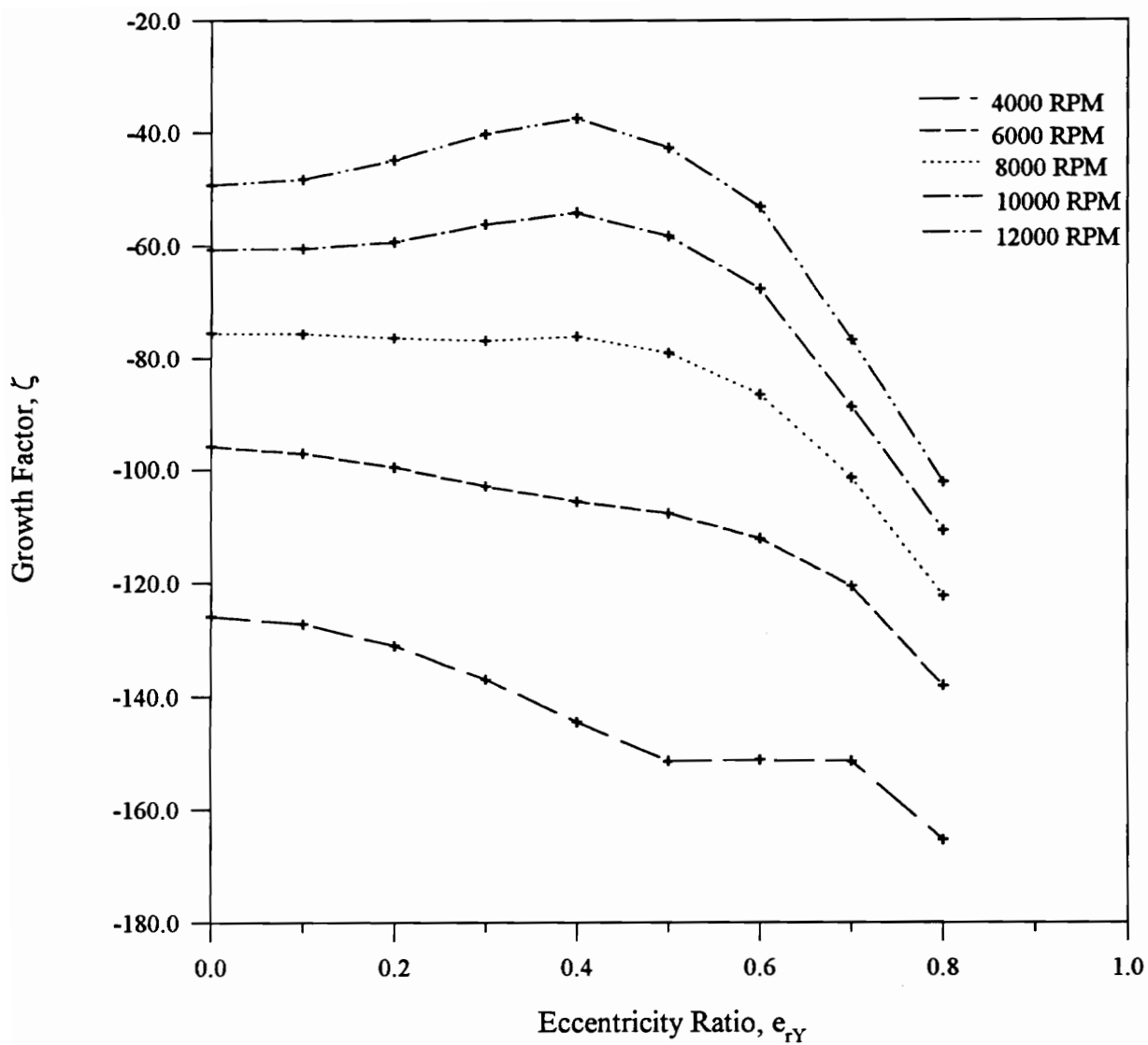


**Figure 34. Plot of Growth Factor vs. Eccentricity Ratio for Different Speeds  
Supply Pressure = 0.827 MPa**

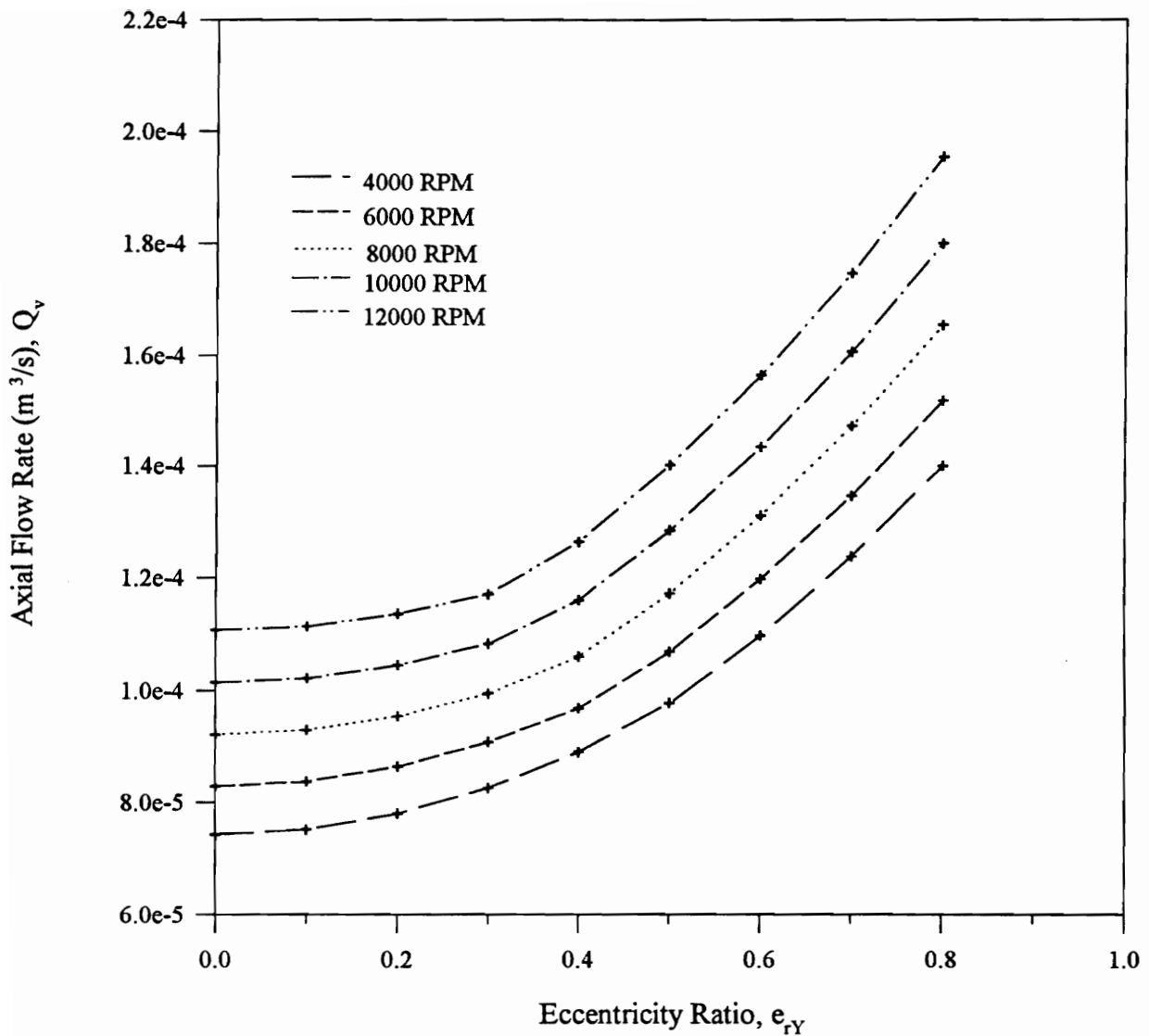


**Figure 35. Plot of Axial Flow Rate vs. Eccentricity Ratio for Different Speeds  
Supply Pressure = 0.827 MPa**

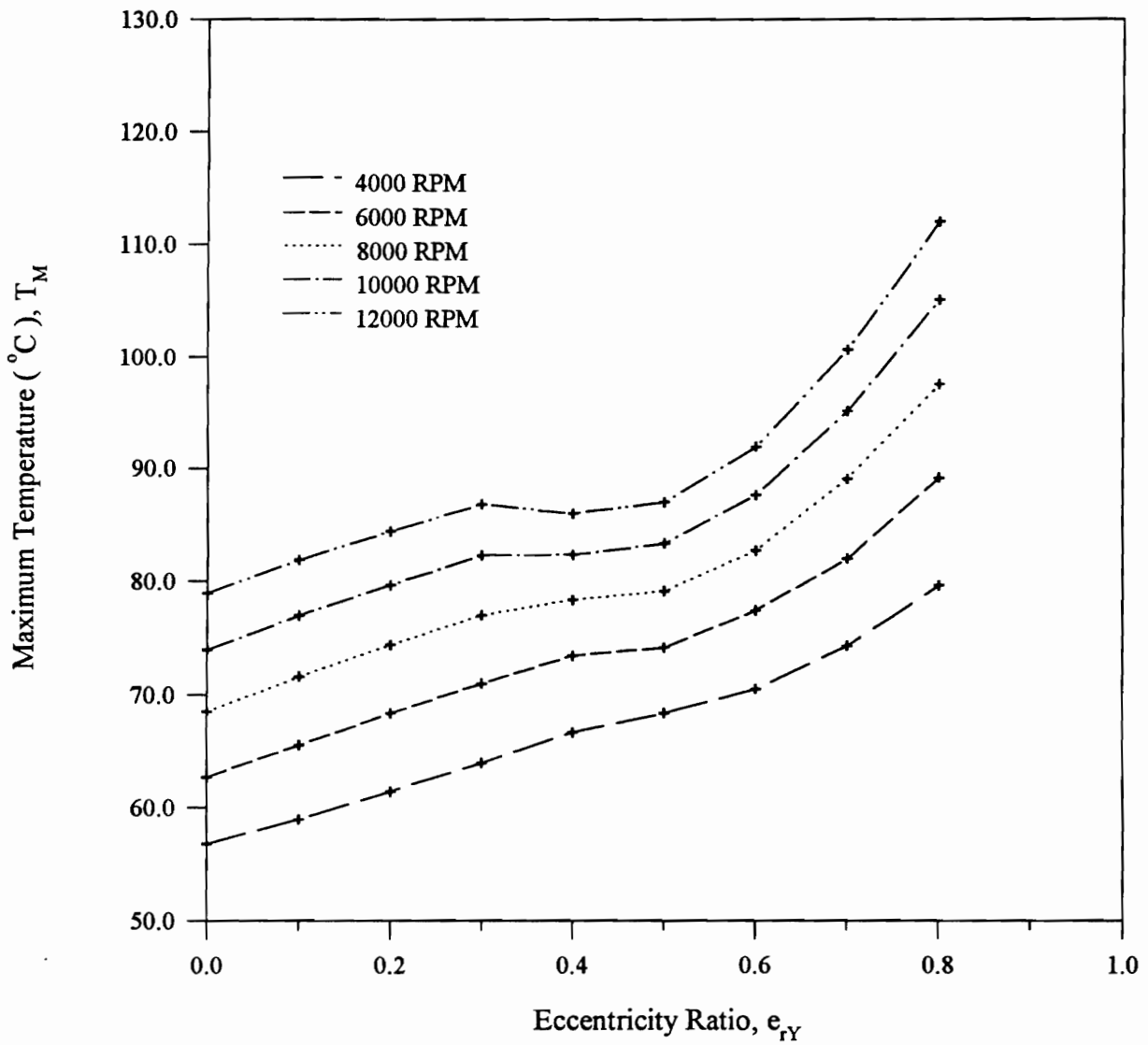


**Figure 36. Plot of Maximum Temperature vs. Eccentricity Ratio for Different Speeds  
Supply Pressure = 0.827 MPa**

lapped face area and the coefficient of friction between the lapped face and the compressor casing. For the results presented in this dissertation the dynamic frictional forces used are 444.8 N, 889.6 N and 1334.3 N. These values correspond to the lapped face outer diameters of 134.29 mm, 137.83 mm and 141.28 mm respectively when the spring load and the width of the lapped face are 110.1 N and 3.81 mm. Also, the initial velocities of the seal and the journal are assumed to be zero and initially the seal is assumed to be at a distance of 0.0254 mm on the -ve Y axis (see Fig. 6) and the journal is assumed to be at the origin O.

Figure 37 shows the plots of eccentricities and absolute seal positions versus time for the same seal (specifications given in Table 2).  $e_r$ ,  $e_{rY}$ , and  $e_{rZ}$  are the non-dimensional eccentricities. Operating speed of the journal and the frictional force used are 200 Hz (6000 RPM) and 444.8 N. It can be seen that the seal positions  $Z_s$  and  $Y_s$  remain constant after time = 0.04 sec. approximately, indicating that the seal is locked after this time. Also, the eccentricities after this point oscillate with a constant amplitude as small as 0.1 indicating that the rotor whirls with a small radius and reached a steady state. Figure 38 shows similar plots for the above case with an operating speed of 133.33 Hz (8000 RPM). Here, it can be seen that the absolute seal positions  $Z_s$  and  $Y_s$  oscillate with an increasing amplitude until the eccentricity ratio,  $e_r$ , becomes as high as 0.85 indicating that the seal drives the rotor unstable. Figure 39 shows the variation of hydrodynamic forces and the maximum temperature in the fluid as a function of time for this case. Since in this case the eccentricity ratio,  $e_r$ , increases with time the maximum temperature also increases with time and reaches a value of 132 °C approximately. Figure 40 shows the orbits traced by the center of the seal and the rotor in the Z-Y plane for the same case. The red circle and the red orbit correspond to the seal ring and the motion of its center. The blue circle and the blue orbit correspond to the circumference of the rotor and the

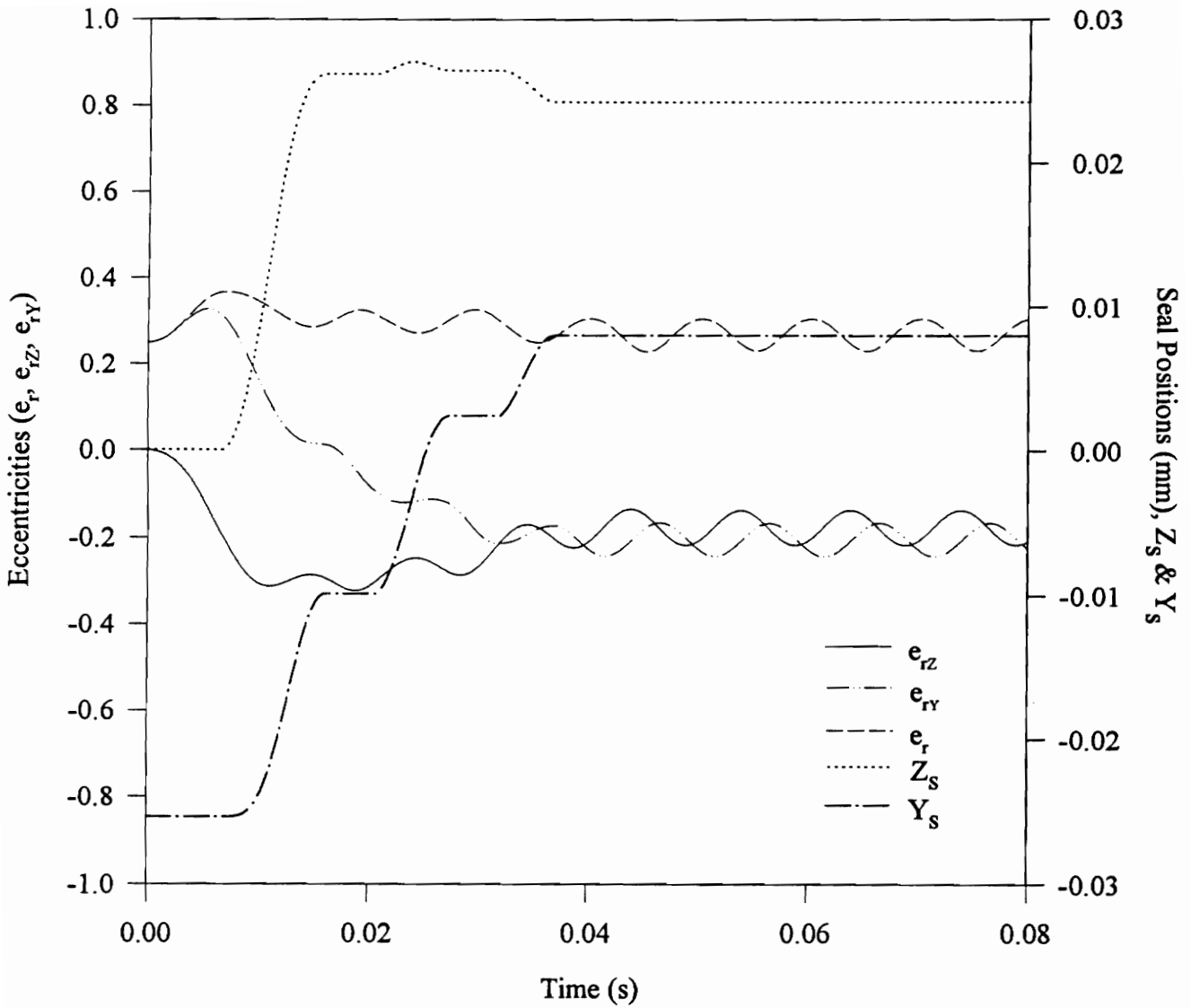


**Figure 37. Plots of Eccentricities and Absolute Seal Positions vs. Time for a Straight Seal Operating Speed = 100 Hz (6000 RPM); Frictional Force = 444.8 N**

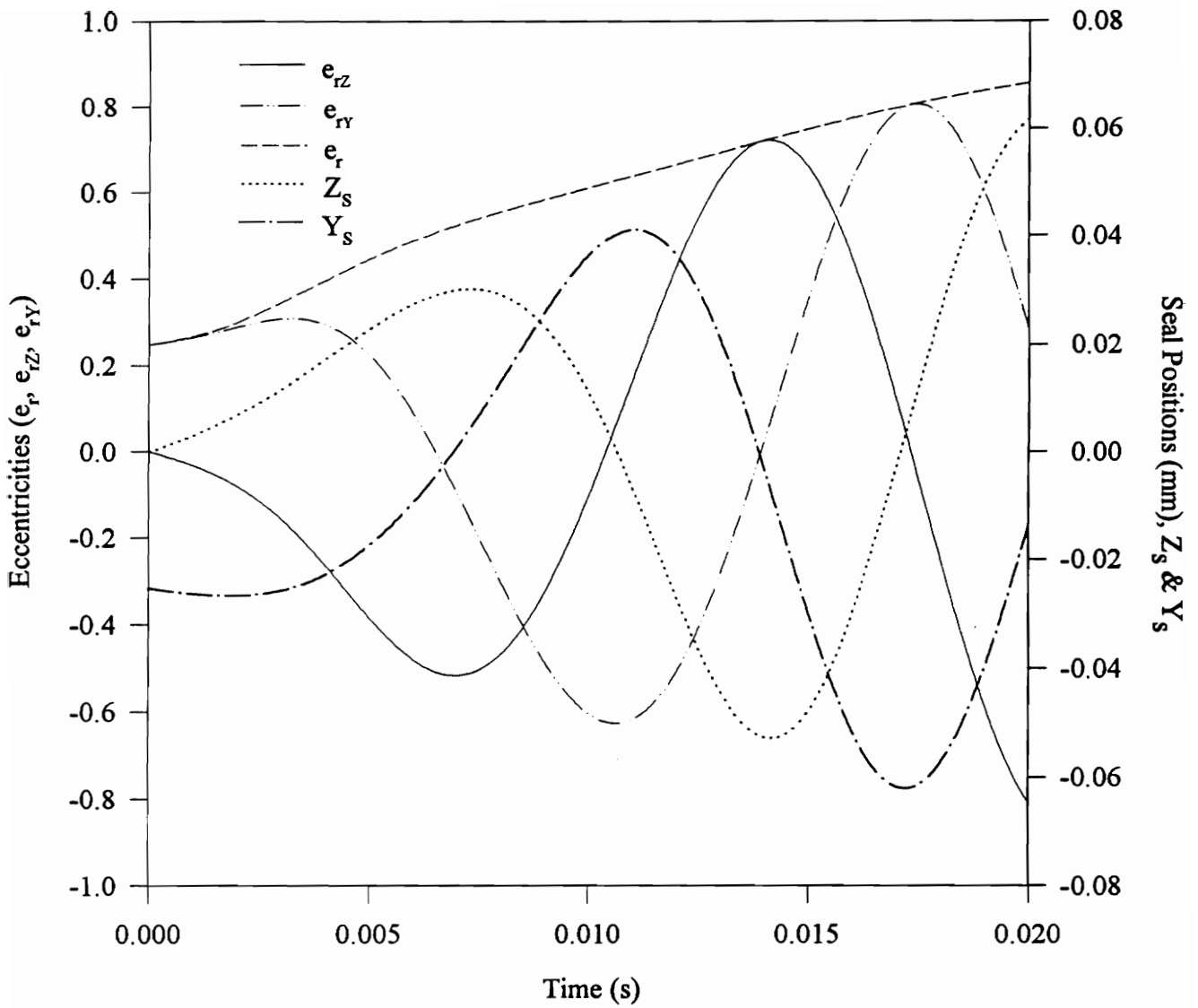


**Figure 38. Plots of Eccentricities and Absolute Seal Positions vs. Time for a Straight Seal Operating Speed = 133.33 Hz (8000 RPM); Frictional Force = 444.8 N**

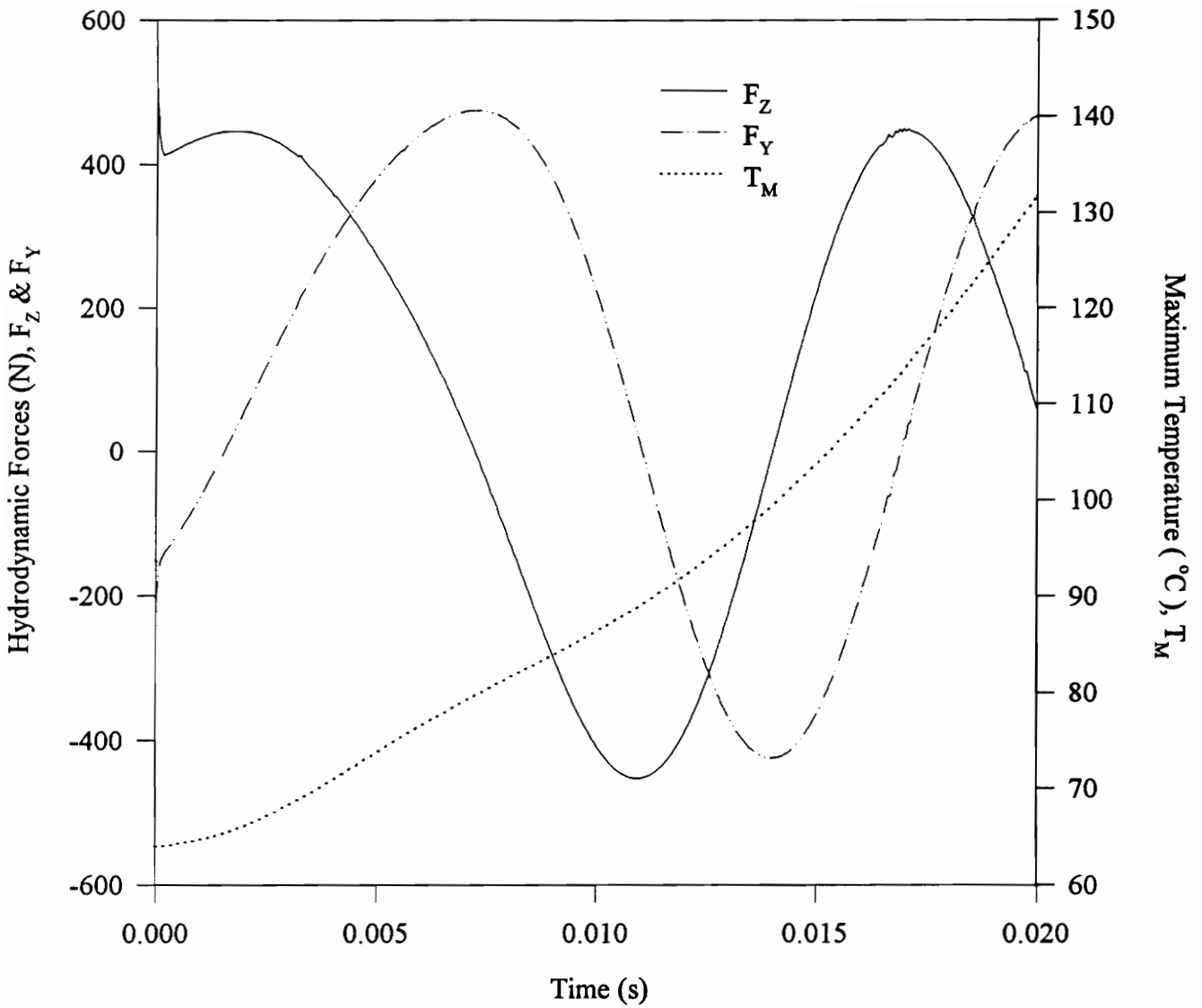


**Figure 39. Plots of Hydrodynamic Forces and Maximum Temperature vs. Time for a Straight Seal**  
**Operating Speed = 133.33 Hz (8000 RPM); Frictional Force = 444.8 N**

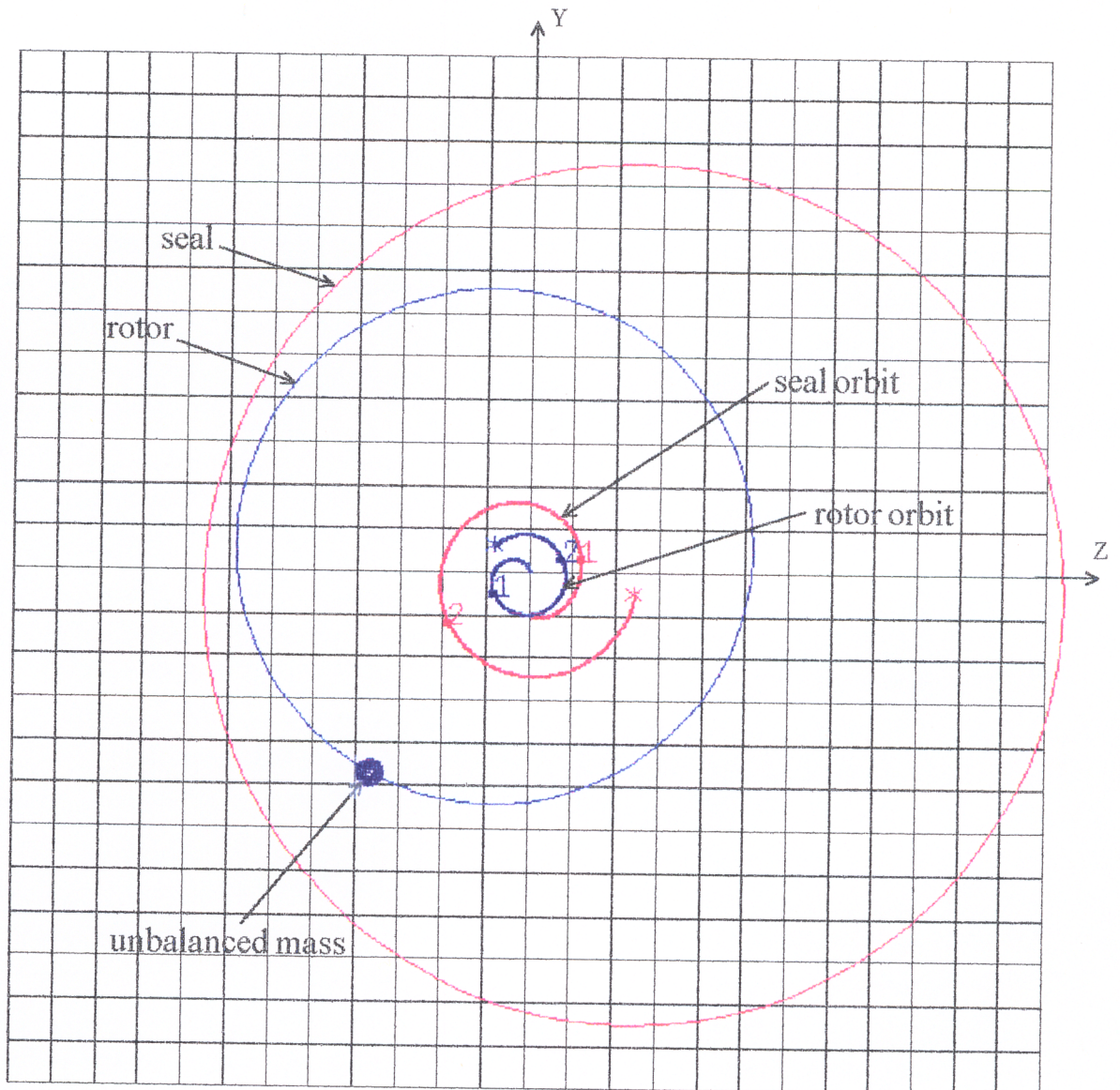
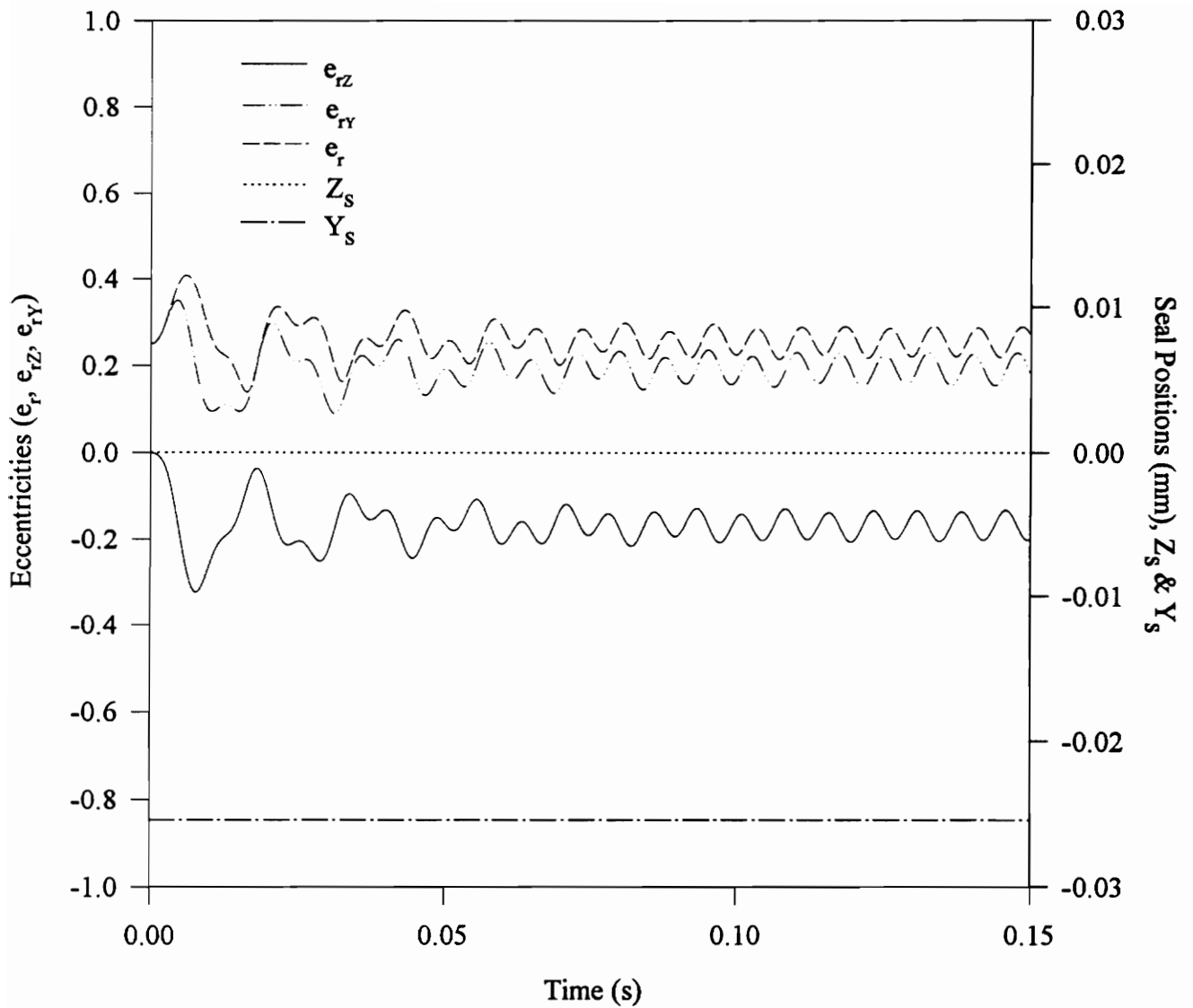


**Figure 40. Transient Response of the Straight Seal and the Rotor**  
**Operating Speed = 133.33 Hz (8000 RPM)**  
**Frictional Force = 444.8 N**

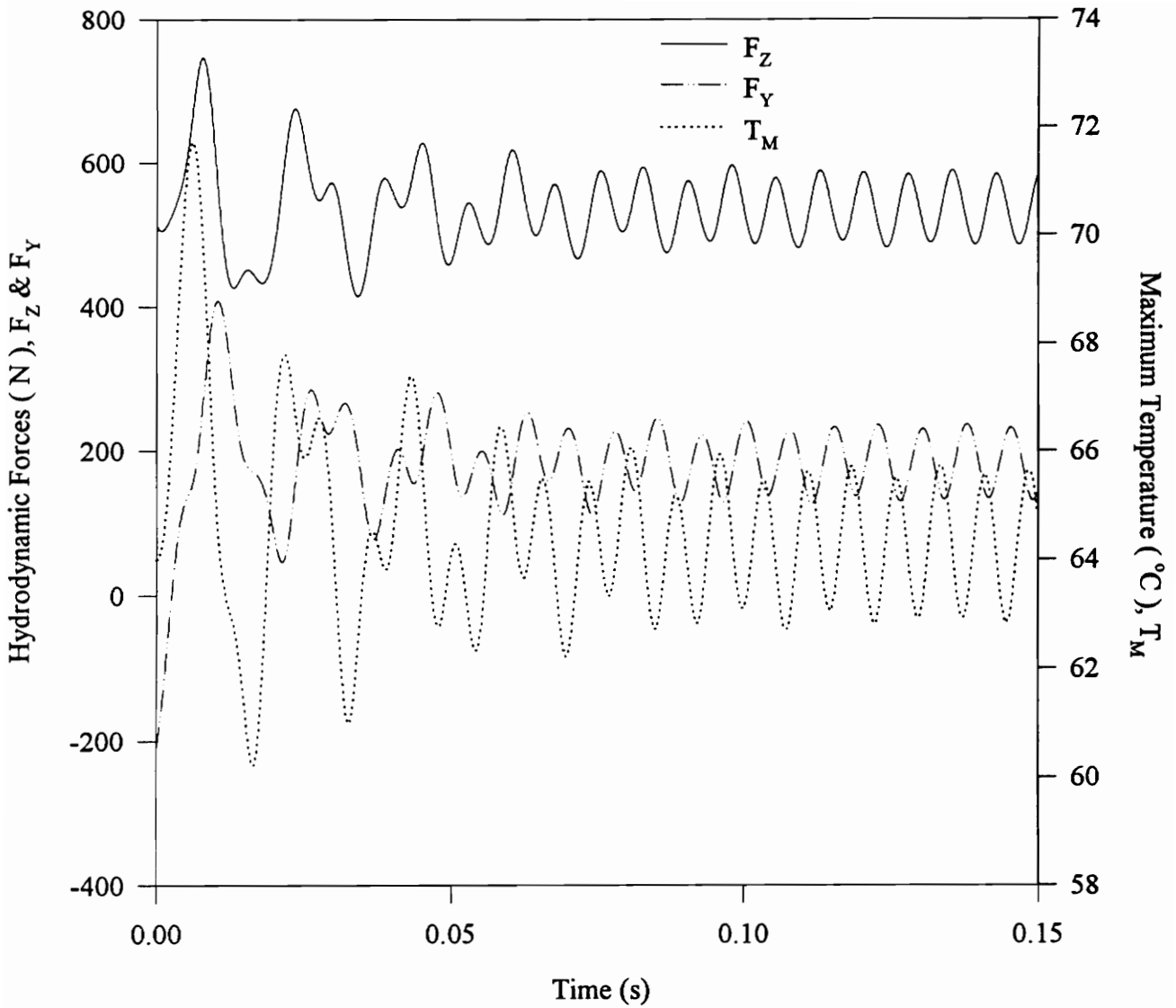
motion of its center. The small blue filled circle on the blue circle indicates the position of the unbalanced mass of the rotor. The endpoints of the orbits with stars show the final positions of the seal and the rotor whereas the other endpoints show the initial positions of the seal and the rotor. The completion of each revolution of the shaft is indicated by the numbers on the orbits. The clearance space between the rotor and the seal ring and the seal and the rotor orbits are highly magnified. Each cell in the grid represents an actual dimension of 0.0254 mm. It can be seen from this figure that the seal and rotor orbits grow until the eccentricity becomes as high as 0.85 during the third revolution of the rotor.

Figure 41 shows the variation of eccentricities and absolute seal positions as a function of time in the above seal with operating speed of 133.33 Hz (8000 RPM) and the frictional force of 889.6 N. It can be seen that the seal absolute position remains constant while the relative eccentricities oscillate with a constant amplitude of 0.1 after about time = 0.1 sec. indicating that the ring remains locked throughout the transient analysis and the rotor finds a steady state equilibrium position. Figure 42 shows the plots of hydrodynamic forces and maximum temperature versus time for this case. Since in this case the rotor is stable and whirls with a small radius after time = 0.1 sec. The oscillation in the forces and the maximum temperature also reach a steady state after about time = 0.1 sec. The maximum value of maximum temperature in the steady state condition is below 66 °C. Figure 43 shows the initial position of the seal where it remains locked and the orbit traced by the center the rotor for this case. So, at the operating speed of 133.33 Hz (8000 RPM) increasing the frictional force can lock the straight seal ring and stabilize the operation of the rotor.

Figures 44 and 45 show the plots of eccentricities and seal positions versus time for the above seal with operating speed of 200 Hz (12000 RPM) and frictional forces of



**Figure 41. Plots of Eccentricities and Absolute Seal Positions vs. Time for a Straight Seal Operating Speed = 133.33 Hz (8000 RPM); Frictional Force = 889.6 N**



**Figure 42. Plots of Hydrodynamic Forces and Maximum Temperature vs. Time for a Straight Seal**  
**Operating Speed = 133.33 Hz (8000 RPM); Frictional Force = 889.6 N**

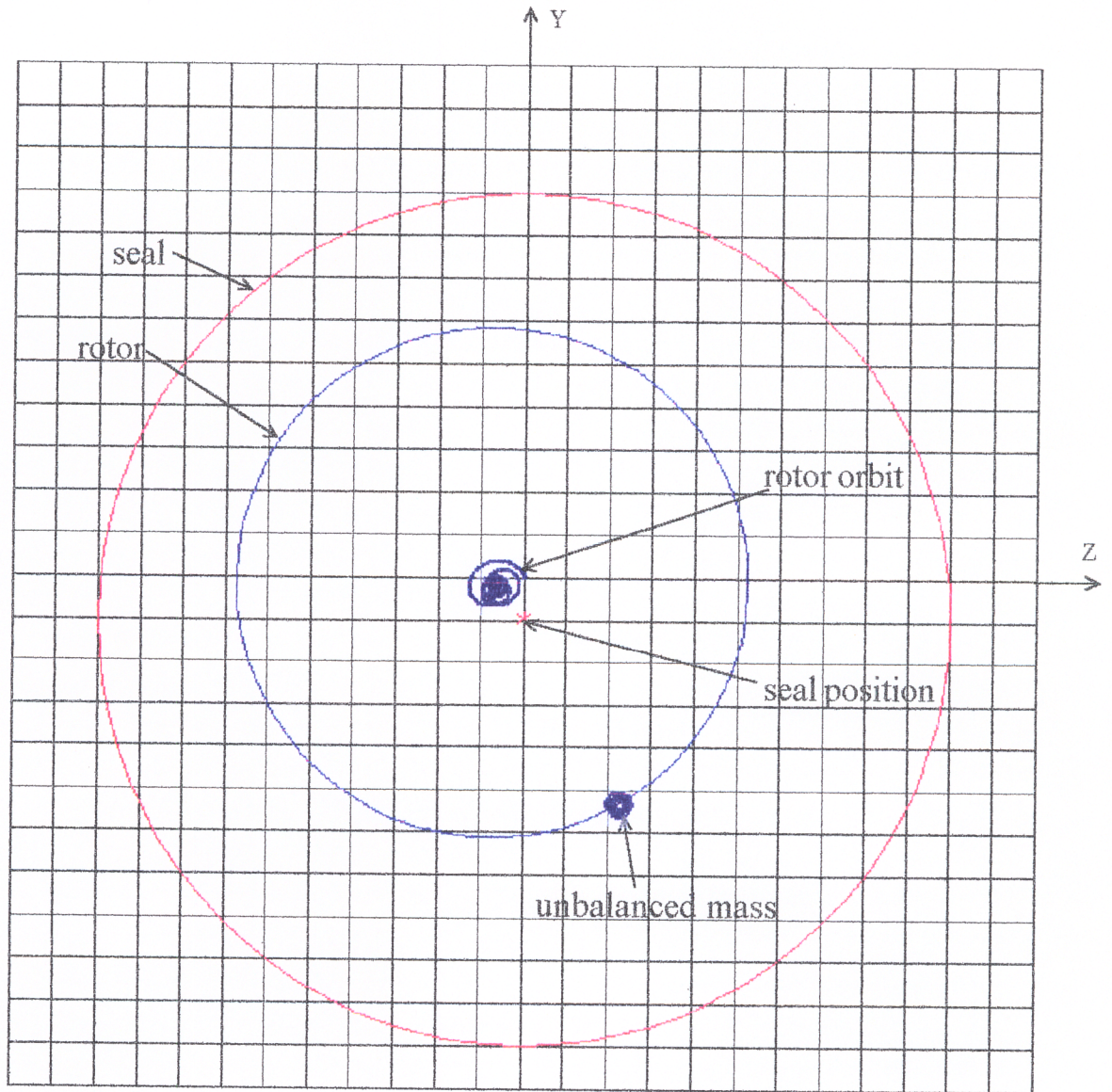


**Figure 43. Transient Response of the Straight Seal and the Rotor**  
**Operating Speed = 133.33 Hz (8000 RPM)**  
**Frictional Force = 889.6 N**

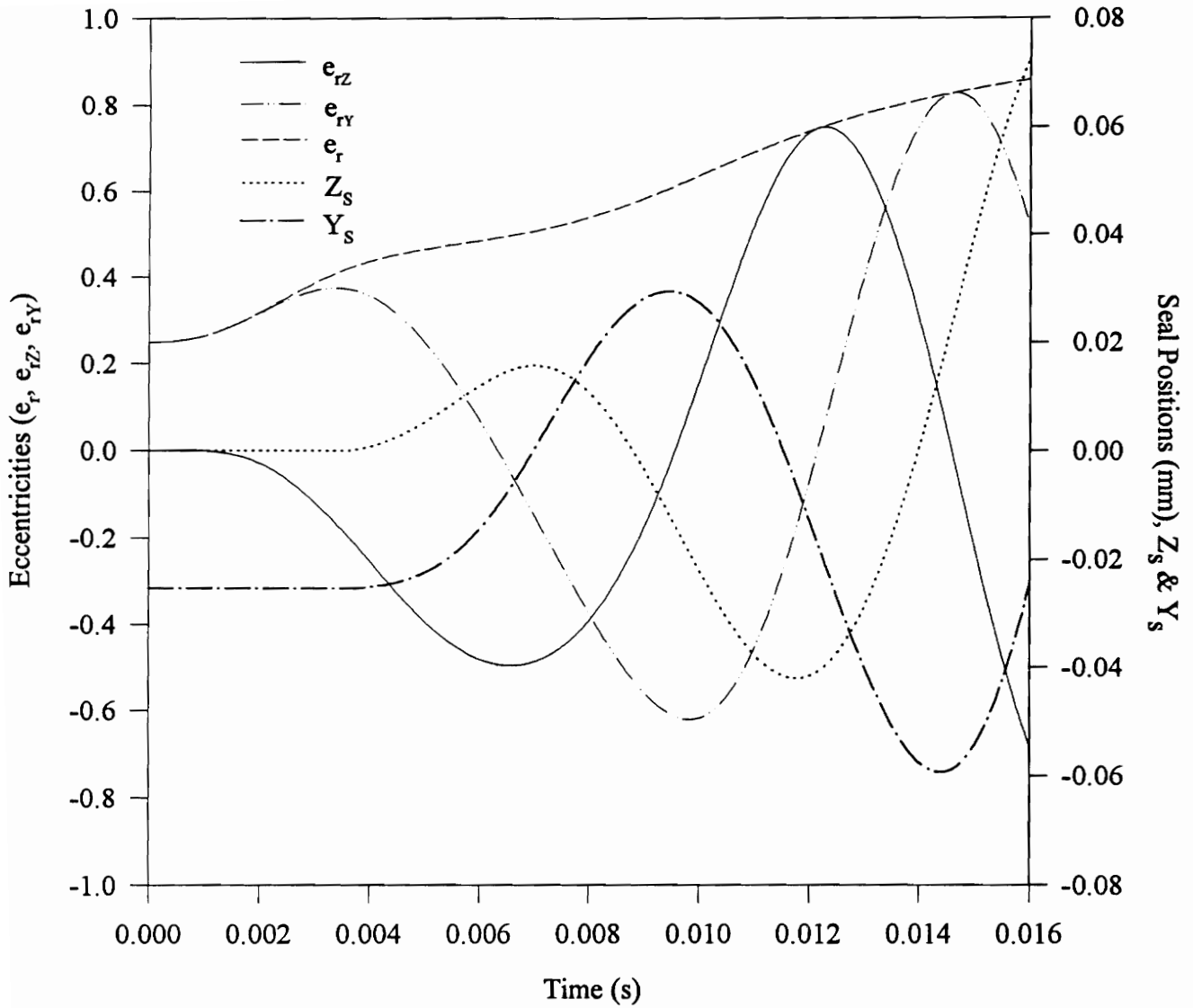


**Figure 44. Plots of Eccentricities and Absolute Seal Positions vs. Time for a Straight Seal Operating Speed = 200 Hz (12000 RPM); Frictional Force = 889.6 N**

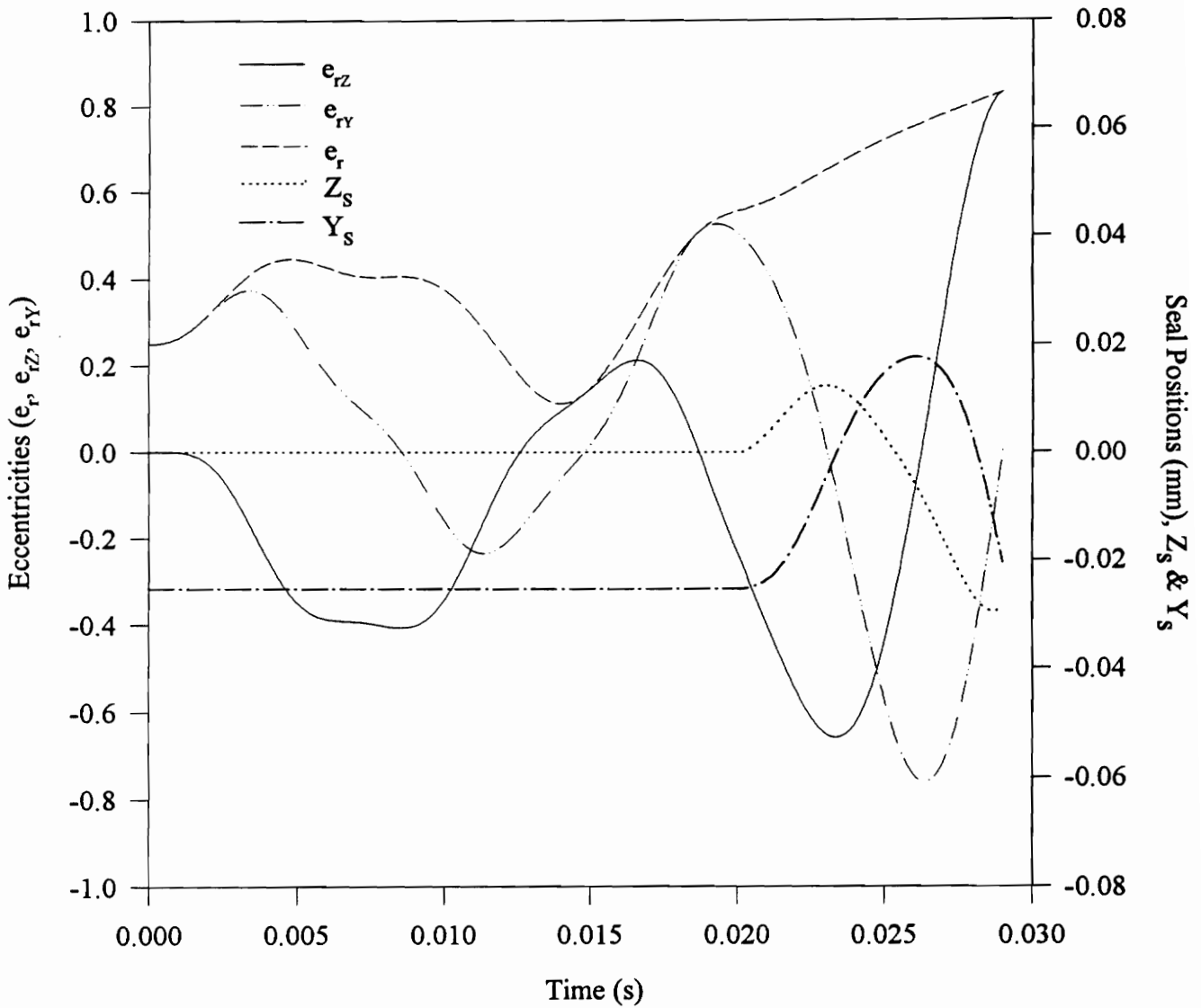


**Figure 45. Plots of Eccentricities and Absolute Seal Positions vs. Time for a Straight Seal Operating Speed = 200 Hz (12000 RPM); Frictional Force = 1334.4 N**

889.6 N and 1334.4 N respectively. It can be seen that at this speed the frictional forces of both 889.6 N and 1334.4 N are not sufficient to make the ring locked. In the case with frictional force of 889.6 N (see Fig. 44), the seal remains locked until time = 0.004 sec. approximately, but the unstable rotor increases the eccentricity ratio which unlocks the seal at about time = 0.004 sec. after which the seal positions and eccentricity components,  $e_{rZ}$  and  $e_{rY}$  oscillate with increasing amplitude until the resultant eccentricity ratio,  $e_r$ , becomes as high as 0.85 at about time = 0.016 sec. The same phenomenon takes place when the frictional force is increased to 1334.4 N (see Fig. 45) but the unlocking of the seal is delayed to time = 0.02 sec. approximately and the eccentricity becomes as high as 0.85 again at about time = 0.028 sec. So, the instability is delayed when the frictional force is increased, as expected.

## Chapter 6

### Influence of Tapered Geometry on the Seal Characteristics

This chapter presents the modification required in the governing equations to handle tapered seals. Then the results comparing the various parameters from linear stability analysis of tapered seals with straight seals are presented. Finally, the results obtained from transient analysis of tapered seals are presented at the end of this chapter.

#### 6.1 Tapered Seals

Figure 46 shows the geometry of a typical tapered seal. The seal ring inner diameter reduces from inlet to exit. In a straight seal, the fluid film thickness,  $h$ , varies only in the circumferential direction. Whereas, in a tapered seal, the fluid film thickness,  $h$ , varies in both the axial and the circumferential directions. The derivation of the equation for film thickness is as follows:

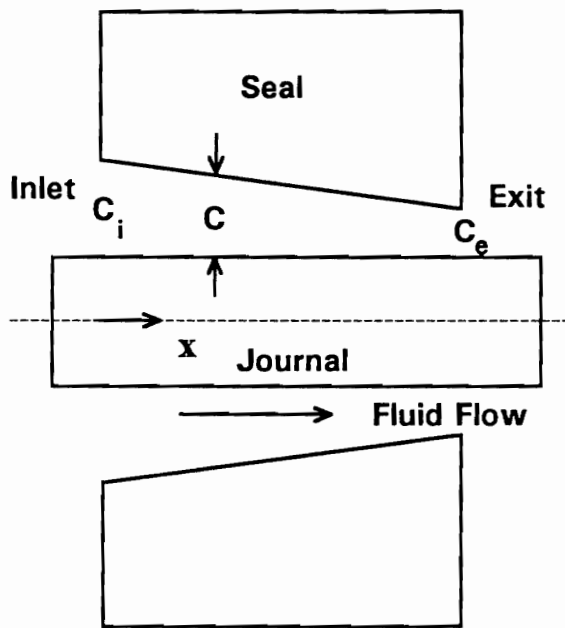


**Figure 46. Geometry of a Typical Tapered Seal**

From Eq. [2]

$$h = C + e_d \cos\left(\frac{y}{R} + \alpha\right) \quad [65]$$

From Fig. 46 clearance  $C$  for tapered seals can be written as

$$C = \left(\frac{C_e - C_i}{L}\right)x + C_i \quad [66]$$

where  $C_i$  and  $C_e$  are the clearance at entrance and exit respectively and  $L$  is the length of the seal.

Substituting for  $C$ ,  $h$  can be written as

$$h = \left(\frac{C_e - C_i}{L}\right)x + C_i + e_d \cos\left(\frac{y}{R} + \alpha\right) \quad [67]$$

The above expression for the fluid film thickness,  $h$  is used to analyze the tapered seals.

## 6.2 Linear Stability Analysis Results

All the specifications excluding the clearance given in Table 2 are used for all the results of tapered seals in this chapter. The supply pressure and the inlet clearance used for all the results in this chapter are 4.136 MPa and 0.1016 mm respectively. Figure 47 shows the temperature and pressure distributions in a tapered seal with the exit clearance,  $C_e =$

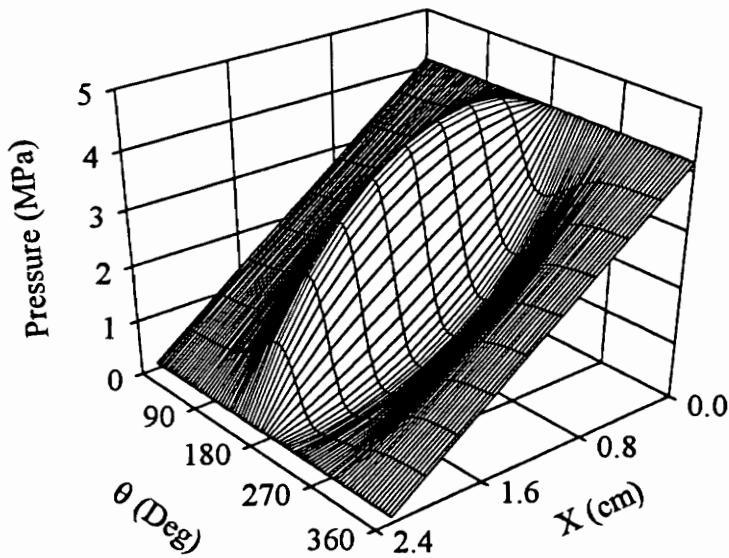
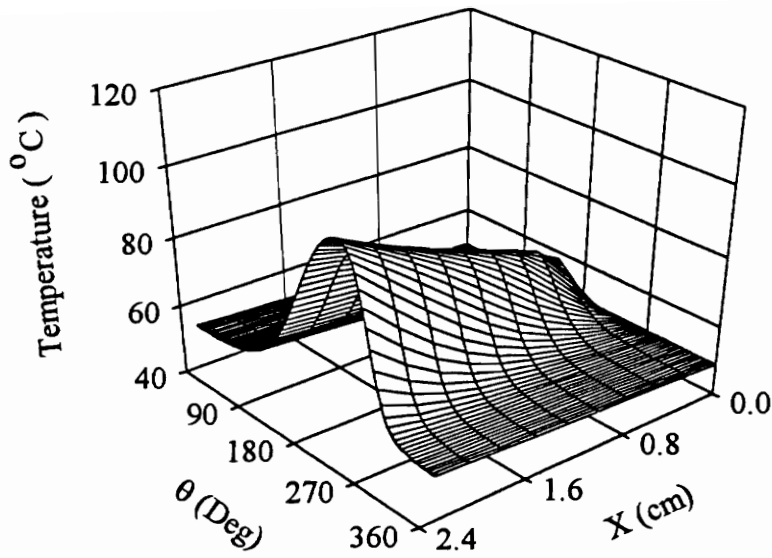


**Figure 47. Temperature and Pressure Distributions in the Tapered Seal**

$C_1 = 0.1016\text{mm}$  (0.004 in);  $C_e = 0.0889\text{ mm}$  (0.0035 in)

Operating Speed = 133.33 Hz (8000 RPM)

Operating Eccentricity ( $e_{rY}$ ) = 0.7

0.0889 mm. The operating speed and eccentricity ratio,  $e_{rY}$ , used are 133.33 Hz (8000 RPM) and 0.7. The eccentricity ratio is calculated based on the exit clearance for the tapered seals. It is interesting to see that there is no cavitation in this case as against some in the straight seal operating in the same conditions (see Fig. 19). So, the tapered seals have a tendency to reduce cavitation.

Figures 48-59 compare the various parameters of the two tapered seals and a straight seal. The exit clearances are 0.0889 mm and 0.0762 mm. The clearance of the straight seal is 0.1016 mm. The operating speed is 166.67 Hz (10000 RPM). It can be seen in Figs. 48 and 49 that the taper increases the direct stiffness and has a tendency to make the stiffness positive which enhances the stability of the compressor rotor. The graphs for the direct stiffness coefficient,  $K_{YY}$ , crossover at high eccentricity because of cavitation which is diminished in the case of tapered seals as explained above. Figures 50-53 compare the plots of cross-coupled stiffness and direct damping coefficients. Their magnitudes are increased by the tapered seals as expected. Figures 54 and 55 compare the plots of cross-coupled damping coefficients. Their values remain almost zero for the eccentricities below 0.6. At higher eccentricities cavitation abruptly raises their values. The cross-coupled damping decreases with the taper as the cavitation is reduced.

Figures 56 and 57 compare the damped natural frequency of the rotor and the growth factor. The taper increases the damped natural frequency because the direct stiffness is increased. The growth factor decreases with increase in taper and becomes negative for the tapered case with the exit clearance of 0.0762 mm indicating that the tapered geometry enhances the stability of the compressor rotor. The graphs of the growth factor crossover at high eccentricity because of cavitation which is diminished in the case of tapered seals as explained above. Figures 58 and 59 compare the axial flow rate through the seal and maximum temperature. The axial flow rate decreases with the

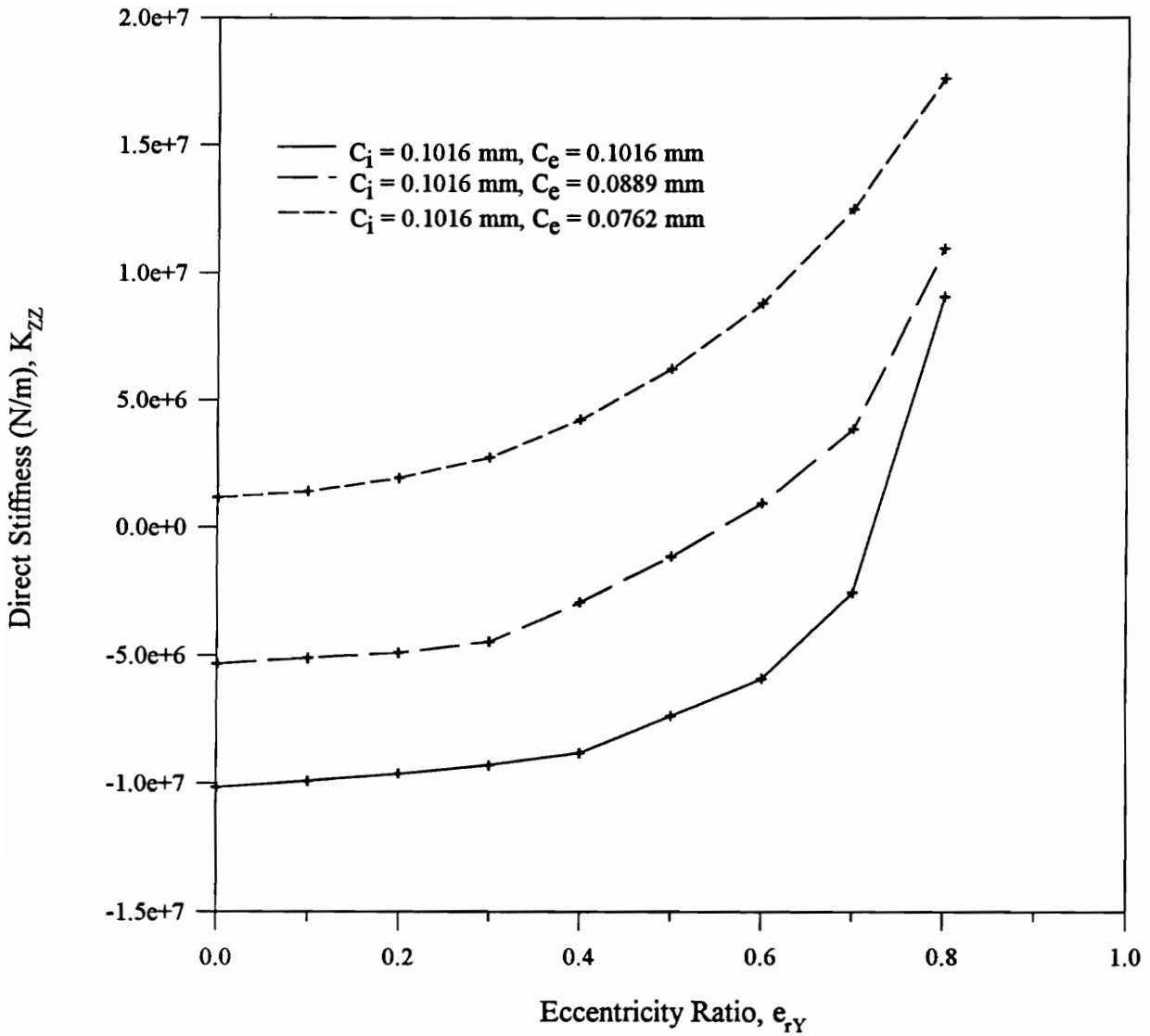


**Figure 48. Plot of Direct Stiffness vs. Eccentricity Ratio for Seals with and without Taper  
Operating Speed = 166.67 Hz (10000 RPM)**

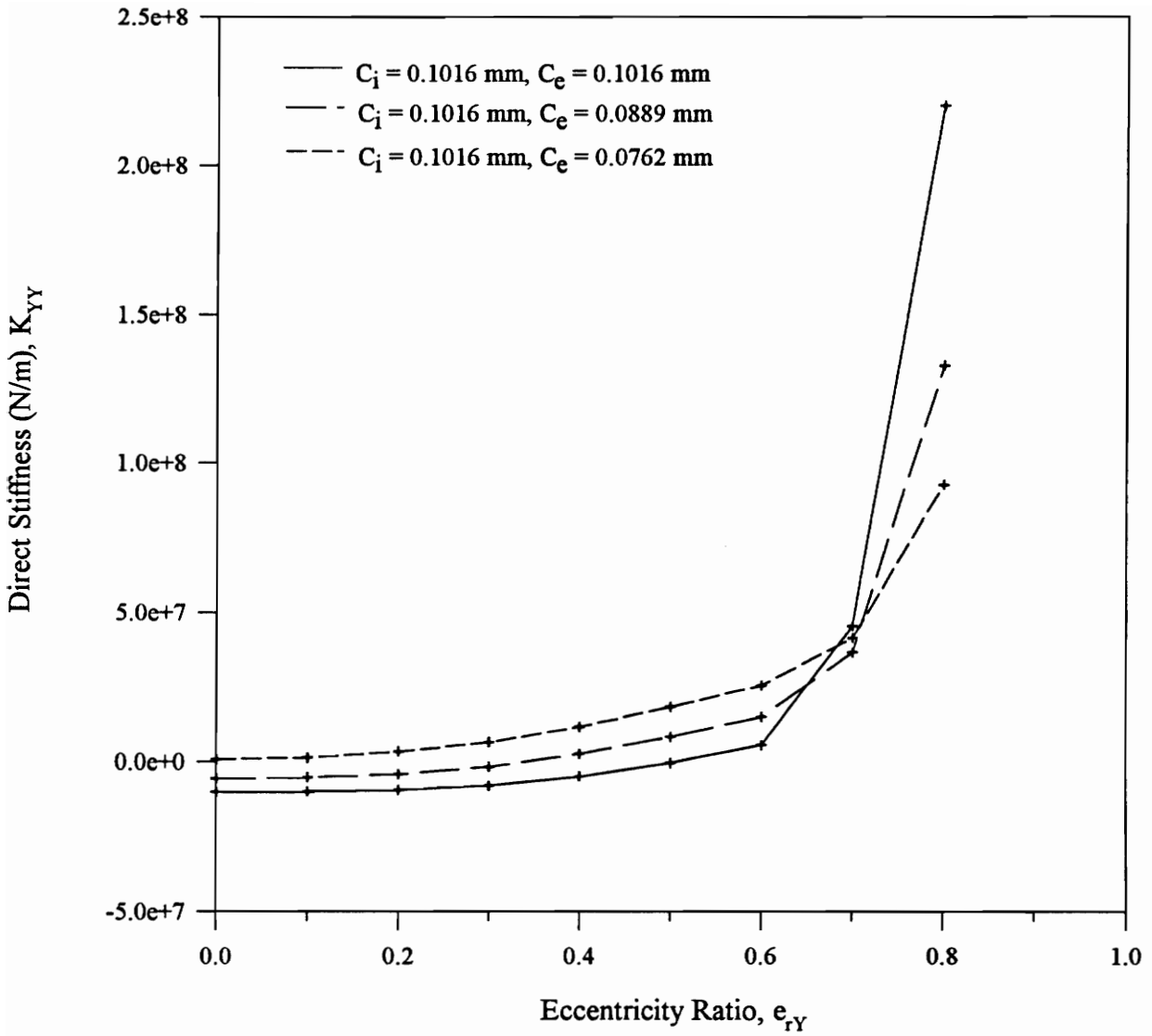


**Figure 49. Plot of Direct Stiffness vs. Eccentricity Ratio for Seals with and without Taper  
Operating Speed = 166.67 Hz (10000 RPM)**

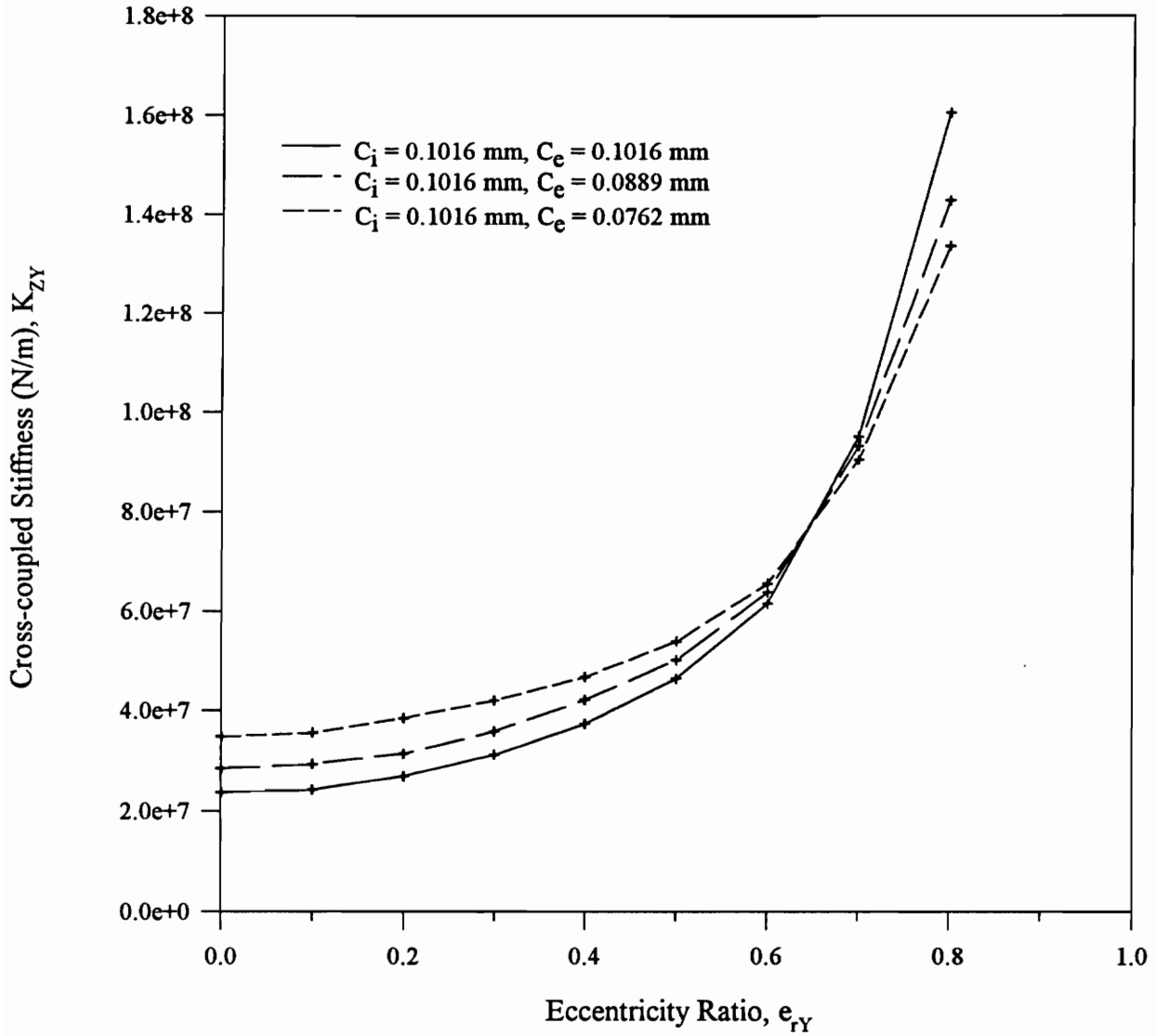


**Figure 50. Plot of Cross-coupled Stiffness vs. Eccentricity Ratio for Seals with and without Taper**  
**Operating Speed = 166.67 Hz (10000 RPM)**

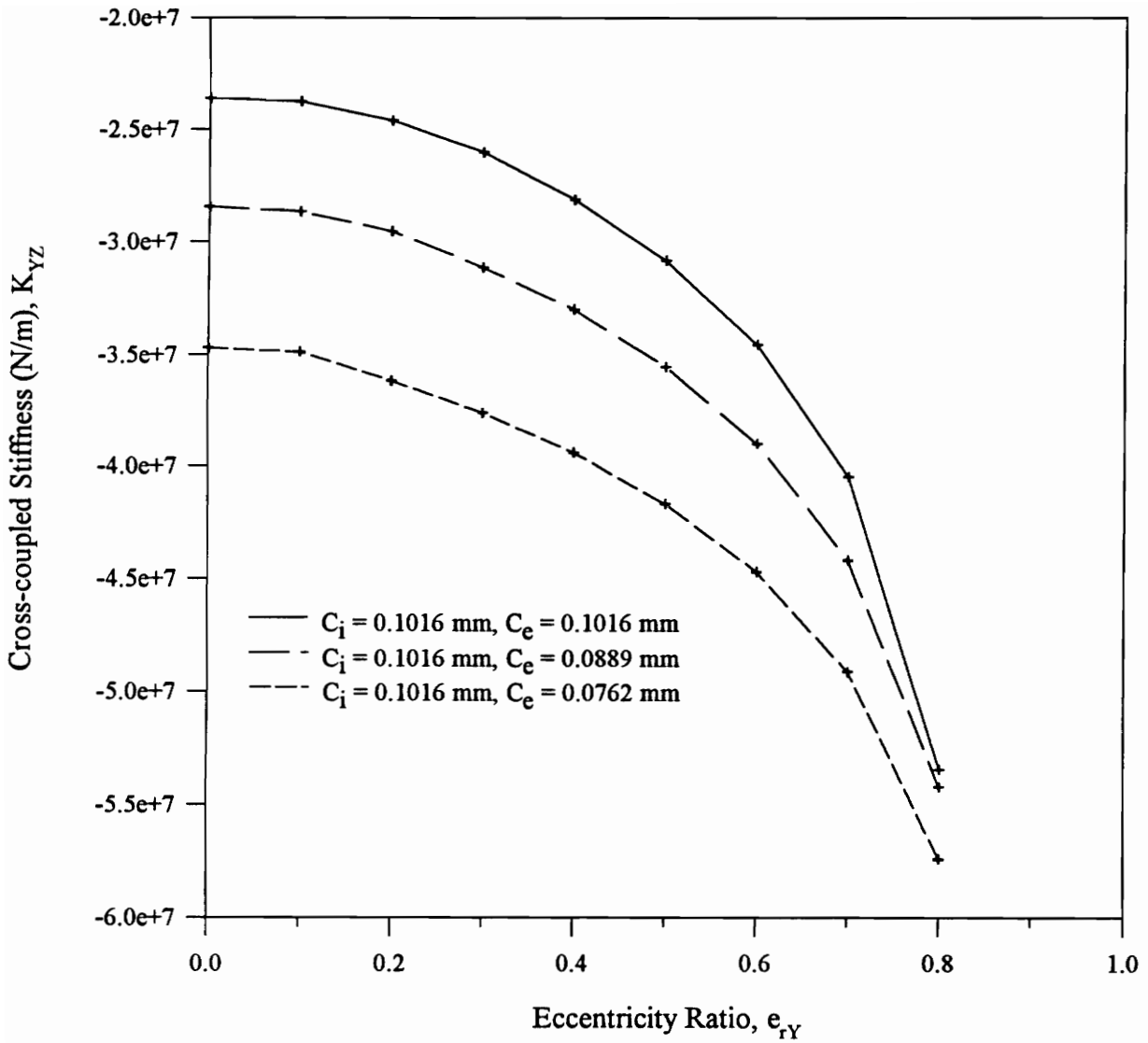


**Figure 51. Plot of Cross-coupled Stiffness vs. Eccentricity Ratio for Seals with and without Taper**  
**Operating Speed = 166.67 Hz (10000 RPM)**

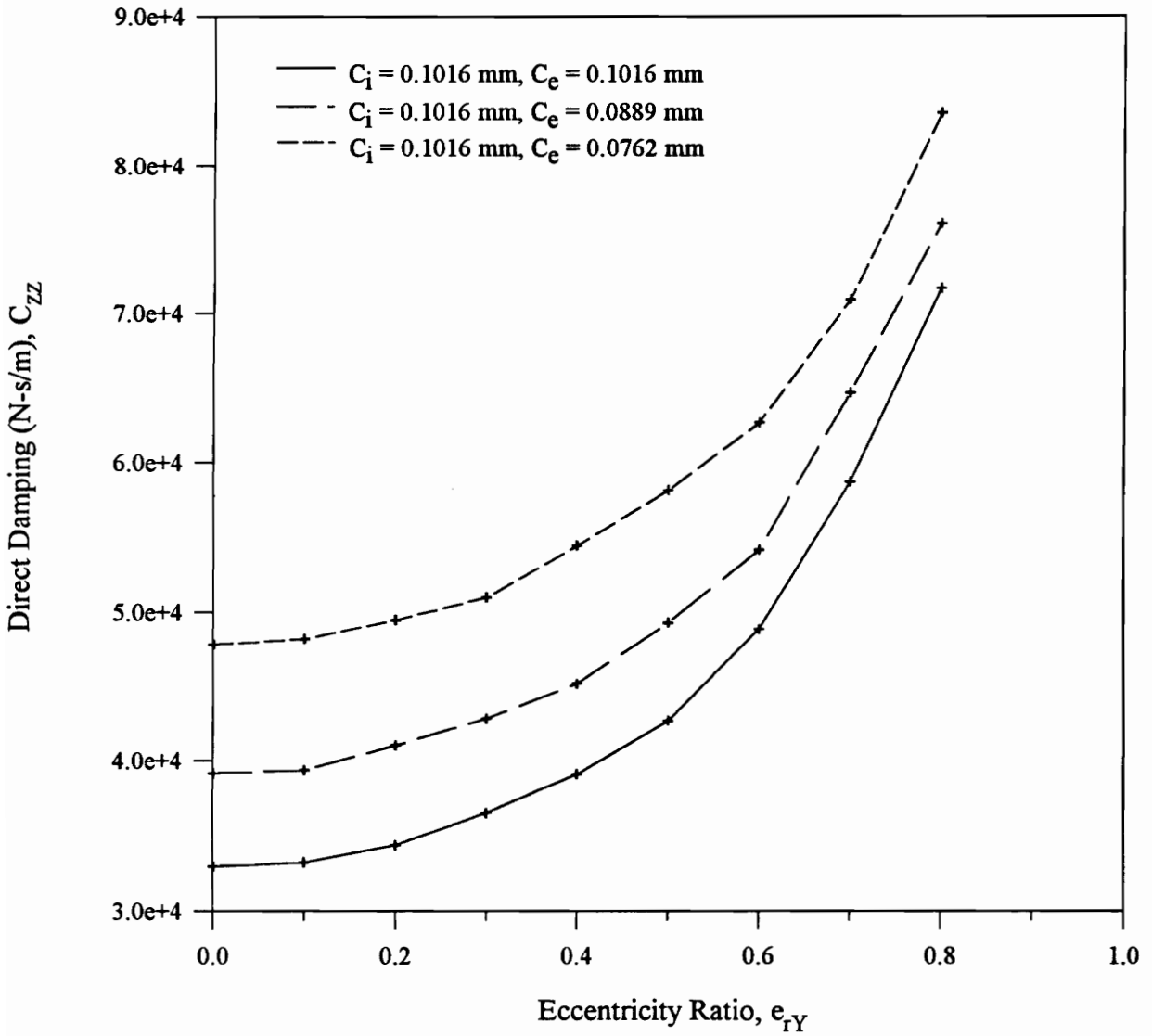


**Figure 52. Plot of Direct Damping vs. Eccentricity Ratio for Seals with and without Taper**  
**Operating Speed = 166.67 Hz (10000 RPM)**

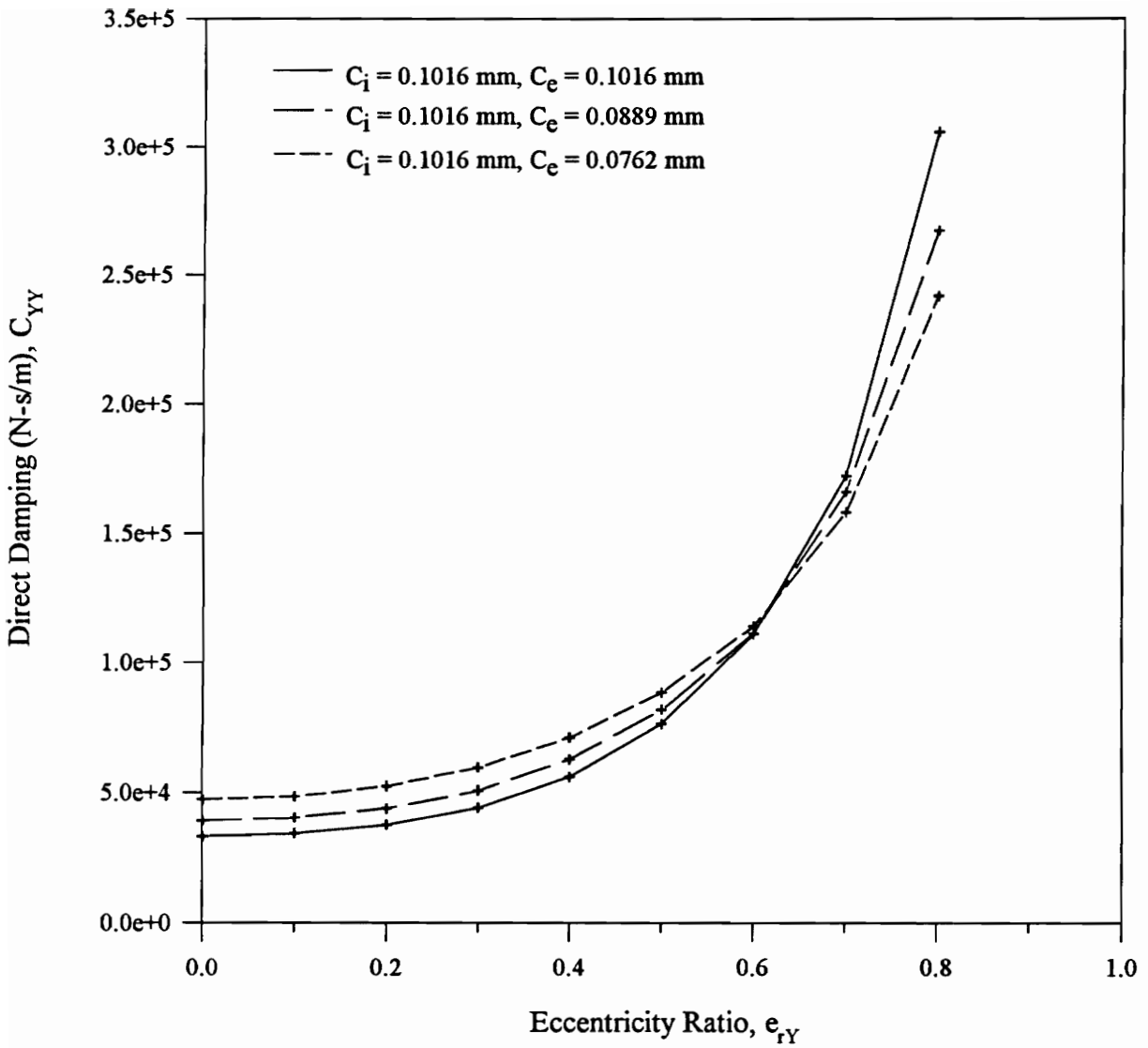


**Figure 53. Plot of Direct Damping vs. Eccentricity Ratio for Seals with and without Taper  
Operating Speed = 166.67 Hz (10000 RPM)**

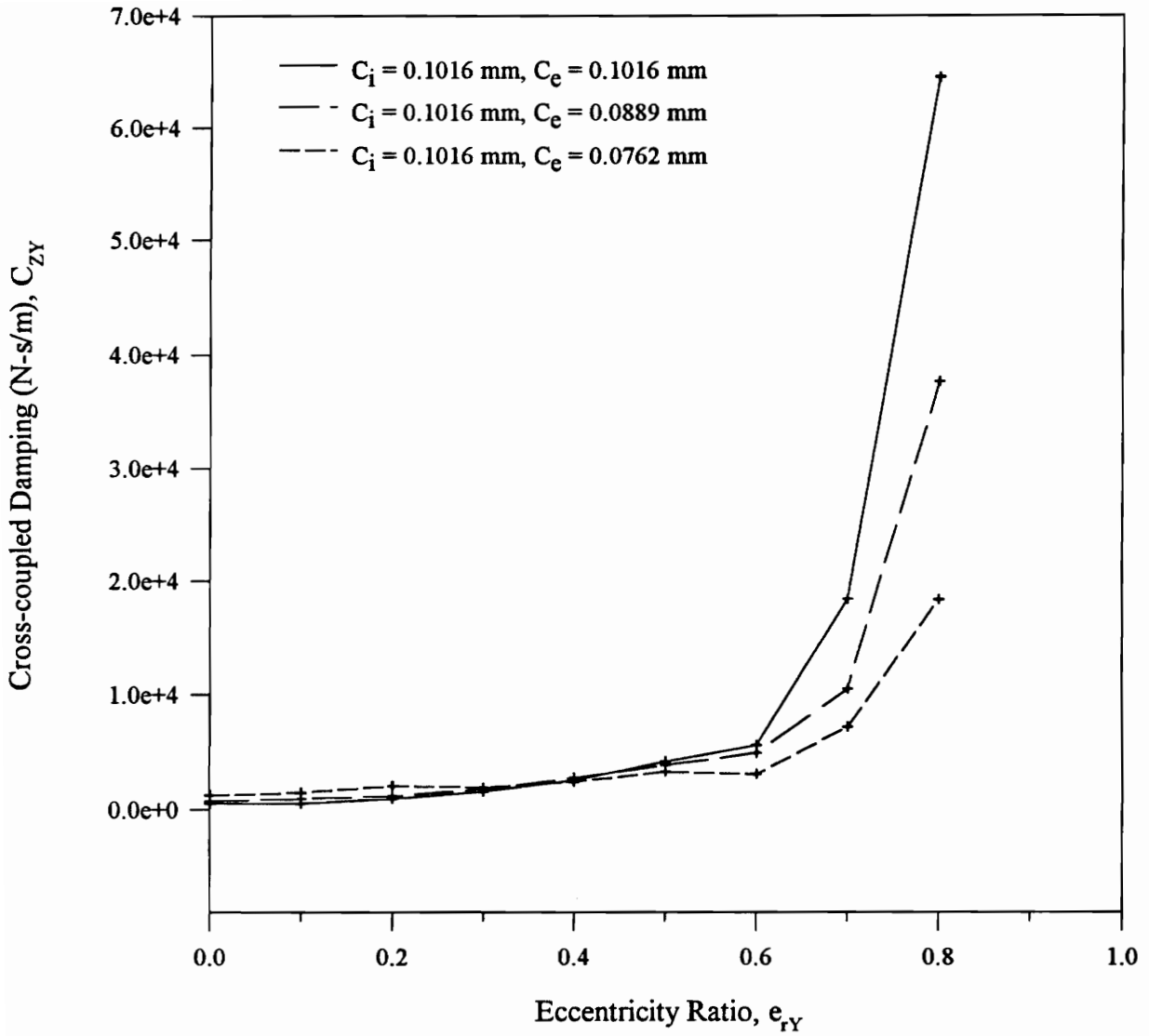


**Figure 54. Plot of Cross-coupled Damping vs. Eccentricity Ratio for Seals with and without Taper  
Operating Speed = 166.67 Hz (10000 RPM)**

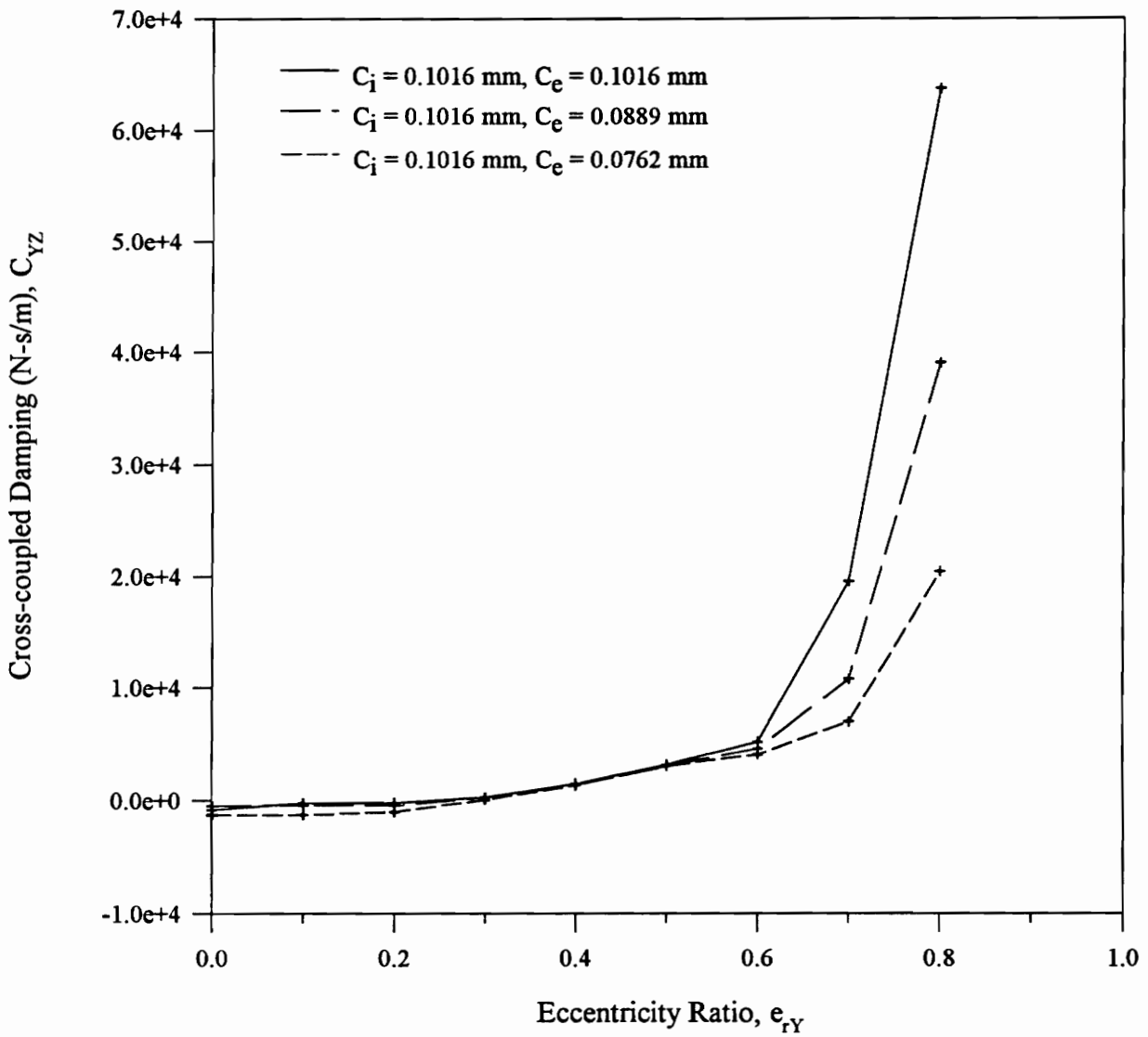


**Figure 55. Plot of Cross-coupled Damping vs. Eccentricity Ratio for Seals with and without Taper**  
**Operating Speed = 166.67 Hz (10000 RPM)**

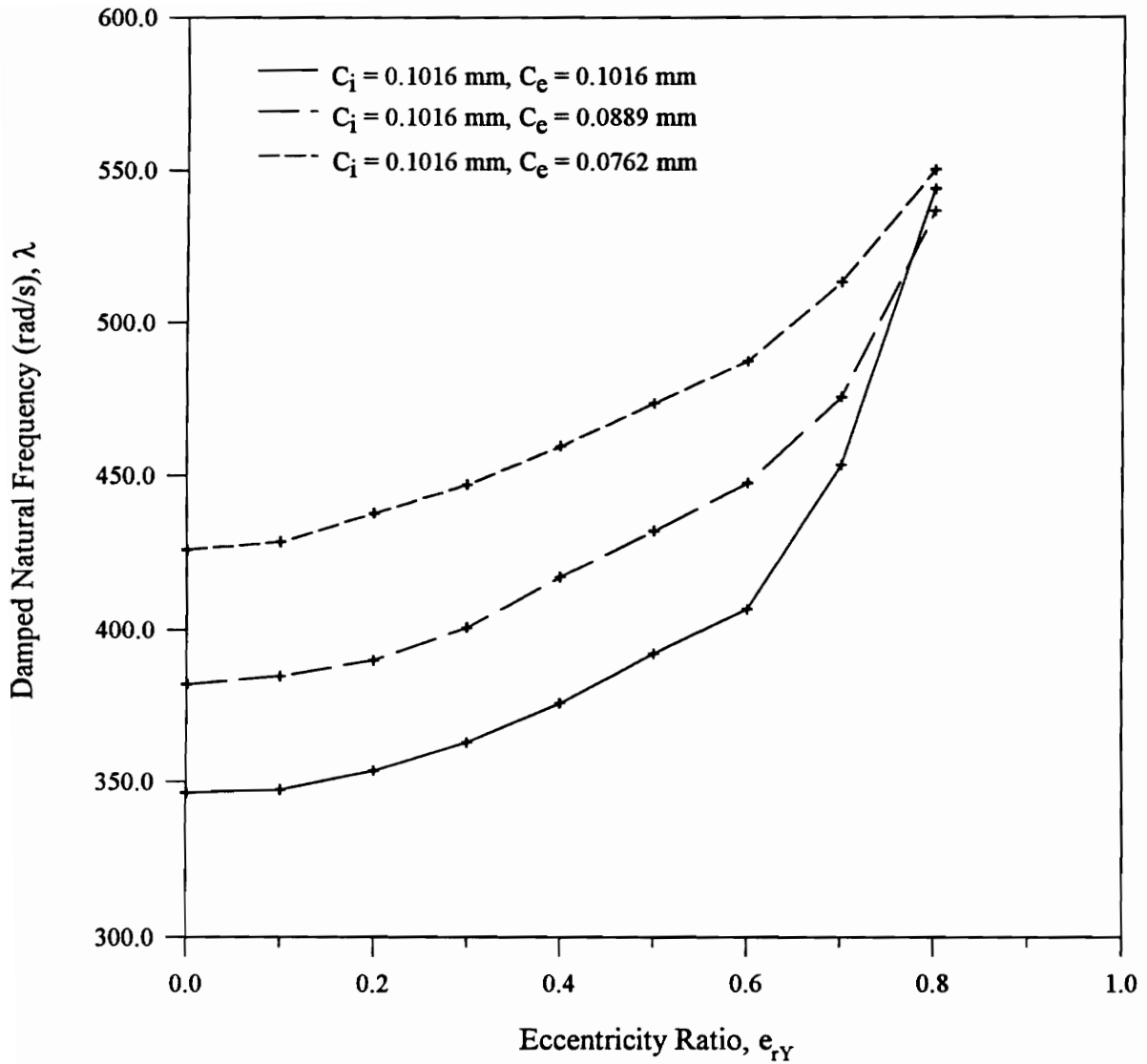


**Figure 56. Plot of Damped Natural Frequency vs. Eccentricity Ratio for Seals with and without Taper**  
**Operating Speed = 166.67 Hz (10000 RPM)**

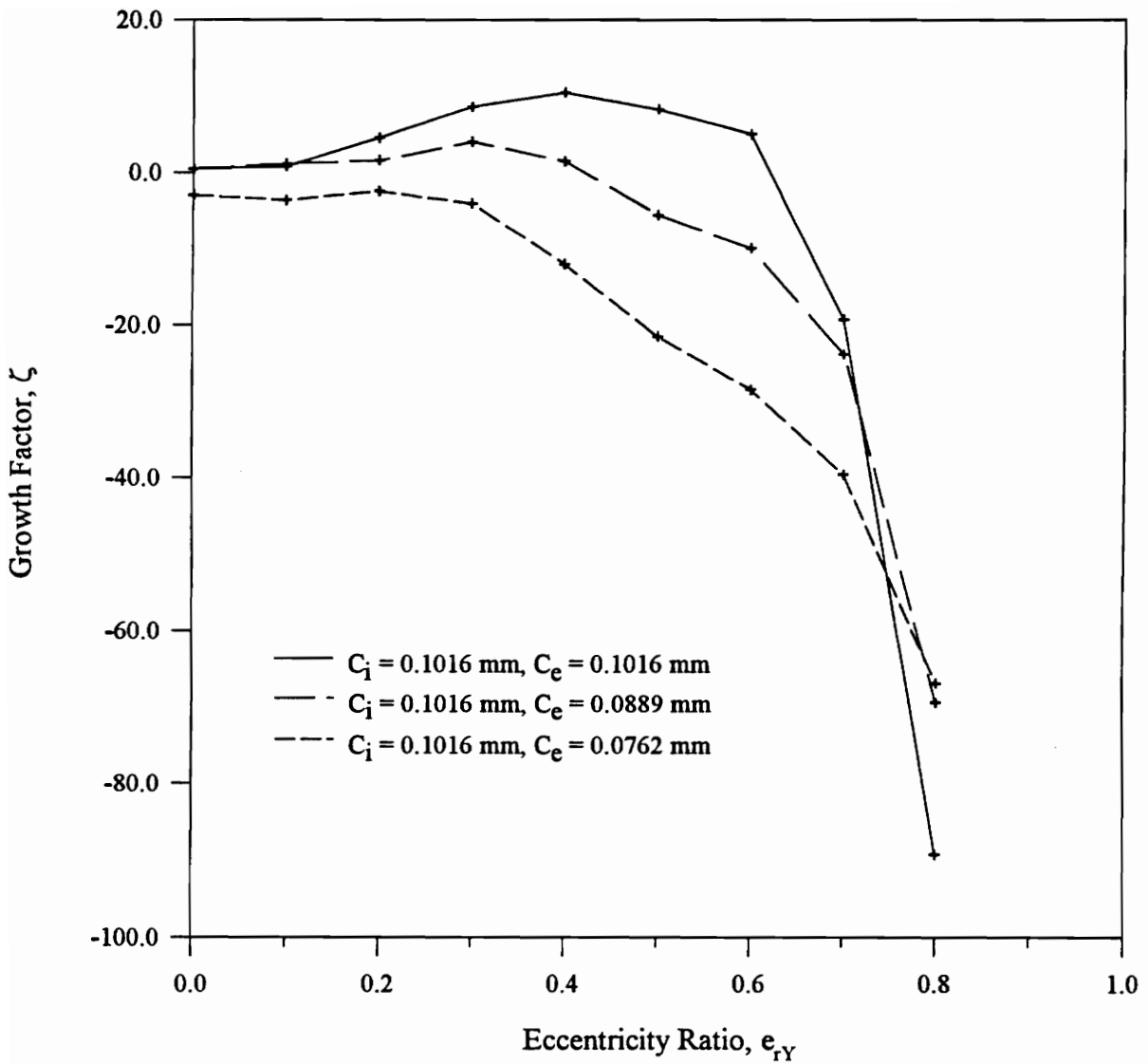


**Figure 57. Plot of Growth Factor vs. Eccentricity Ratio for Seals with and without Taper  
Operating Speed = 166.67 Hz (10000 RPM)**

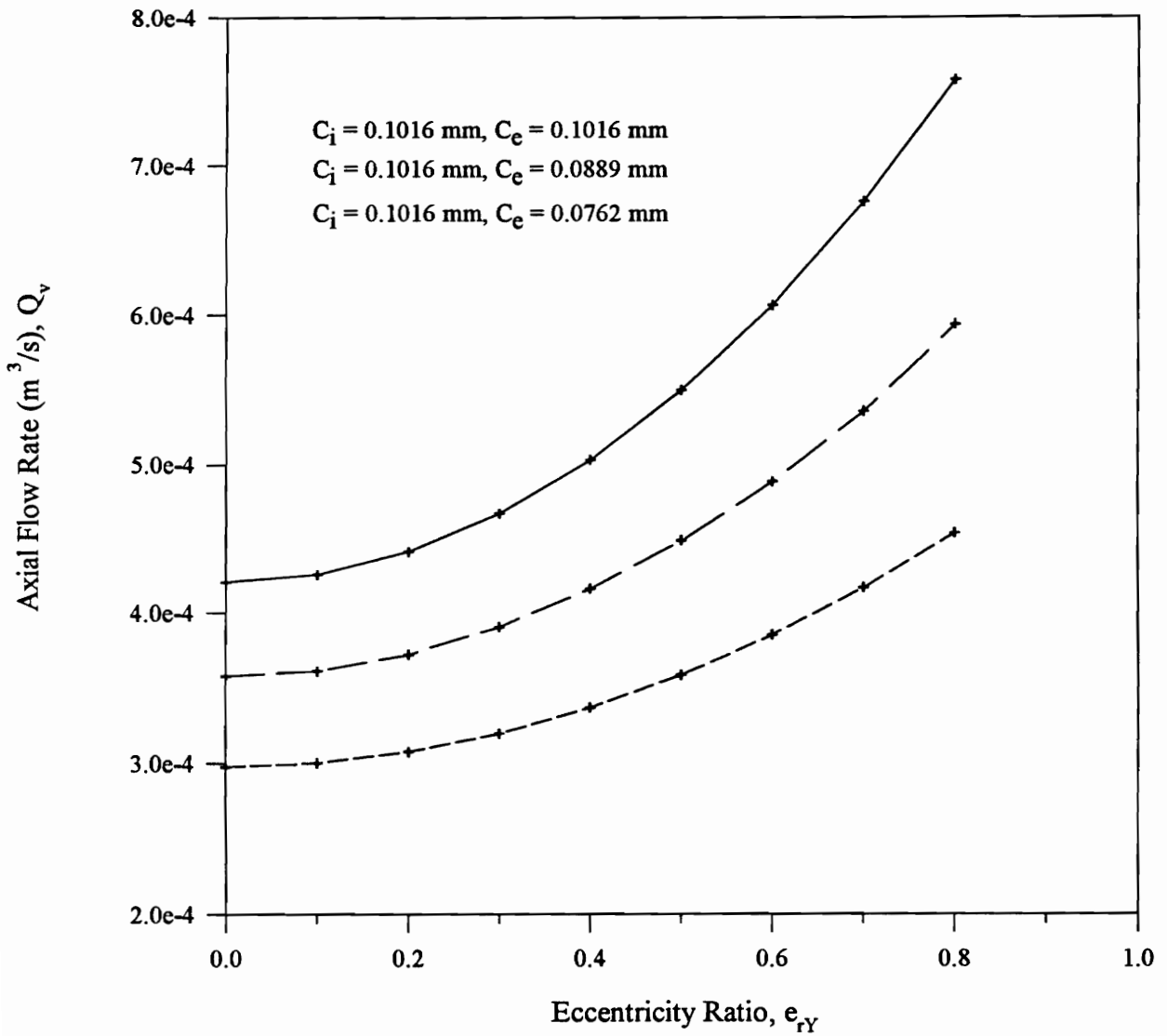


**Figure 58. Plot of Axial Flow Rate vs. Eccentricity Ratio for Seals with and without Taper**  
**Operating Speed = 166.67 Hz (10000 RPM)**

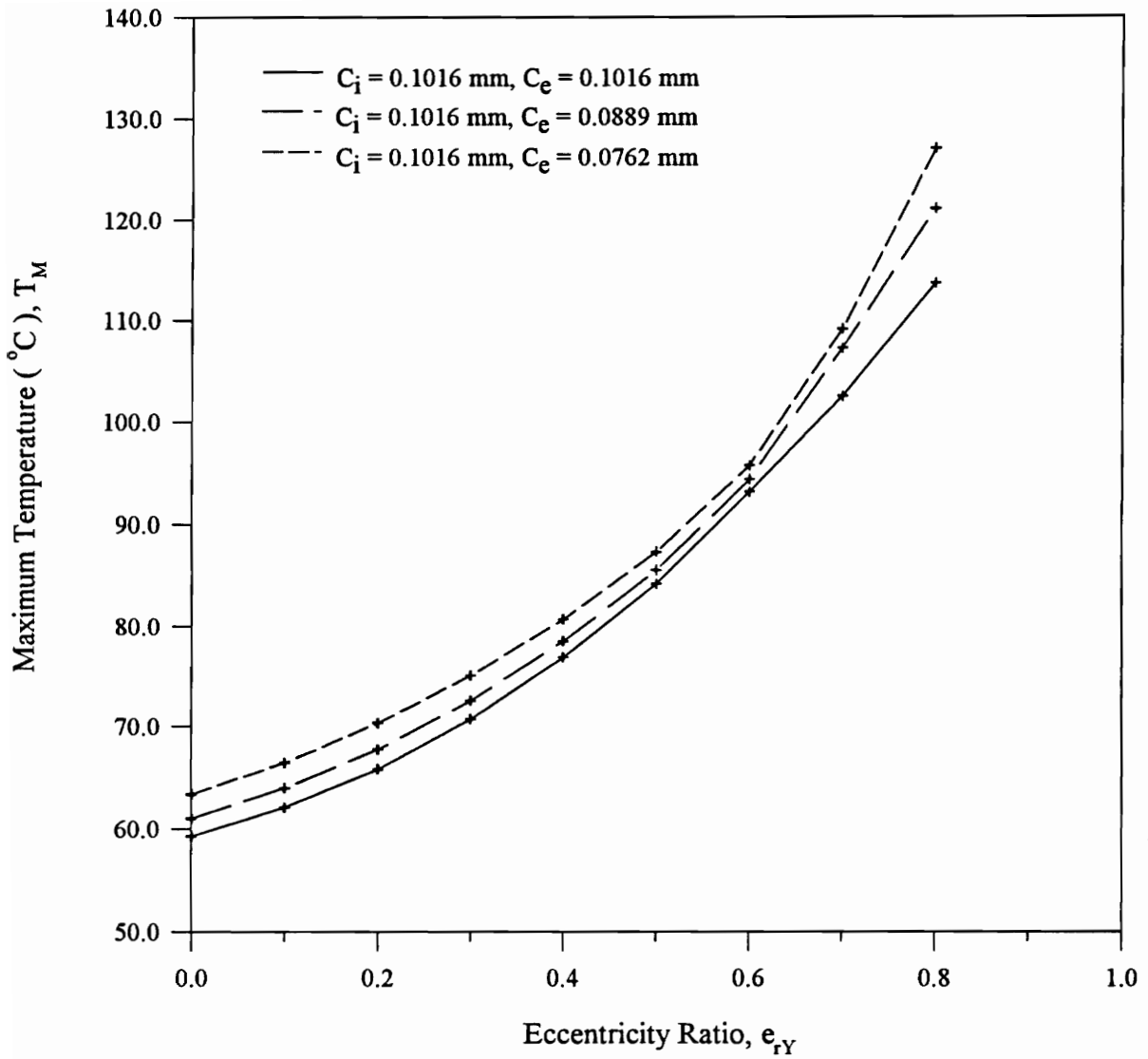


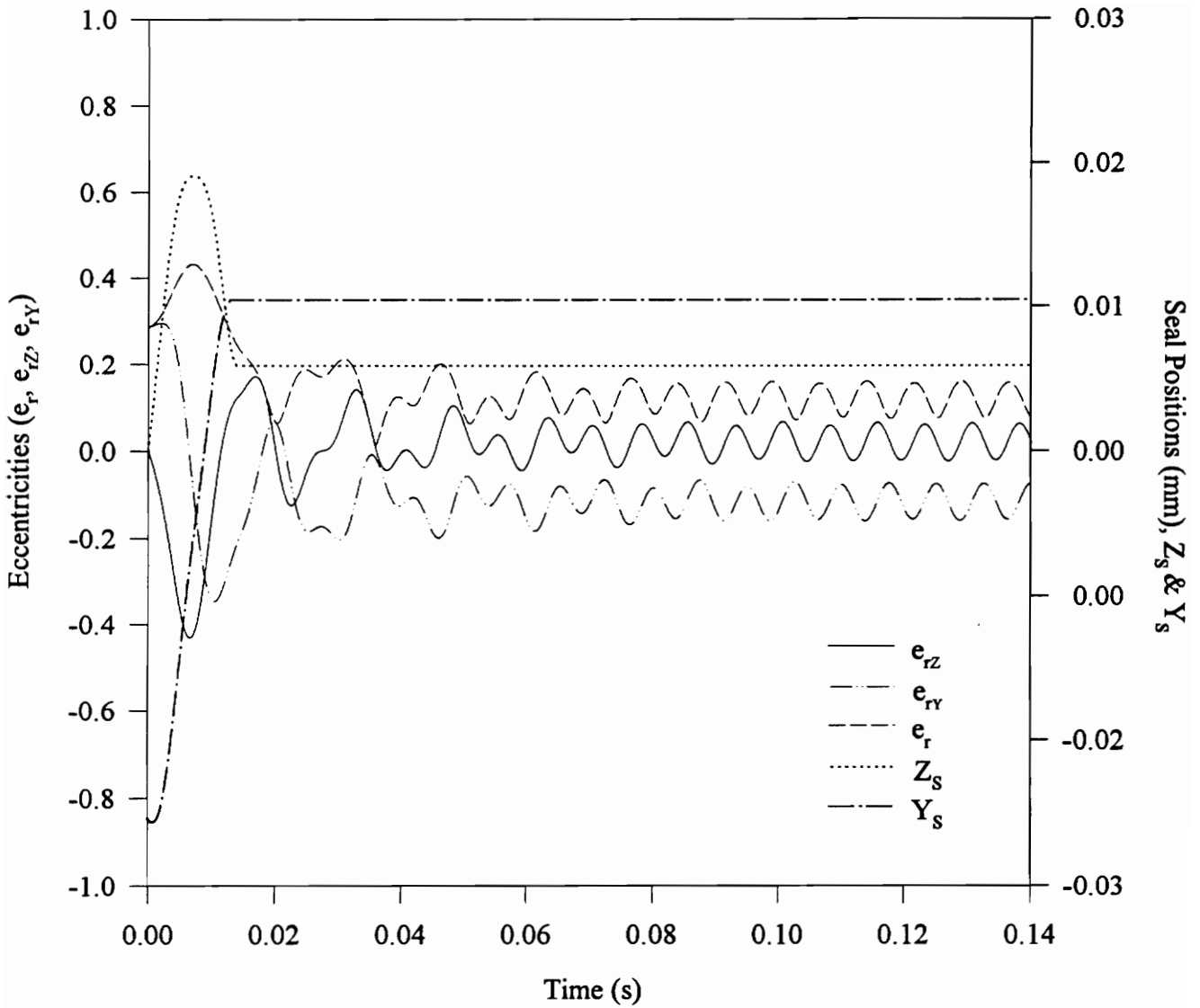
**Figure 59. Plot of Maximum Temperature vs. Eccentricity Ratio for Seals with and without Taper**  
**Operating Speed = 166.67 Hz (10000 RPM)**

increase in taper as the effective clearance reduces. The maximum temperature increases with the taper as the viscous dissipation is increased with the reduction in the clearance.

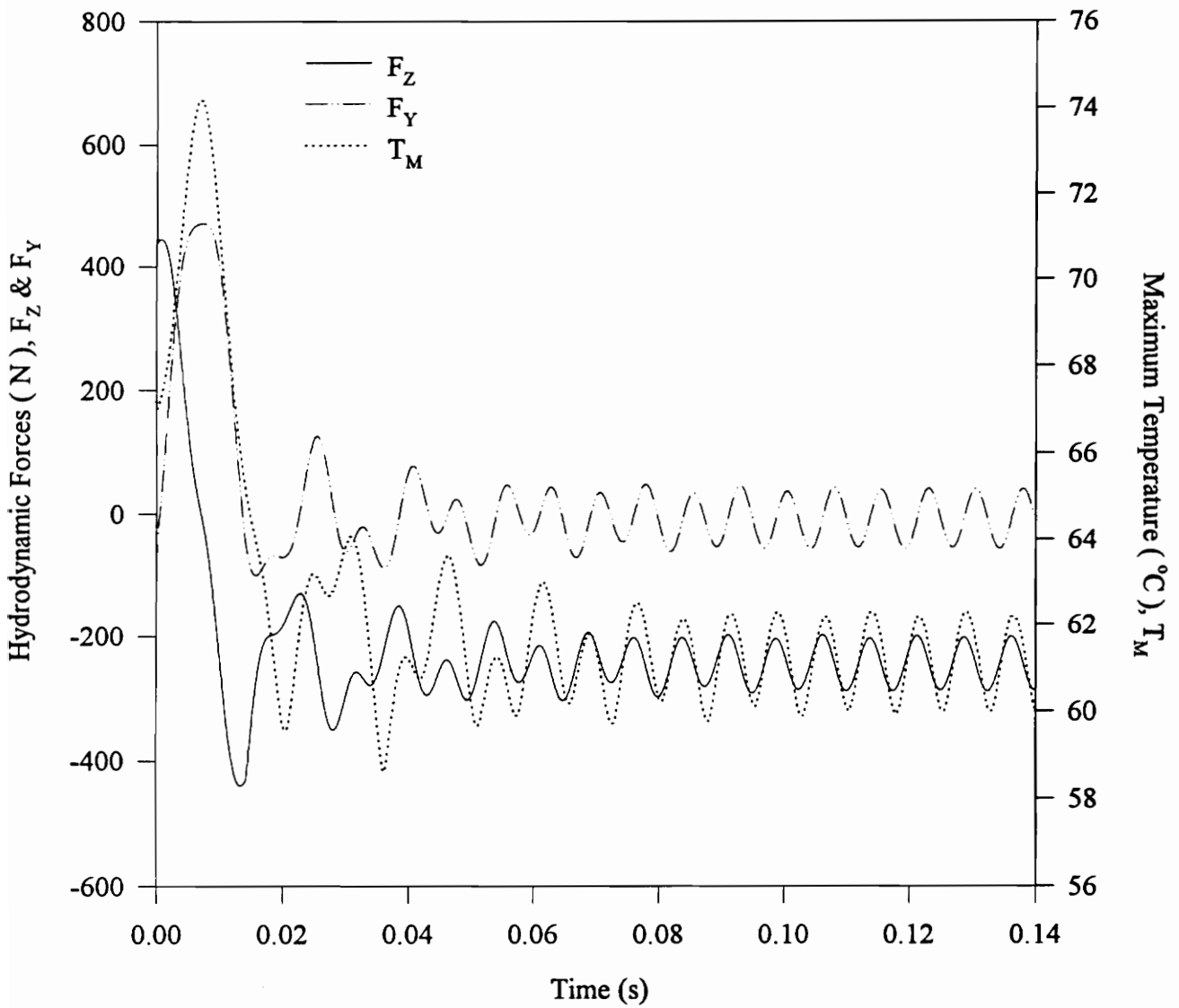
### 6.3 Non-linear Transient Analysis Results

Figure 60 shows the plots of eccentricities and the seal positions versus time for a tapered seal with the exit clearance of 0.0889 mm. The frictional force used is 444.8 N and the operating speed used is 133.33 Hz (8000 RPM). The straight seal operating under same conditions turned out to be unstable as discussed in section 5.3. But the tapered seal gets locked after time = 0.015 sec. (approximately) as the seal positions remain constant in Fig. 60 after this time. Also, the rotor vibration reaches a steady state condition as the eccentricities in the Fig. 60 oscillate with a constant amplitude. Figure 61 shows the corresponding variation of the hydrodynamic forces and maximum temperature as a function of time. It can be seen that these parameters also oscillate with a small amplitude in the steady state condition as expected. Figure 62 shows the orbits traced by the seal and the rotor in this case. The seal remains locked after it reaches the endpoint of the red orbit indicated with a star and the rotor finds a stable equilibrium position. So, the tapered geometry has a tendency to improve the locking mechanism in the floating seal ring and the stability of the compressor rotor operating at about 8000 RPM.

Figures 63 and 64 show the plots of different parameters for the same tapered seal with the operating speed of 200 Hz (12000 RPM) and locking force of 889.6 N. Though the taper in this case does not stabilize the operation of the compressor as the eccentricity in Fig. 63 becomes as high as 0.85 at about time = 0.03 sec., but it slows down the growth rate of vibration as compared to a straight seal in the same conditions (see Fig. 44). The



**Figure 60. Plots of Eccentricities and Absolute Seal Positions vs. Time For a Tapered Seal  
 Operating Speed = 133.33 Hz (8000 RPM); Frictional Force = 444.8 N;  
 Exit Clearance = 0.0889 mm**



**Figure 61. Plots of Hydrodynamic Forces and Maximum Temperature vs. Time for a Tapered Seal**  
**Operating Speed = 133.33 Hz (8000 RPM); Frictional Force = 444.8 N;**  
**Exit Clearance = 0.0889 mm**

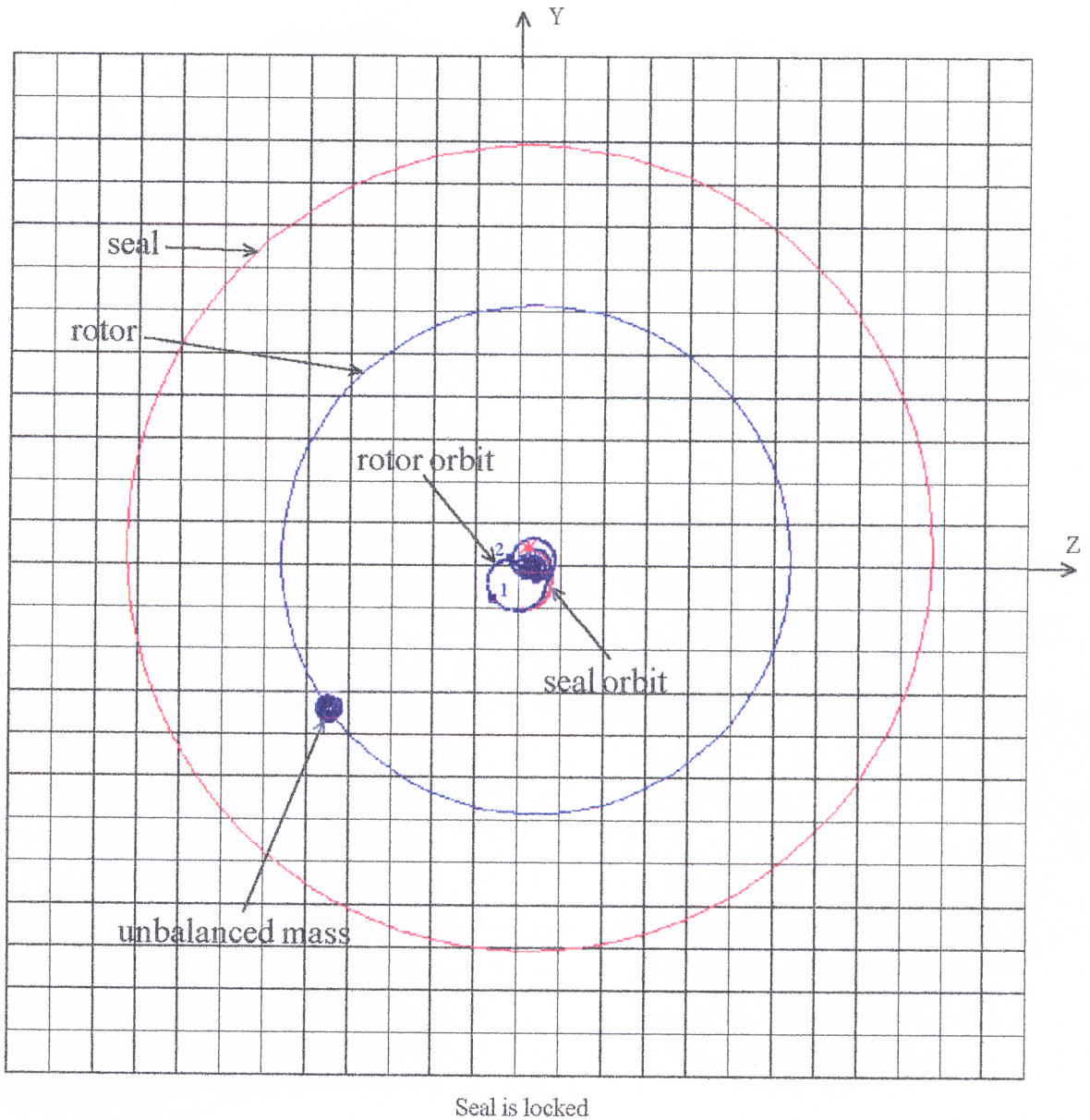


**Figure 62. Transient Response of the Tapered Seal and the Rotor**  
**Operating Speed = 133.33 Hz (8000 RPM)**  
**Frictional Force = 444.8 N**  
**Exit Clearance = 0.0889 mm**

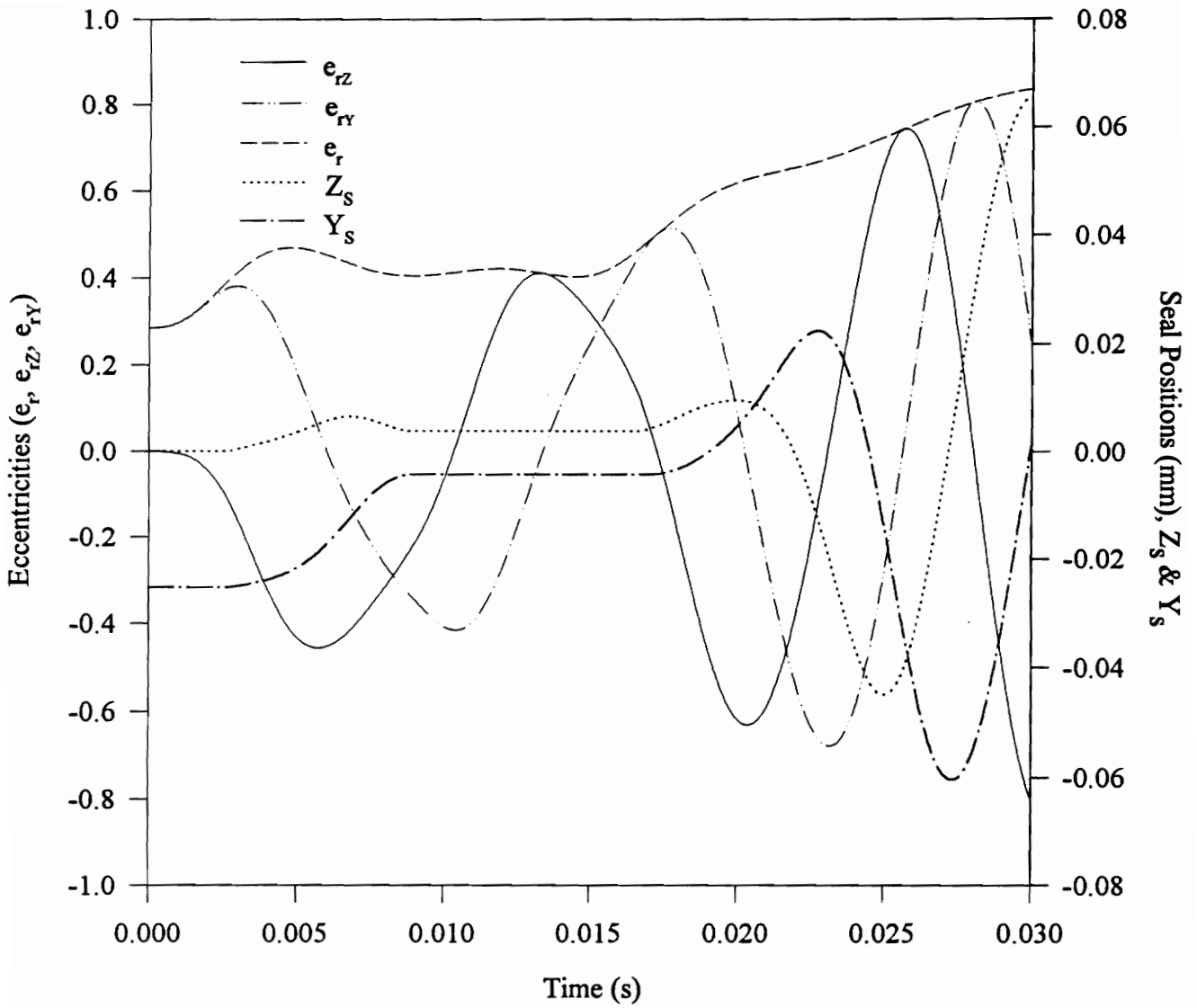


**Figure 63. Plots of Eccentricities and Absolute Seal Positions vs. Time for a Tapered Seal**  
**Operating Speed = 200 Hz (12000 RPM); Frictional Force = 889.6 N;**  
**Exit Clearance = 0.0889 mm**

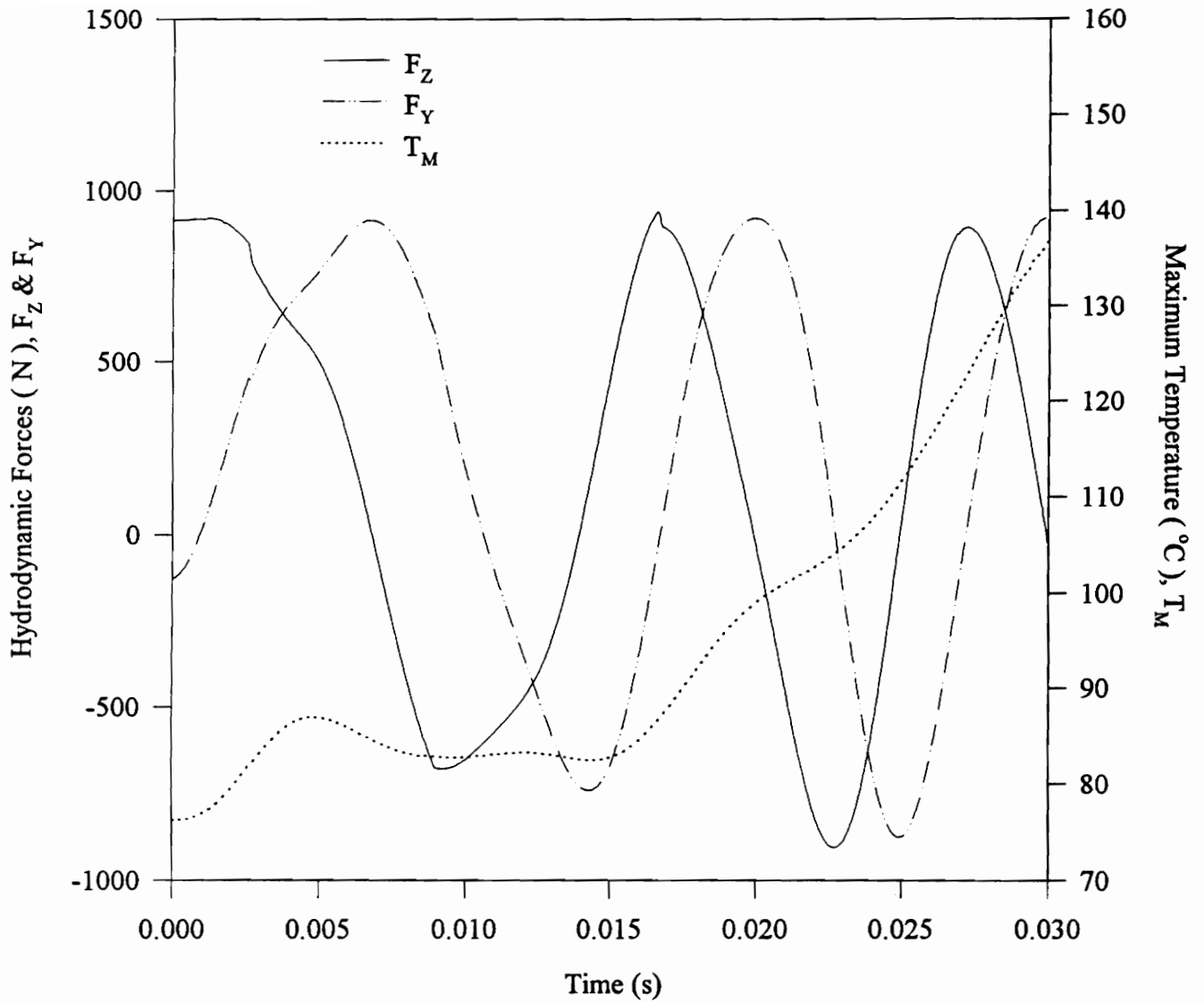


**Figure 64. Plots of Hydrodynamic Forces and Maximum Temperature vs. Time for a Tapered Seal**

**Operating Speed = 200 Hz (12000 RPM); Frictional Force = 889.6 N;  
Exit Clearance = 0.0889 mm**

maximum temperature in this case becomes as high as  $137^{\circ}\text{C}$  as shown in Fig. 64. Figure 65 shows the plots of eccentricities and the seal positions versus time for the above tapered seal with frictional force of 1334.4 N. The system becomes unstable again but the growth rate of vibration in this case is further reduced as it takes longer for the eccentricity ratio,  $e_r$ , to become 0.85 as compared to the previous case. Also, the seal remains locked for a longer time in this case when compared to the straight seal in the same conditions (see Fig. 45).

Figure 66 shows the plots of eccentricity ratios and the seal positions versus time for the tapered seal with the exit clearance of 0.0635 mm. The frictional force used is 889.6 N and the operating speed used is 200 Hz (12000 RPM). The growth rate of the vibration in the compressor rotor is significantly reduced as the increase in the amplitudes of the oscillations of the eccentricities,  $e_{rY}$  and  $e_{rZ}$ , in Fig. 66 is significantly reduced when compared to the tapered seal with the exit clearance of 0.0889 mm operating under same conditions (see Fig. 63), but the rotor is not still completely stabilized as the eccentricity ratio,  $e_r$ , gradually increases with time.

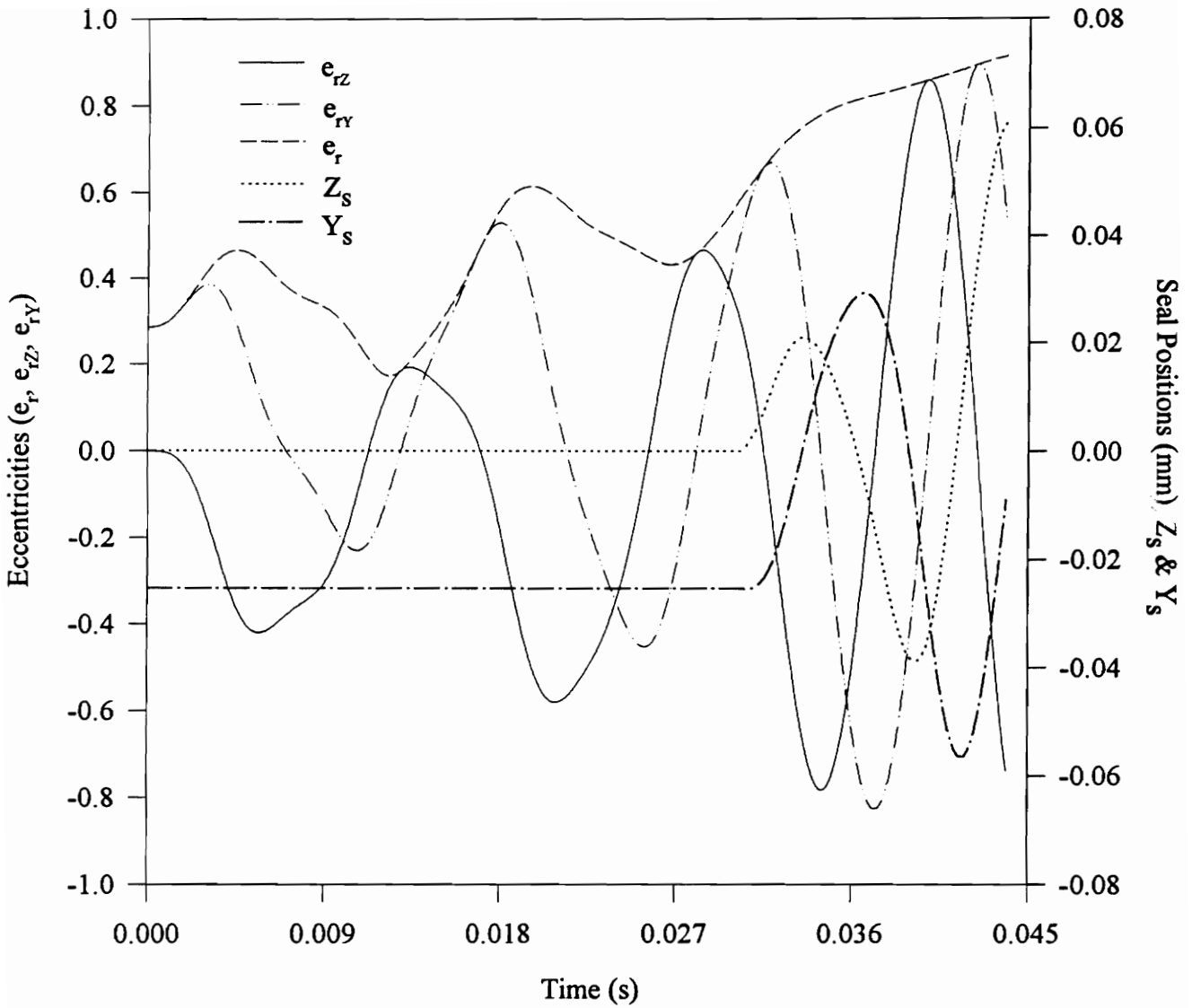


**Figure 65. Plots of Eccentricities and Absolute Seal Positions vs. Time for a Tapered Seal**  
**Operating Speed = 200 Hz (12000 RPM); Frictional Force = 1334.4 N;**  
**Exit Clearance = 0.0889 mm**

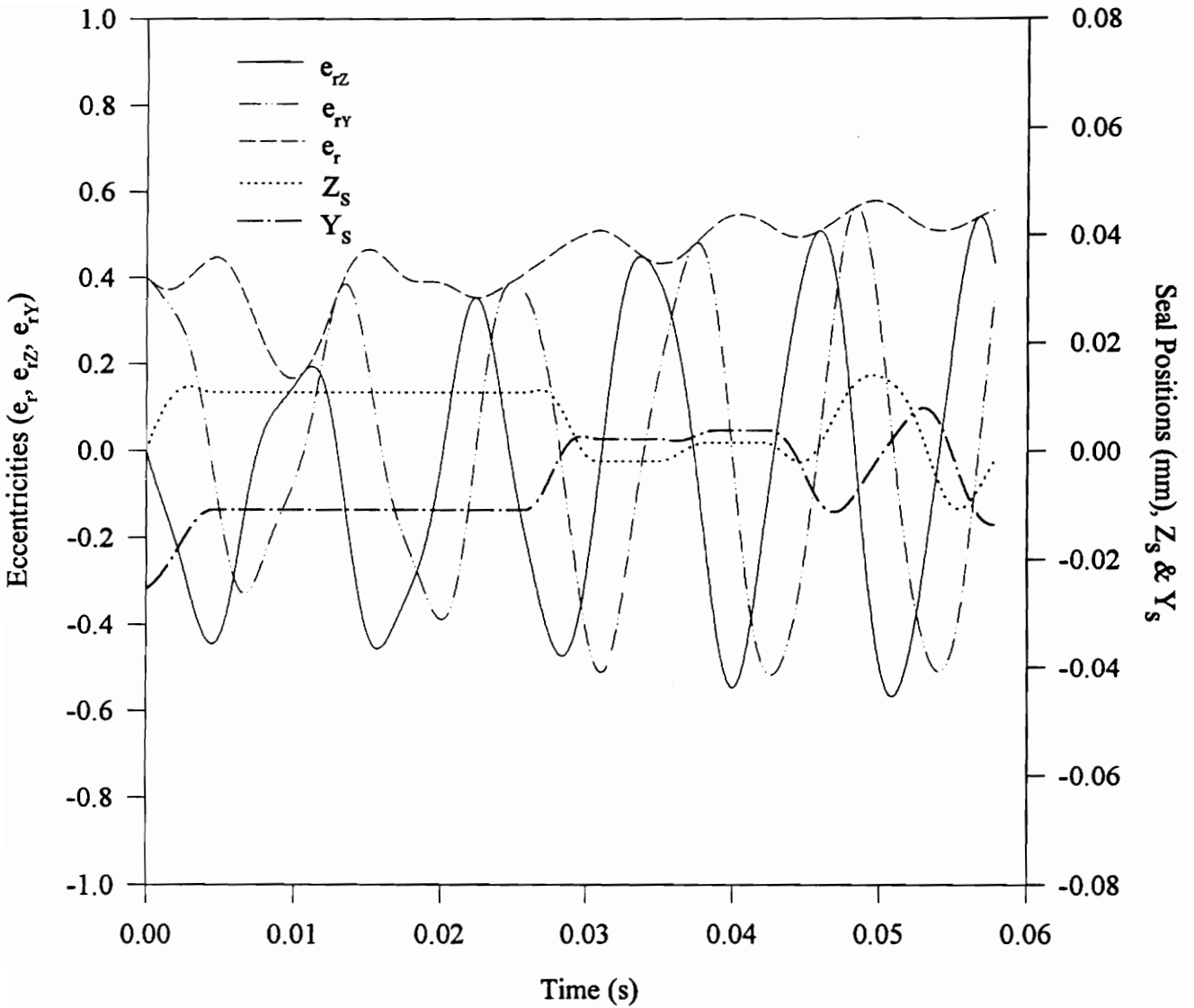


**Figure 66. Plots of Eccentricities and Absolute Seal Positions vs. Time for a Tapered Seal**  
**Operating Speed = 200 Hz (12000 RPM); Frictional Force = 889.6 N;**  
**Exit Clearance = 0.0635 mm**

## **Chapter 7**

### **Influence of Circumferential Grooves on the Seal Characteristics**

The modification required in the governing equations to permit analysis of seals with rounded and sharp edged circumferential grooves is presented in this chapter. Results are given that compare the various parameters from the linear stability analysis of circumferentially grooved seals with straight (ungrooved) seals. Finally, the results obtained from non-linear transient analysis of various circumferentially grooved seals are discussed.

#### **7.1 Circumferentially Grooved Seals**

Figure 67 shows a typical circumferentially grooved seal. Lands are separated by the circumferential groove. In modeling circumferentially grooved seals, it is assumed that the fluid inertia in the groove is negligible and the Reynolds equation is applicable. Different geometries are used to model grooves with sharp and rounded edges. Just the circumferential groove geometry is used to model the groove with rounded edges. A

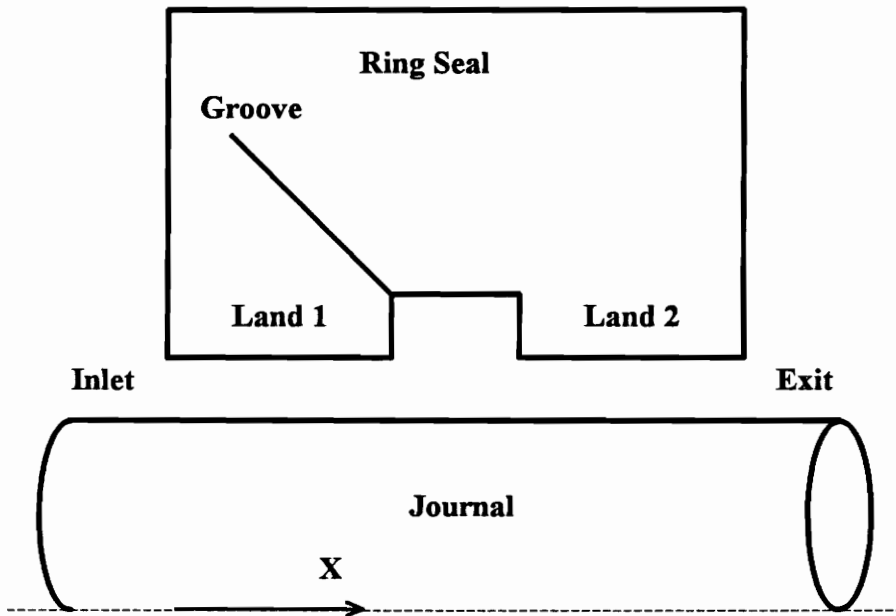


**Figure 67. Circumferentially Grooved Seal**

circumferential groove with a step at the next land entrance is used to model a groove with sharp edges. The purpose of the step is to account for the entrance losses of the fluid passing over the sharp edged groove.

### 7.1.1 Seal with Circumferential Groove

If the edges of the groove are rounded then the entrance losses as the fluid flows from the groove into the land are not significant and hence a circumferential groove with sinusoidal cross-section, as shown in Fig. 68, is used to model rounded or chamfered edge groove. It does not account for the entrance losses as the fluid flows over the groove and enters the next land. For this type of groove, the expression for fluid film thickness is given by

$$h = C + e_d \cos\left(\frac{y}{R} + \alpha\right) + D_g \sin\left(\pi \frac{x - L_1}{L_g}\right) \quad [68]$$

where  $D_g$  and  $L_g$  are the depth and the length of the groove.  $L_1$  is the length of the land.

### 7.1.2 Seal with Circumferential Groove and Step

If the edges of the groove are sharp then the entrance losses as the fluid flows from the groove into the land can become significant. Hence, circumferential groove and step

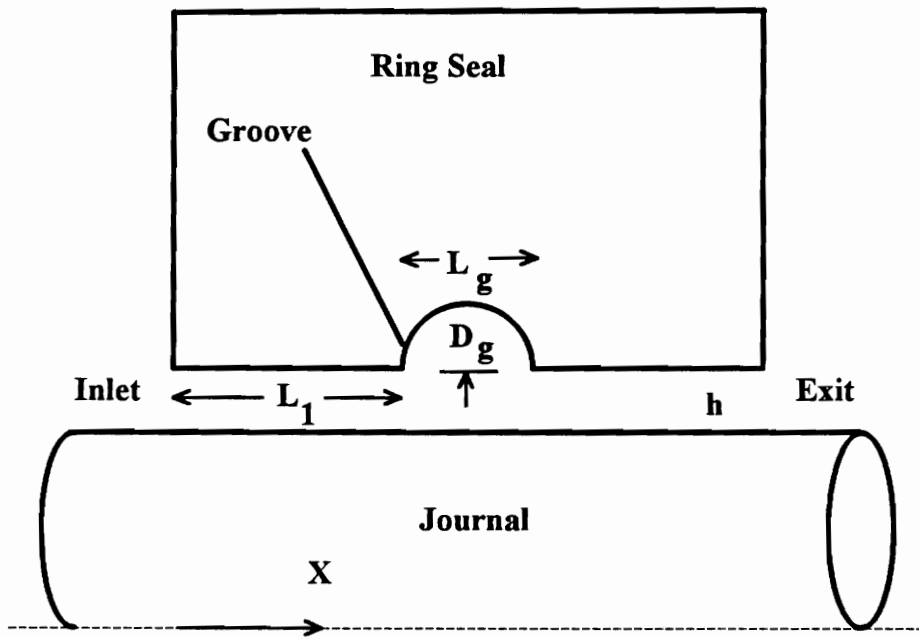


**Figure 68. Seal having Circumferential Groove with Sinusoidal Cross-section**

with sinusoidal cross-sections, as shown in Fig. 69, are used to model the groove and the vena contracta.  $H_s$  and  $L_s$  are the maximum height and the length of the step. The expressions for  $h$  are given as follows:

for the groove,

$$h = C + e_d \cos\left(\frac{y}{R} + \alpha\right) + D_g \sin\left(\pi \frac{x - L_1}{L_g}\right) \quad [69]$$

for the step,

$$h = \left[ C + e_d \cos\left(\frac{y}{R} + \alpha\right) \right] \left[ 1.0 - (1.0 - C_c) \sin\left(\pi \frac{x - L_1 - L_g}{L_s}\right) \right] \quad [70]$$

where  $L_1$  is the length of the land,  $C_c$  is the coefficient of contraction and is given by

$$C_c = h / (h + H_s) \quad [71]$$

## 7.2 Linear Stability Analysis Results

The specifications given in Table 2 are used for all the results presented in this chapter. The supply pressure is 4.136 MPa. A coefficient of contraction,  $C_c$ , equal to 0.6 is used for the seals with the sharp grooves. Lengths of the groove and the step used are 2.54 mm. Since the groove or the step changes the fluid film thickness abruptly, more than one element in the axial direction is required in the groove and the step for accurate finite element results. Convergence study was performed for different operating eccentricities using one, two, four, and eight elements in the groove and the step each. In a seal with just a circumferential groove, the pressure and temperature in the groove (near the

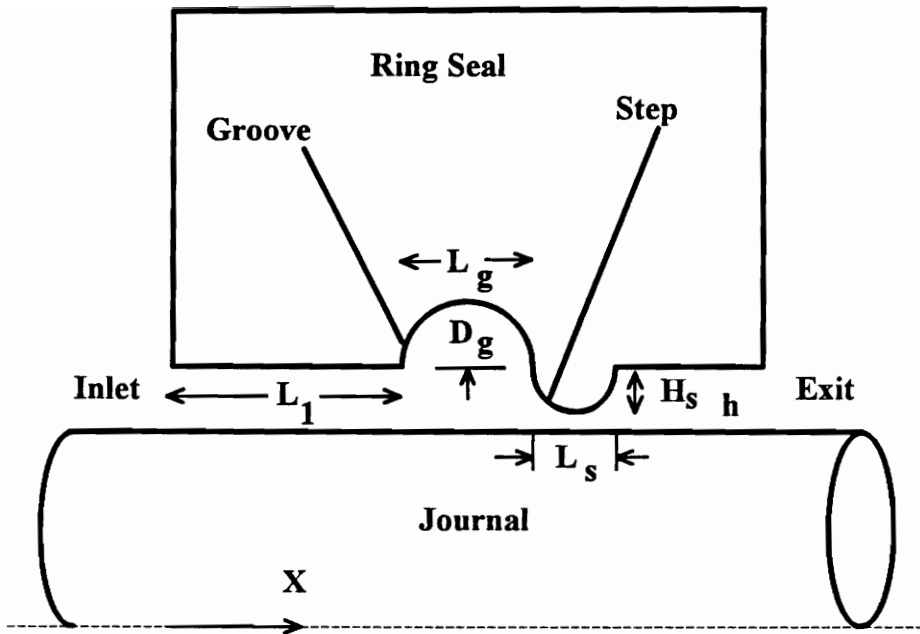
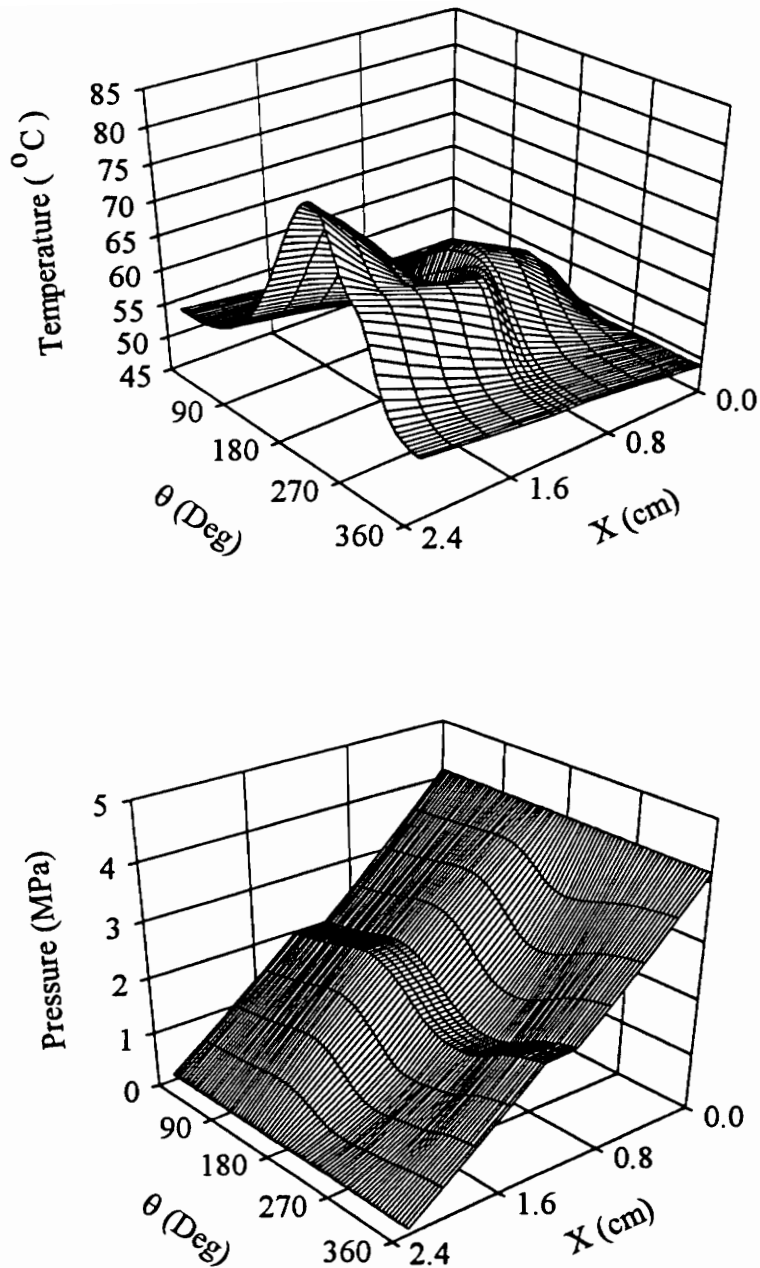


**Figure 69. Seal having Circumferential Groove and Step with Sinusoidal Cross-sections**

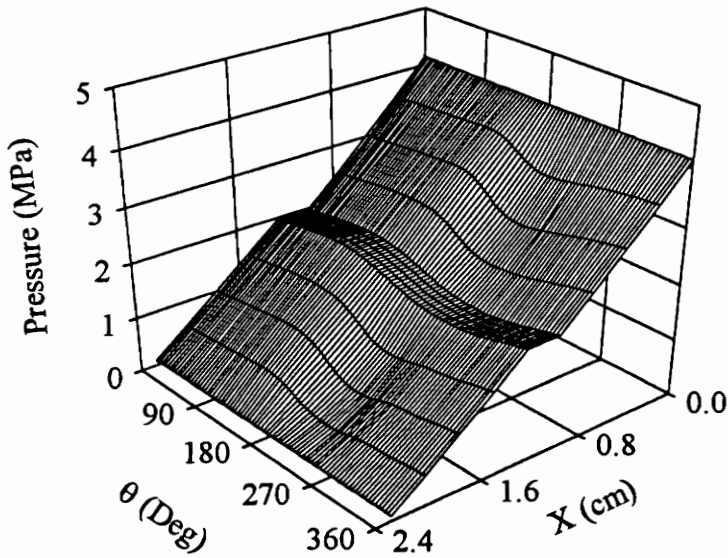
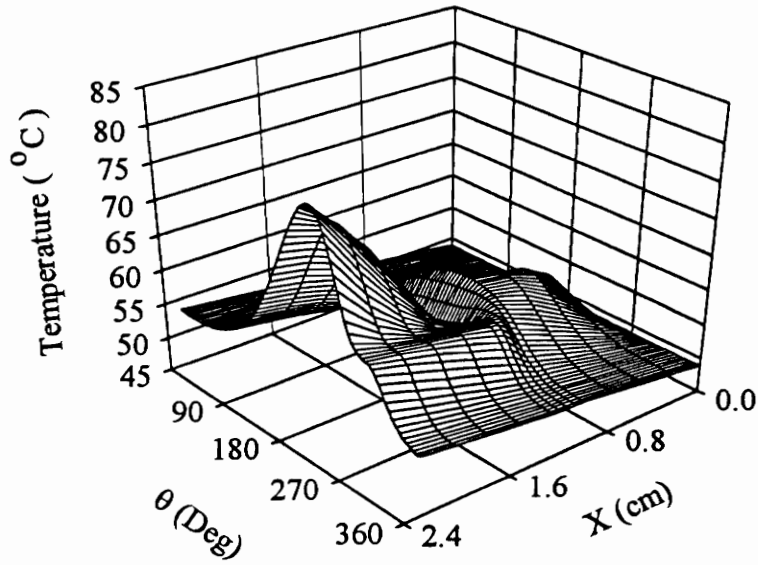
minimum fluid film thickness) changed by about 0.05 % and 0.37 % respectively, when the number of elements in the groove were changed from four to eight. These deviations did not change much with the change in operating eccentricity. In a seal with a circumferential groove and step, the pressure and temperature on the edge of the groove and the step (near the minimum fluid film thickness) changed by about 0.07 % and 0.5 % respectively at the operating eccentricity of 0.3 and 0.73 % and 1.2 % respectively at the operating eccentricity of 0.7, when the number of elements in both the groove and the step were increased from four to eight. All the results presented in this chapter are obtained using four elements in the groove and the step each.

Figure 70 shows the temperature and pressure distributions in a seal with circumferential groove. Operating speed and eccentricity used are 183.33 Hz (11000 RPM) and 0.5. The groove depth used is 0.381 mm. In the groove, the axial pressure gradient is almost reduced to zero and the circumferential pressure gradient still exists. The temperature in the groove reduces because of the reduction of viscous dissipation. If the groove depth is increased to 0.762 mm, the temperature and the circumferential pressure gradient in the groove reduce further as shown in Fig. 71. If the groove depth is increased further to 1.27 mm, the circumferential pressure gradient is eliminated as shown in Fig. 72. This phenomenon can reduce the cavitation in the seal and also enhance the stability of the compressor rotor. If a step is used in the above grooved seal with groove depth of 0.762 mm the pressure in the groove is elevated as shown in Fig. 73. The overall temperature is also increased because the step increases the viscous dissipation.

Figures 74-83 compare various parameters of three seals with circumferential grooves and an ungrooved (straight) seal. The three grooved seals have groove depths of 0.381 mm, 0.762 mm and 1.27 mm. The operating speed used is 183.33 Hz (11000 RPM). Figures 74-80 compare the stiffness and damping coefficients. The grooves



**Figure 70. Temperature and Pressure Distributions in a Seal with Circumferential Groove**  
**Groove Depth = 0.381 mm (0.015 in)**  
**Operating Speed = 183.33 Hz (11000 RPM)**  
**Operating Eccentricity ( $e_{r,y}$ ) = 0.5**



**Figure 71. Temperature and Pressure Distributions in a Seal with Circumferential Groove**

**Groove Depth = 0.762 mm (0.030 in)**  
**Operating Speed = 183.33 Hz (11000 RPM)**  
**Operating Eccentricity ( $e_{rY}$ ) = 0.5**

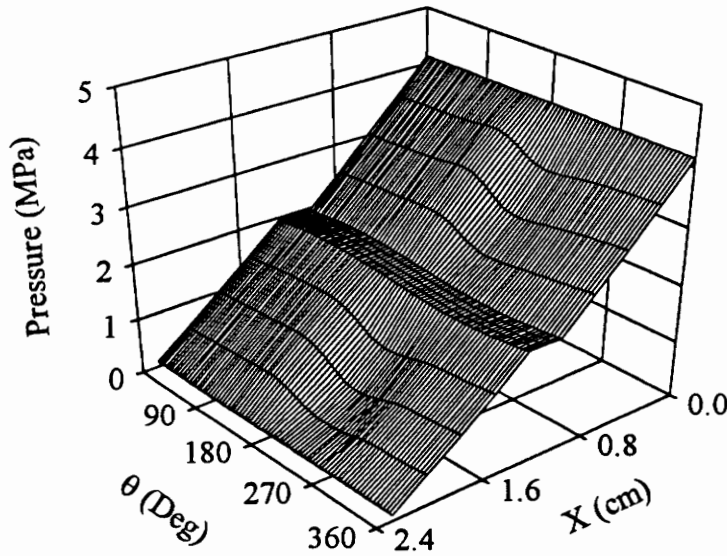
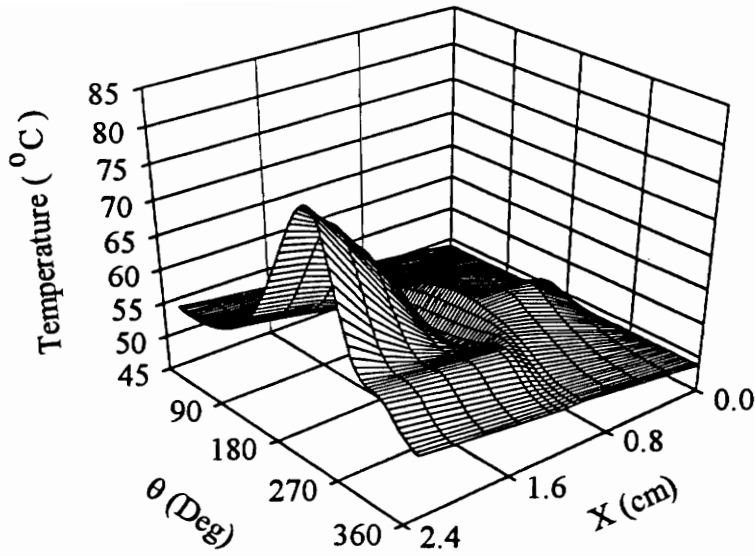


**Figure 72. Temperature and Pressure Distributions in a Seal with Circumferential Groove**  
**Groove Depth = 1.270 mm (0.050 in)**  
**Operating Speed = 183.33 Hz (11000 RPM)**  
**Operating Eccentricity ( $e_{rV}$ ) = 0.5**

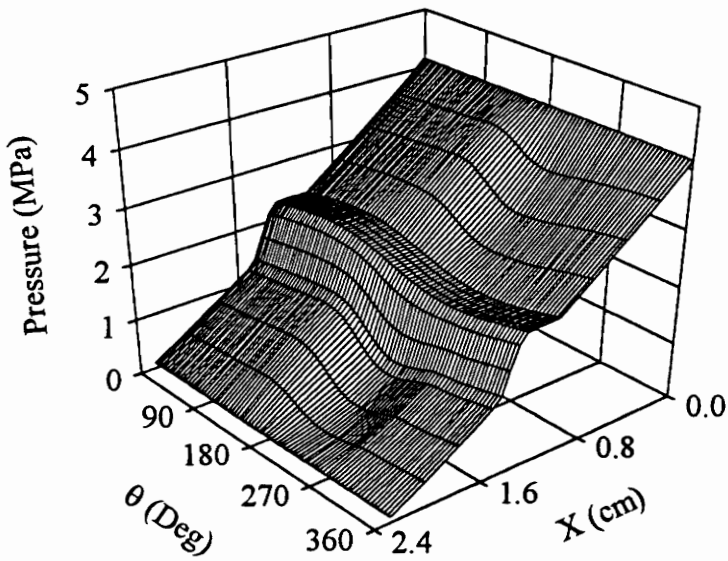
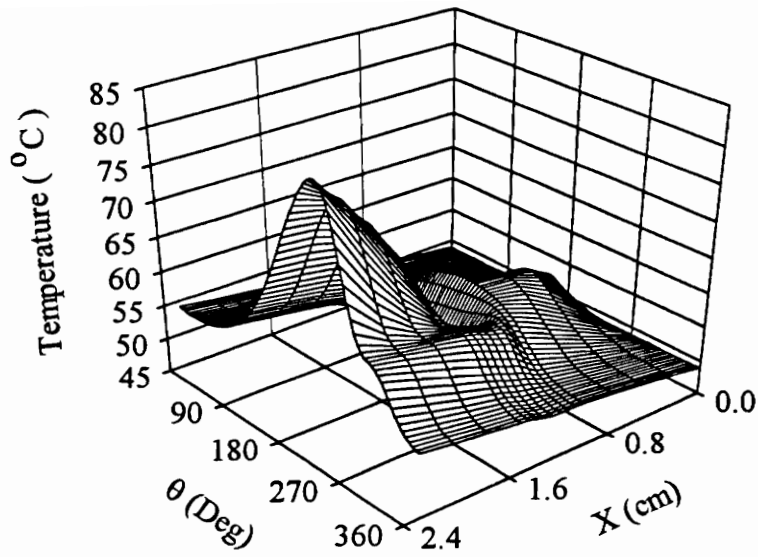


**Figure 73. Temperature and Pressure Distributions in a Seal with Circumferential Groove and Step**

**Groove Depth = 0.762 mm (0.030 in)**

**Operating Speed = 183.33 Hz (11000 RPM)**

**Operating Eccentricity ( $e_{rY}$ ) = 0.5**

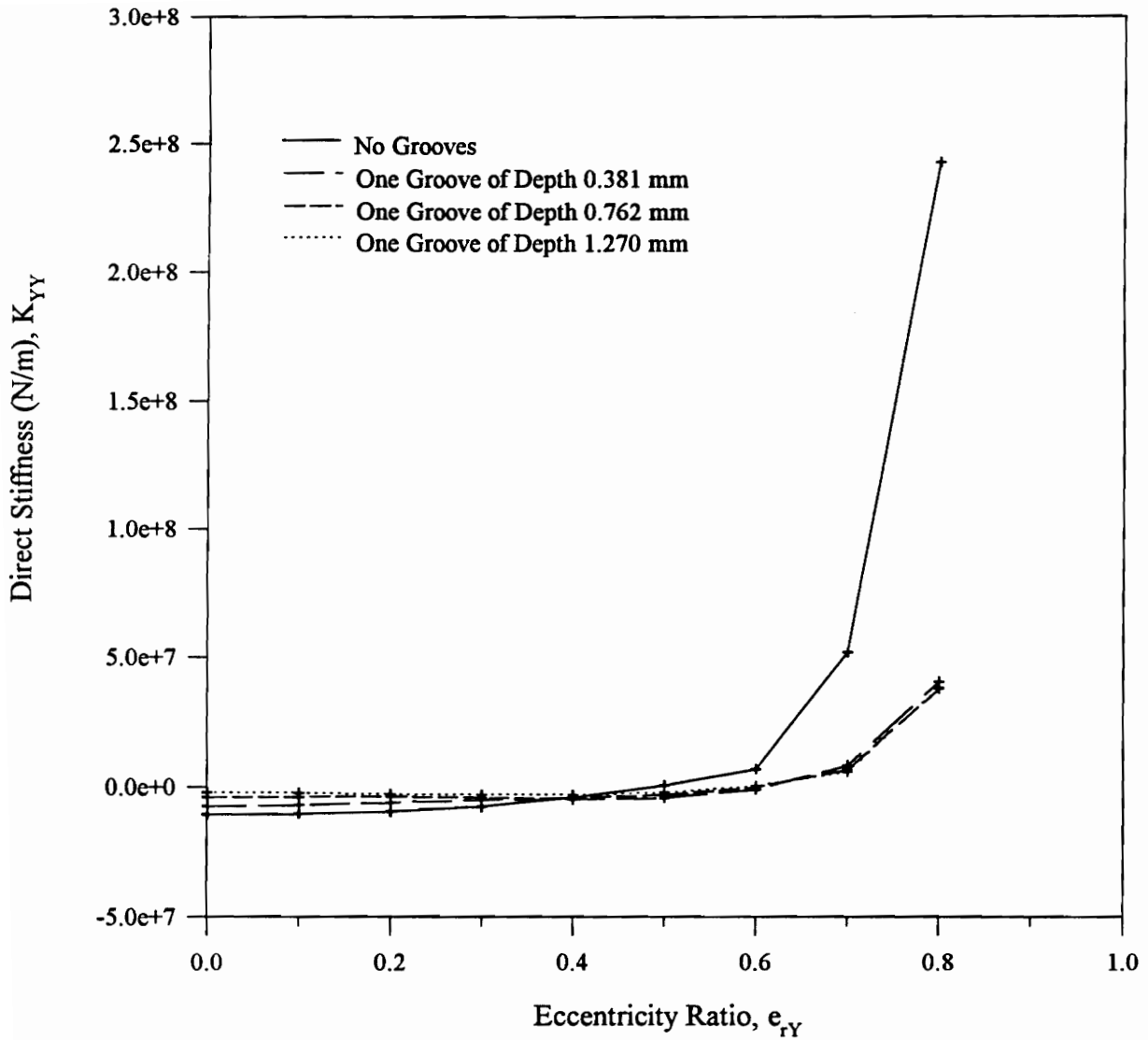


**Figure 74. Plot of Direct Stiffness vs. Eccentricity Ratio for Seals with and without Circumferential Grooves  
Operating Speed = 183.33 Hz (11000 RPM)**

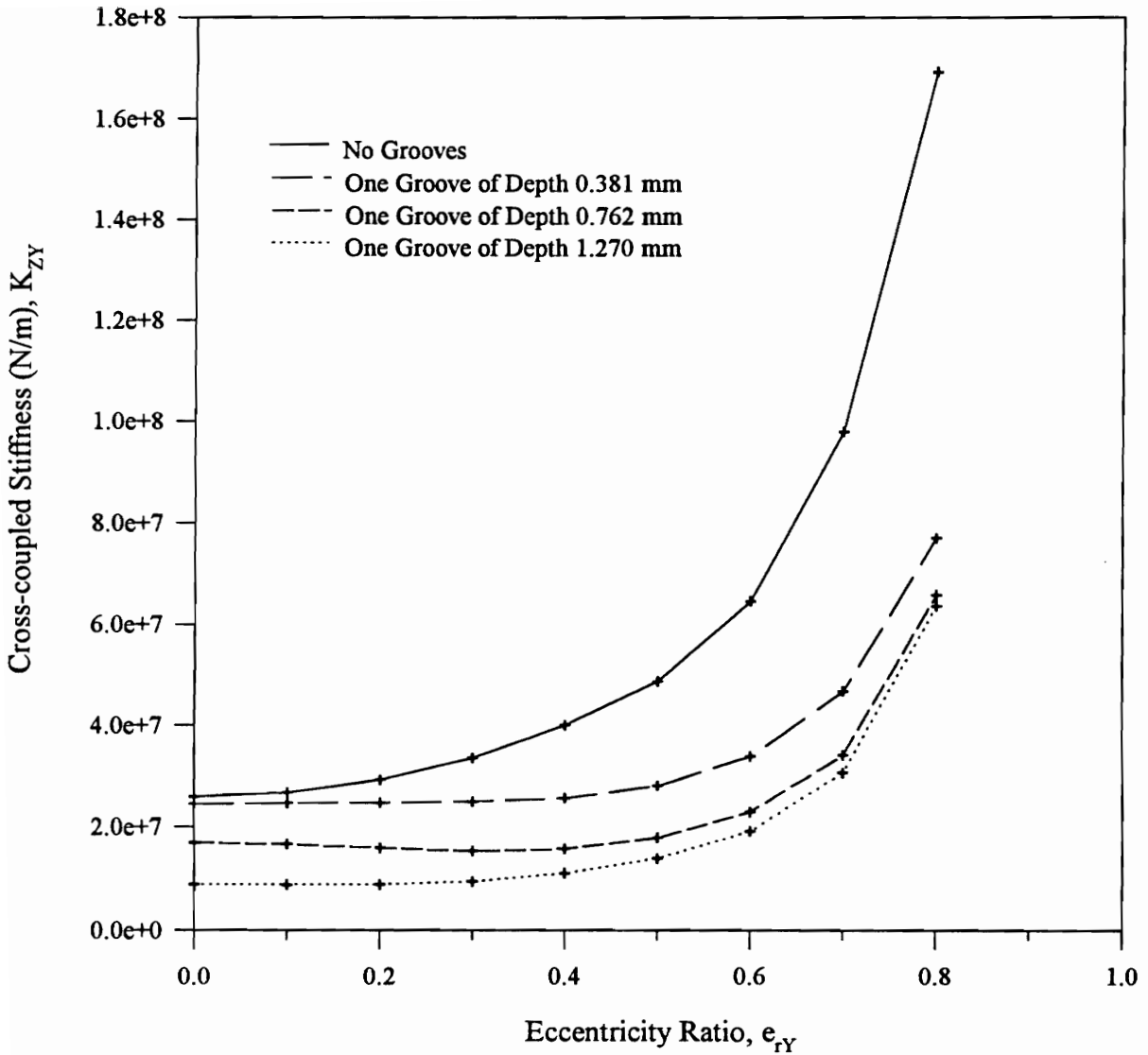


**Figure 75. Plot of Cross-coupled Stiffness vs. Eccentricity Ratio for Seals with and without Circumferential Grooves**  
**Operating Speed = 183.33 Hz (11000 RPM)**

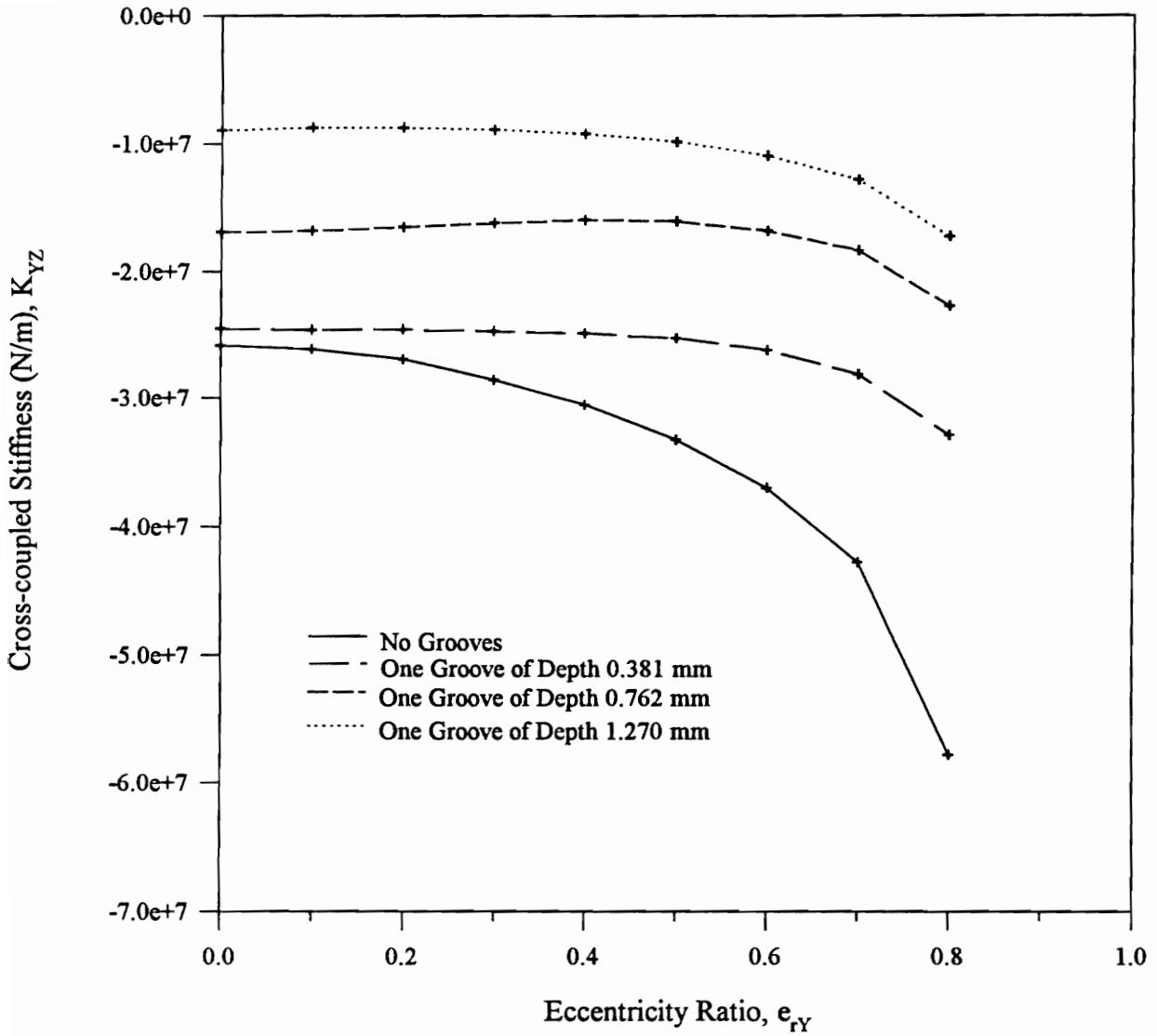


**Figure 76. Plot of Cross-coupled Stiffness vs. Eccentricity Ratio for Seals with and without Circumferential Grooves**  
**Operating Speed = 183.33 Hz (11000 RPM)**

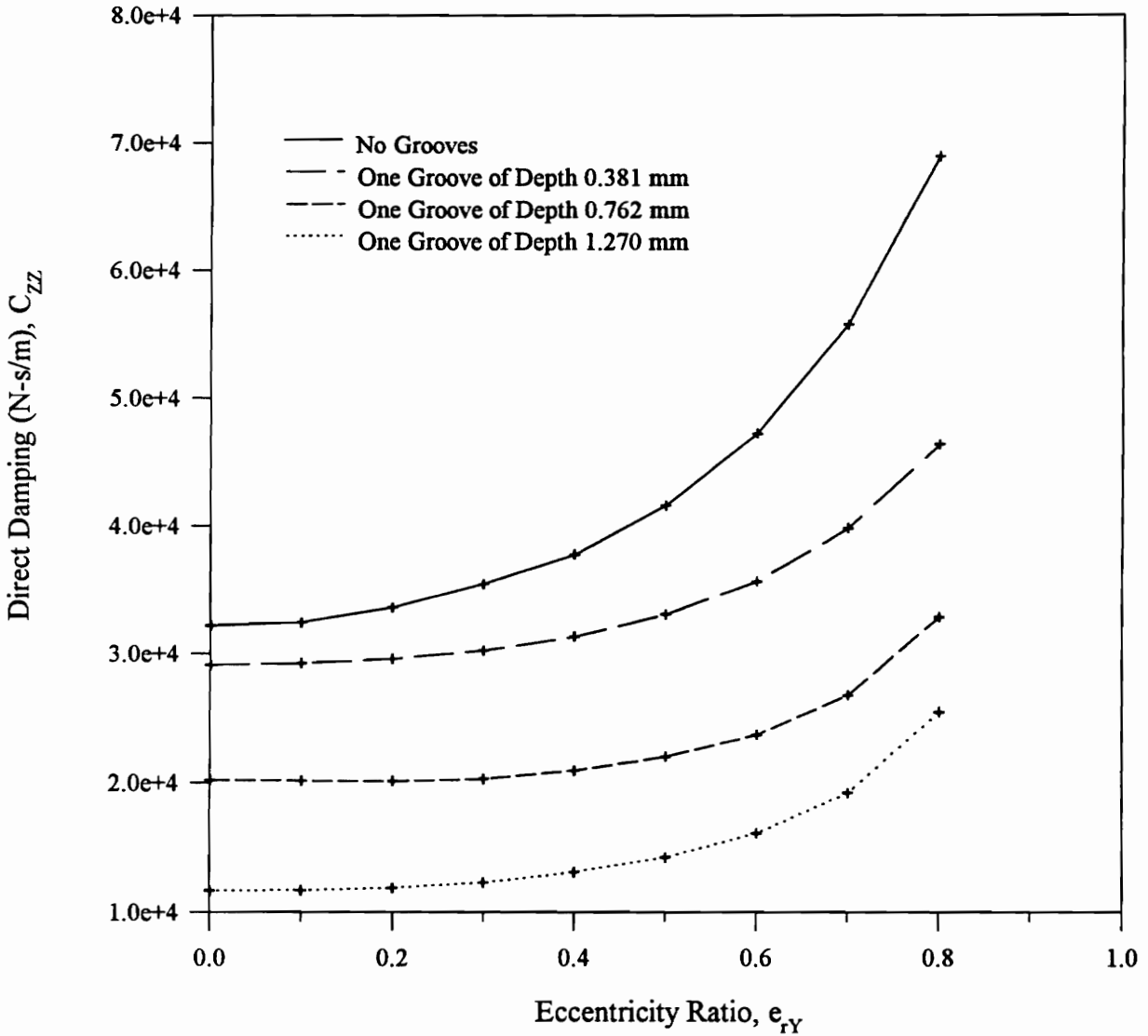


**Figure 77. Plot of Direct Damping vs. Eccentricity Ratio for Seals with and without Circumferential Grooves  
Operating Speed = 183.33 Hz (11000 RPM)**

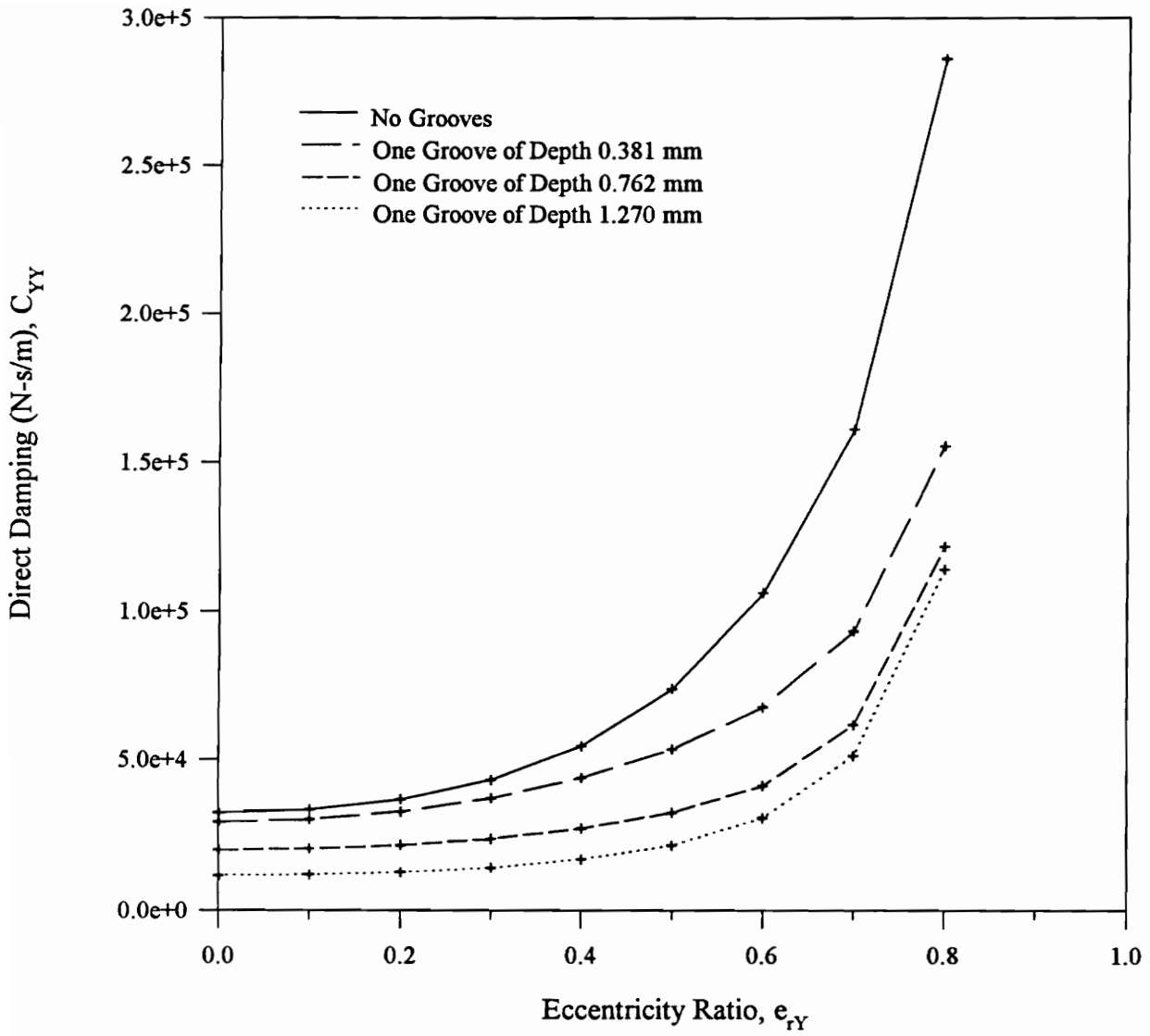


**Figure 78. Plot of Direct Damping vs. Eccentricity Ratio for Seals with and without Circumferential Grooves  
Operating Speed = 183.33 Hz (11000 RPM)**

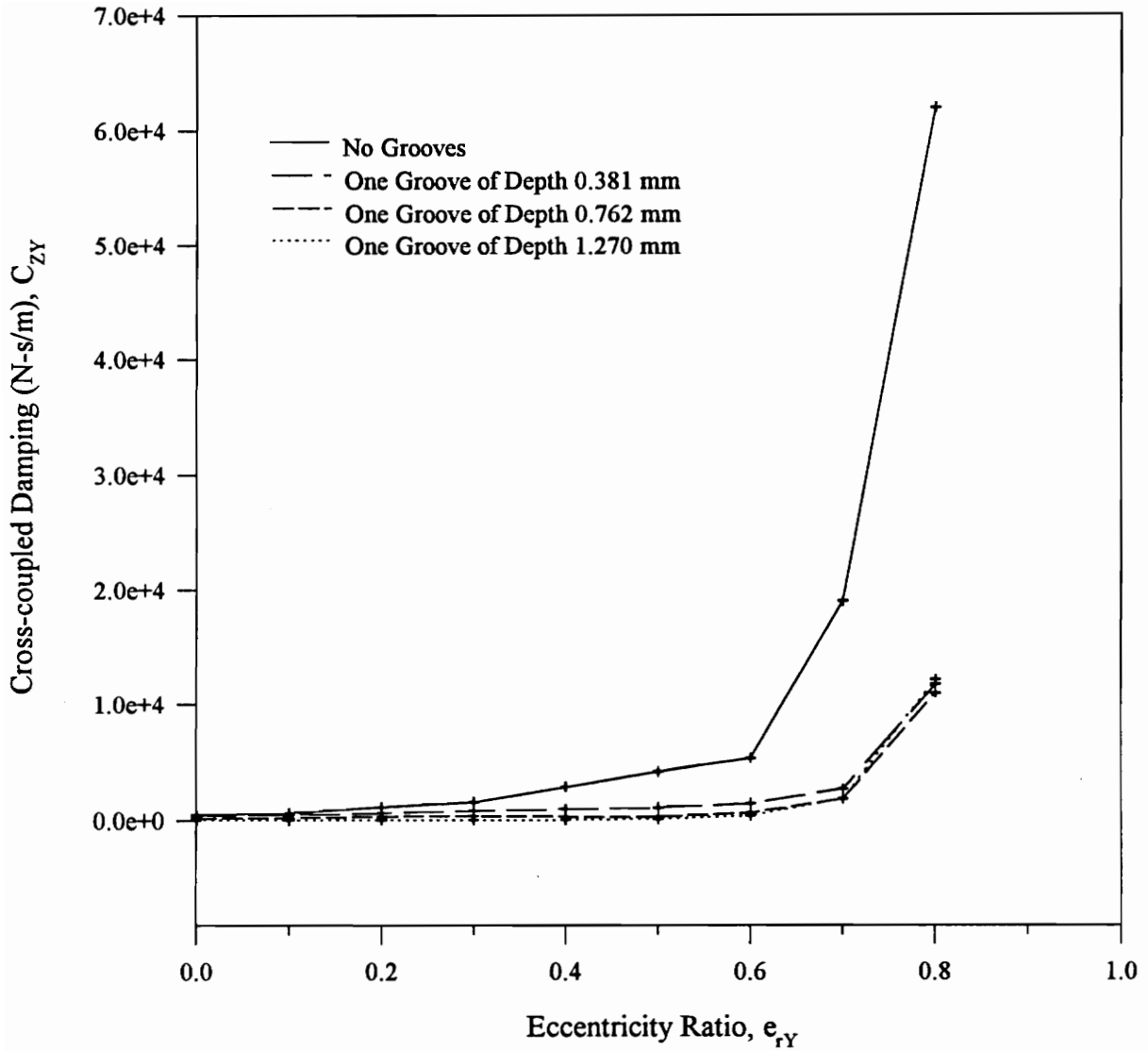


**Figure 79. Plot of Cross-coupled Damping vs. Eccentricity Ratio for Seals with and without Circumferential Grooves**  
**Operating Speed = 183.33 Hz (11000 RPM)**

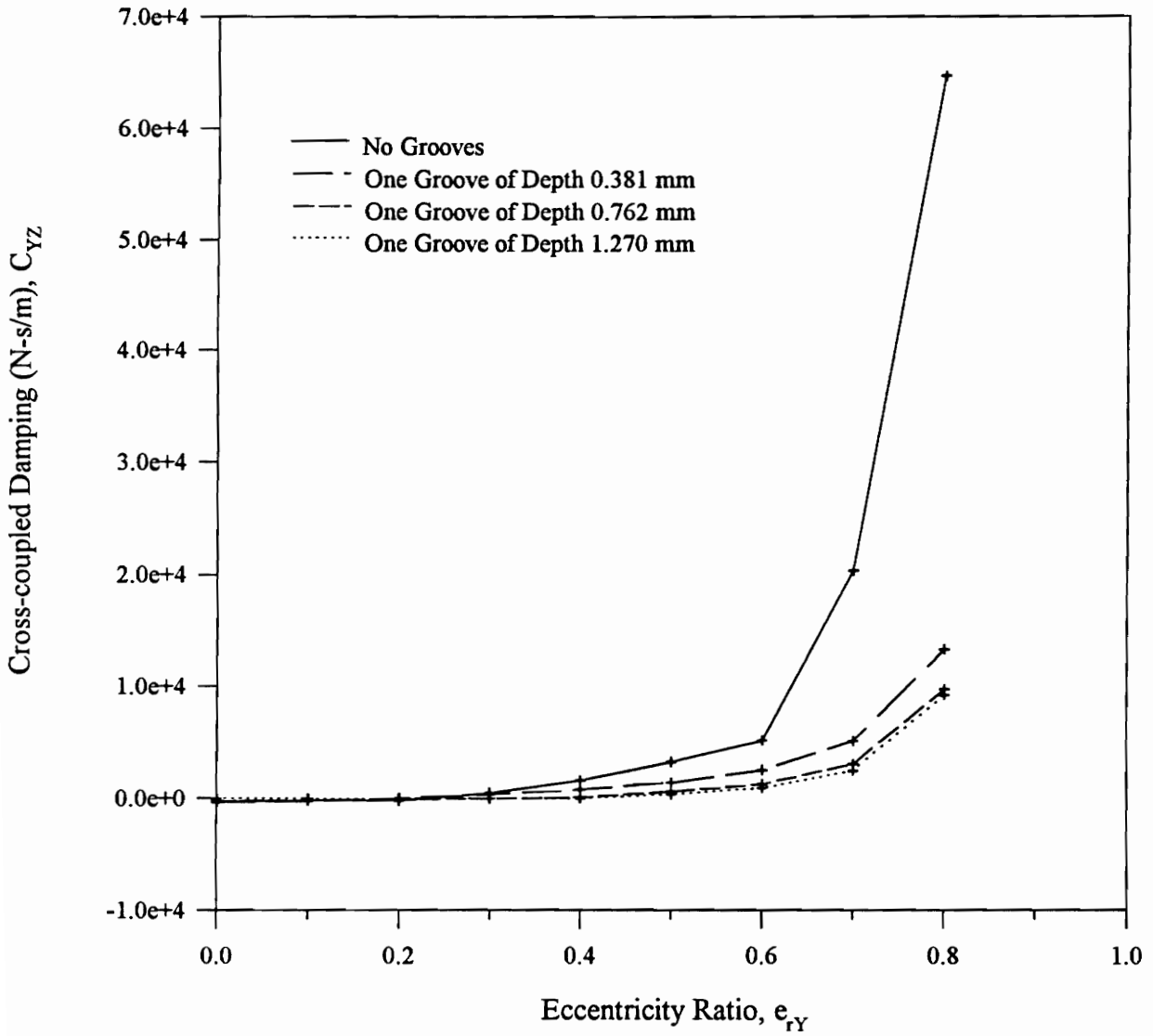
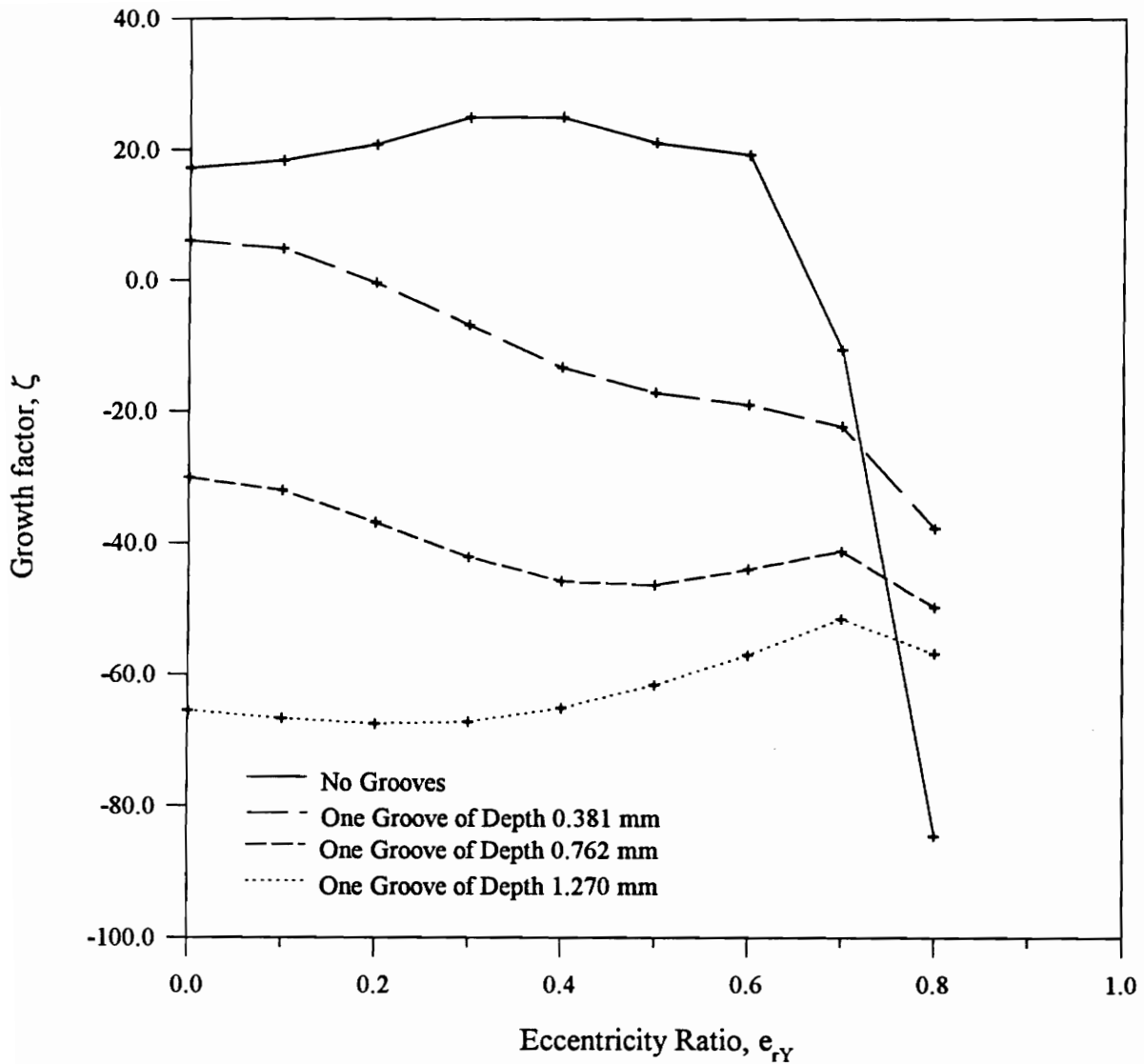


**Figure 80. Plot of Cross-coupled Damping vs. Eccentricity Ratio for Seals with and without Circumferential Grooves**  
**Operating Speed = 183.33 Hz (11000 RPM)**

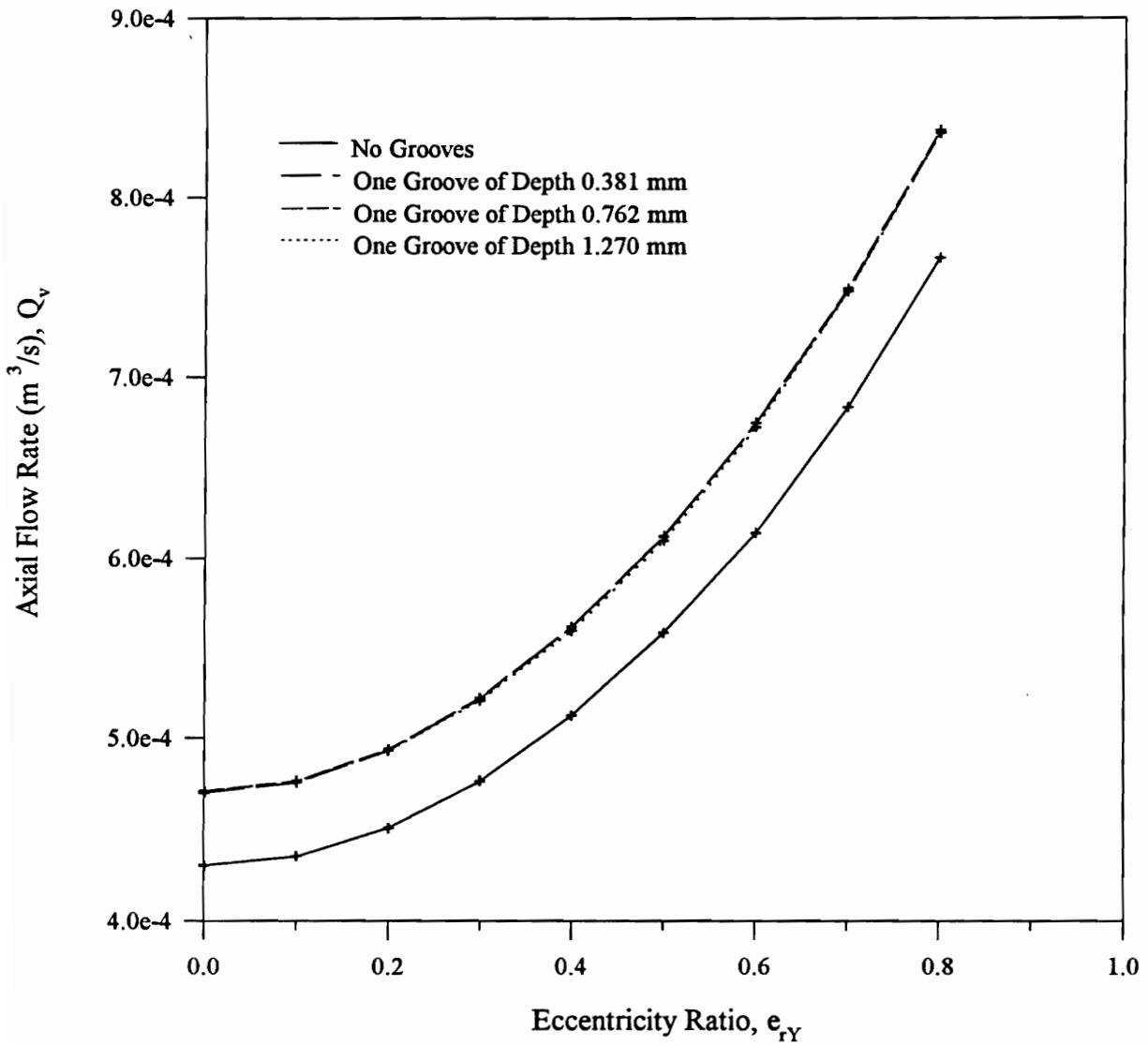
reduce the magnitude of these coefficients as they reduce the hydrodynamic forces. The larger the groove depth, the larger is the reduction in the magnitudes of these coefficients. The decrease in the magnitudes of cross-coupled coefficients improves the stability of the compressor rotor.

Figure 81 compares the growth factors of the above seals. It can be seen that the grooves reduce the growth factor significantly more than the tapered geometry (see Fig. 57) and hence can improve the stability of the compressor rotor more than the tapered seals. Figures 82 and 83 compare the plots of axial flow rate and the maximum temperature. The grooves increase the axial flow rate. The axial flow rate does not change with the groove depths used because all the groove depths used have similar effect on the axial pressure gradient in the groove as shown in Figs. 70-72. The maximum temperature of the grooved seals is less than that of the ungrooved seal as the viscous dissipation is reduced by the grooves. For eccentricities below 0.6 the maximum temperature decreases as the groove depth is increased, as expected. For higher eccentricities, the trend reverses because of cavitation which is diminished most by the deepest groove.

Figures 84-88 compare the various parameters of a ungrooved (straight) seal, seal with circumferential groove and seal with circumferential groove and step. The groove depth used is 0.762 mm. The coefficient of contraction used for the step is 0.6. The effect of the step is not significant on the stiffness and the damping coefficients as seen in Figs. 84-86 for some of them. In general, the step slightly increases the stiffness and the damping coefficients of the grooved seal. Figure 87 compares the growth factors for these three seals. Since the stiffness and the damping coefficients do not change significantly because of the step, the growth factor also is not influenced significantly. Figure 88 compares the axial flow rates. It is interesting to see that the seal with just a circumferential groove increases the axial flow rate when compared to that of an



**Figure 81. Plot of Growth Factor vs. Eccentricity Ratio for Seals with and without Circumferential Grooves**  
**Operating Speed = 183.33 Hz (11000 RPM)**



**Figure 82. Plot of Axial Flow Rate vs. Eccentricity Ratio for Seals with and without Circumferential Grooves**  
**Operating Speed = 183.33 Hz (11000 RPM)**

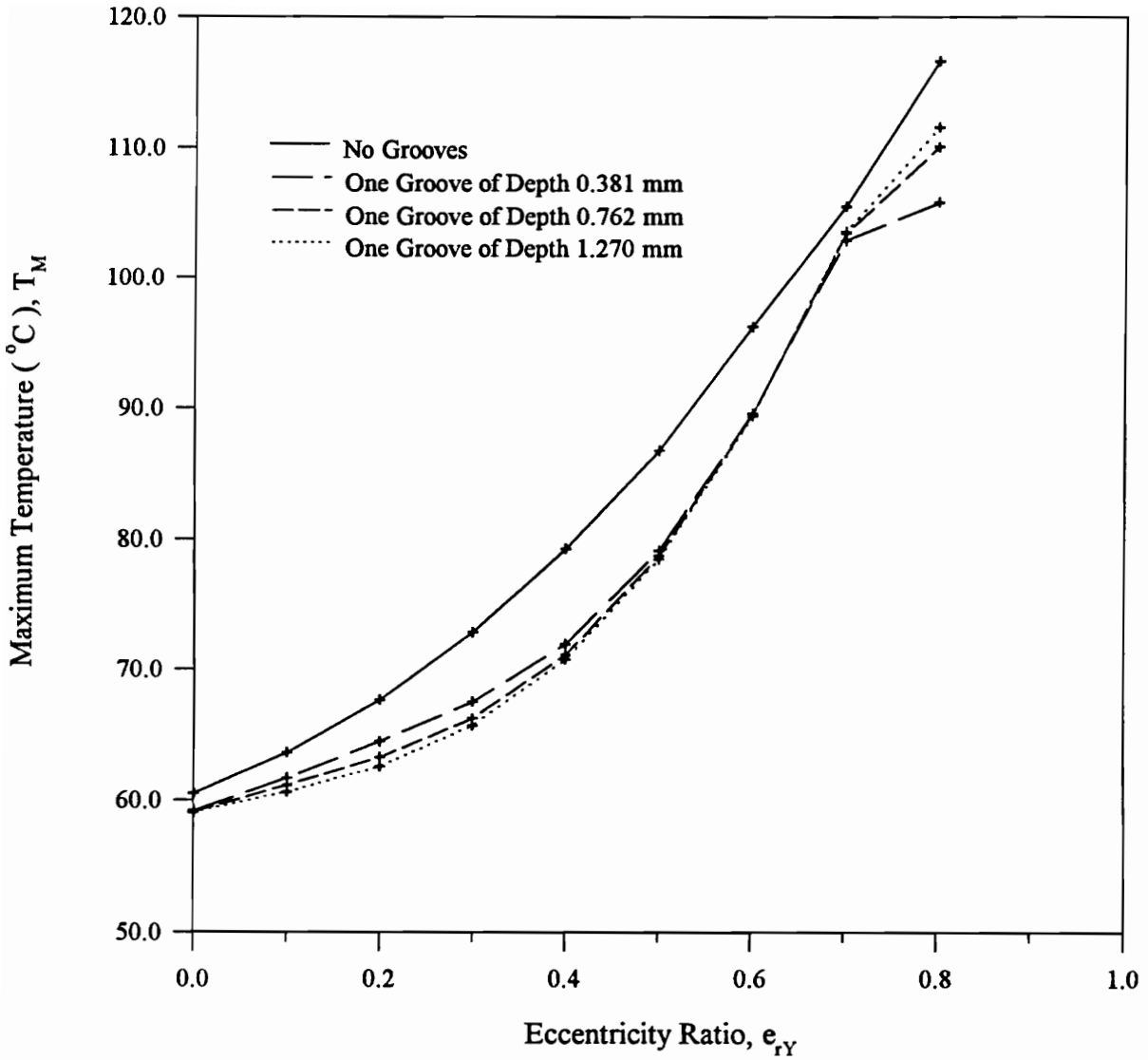


**Figure 83. Plot of Maximum Temperature vs. Eccentricity Ratio for Seals with and without Circumferential Grooves**  
**Operating Speed = 183.33 Hz (11000 RPM)**

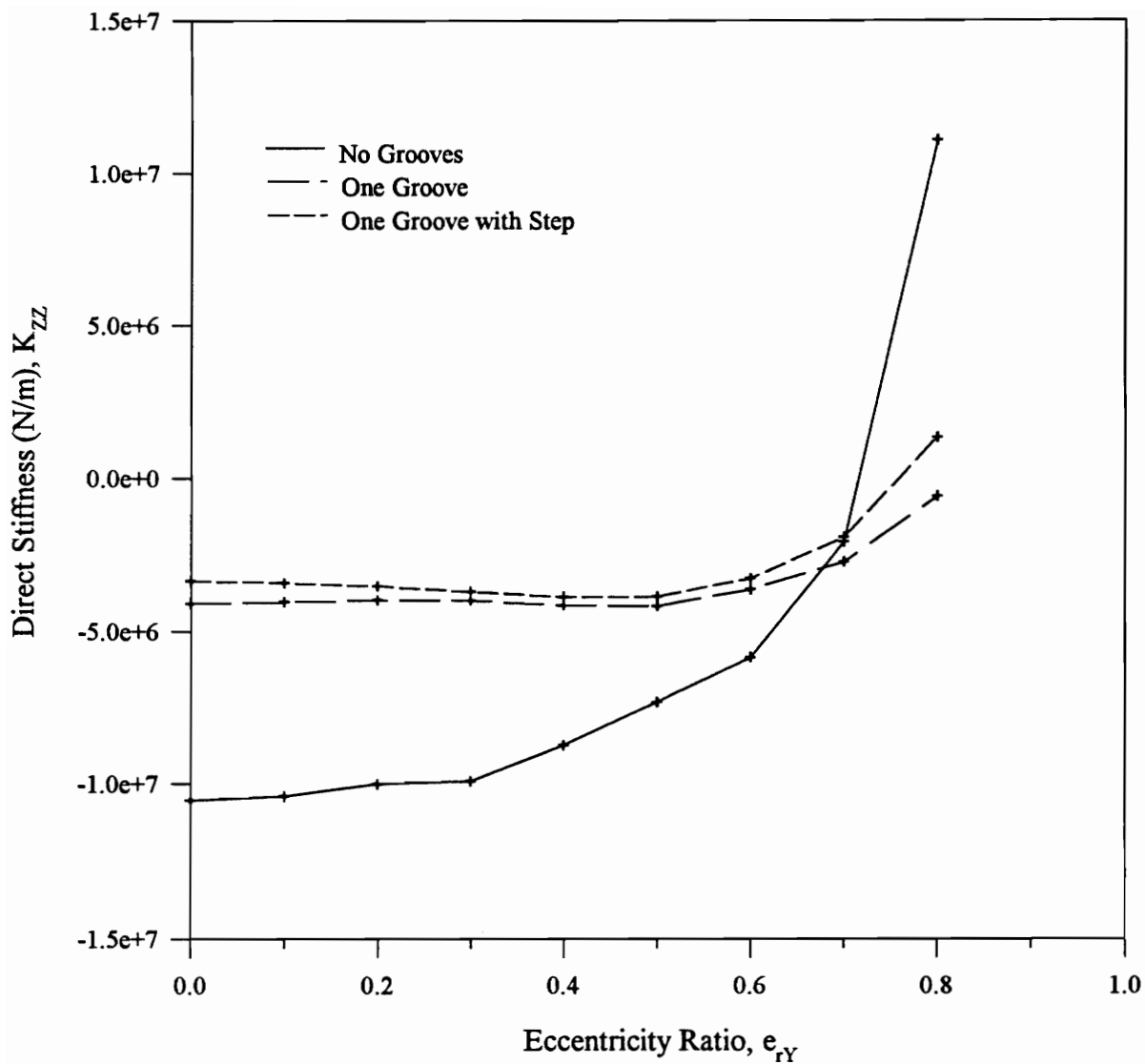


**Figure 84. Plot of Direct Stiffness vs. Eccentricity Ratio for Seals with and without Circumferential Grooves and Steps**  
**Groove Depth = 0.762 mm**  
**Operating Speed = 183.33 Hz (11000 RPM)**

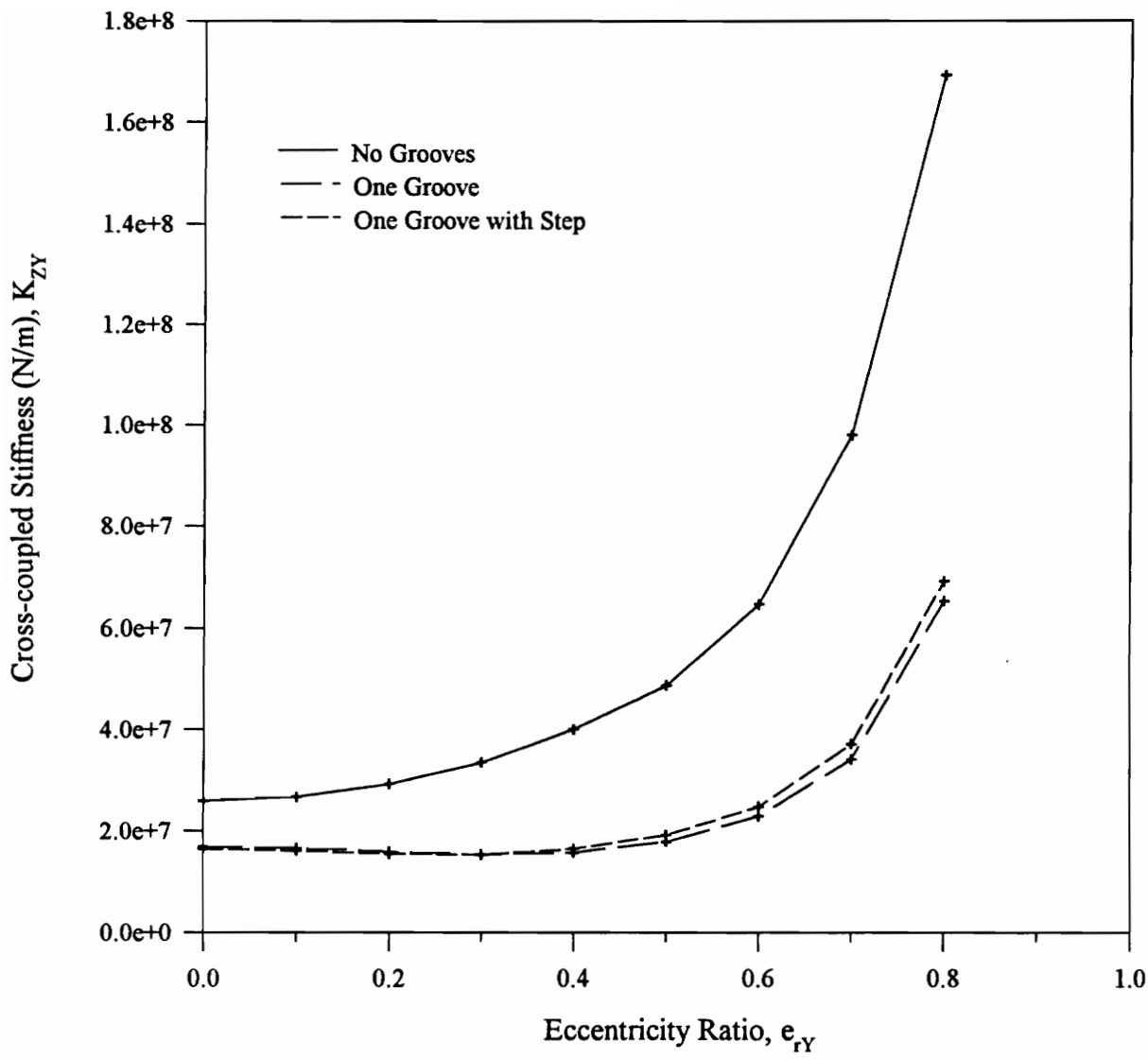


**Figure 85. Plot of Cross-coupled Stiffness vs. Eccentricity Ratio for Seals with and without Circumferential Grooves and Steps**  
**Groove Depth = 0.762 mm**  
**Operating Speed = 183.33 Hz (11000 RPM)**

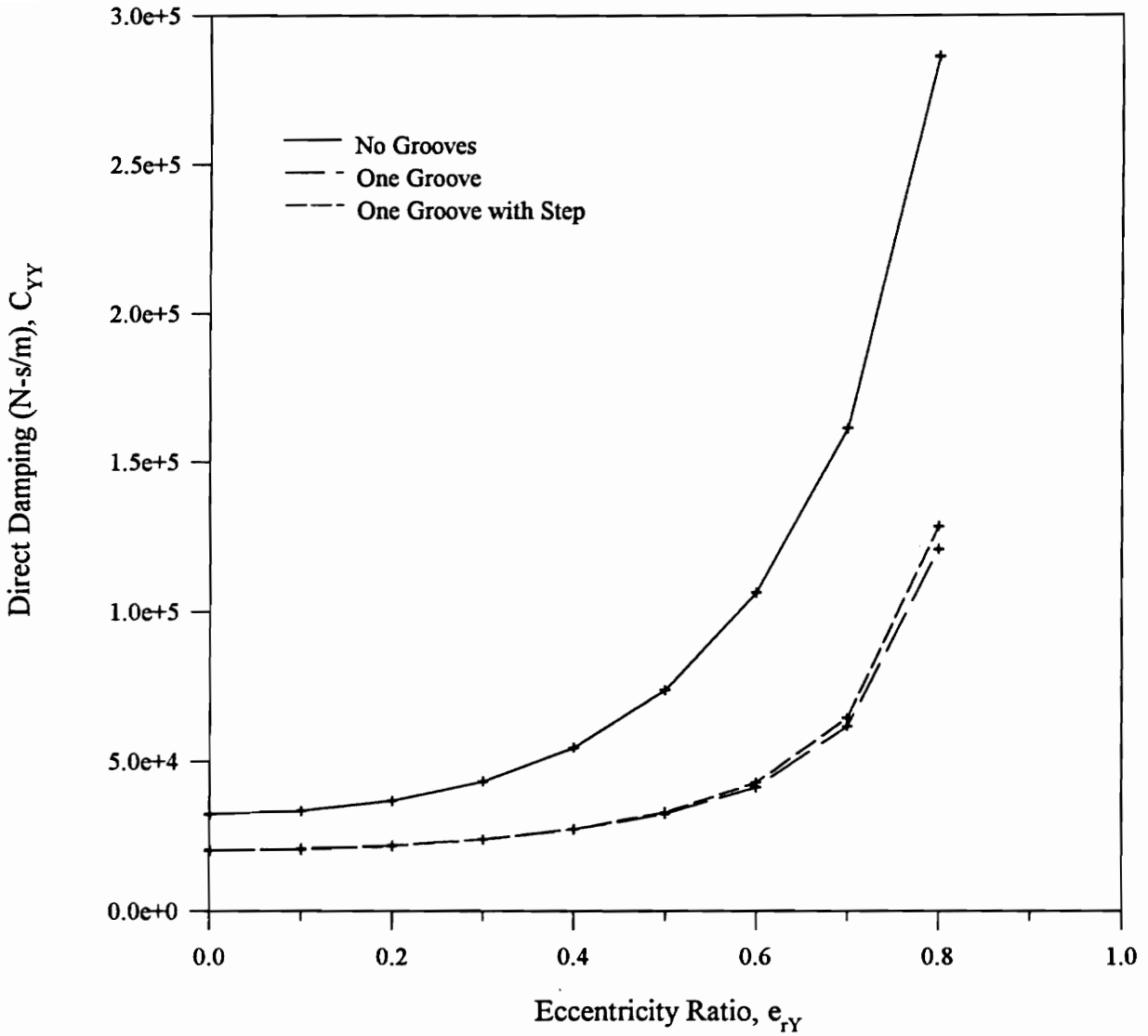


**Figure 86. Plot of Direct Damping vs. Eccentricity Ratio for Seals with and without Circumferential Grooves and Steps**

**Groove Depth = 0.762 mm**

**Operating Speed = 183.33 Hz (11000 RPM)**

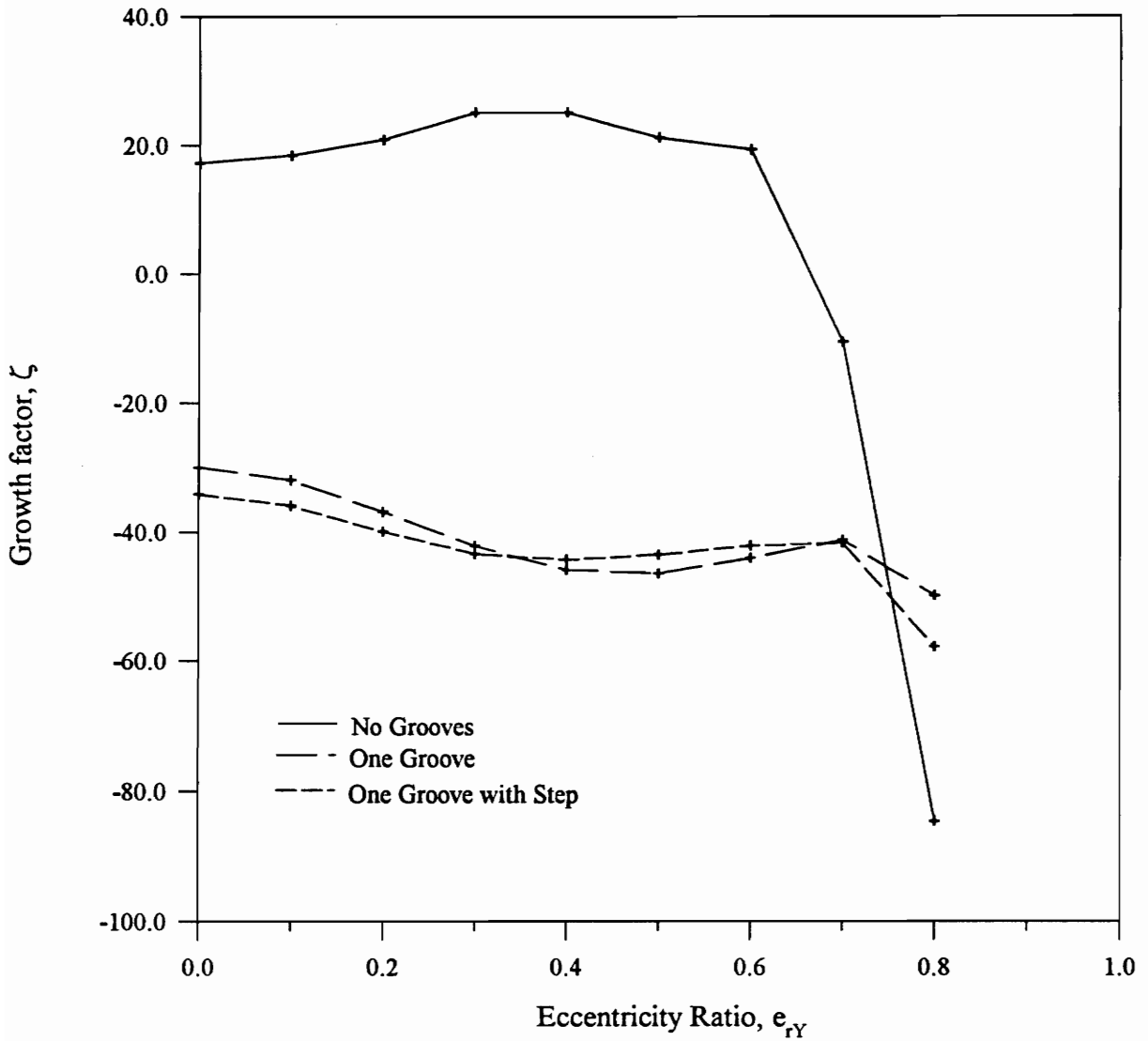


**Figure 87. Plot of Growth Factor vs. Eccentricity Ratio for Seals with and without Circumferential Grooves and Steps**  
**Groove Depth = 0.762 mm**  
**Operating Speed = 183.33 Hz (11000 RPM)**

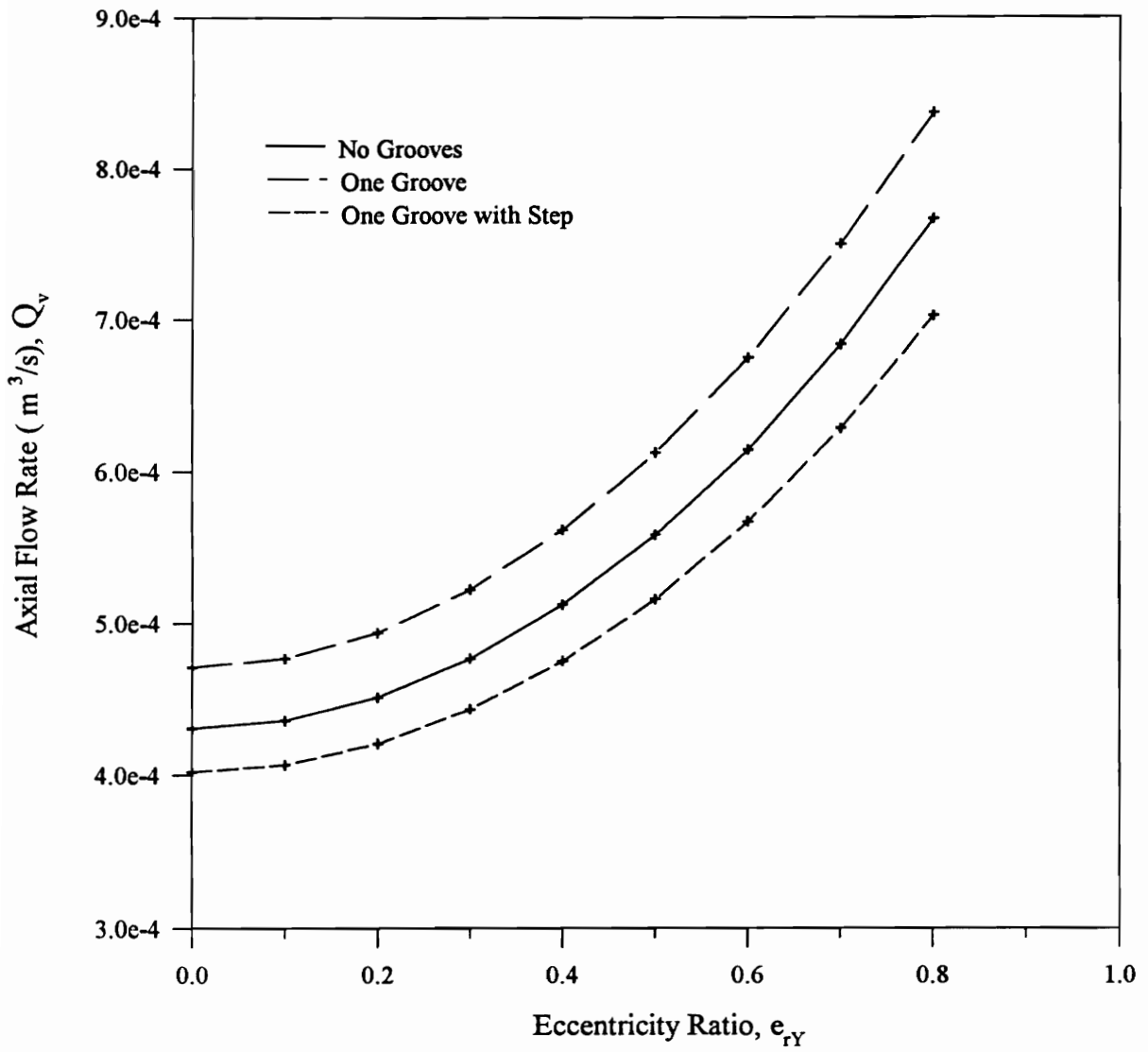


**Figure 88. Plot of Axial Flow Rate vs. Eccentricity Ratio for Seals with and without Circumferential Grooves and Steps**

**Groove Depth = 0.762 mm**

**Operating Speed = 183.33 Hz (11000 RPM)**

ungrooved seal, whereas the seal with the sharp edged circumferential groove decreases the leakage flow.

### 7.3 Non-linear Transient Analysis Results

In this section results obtained from transient analysis of circumferentially grooved smooth entry seals are presented. The operating speed used is 200 Hz (12000 RPM). Figure 89 shows the plots of the eccentricity ratios and seal positions versus time in the case of a seal with circumferential groove of depth 0.381 mm. The frictional force used is 889.6 N. In this case the seal gets locked and unlocked four times before the eccentricity ratio,  $e_r$ , becomes as high as 0.85 approximately at about time = 0.082 sec. Though this circumferential groove increases the time taken for the eccentricity ratio to become 0.85 from 0.03 sec. in the case of tapered seal operating under same conditions (see Fig. 63) to 0.082 sec., but is not able to make the ring locked or stabilize the rotor completely. But if the groove depth is increased to 0.762 mm, then the seal remains locked through out the transient analysis and the rotor whirls with a small whirl radius as indicated by the plots of eccentricities and the seal positions versus time for this case in Fig. 90. This happens because the magnitude of the hydrodynamic forces are reduced by the deeper groove.

Figures 91 and 92 show the variation of hydrodynamic forces and the axial flow rate through the seal as a function of time for the above two cases. In the case with groove depth of 0.381 mm, the hydrodynamic forces diverge and the axial flow rate increases with time as this is an unstable case. In the case with groove depth of 0.762 mm, the hydrodynamic forces and the axial flow rates oscillate with a constant amplitude in the steady state condition as expected.

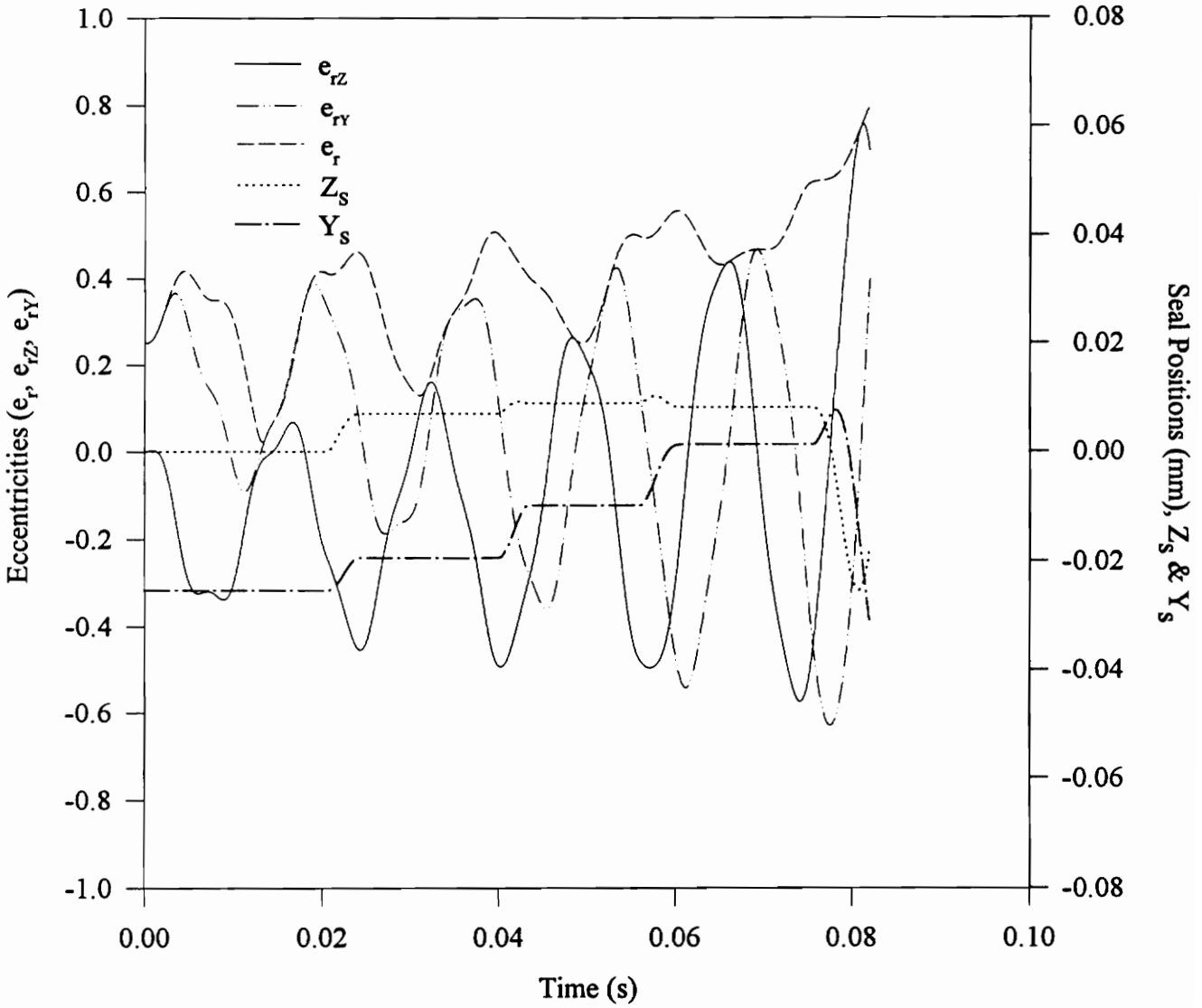


**Figure 89. Plots of Eccentricities and Absolute Seal Positions vs. Time for a Seal with Circumferential Groove**

**Operating Speed = 200 Hz (12000 RPM); Frictional Force = 889.6 N;  
Groove Depth = 0.381 mm**

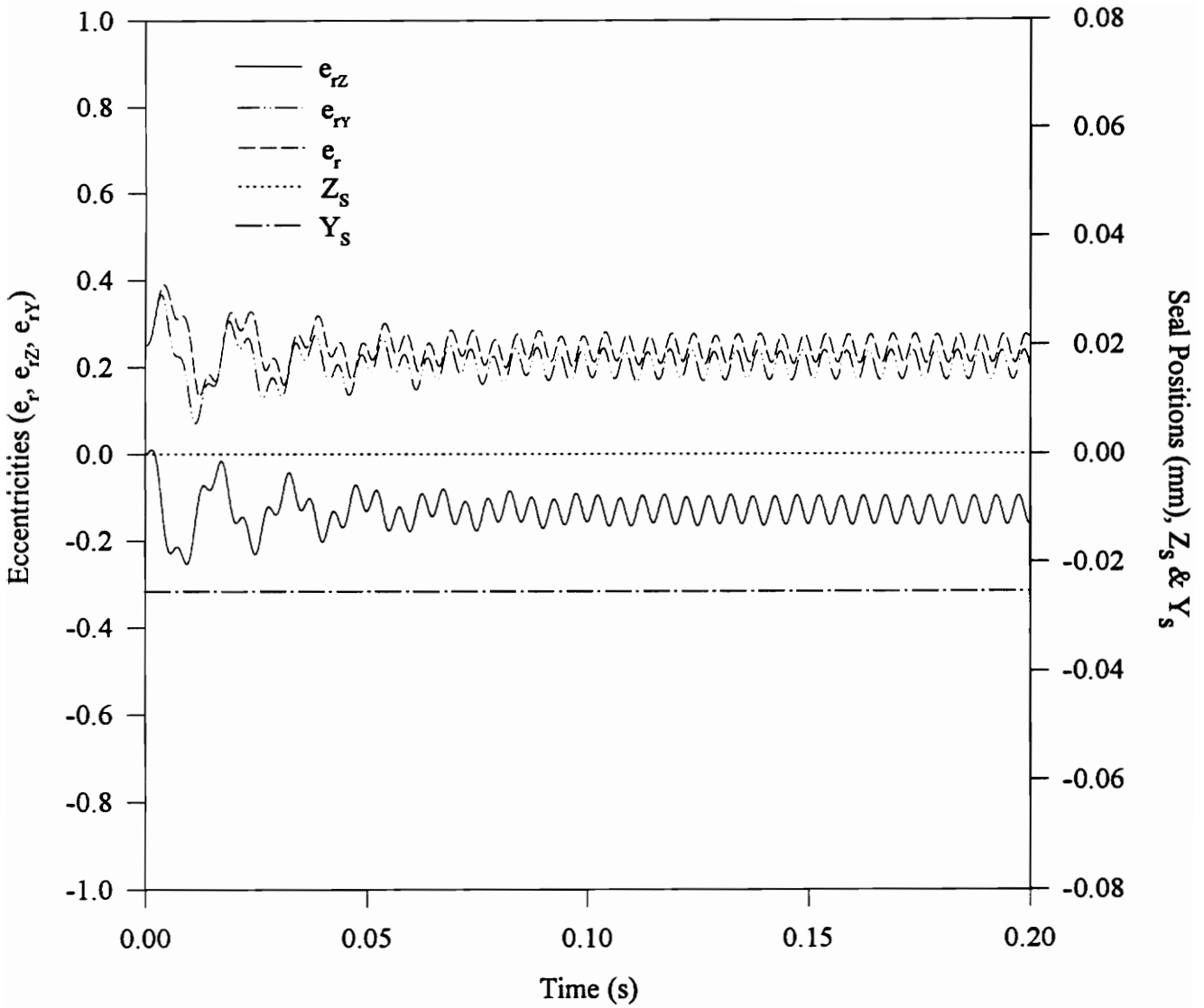


**Figure 90. Plots of Eccentricities and Absolute Seal Positions vs. Time for a Seal with Circumferential Groove**

**Operating Speed = 200 Hz (12000 RPM); Frictional Force = 889.6 N;  
Groove Depth = 0.762 mm**

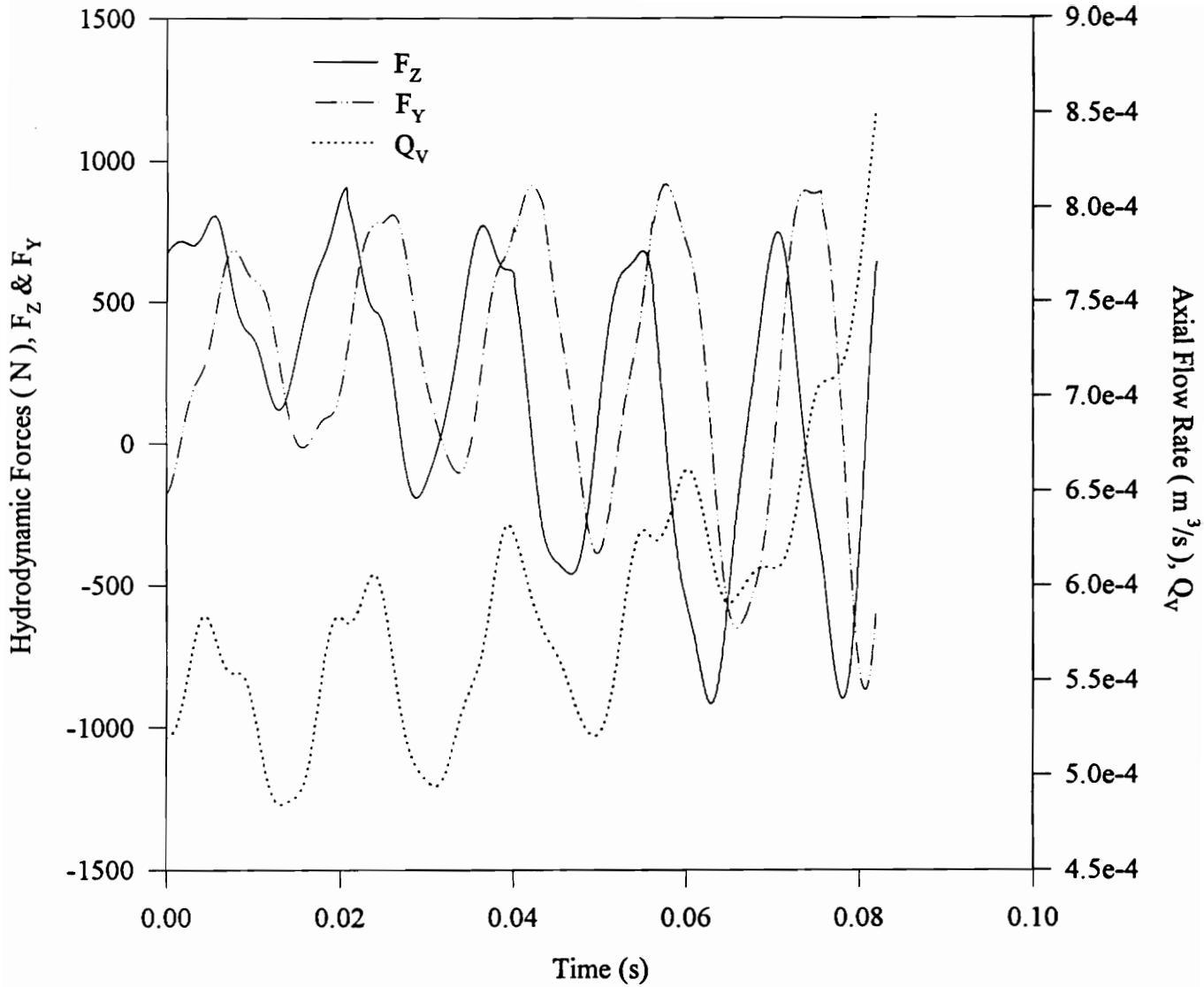


**Figure 91. Plots of Hydrodynamic Forces and Axial Flow Rate vs. Time for a Seal with Circumferential Groove**

**Operating Speed = 200 Hz (12000 RPM); Frictional Force = 889.6 N;  
Groove Depth = 0.381 mm**

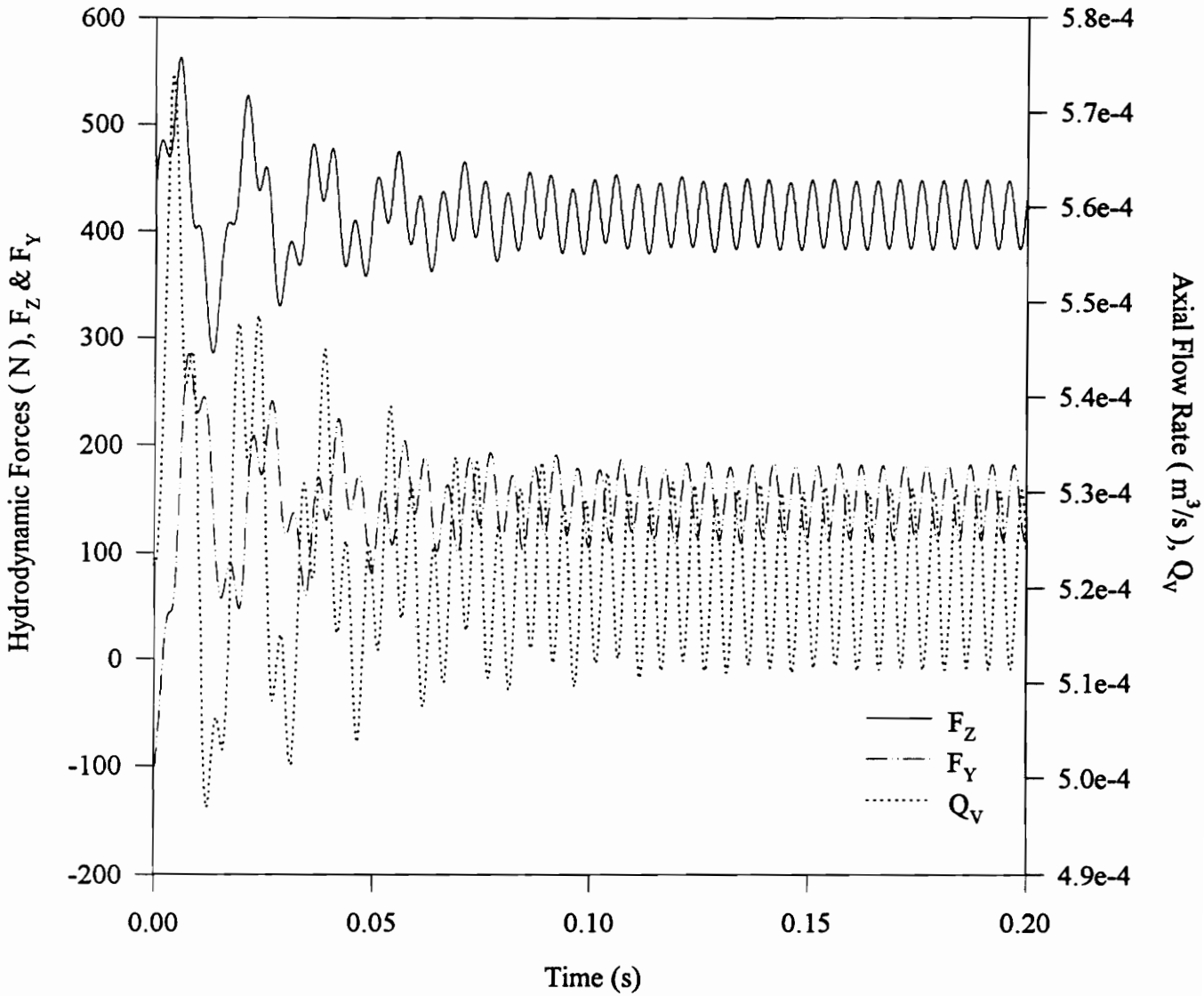
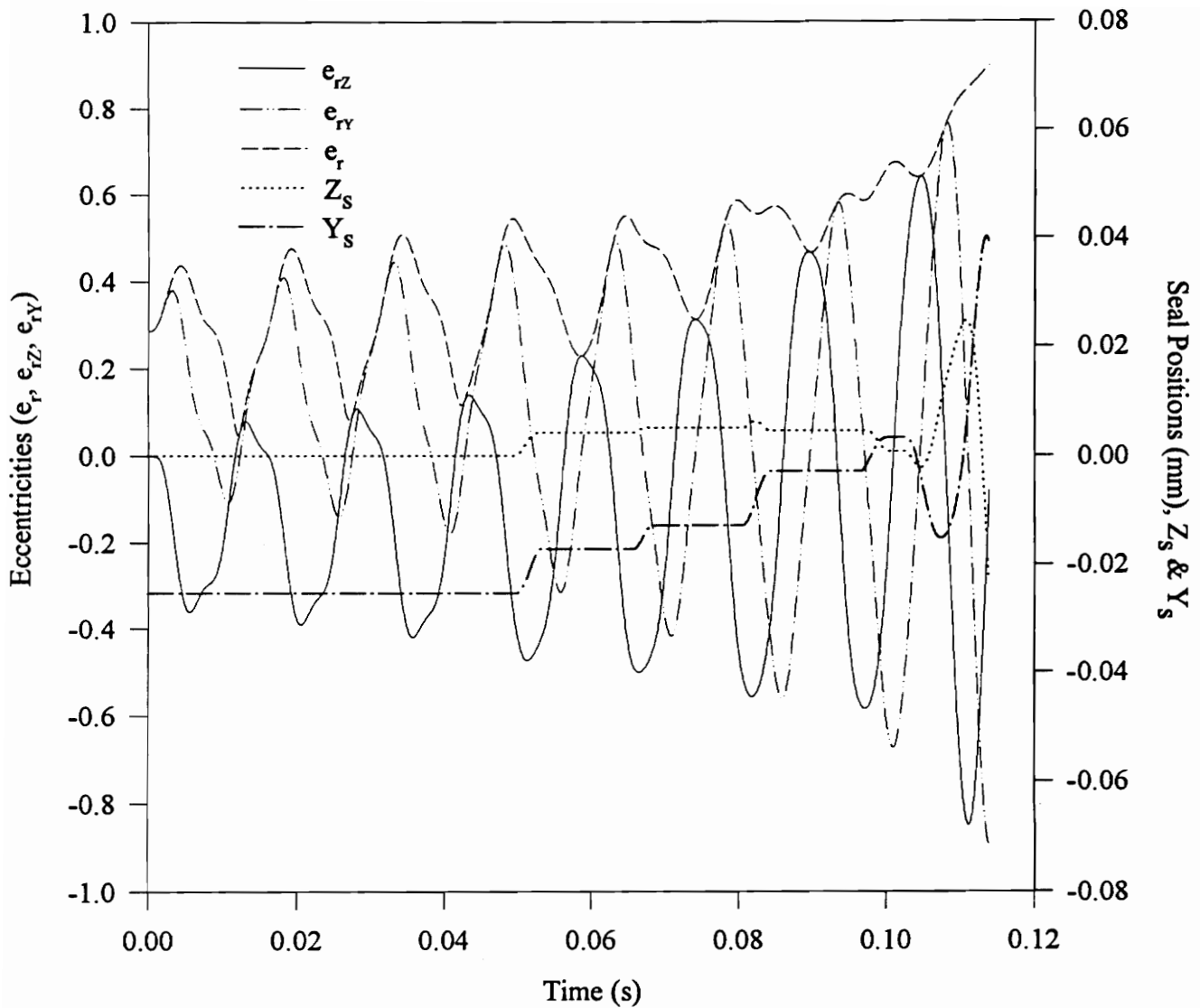


**Figure 92. Plots of Hydrodynamic Forces and Axial Flow Rate vs. Time for a Seal with Circumferential Groove**

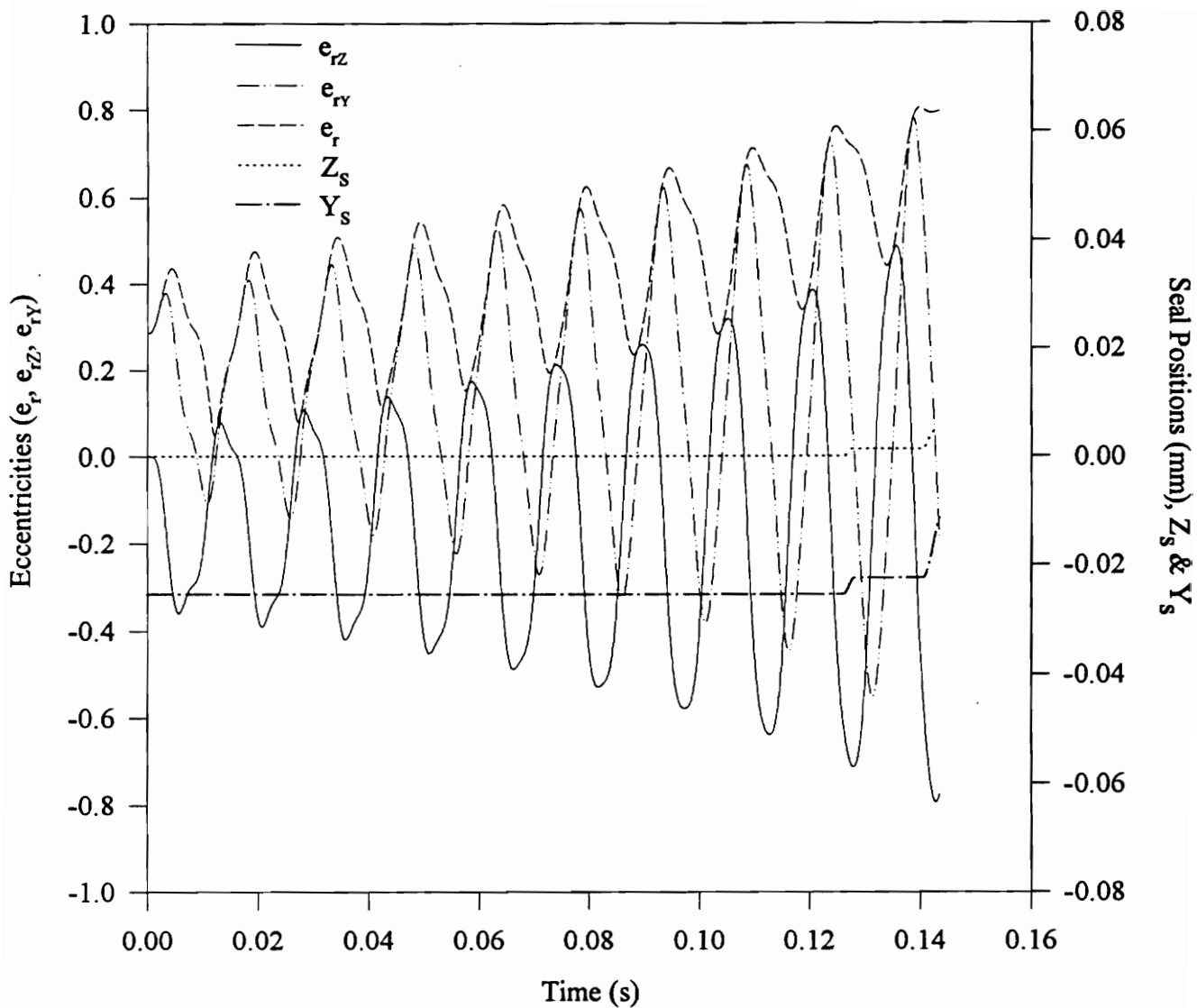
**Operating Speed = 200 Hz (12000 RPM); Frictional Force = 889.6 N;  
Groove Depth = 0.762 mm**

Figure 93 shows the plots of eccentricities and seal positions as a function of time for a grooved seal with a taper. The groove depth used is 0.381 mm and the exit clearance for the taper is 0.0889 mm. The frictional force in this case is 889.6 N. This taper increases the time taken for the eccentricity,  $e_r$ , to become 0.85 when compared to the seal without taper (see Fig. 89) but does not stabilize the system. Also, increasing the frictional force from 889.6 N in the above case to 1334.4 N just further increases the time for which the seal remains locked and the eccentricity,  $e_r$ , to become approximately 0.85 as shown in Fig. 94, but does not still stabilize the system. Figures 95 and 96 show the plots of hydrodynamic forces and maximum temperatures for the above two cases. Since both the cases are unstable the forces diverge and the maximum temperatures increase with time. In the case with the frictional force of 889.6 N, the maximum temperature becomes as high as 170 °C which is slightly above the melting point of babbitt.

Figure 97 shows the variation of the eccentricities and the seal positions as a function of time for the same seal with exit clearance reduced to 0.0635 mm. The frictional force is 889.6 N. In this case, the seal ring essentially remains locked through out the transient analysis and the eccentricities oscillate with a large constant amplitude indicating the rotor whirls in a limit cycle. Figure 98 shows the orbits traced by the rotor and the seal in this case. The seal essentially remains locked at the endpoint marked with a star and the rotor traces the same orbit in a cyclic manner. The combination of the taper and the circumferential groove will stabilize the rotor for operation at 200 Hz (12000 RPM) more than the axial taper alone.



**Figure 93. Plots of Eccentricities and Absolute Seal Positions vs. Time for a Seal with Circumferential Groove and Taper**  
**Operating Speed = 200 Hz (12000 RPM); Frictional Force = 889.6 N;**  
**Groove Depth = 0.381 mm; Exit Clearance = 0.0889 mm**



**Figure 94. Plots of Eccentricities and Absolute Seal Positions vs. Time for a Seal with Circumferential Groove and Taper**

**Operating Speed = 200 Hz (12000 RPM); Frictional Force = 1334.4 N;  
Groove Depth = 0.381 mm; Exit Clearance = 0.0889 mm**

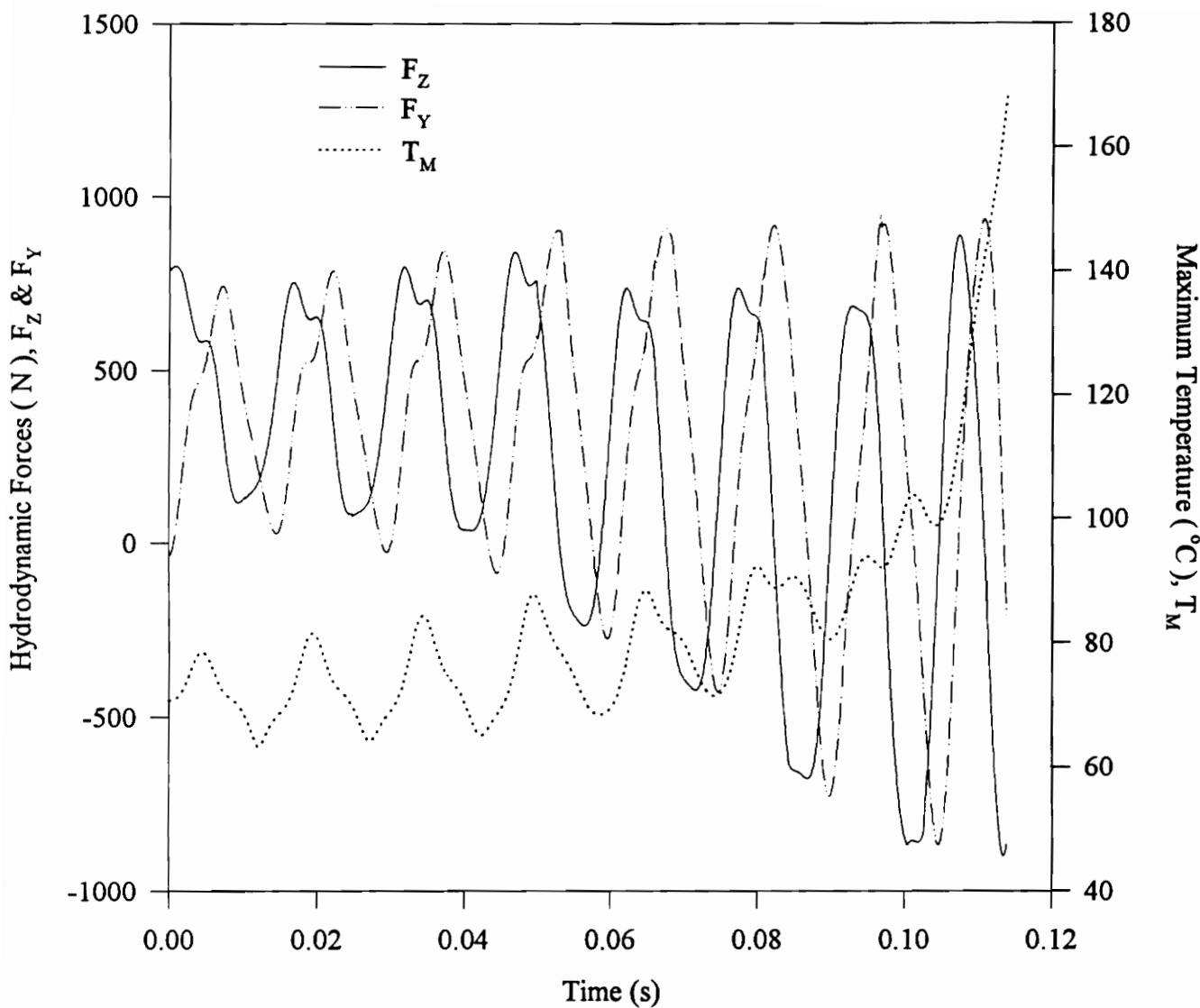


**Figure 95. Plots of Hydrodynamic Forces and Maximum Temperature vs. Time for a Seal with Circumferential Groove and Taper**

**Operating Speed = 200 Hz (12000 RPM); Frictional Force = 889.6 N;  
Groove Depth = 0.381 mm; Exit Clearance = 0.0889 mm**

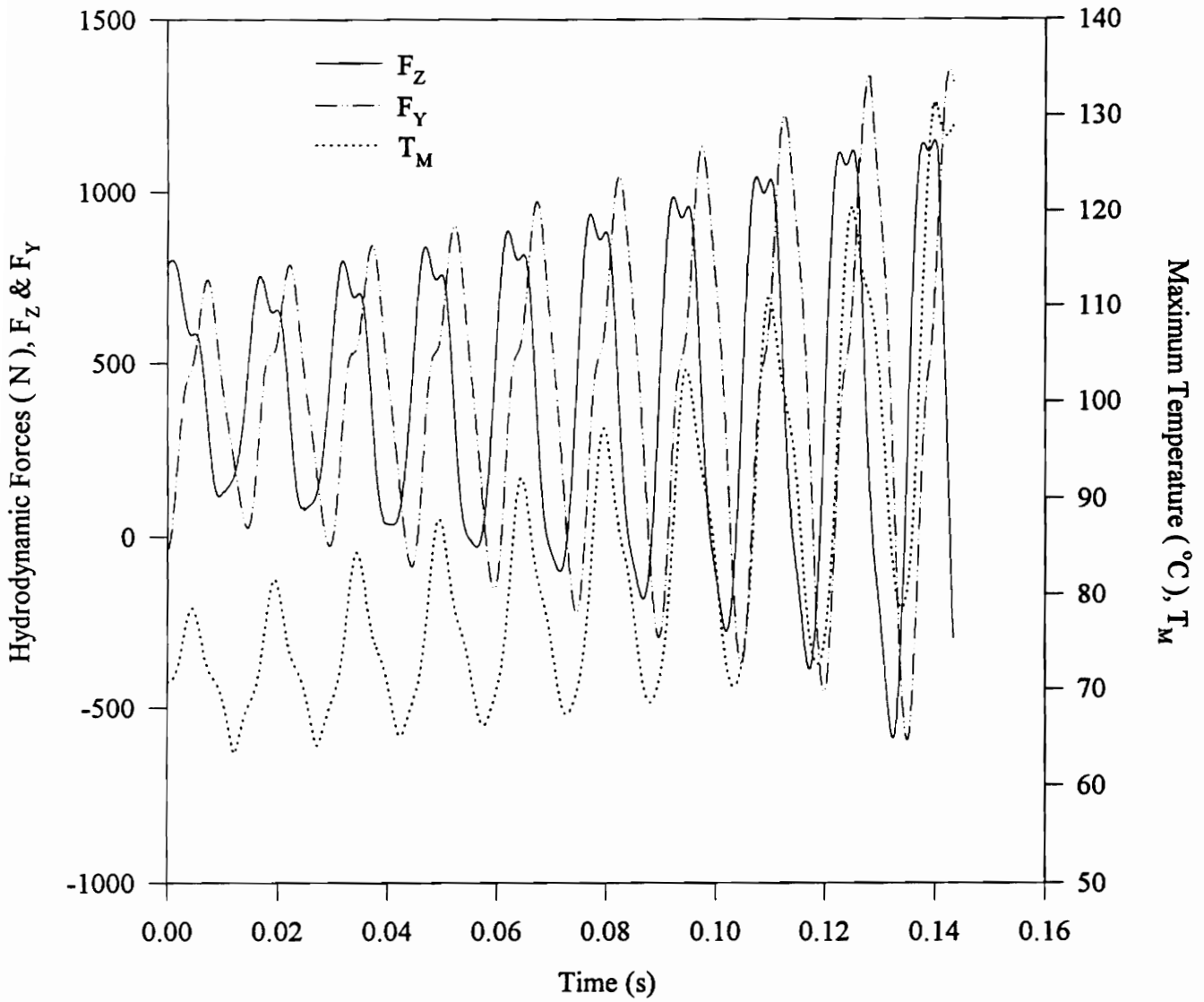


**Figure 96. Plots of Hydrodynamic Forces and Maximum Temperature vs. Time for a Seal with Circumferential Groove and Taper**

**Operating Speed = 200 Hz (12000 RPM); Frictional Force = 1334.4 N;  
Groove Depth = 0.381 mm; Exit Clearance = 0.0889 mm**

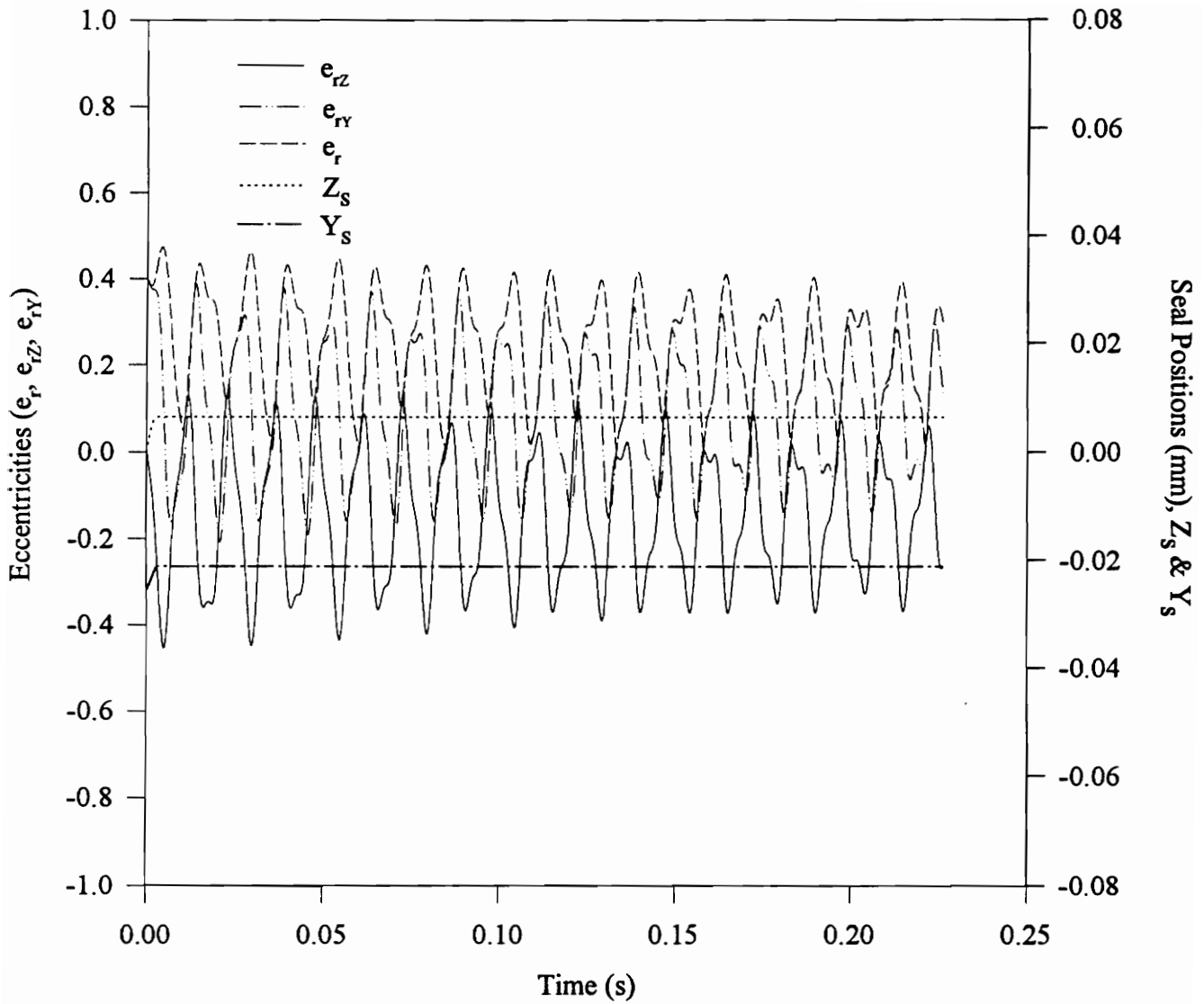
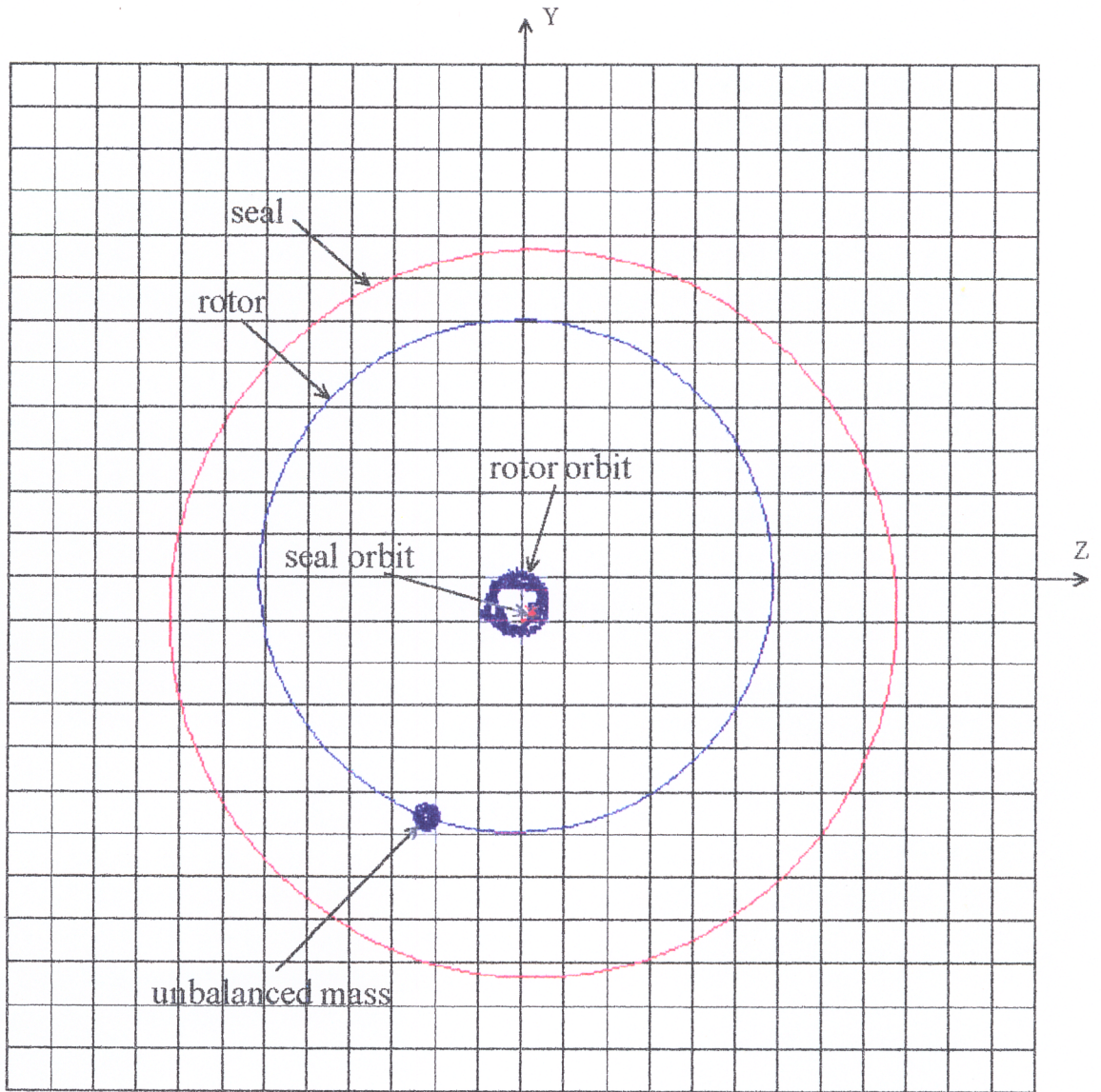


**Figure 97. Plots of Eccentricities and Absolute Seal Positions vs. Time for a Seal with Circumferential Groove and Taper**

**Operating Speed = 200 Hz (12000 RPM); Frictional Force = 889.6 N;  
Groove Depth = 0.381 mm; Exit Clearance = 0.0635 mm**



Seal is locked

**Figure 98. Transient Response of the Tapered and Circumferentially Grooved Seal and the Rotor**

**Operating Speed = 200 Hz (12000 RPM); Frictional Force = 889.6 N;  
Groove Depth = 0.381 mm; Exit Clearance = 0.0635 mm**

## Chapter 8

### Influence of Shaft Misalignment on the Seal Characteristics

This chapter presents the modification required in the governing equations to handle seals including shaft misalignment. Results showing the influence of shaft misalignment on various design parameters, obtained from linear stability analysis, will then be discussed.

#### 8.1 Shaft Misalignment

The shaft misalignment can take place in both the vertical and horizontal planes. Figure 99 shows the geometrical description of the shaft misalignment in X-Y(vertical) and X-Z(horizontal) planes. In case of shaft misalignment, attitude angle,  $\alpha$ , and eccentricity,  $e_d$ , are functions of  $x$ . Therefore, the expression for fluid film thickness changes as a function of axial position along the seal length. From Eq. [2],  $h$  is given by

$$h = C + e_d \cos\left(\frac{y}{R} + \alpha\right)$$

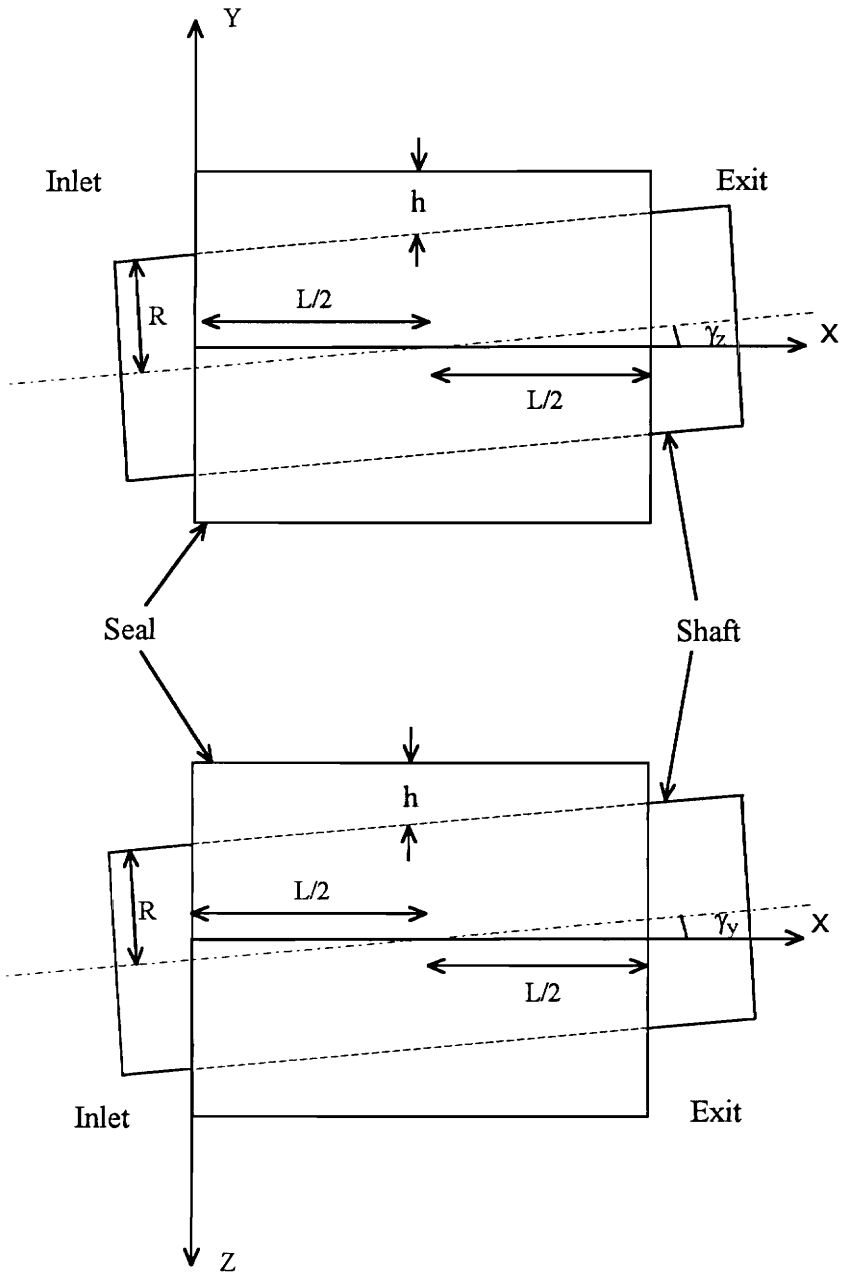


**Figure 99. Misalignment of Shaft in X-Y and X-Z Planes**

where  $e_d$  and  $\alpha$  are given by Eq. [3],

$$e_d = \sqrt{e_{dZ}^2 + e_{dY}^2} \quad \text{and} \quad \alpha = \tan^{-1}\left(\frac{e_{dZ}}{e_{dY}}\right)$$

$e_{dZ}$  and  $e_{dY}$  are eccentricities in Z and Y directions respectively, shown in Fig. 4. They are constants for aligned seals. For the seals with shaft misalignment  $e_{dZ}$  and  $e_{dY}$  can be written as

$$\begin{aligned} e_{dZ} &= e_{dZC} - (x - L/2) \tan(\gamma_Y) \\ e_{dY} &= e_{dYC} + (x - L/2) \tan(\gamma_Z) \end{aligned} \quad [72]$$

where  $e_{dZC}$  and  $e_{dYC}$  are the eccentricities in Y and Z directions respectively at the center of the seal and  $\gamma_Z$  and  $\gamma_Y$  are the shaft misalignment angles defined in Fig. 99.

## 8.2 Linear Stability Analysis Results

The specifications given in Table 2 are used for the results presented in this section. Figures 100 and 101 show the temperature and pressure distributions for seals with shaft misalignment angles  $\gamma_Z = 0.102^\circ$  ( $\gamma_Y = 0.0^\circ$ ) and  $\gamma_Y = -0.102^\circ$  ( $\gamma_Z = 0.0^\circ$ ) respectively. The operating speed used is 166.67 Hz (10000 RPM) and operating eccentricity,  $e_{rYC}$  (ratio of  $e_{dYC}$  and clearance), of the seal is 0.4. The shaft misalignment angle of  $0.102^\circ$  changes the eccentricity of the seal (in the plane of misalignment) at each end by 0.2. In the case of the seal with shaft misalignment angle,  $\gamma_Z = 0.102^\circ$ , the eccentricity in the Y-direction changes along the axis of the seal. It

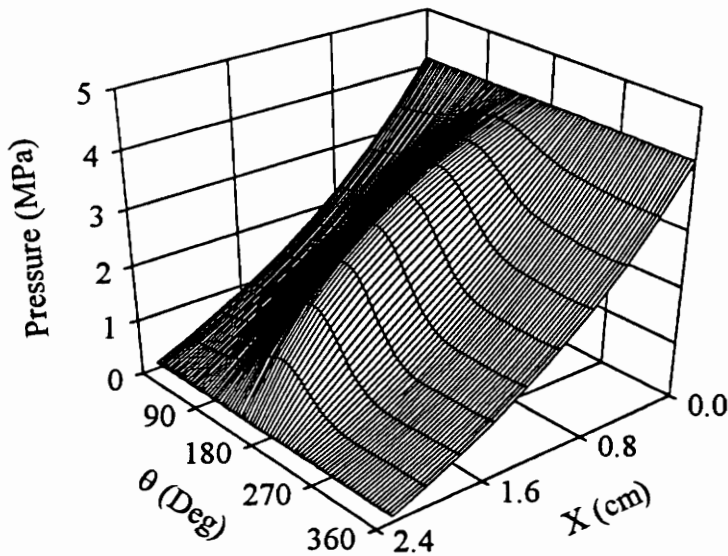
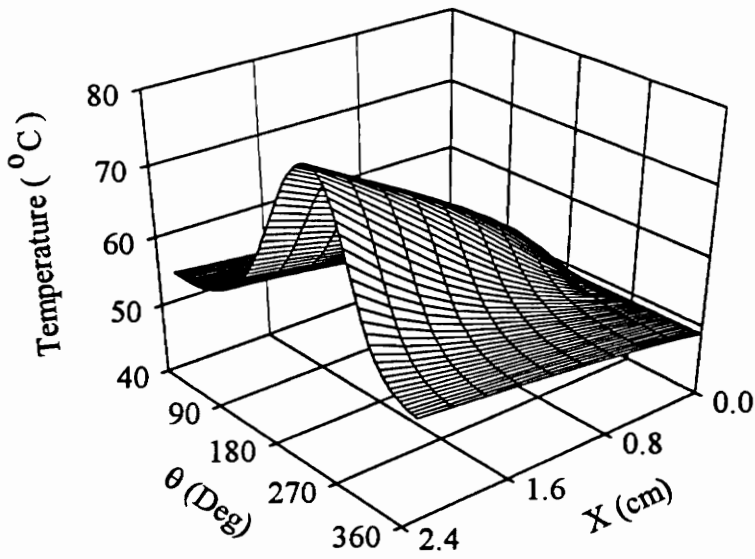


**Figure 100. Temperature and Pressure Distributions in Seal with Shaft Misalignment**

$\gamma_z = 0.102$  Degrees

Operating Speed = 166.67 Hz (10000 RPM)

Operating Eccentricity ( $e_{rYC}$ ) = 0.4

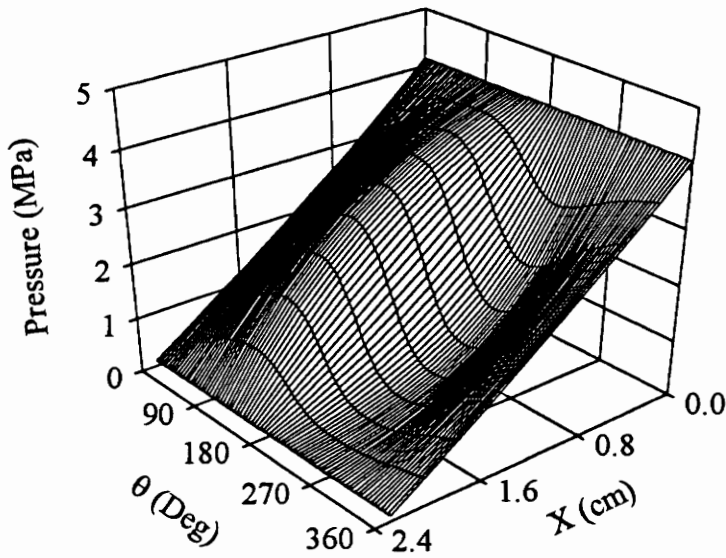
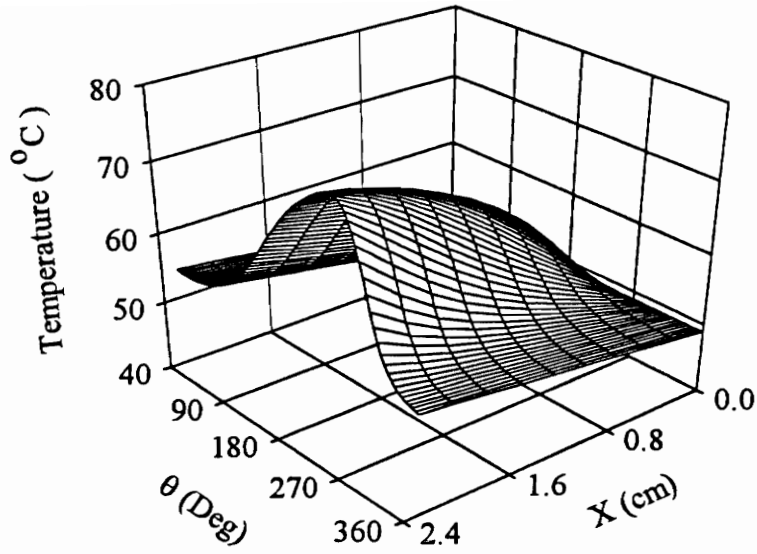


**Figure 101. Temperature and Pressure Distributions in a Seal with Shaft Misalignment**

$\gamma_Y = -0.102$  Degrees

Operating Speed = 166.67 Hz (10000 RPM)

Operating Eccentricity ( $e_{rYC}$ ) = 0.4

becomes 0.6 and 0.2 at the exit and the inlet ends respectively. The eccentricity in the Z direction remains zero along the axis of the seal. Therefore, the temperature and pressure distributions in Fig. 100 look similar to that in Fig. 18 in which the eccentricity is only in the Y-direction. But in the other case, where the misalignment angle  $\gamma_Y = -0.102^\circ$  the eccentricity changes in the Z direction along the axis and has a constant value of 0.4 in the Y-direction. The eccentricity in the Z-direction changes from -0.2 to 0.2 from the inlet to the exit end of the seal. This changes the angular location of the minimum fluid film thickness along the axis of the seal which results in shifting the peak pressure away from  $\theta = 180^\circ$  as shown in figure 101. The maximum temperature in this case is less than that in the previous case (see Fig. 100) because the maximum eccentricity in this case is 0.447, whereas it was 0.6 in the previous case.

Figures 102-109 show the plots of various parameters versus the shaft misalignment angle,  $\gamma_Z$  for the same seal operating with the eccentricities,  $e_{rYC}$ , of 0.2 and 0.4. The misalignment angle,  $\gamma_Z = 0.102^\circ$  increases and decreases the value of the eccentricities in the Y-direction at the exit and inlet ends of the seal by 0.2. It can be seen from Figs. 102 and 103 that the direct stiffness coefficients increase/decrease with the increase/decrease of the misalignment angle,  $\gamma_Z$ . The cross-coupled stiffness and damping coefficients do not change significantly with the misalignment angle,  $\gamma_Z$ , as shown in Figs. 104 and 105. The increase in the direct stiffness coefficients with the shaft misalignment angle,  $\gamma_Z$ , increases the stability of the compressor rotor and the damped natural frequency as shown in Figs. 106 and 107.

The axial flow rate decreases with both the positive and negative shaft misalignment angle as shown in Fig. 108 because the misalignment decreases the projected clearance through the seal. The maximum temperature increases slightly with the shaft misalignment as shown in Fig. 109. This can be because the axial flow rate is

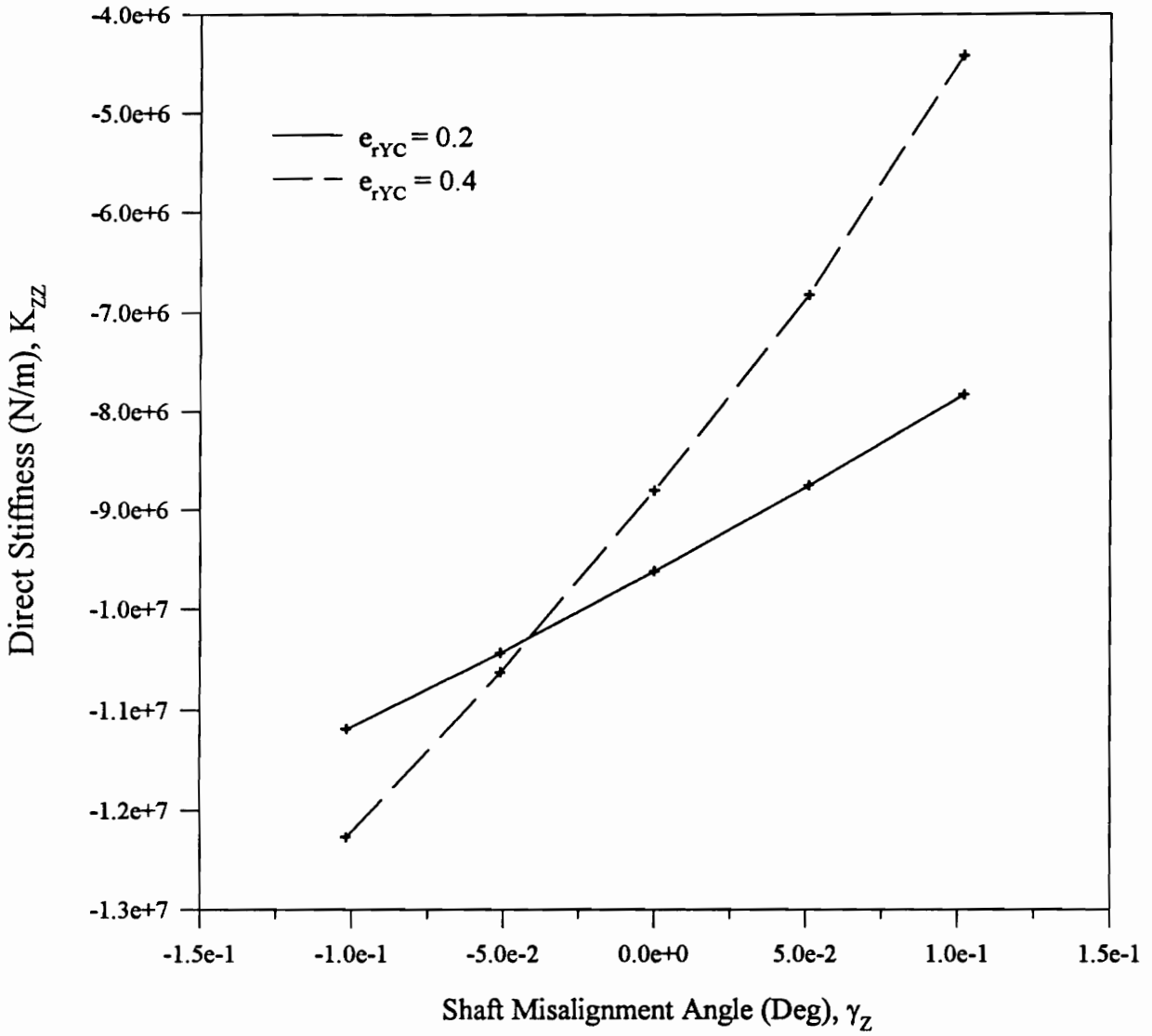


**Figure 102. Plot of Direct Stiffness vs. Shaft Misalignment Angle for Seals Operating at Different Eccentricity Ratios  
Operating Speed = 166.67 Hz (10000 RPM)**

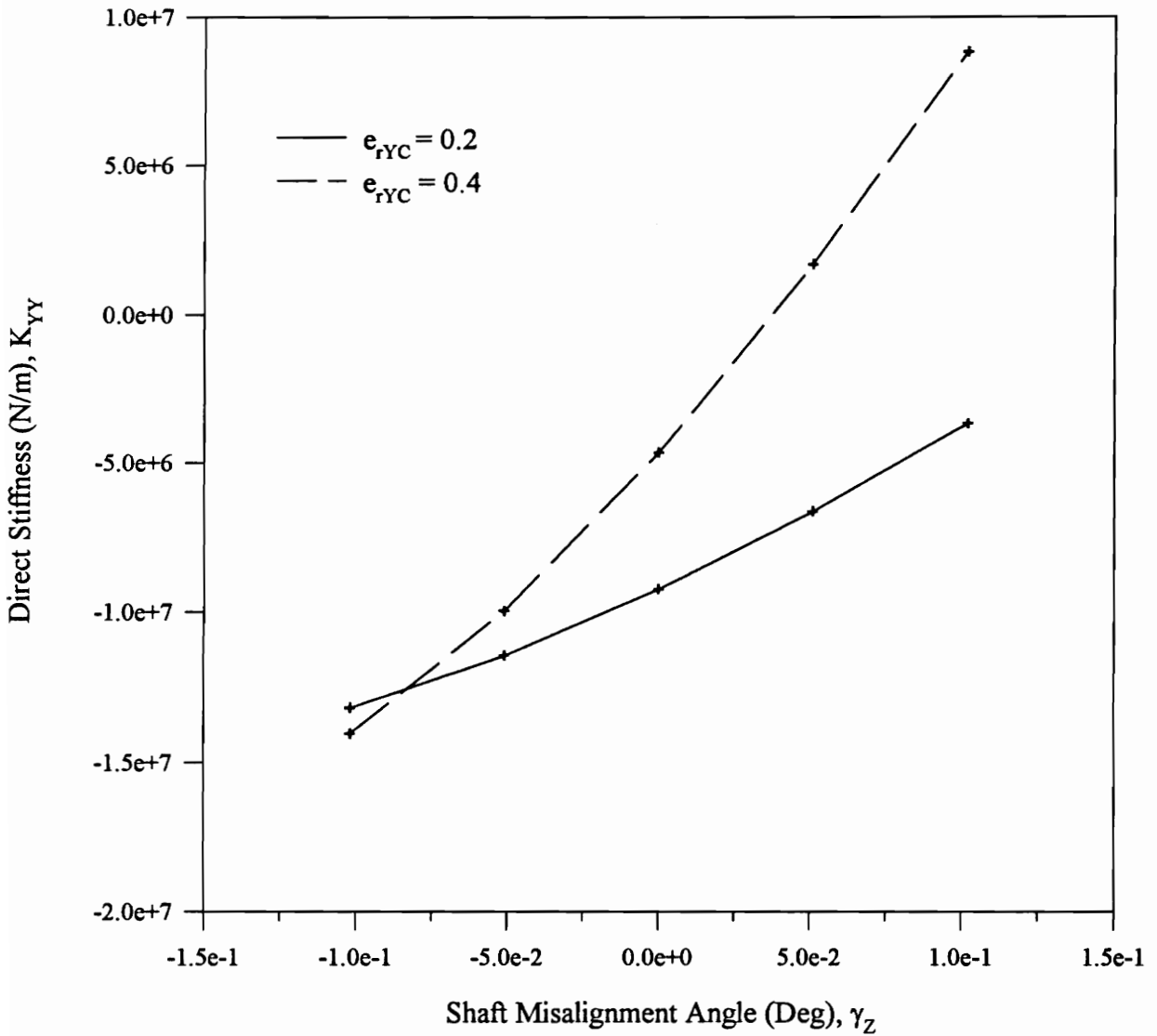


**Figure 103. Plot of Direct Stiffness vs. Shaft Misalignment Angle for Seals Operating at Different Eccentricity Ratios**  
**Operating Speed = 166.67 Hz (10000 RPM)**

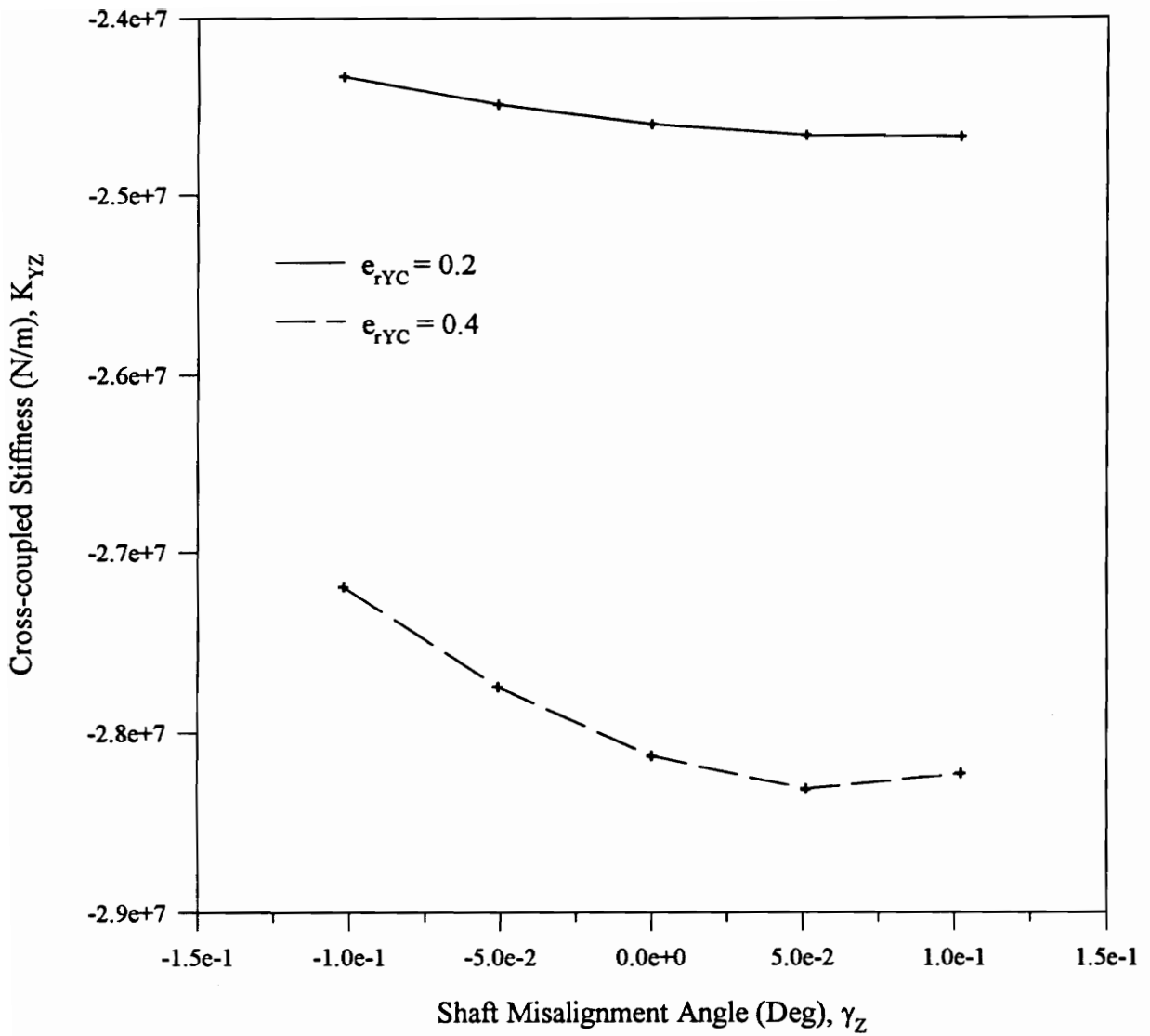


**Figure 104. Plot of Cross-coupled Stiffness vs. Shaft Misalignment Angle for Seals Operating at Different Eccentricity Ratios  
Operating Speed = 166.67 Hz (10000 RPM)**

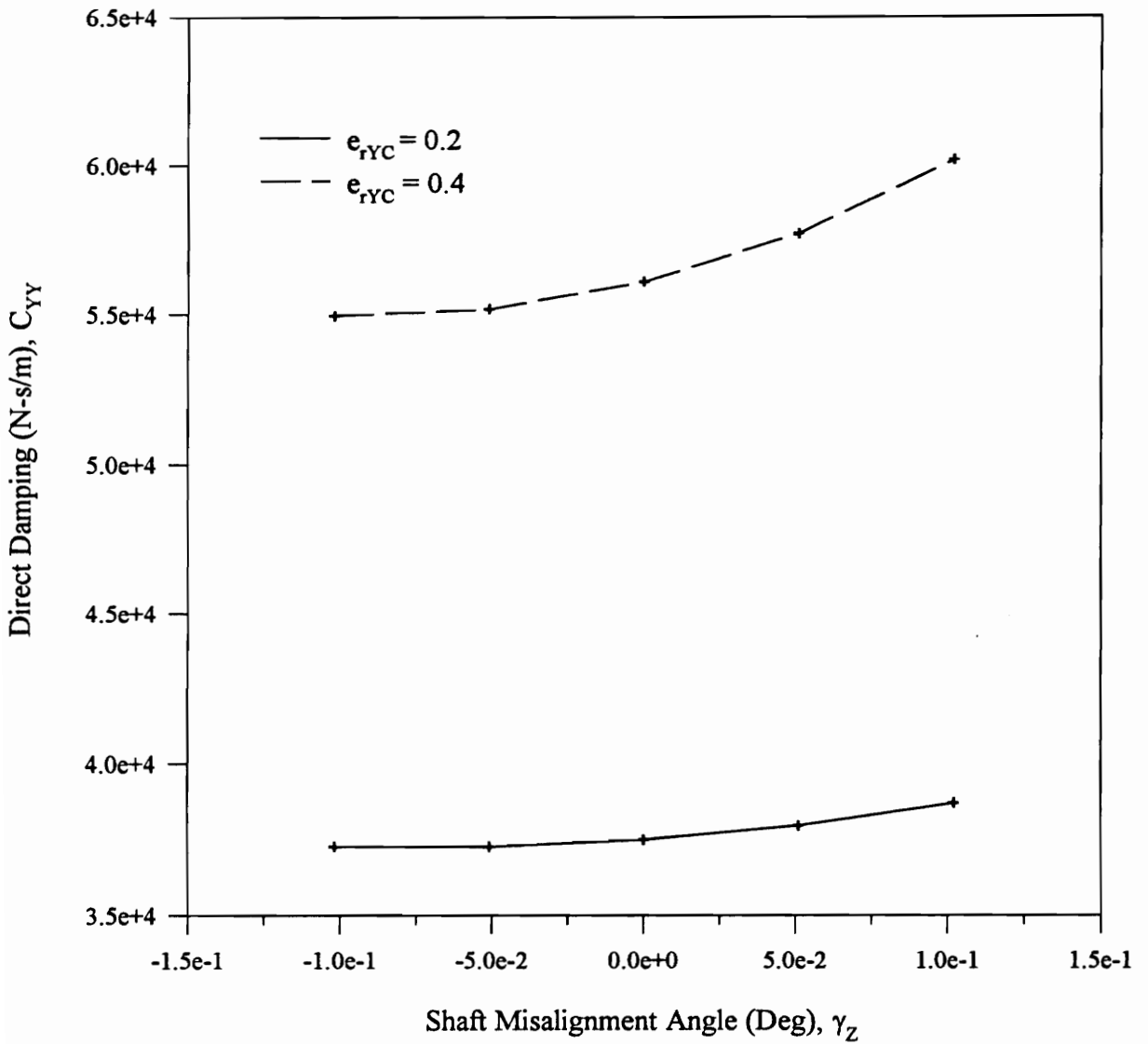


**Figure 105. Plot of Direct Damping vs. Shaft Misalignment Angle for Seals Operating at Different Eccentricity Ratios  
Operating Speed = 166.67 Hz (10000 RPM)**

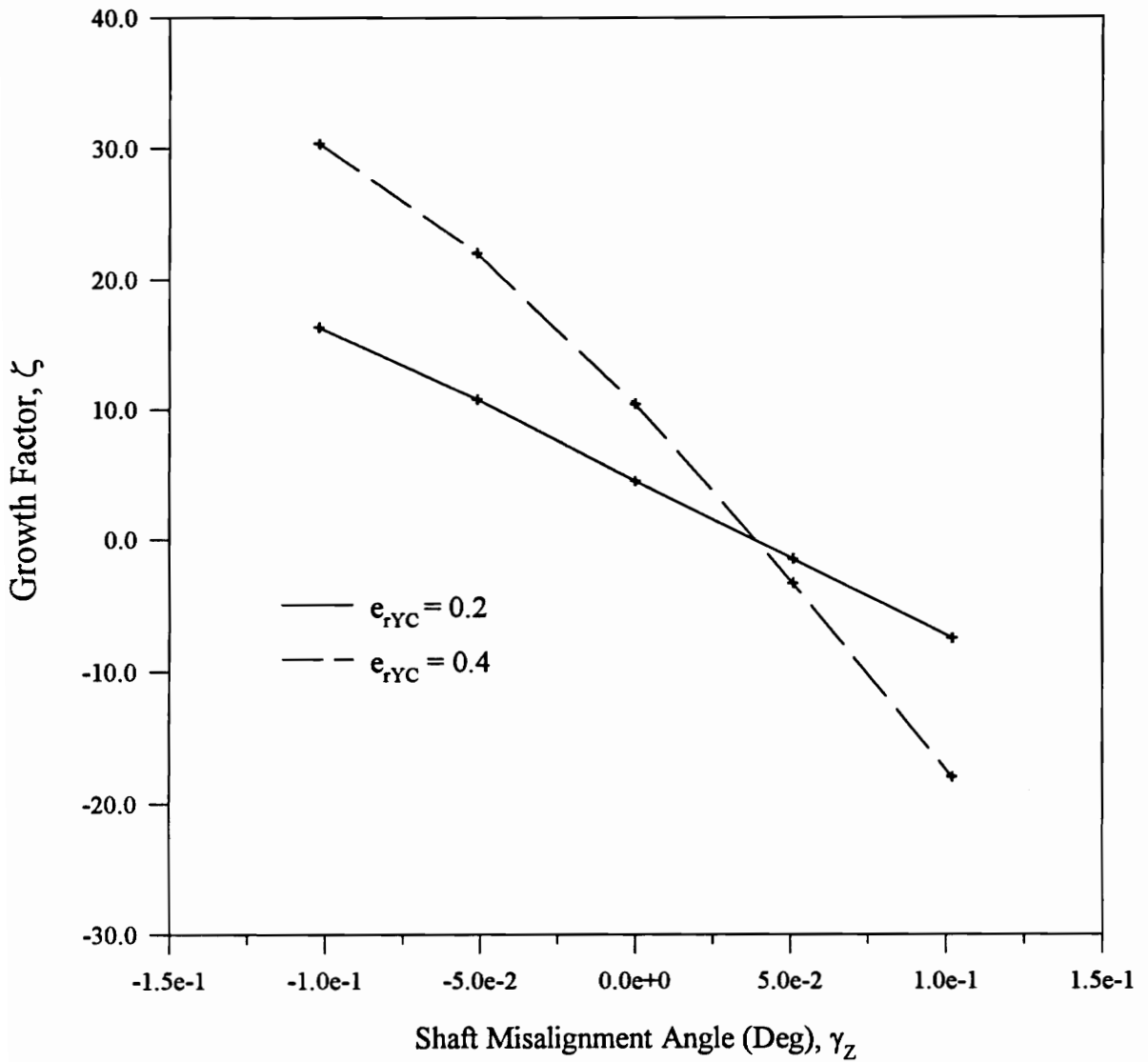


**Figure 106. Plot of Growth Factor vs. Shaft Misalignment Angle for Seals Operating at Different Eccentricity Ratios  
Operating Speed = 166.67 Hz (10000 RPM)**

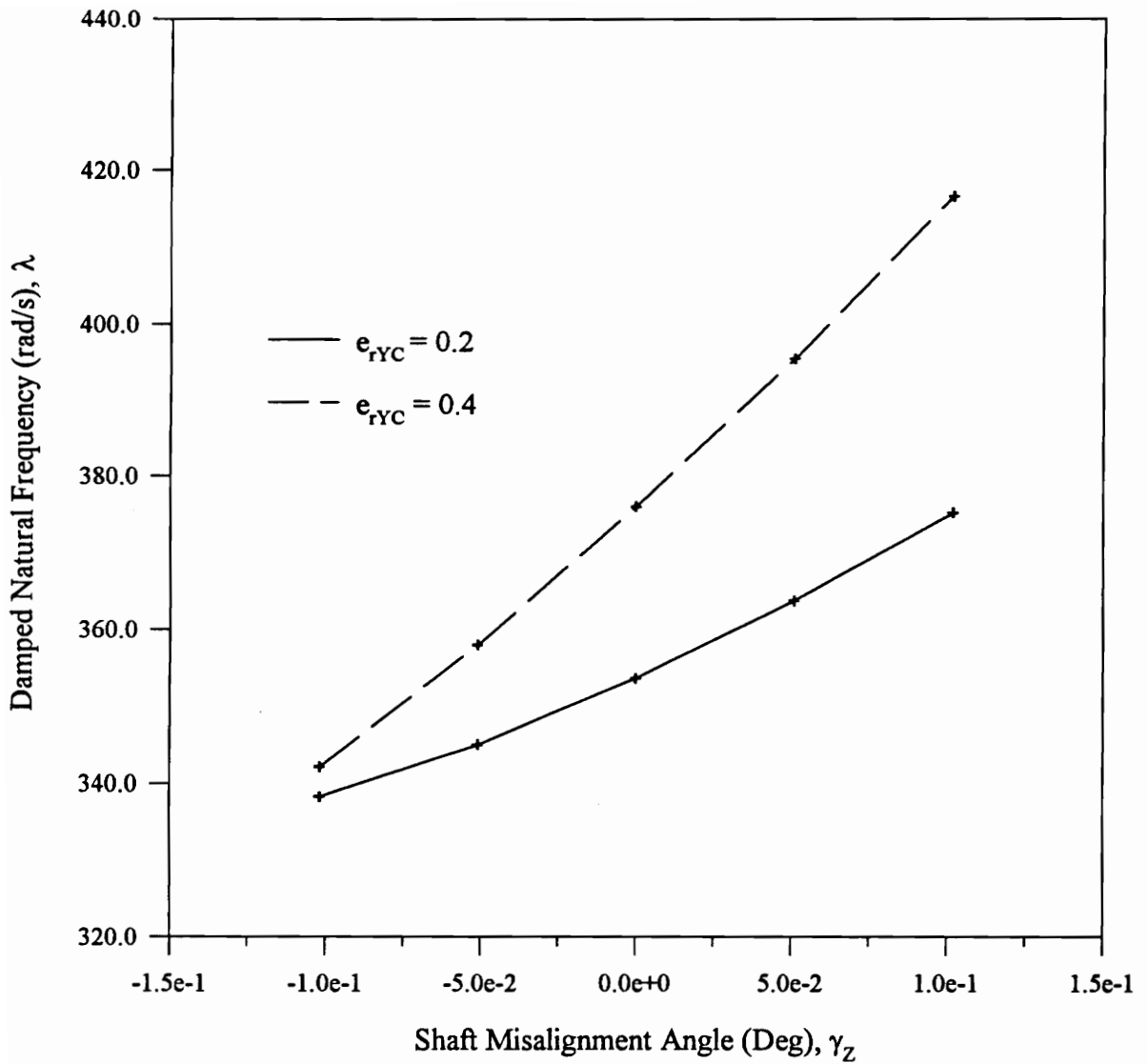


**Figure 107. Plot of Damped Natural Frequency vs. Shaft Misalignment Angle for Seals Operating at Different Eccentricity Ratios  
Operating Speed = 166.67 Hz (10000 RPM)**

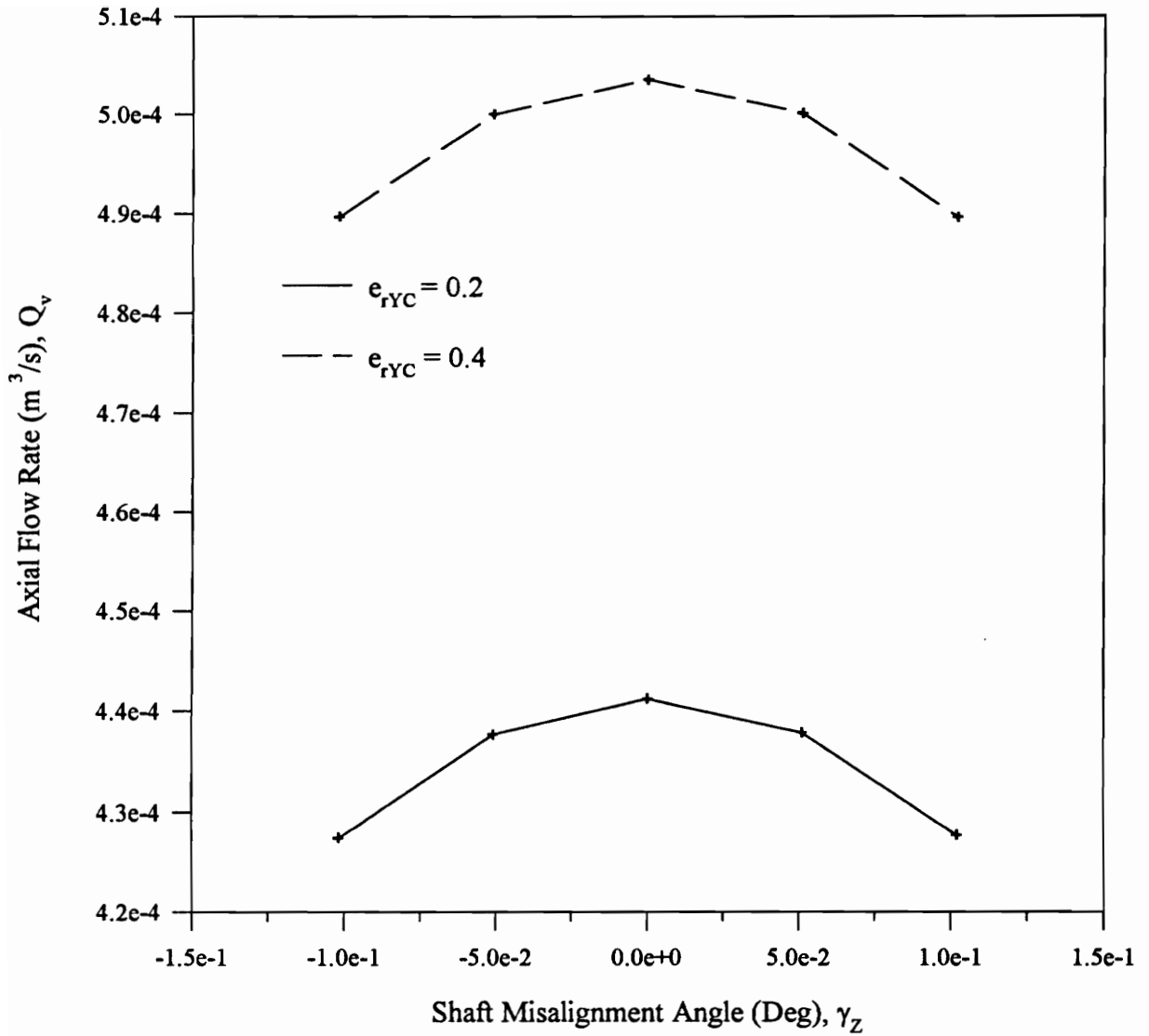


**Figure 108. Plot of Axial Flow Rate vs. Shaft Misalignment Angle for Seals Operating at Different Eccentricity Ratios  
Operating Speed = 166.67 Hz (10000 RPM)**

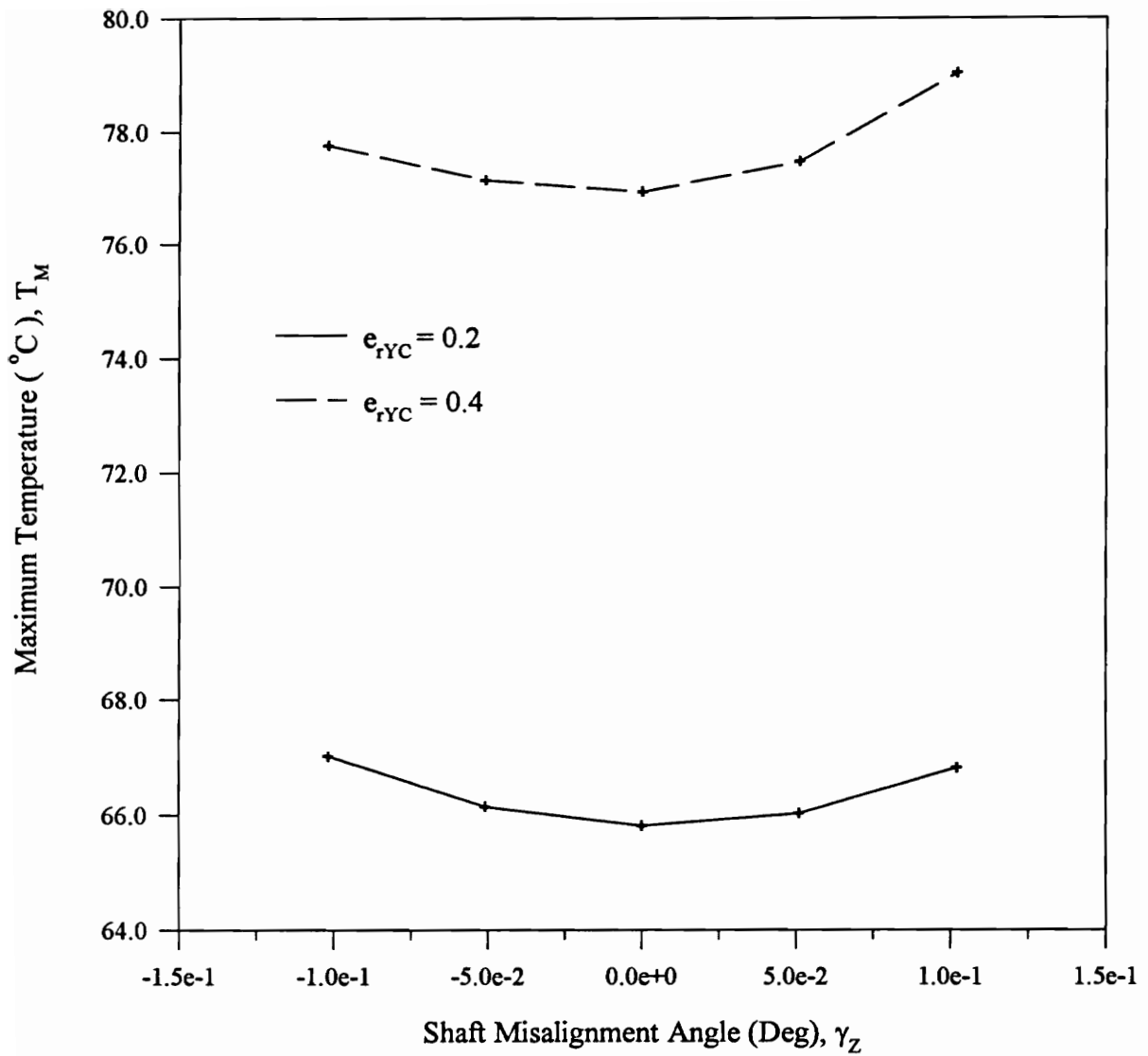


**Figure 109. Plot of Maximum Temperature vs. Shaft Misalignment Angle for Seals Operating at Different Eccentricity Ratios  
Operating Speed = 166.67 Hz (10000 RPM)**

decreased with the shaft misalignment and less heat is taken away by the fluid flowing out of the seal.

Figures 110-114 show the plots of various parameters versus the shaft misalignment angle,  $\gamma_Y$  for the above seal operating with the eccentricities,  $e_{rYC}$ , of 0.2 and 0.4. The misalignment angle,  $\gamma_Y = 0.102^\circ$  decreases and increases the values of the eccentricities in the Z-direction at the exit and inlet ends of the seal by 0.2. It can be seen from Figs. 110 to 112 that the influence of the shaft misalignment angle,  $\gamma_Y$ , is less on the direct stiffness and more on the cross-coupled stiffness as compared to the influence of the shaft misalignment angle,  $\gamma_Z$ . The direct damping coefficient does not change significantly with the shaft misalignment angle,  $\gamma_Y$ , as shown in Fig. 113. Figure 114 shows the plot of the growth factor. The growth factor decreases with the decrease in the shaft misalignment,  $\gamma_Y$ , indicating that the misalignment angle that increases the eccentricity at the exit improves the stability of the rotor.

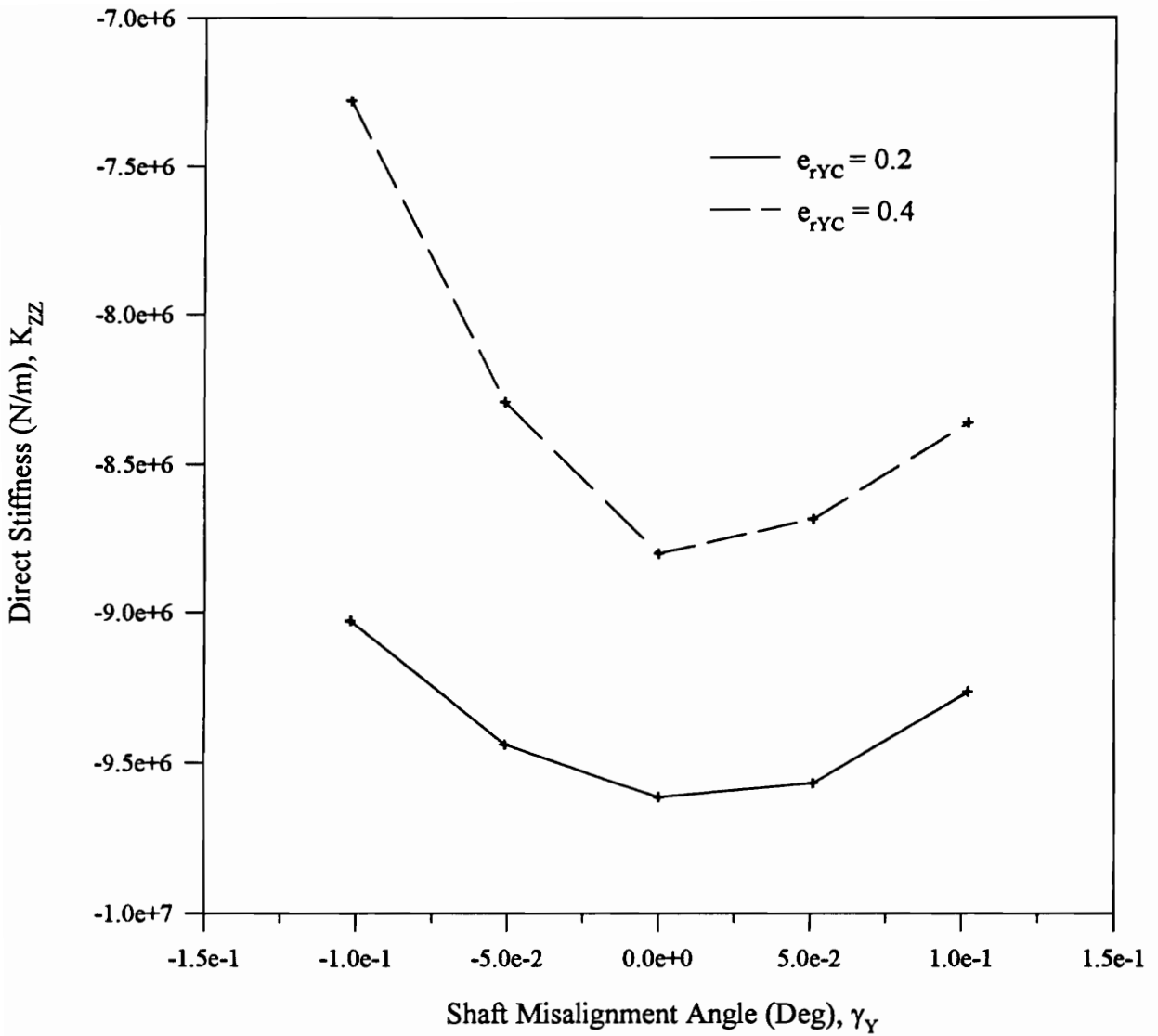


**Figure 110. Plot of Direct Stiffness vs. Shaft Misalignment Angle for Seals Operating at Different Eccentricity Ratios**  
**Operating Speed = 166.67 Hz (10000 RPM)**

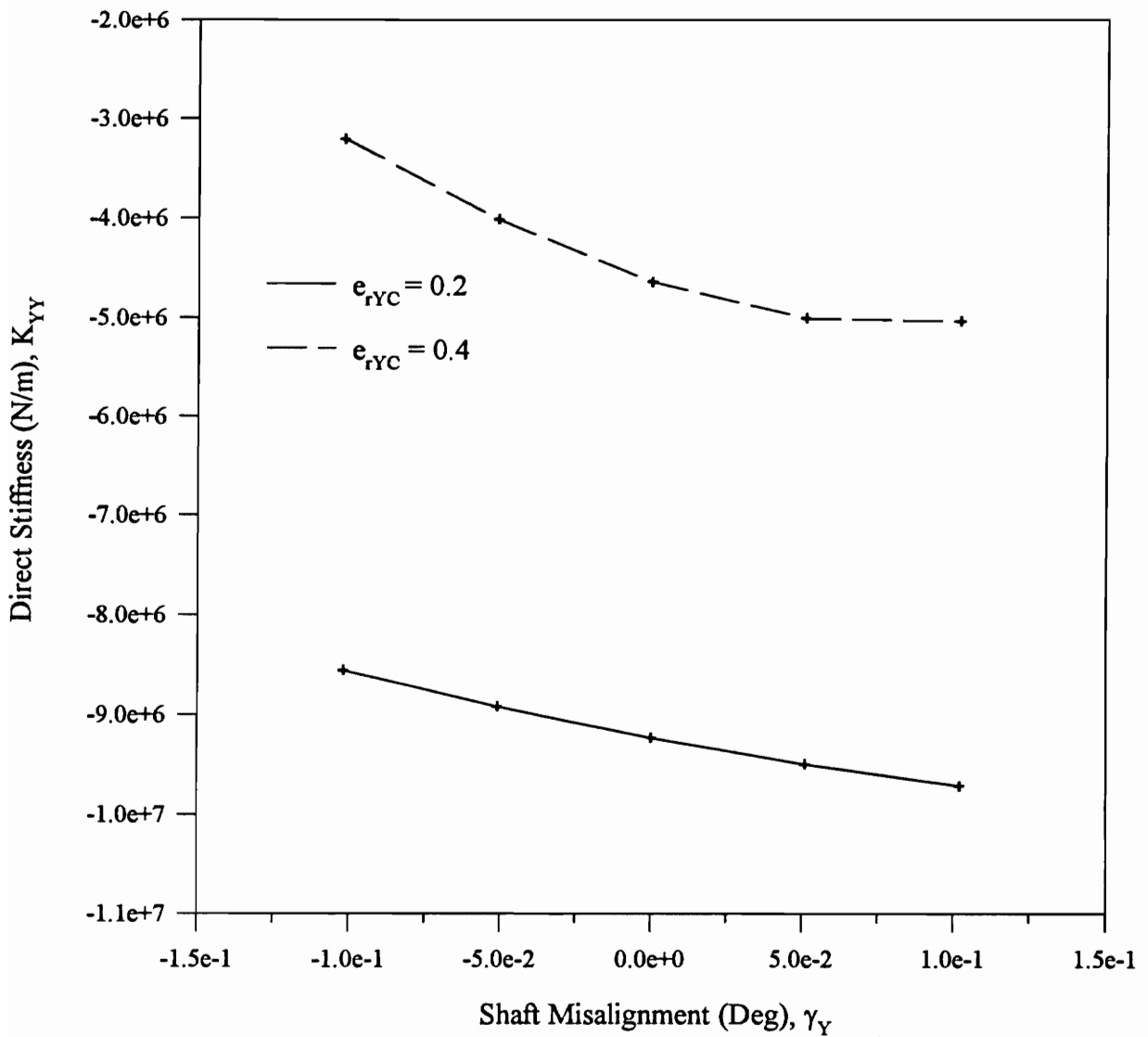


**Figure 111. Plot of Direct Stiffness vs. Shaft Misalignment Angle for Seals Operating at Different Eccentricity Ratios  
Operating Speed = 166.67 Hz (10000 RPM)**

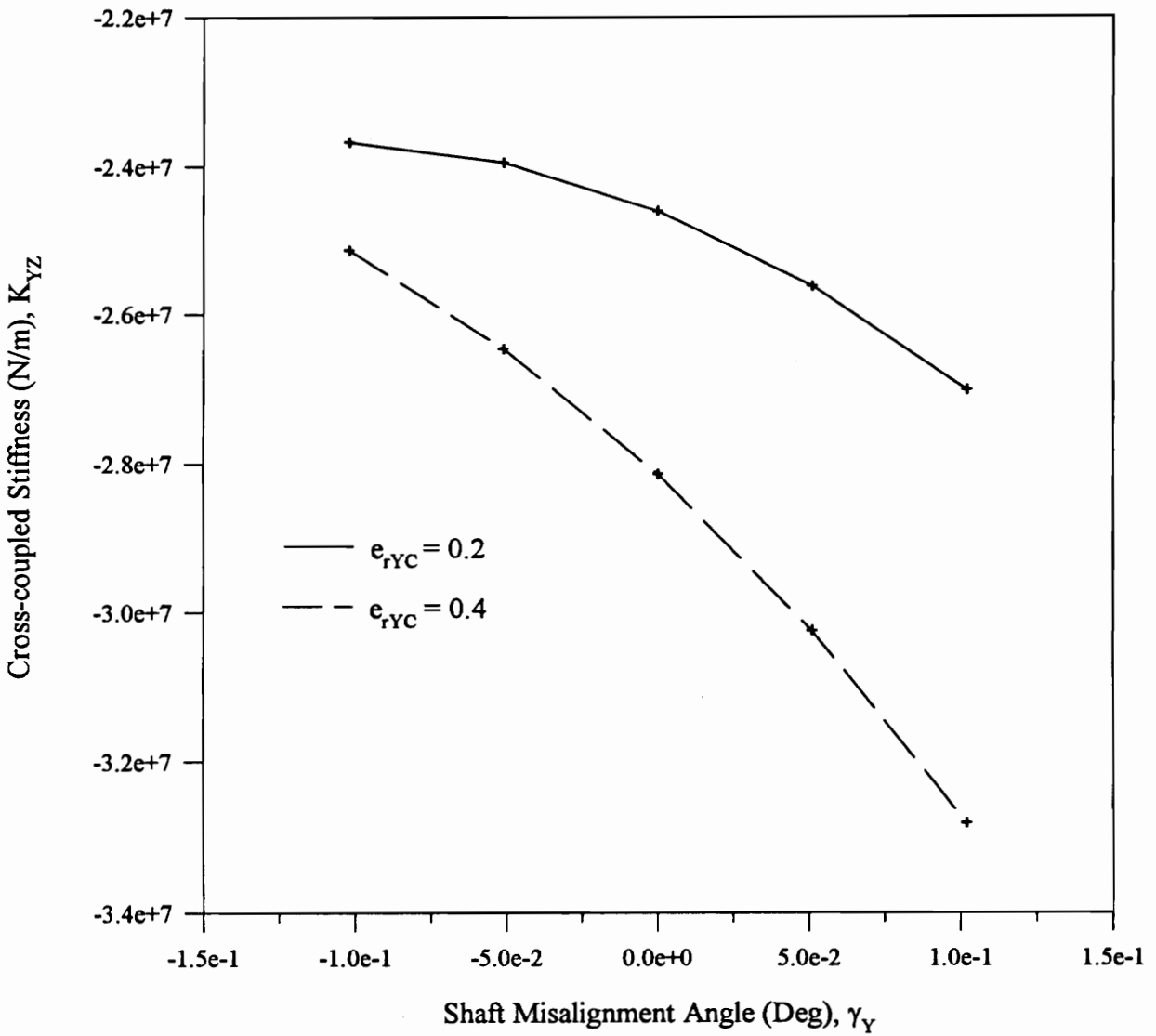


**Figure 112. Plot of Cross-coupled Stiffness vs. Shaft Misalignment Angle for Seals Operating at Different Eccentricity Ratios  
Operating Speed = 166.67 Hz (10000 RPM)**

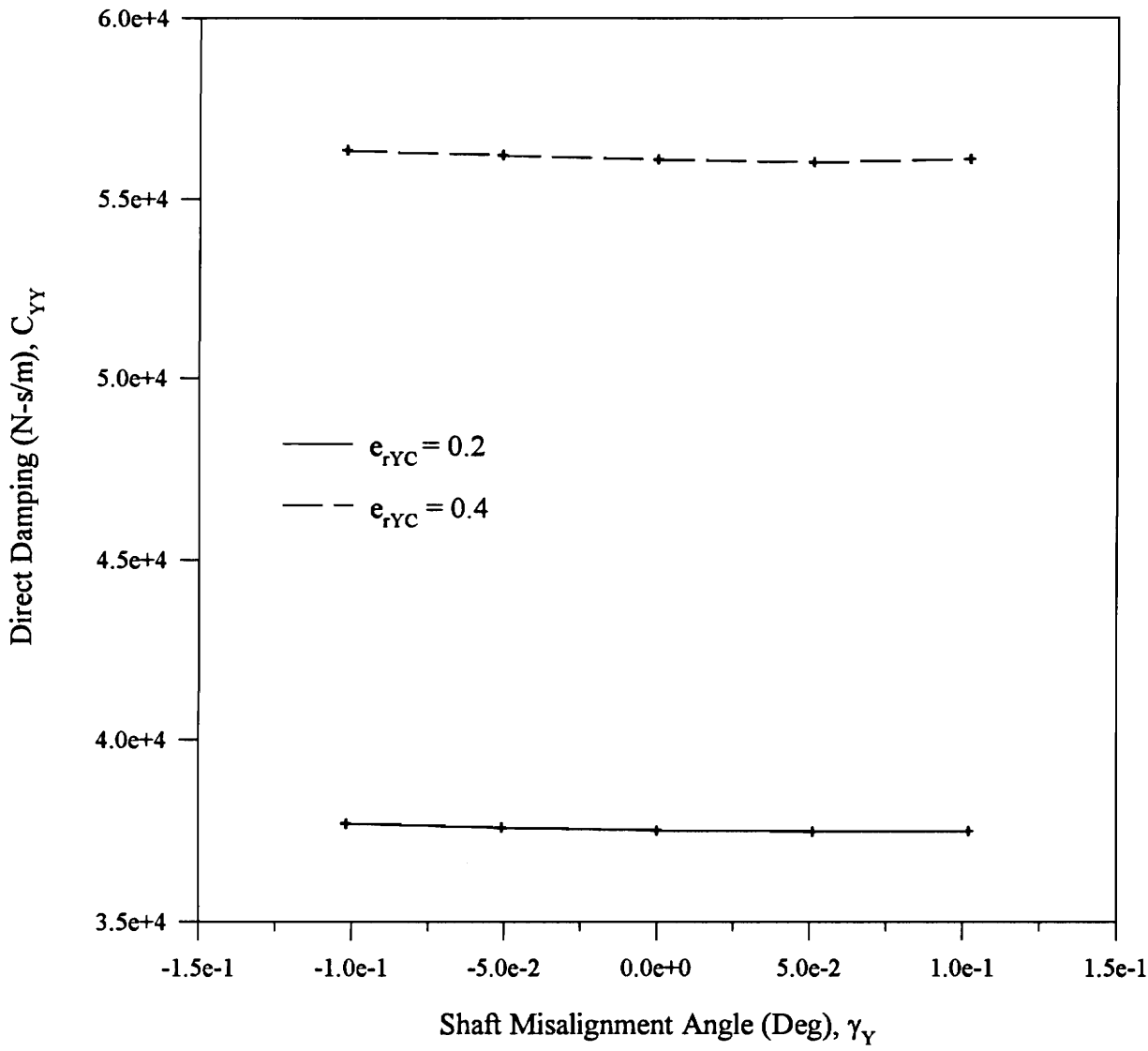


**Figure 113. Plot of Direct Damping vs. Shaft Misalignment Angle for Seals Operating at Different Eccentricity Ratios  
Operating Speed = 166.67 Hz (10000 RPM)**

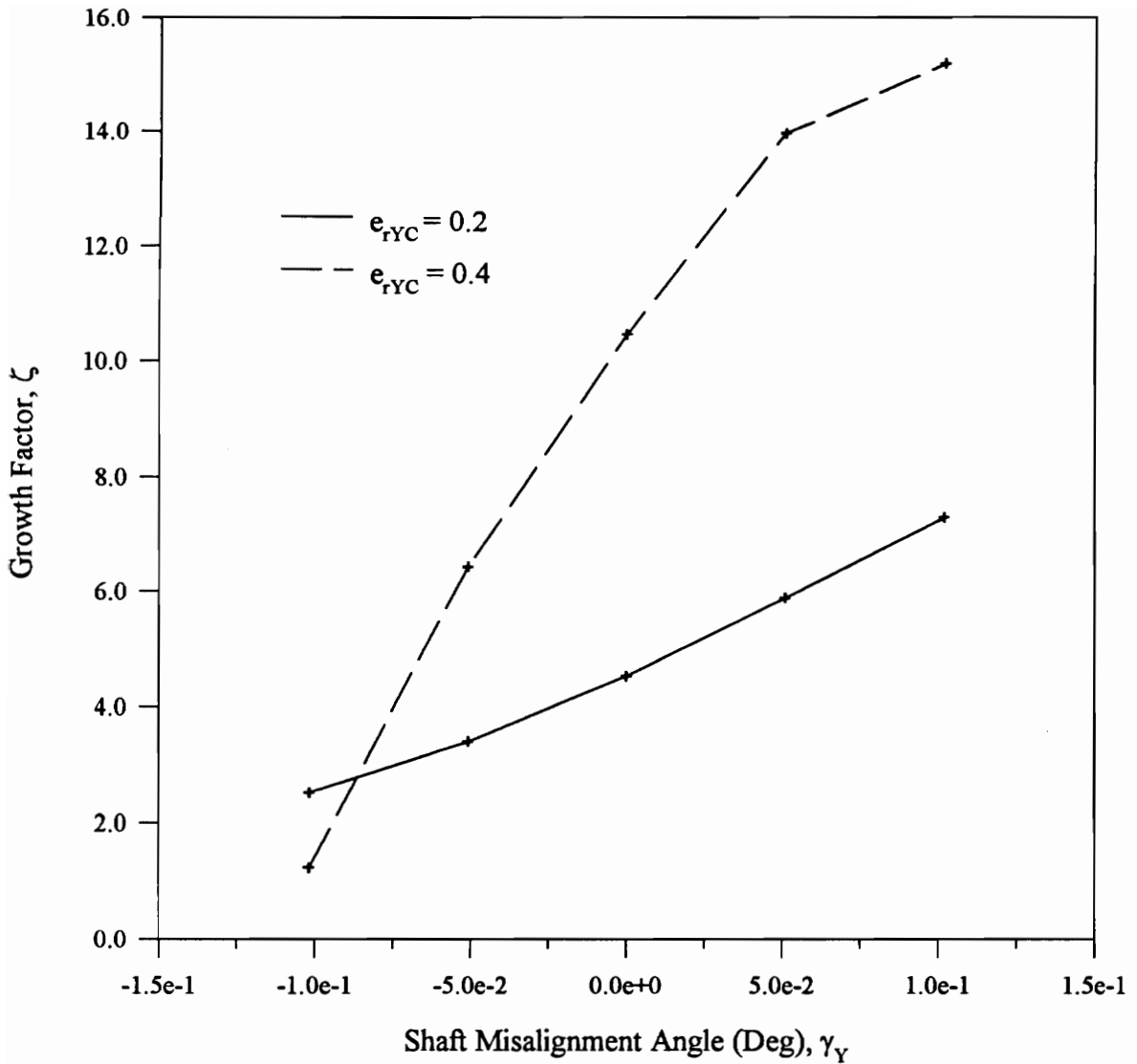


**Figure 114. Plot of Growth Factor vs. Shaft Misalignment Angle for Seals Operating at Different Eccentricity Ratios  
Operating Speed = 166.67 Hz (10000 RPM)**

## **Chapter 9**

### **Conclusions and Future Work**

In this final chapter, the conclusions drawn from the linear stability analysis and non-linear transient analysis results presented in this dissertation are given. Recommendations for future work in this area are also given.

#### **9.1 Conclusions from Linear Stability Analysis Results**

The major conclusions based upon the linear stability analysis results presented in this dissertation are as follows:

- 1) The variation of film temperatures in both the axial and circumferential directions is essential for accurate prediction of oil seal characteristics.

- 2) Increasing the operating speed increases the cross-coupled stiffness and decreases the damping coefficients which decreases the stability of the compressor rotor. The instability onset speed for the case presented in this dissertation was found to be

around 166.67 Hz (10000 RPM) which is close to typical design speeds of the compressor.

3) The axial flow rate through the seal can increase by a factor of two from a concentric seal to highly eccentric seal.

4) Lower supply pressures, typical of compressors in test stand conditions, reduce the axial flow rate and enhance the stability of the rotor.

5) Tapered seals have a tendency to reduce cavitation in oil seals.

6) Tapered seals enhance the stability of the rotor by increasing the direct stiffness and damping coefficients.

7) Tapered seals reduce the axial flow rate through the seal and increase the maximum temperature.

8) The groove depth typically applied to industrial seals is shown to be effective in breaking up the hydrodynamic pressures.

9) Circumferentially grooved seals reduce the magnitudes of stiffness and damping coefficients and enhance the stability of the rotor more than the tapered seals.

10) The sharp edge restriction on the groove does not influence the stiffness and damping coefficients significantly but has been shown to reduce the seal leakage as compared to a ring without a circumferential groove.

11) The axial flow rate through the circumferentially grooved seals does not depend upon the depth of the grooves used in this analysis.

12) Shaft misalignment reduces the leakage flow rate through the seal by reducing the projected clearance through the seal.

13) Shaft misalignment that increases the eccentricity at the exit enhances the stability of the compressor rotor.

## 9.2 Conclusions from Non-linear Transient Analysis Results

The major conclusions based upon the non-linear transient analysis results presented in this dissertation are as follows:

1) At operating speeds in the range of 100 Hz (6000 RPM) to 133.33 Hz (8000 RPM) the straight seals can be locked by using appropriate frictional force and the rotor operation can be stabilized.

2) At operating speeds close to 200 Hz (12000 RPM) increasing the frictional force does not help to make the seal locked because the unstable rotor eventually unlocks the seal and the system becomes unstable.

3) In general, the tapered geometry enhances the locking mechanism in the seals and the stability of the rotor. At the operating speed of 133.33 Hz (8000 RPM), tapered geometry used for the results in this dissertation is able to make the ring locked and stabilize the rotor which was unstable with straight seals under same conditions.

4) At the operating speed of 200 Hz (12000 RPM) tapered geometries with exit clearances of 0.0635 mm (0.0025 in.) and 0.0889 mm (0.0035 in.) reduce the rate of instability as compared to straight seals but do not completely stabilize the compressor rotor, whereas circumferential groove of depth 0.762 mm (0.03 in.) was found to be sufficient to keep the ring locked and stabilize the rotor vibration.

5) Just a circumferential groove of depth 0.381 mm (0.015 in.) or a taper with the exit clearance of 0.0635 mm (0.0025 in.) was found not to be sufficient to stabilize the rotor vibration at the operating speed of 200 Hz (12000 RPM), but their combination could make it stable.

6) Maximum temperature as high as  $170\text{ }^{\circ}\text{C}$ , which is above the melting point of the babbitt ( $165\text{ }^{\circ}\text{C}$ ), is predicted in a particular transient analysis in which the rotor was unstable.

### **9.3 Recommendations for Future Work**

The current research and resulting computer analysis program has greatly extended the current state of the art for analysis of floating oil ring seals. The following recommendations can be made to guide future research work in this area:

1) A test rig should be built to obtain the leakage, static and dynamic characteristics of straight, tapered, and circumferentially grooved seals for comparison with the results of the current analysis.

2) Further analytical investigation is required to determine the length to diameter ratio of oil seals that have significant moment and tilt coefficients to warrant their inclusion in the rotor system stability analysis.

3) The thermal distortion of the oil seal ring bore can also play a significant role in the accurate analysis of oil seals. Therefore, a method to account for the thermal distortion of oil seals should be considered as a direct extension of this current research.

4) In the finite element analysis of oil seals, it may be possible to reduce the solution time and increase the accuracy of the solution by using a non-uniform finite element mesh. Hence, adding a new capability to the current analytical tool for generating a non-uniform finite element mesh should be considered.

## REFERENCES

1. Black, H. F., and Cochrane, E. A., "Leakage and Hybrid Bearing Properties of Serrated Seals in Centrifugal Pumps," Sixth International Conference on Fluid Sealing, Munich, West Germany, 1972.
2. Black, H. F., and Jenssen, D. N., "Effect of High Pressure Ring Seals on Pump Rotor Vibrations," ASME Paper 71-WA/FE-38, 1971.
3. Kirk, R. G., and Miller, W. H., "The Influence of High Pressure Oil Seals on Turbo-Rotor Stability," ASLE Trans., Vol. 22, no. 1, 1979, pp. 14-24.
4. Ocvirk, F. W., "Short-Bearing Approximation for Full Journal Bearing," NACA TN 2808, 1952.
5. Kirk, R. G., and Nicholas, J. C., "Analysis of High Pressure Seals for Optimum Turbo Compressor Dynamic Performance," Proceedings of Conference on Vibration in Rotating Machinery, I.Mech.E., 1980.
6. Kirk, R. G., "Oil Seal Dynamics: Considerations for Analysis of Centrifugal Compressors," Proceedings of the 15th Texas A&M Turbomachinery Symposium, Texas A&M University, November 1986.
7. Reedy, S. W., and R. G. Kirk, "Advanced Analysis of Multi-Ring Liquid Seals," Trans. ASME, J. of Vibration and Acoustics, pp. 42-46, January 1992.
8. Kirk, R. G., and S. W. Reedy, "Analysis of Thermal Gradient Effects in Oil Ring Seals," STLE Tribology Transactions, Vol. 33, 3, pp. 425-435, 1990.
9. Emerick, M. F., "Vibration and Destabilizing Effects of Floating Ring Seals in Compressors," Proc. of the Workshop on Rotordynamic Instability Problems in High Performance Turbo-Machinery, Texas A & M University, pp. 187-204, 1982.
10. Dorton, D., "Experimental Evaluation of Effective Friction Coefficient for Liquid Ring Seals," Master's Thesis, Virginia Polytechnic Institute and State University, Blacksburg, Virginia, 1991.
11. Kirk, R. G., and D. B. Browne, "Experimental Evaluation of Holding Forces in Floating Ring Seals," Proceedings of the International Federation for Theory of Machines and Mechanisms International Conference, Lyon, France, pp. 319-323, September 1990.

12. Fuller, D. D., Theory and Practice of Lubrication for Engineers, 2nd ed., Wiley, New York, 1984.
13. Pinkus, O., Thermal Aspects of Fluid Film Tribology, ASME Press, New York, 1990, ISBN 0-7918-0011-3.
14. Huebner, K. H., The Finite Element Method for Engineers, John Wiley & Sons, 1975, ISBN 0-471-41950-8.
15. Reddy, J. N., An Introduction to the Finite Element Method, McGraw-Hill, Inc., New York, 1993, ISBN 0-07-112799-2.
16. Ramamurti, V., Computer Aided Design in Mechanical Engineering, Tata McGraw-Hill Publishing Company Ltd., 1987.
17. Bathe, K. J., and Wilson, E. L., Numerical Methods in Finite Element Analysis, Prentice-Hall, Inc., New Jersey, 1976, ISBN 0-13-627190-1.
18. Reedy, S. W., "The Determination of Pressure Profiles in Oil Ring Seals Considering the Influence of Temperature Gradients in the Sealing Fluid," Master's Thesis, Virginia Polytechnic Institute and State University, Blacksburg, Virginia, 1988.

## Vita

Sanjay Kumar Baheti was born on June 23, 1970 in Aurangabad, India. He received his Bachelor of Technology in Mechanical Engineering (1991) from Indian Institute of Technology, Madras, India. He began Graduate School at Virginia Polytechnic Institute and State University in August 1991.

During his graduate studies, he has compiled the following list of publications:

Baheti, S. K., and Kirk, R. G., "Thermo-hydrodynamic Solution of Floating Ring Seals for High Pressure Compressors Using Finite-Element Method," STLE, Tribology Transactions, Vol. 37, No. 2, 1994, pp.336-346.

Baheti, S. K., and Kirk, R. G., "Finite Element Thermo-Hydrodynamic Analysis of a Circumferentially Grooved Floating Oil Ring Seal," STLE, Tribology Transactions, Vol. 38, No. 1, 1995, pp.86-96.

Baheti, S. K., Kirk, R. G., and Ramesh, K., "Effect of Axially Grooved Oil Seals on the Leakage Flow and Stability of a Centrifugal Compressor," accepted for ASME/STLE joint conference, Florida, October 1995, and STLE Tribology Transactions.

Baheti, S. K., Kirk, R. G., and Ramesh, K., "Modeling of Rotor Shafting for Lower Mode Accuracy: Influence of section L/D," accepted for ASME 15th Biennial Conference on Mechanical Vibration and Noise, Boston, Massachusetts, September 17-21, 1995.

A handwritten signature in black ink, appearing to read 'Sanjay Baheti', is written over two parallel horizontal lines.